



Πολυτεχνείο
Κρήτης

Ανάπτυξη νανο-σύνθετων υλικών με βάση το ασβέστιο για την ενίσχυση των πορωδών υλικών δόμησης σε αρχιτεκτονικά μνημεία και παραδοσιακές κατασκευές

Διδακτορική
Διατριβή
Αναστασία
Μιχαλοπούλου

Συμβουλευτική Επιτροπή:

Νόνη Μαραβελάκη (επιβλέπουσα)
Βασίλης Κυλίκογλου (μέλος τριμελούς)
Νικόλαος Καλλίθρακας-Κόντος (μέλος τριμελούς)

Εξεταστική Επιτροπή:

Κωνσταντίνος Προβιδάκης (μέλος επταμελούς)
Μαρία Σταυρουλάκη (μέλος επταμελούς)
Αστέριος Καραγιάννης-Μπακόλας (μέλος επταμελούς)
Παναγιώτης Θεουλάκης (μέλος επταμελούς)



Technical
University
of Crete

Development of innovative nano-composite lime-based materials for the consolidation of porous building materials and the protection of built heritage

PhD Thesis

Michalopoulou Anastasia

Chania, December 2019

The implementation of the doctoral thesis was co-financed through the action "HUMAN RESEARCH POTENTIAL STRENGTHENING BY DOCTORAL RESEARCH" of the Operational Program "Human Resources Development, Education and Lifelong Learning", NSRF 2014-2020 with the co-financing of the European Social Fund and the European Social Fund Of the Greek State



Operational Programme
Human Resources Development,
Education and Lifelong Learning

Co-financed by Greece and the European Union



Acknowledgments

This research work was carried out at the Institute of Nanoscience and Nanotechnology (INN) of the National Center for Scientific Research "Demokritos" (NCSR "D") and the School of Architecture of the Technical University of Crete (TUC) under the supervision of **Professor Noni Maravelaki** (TUC), **Professor Nikos Kalithrakas** (TUC) and **Director of Research Dr. Vassilis Kilikoglou** (NCSR "D"). I would like to thank you all for providing me with the opportunity to carry out this research. I would like to thank the members of the examination committee for accepting to contribute at the final and most demanding part of this research: Professor Kwnstantinos Providakis (Technical University of Crete), Assistant Professor Maria Stavroulaki (Technical University of Crete), Associate Professor Asterios Karagiannis-Mpakolas (National Technical University of Athens) and Professor Panagiotis Theoulakis (University of West Attica).

I would like also to thank the **State Scholarship Foundation** for honoring me with the Phd Schoalrship co-financing through the action "HUMAN RESEARCH POTENTIAL STRENGTHENING BY DOCTORAL RESEARCH" of the Operational Program "Human Resources Development, Education and Lifelong Learning", NSRF 2014-2020 with the co-financing of the European Social Fund and the European Social Fund Of the Greek State, three years ago.

I would like to thank **Dr. Vassilis Kilikoglou** (NCSR "D") for providing me with the opportunity to be a member of the Ceramics and Composite Materials (CCM) group and scientifically guiding me through all the years I have been working there.

My great gratitude goes to my supervisor, **Prof. Noni Maravelaki** (TUC) for the guidance, support and encouragement throughout the course of this scientific research.

I would like to thank in particular my scientific supervisor **Dr. Ioannis Karatasios** (NCSR "D"), being a mentor to me both scientifically and professionally. Through his guidance and support, I was able to realize the transition from a post-graduate student to an early researcher.

I would like to express my appreciation to:

Professor Eleni Efthimiadou, Dr. Evangelos Favvas and **PhD candidate Ellisavet Michailidou** (NCSR D) for the collaboration on the use of the innovative dispersion of water enriched with O₂ nanobubbles, N₂ porosity measurements and the DLS measurements. This collaboration underlined the importance of a multi-disciplinary approach towards a scientific research.

Dr. Nikolaos Boukos (NCSR D) for trusting me with the use of SEM and for providing me the access and guiding to the interpretation of the results obtain with TEM.

Dr. Christos Trapalis (NCSR D) for trusting with the use of the UIP 1000 hdT Hielser.

Dr. Panagiotis Argitis and Dr. Anastasia Soutati (NCSR D) for trusting with the use of FTIR.

Dr. Andreas Sapalidis (NCSR D) for trusting me and collaborating with me in the use of MIP.

I would like to give special thanks all the members of the Ceramics and Composite Materials (CCM) group: Dr. Anno Hein, Dr. Maria Amenta, Dr. Dimitra Koumpouri, PhD candidate Stamatina Papaioannou and PhD candidate Ioannis Papadias (NCSR "D") who provided me with both professional and personal support, highly contributing to the implementation of this research.

Finally, and most importantly, I would like to thank my parents Michael and Elena, my brother George, the rest of my family and my "second" family, my close friends for enduring and supporting me all these years. I am really grateful for all the unconditional love and support....

Abstract

The consolidation of porous building materials aims at the re-establishment of the internal cohesion among the decayed stone particles and contributes to the sustainability of architectural monuments and protection of their aesthetical and historical values. A breakthrough point on the preservation of architectural heritage and the potential materials science in the consolidation and protection field was the introduction of nanotechnology in the synthesis and development of new materials

Among the vast range of the products applied for the consolidation of calcareous stones, of the most effective consolidants are considered the **nanolime (Ca(OH)₂ dispersions**. Nanolimes are colloidal dispersions of calcium hydroxide nanoparticles and their effectivity is due to the physical and chemical compatibility with the calcareous substrate and the enrichment of the active component, especially when compared with the traditional saturated solutions of Ca(OH)₂. The replacement of water by alcohol has improved the colloidal stability and the penetration ability of the dispersions of Ca(OH)₂, but, it has proven to create limitations on the consolidation efficiency through the incompleteness of the carbonation reaction and the migration of the Ca(OH)₂ nanoparticles to the layers of the substrate that are close to the surface during the fast evaporation of the alcohol. In addition to this, the lack of control of the morphological characteristics (size and shape) of the Ca(OH)₂ nanoparticles leads to an uncertainty concerning the morphological characteristics of the final product, thus, reducing the consolidation effectiveness.

Aiming to contribute on the optimization of the nanolime (Ca(OH)₂) dispersions, this study aims the development of **aqueous nanolime dispersions**. In particular, this study focuses on the control of the **morphological characteristics** of the Ca(OH)₂ nanoparticles, through the determination of the parameters affecting the surface modification of the nanoparticles. In addition to this, this study also focuses on the use of either aqueous dispersion medium or mixed polar dispersion medium, as a means to achieve the completion of the carbonation process.

The experimental outline was based on the comparative evaluation of the synthesis implemented via the two main synthetic routes: top-down and bottom-up. The first parameter being studied concerned the **experimental conditions**. The use of high-energy sonication led to the dissolution of the agglomerates (top-down) and to the reduction of size of the Ca(OH)₂ nanoparticles (bottom-up). The combined use of high-energy sonication and implementation of the experimental procedure under inert conditions (He) underlined the production of plate-like Ca(OH)₂ nanoparticles characterized by homogeneity in terms of size (bottom-up).

The second parameter studied in this research was the possibility of the **modification of the surface** of the nanoparticles through the addition of three **surfactants** in the aqueous dispersions: the non-ionic Triton X-100 and n-octylamine and the cationic amylamine. The comparative evaluation among those three surfactants revealed that the addition of **Triton**

X-100 led to the reduction of the size of both the nanoparticles (top-down and bottom-up) and the crystallites (bottom-up) and to the homogeneity of nanoparticles in terms both size and shape (bottom-up). This was attributed to the steric stabilization achieved by the addition of the non-ionic surfactant during the synthesis of the nanoparticles.

The third parameter being studied was the **modification of the dispersion medium**. The first modification concerned the **innovative use of water enriched with O₂ nanobubbles**. This aqueous dispersion medium led to the synthesis of hexagonal-plate like nanoparticles Ca(OH)₂ and to the absence of aggregates, achieving the steric stabilization. Also, the combined use of water enriched with O₂ nanobubbles with Triton X-100 and 2-propanol was proved to be effective. The second modification concerned the study of the effect of the addition of **2-propanol**. The addition of 2-propanol led to the production of spherical nanoparticles and to the increase of the specific surface area.

Furthermore, the determination of the effect of the modifications on the **colloidal stability** of the nanodispersions was implemented. The addition of the two non-ionic surfactants on the aqueous dispersions led to the increase of the colloidal stability of the aqueous dispersions for the first 60 min. The addition of 2-propanol led to the increase of the colloidal stability of the dispersions, through the achievement of steric stabilization and the lower sedimentation rates.

Finally, the newly synthesized dispersions of Ca(OH)₂ nanoparticles were applied into **different inorganic porous substrates**. The application of the dispersions on three sintered glass filters of different and pre-determined porosity underlined their diffusion inside the filters without the phase separation of the dispersions. The application on the dispersion on three porous building materials (limestone, sandstone, mortar) underlined the key role of the correlation between the microstructural characteristics of the substrate with the characteristics of the nanolime dispersions.

Overall, the synthesis of aqueous dispersions of Ca(OH)₂ nanoparticles was achieved. In addition to this, the innovative use of water enriched with O₂ nanobubbles was proved to be a successful replacement of water.

Περίληψη διδακτορικής διατριβής

Τα υλικά στερέωσης έχουν ιδιαίτερη βαρύτητα στον τομέα της πολιτιστικής κληρονομιάς, τόσο για την ενίσχυση της συνοχής των διαβρωμένων δομικών στοιχείων και των διακοσμημένων επιφανειών (φυσικοί λίθοι, κονιάματα, επιχρίσματα, πλάκες επένδυσης), όσο και για την προστασία και διατήρηση της ιστορικής και καλλιτεχνικής αξίας των μνημείων. Η πολυπλοκότητα που χαρακτηρίζει τις κατεργασίες στερέωσης, δημιουργεί μια συνεχή ανάγκη αποτίμησης των διάφορων κατεργασιών στερέωσης, καθώς και της τροποποίησης/βελτιστοποίησης της χημικής σύστασης και των ιδιοτήτων των υλικών στερέωσης.

Τα τελευταία χρόνια η **νανοτεχνολογία** έχει προσφέρει την προοπτική ανάπτυξης υλικών στερέωσης με βελτιωμένες ιδιότητες σε σχέση με τα παραδοσιακά υλικά στερέωσης. Εστιάζοντας στα πλεονεκτήματα της αυξημένης ειδικής επιφάνειας και περιεκτικότητας ενεργής ουσίας, έχει ως στόχο την παραγωγή συμβατών, πολύ-λειτουργικών ανόργανων υλικών σε μορφή διασποράς κατάλληλης να μεταφέρει ενεργά σωματίδια στο εσωτερικό του υπό στερέωση υποστρώματος στα σύγχρονα κτίρια και στα αρχιτεκτονικά μνημεία.

Ανάμεσα στο πλήθος υλικών που έχει χρησιμοποιηθεί κατά καιρούς σε κατεργασίες στερέωσης, πρωταγωνιστικό ρόλο κατέχει το **υδροξειδίου του ασβεστίου** $\text{Ca}(\text{OH})_2$. Η δράση του έγκειται αρχικά στην διείσδυση και εναπόθεση των σωματιδίων του υδροξειδίου του ασβεστίου στο πορώδες υπόστρωμα (ασβεστιτικής συστάσεως). Μετά την εξάτμιση του διαλύτη, εξαιτίας της φυσικής υγρασίας, πραγματοποιείται εν δυνάμει η αντίδραση της ενανθράκωσης με αποτέλεσμα τη δημιουργία συσσωματωμάτων παρόμοιας φύσης και υφής με το ασβεστιτικό συνδετικό υλικό. Σημείο τομής ήταν η μετάβαση από τη χρήση υδατικών κορεσμένων διαλυμάτων $\text{Ca}(\text{OH})_2$ στη χρήση αλκοολικών/υδρο-αλκοολικών διασπορών νανοσωματιδίων του $\text{Ca}(\text{OH})_2$. **Κύρια πλεονεκτήματα** των νανοδιασπορών υδροξειδίου του ασβεστίου αποτελούν η φυσικοχημική συμβατότητα (μεταξύ της ενεργής ουσίας και του ανθρακικού συνήθως υποστρώματος), η σταθερότητα των διασπορών και το αυξημένο ποσοστό της διεσπαρμένης δραστικής ουσίας ($\text{Ca}(\text{OH})_2$), ιδιαίτερα σε σύγκριση με τα κορεσμένα υδατικά διαλύματα.

Η μέχρι τώρα μελέτη της σύνθεσης, παραγωγής και εφαρμογής των νανοδιασπορών υδροξειδίου του ασβεστίου αναδεικνύει συγκεκριμένα **ζητήματα** όπως η μειωμένη ικανότητα διείσδυσης, ο διαχωρισμός φάσης μεταξύ του διασπορέα και των νανοσωματιδίων, η επιστροφή των νανοσωματιδίων στα επιφανειακά στρώματα κατά την γρήγορη εξάτμιση του αλκοολικού διασπορέα, η μη ολοκλήρωση της αντίδρασης της ενανθράκωσης λόγω έλλειψης υγρασίας και τέλος η μη δημιουργία ενός ομοιόμορφου και συνεχούς στρώματος ανθρακικού ασβεστίου CaCO_3 ως τελικό προϊόν της δράσης εξαιτίας των ανομοιόμορφων μορφολογικών χαρακτηριστικών των νανοσωματιδίων.

Στόχος της παρούσας μελέτης ήταν η **σύνθεση υδατικών νανοδιασπορών υδροξειδίου του ασβεστίου** $\text{Ca}(\text{OH})_2$. Συγκεκριμένα, εστίασε στην μελέτη των παραγόντων που επιδρούν στα **μορφολογικά χαρακτηριστικά των νανοσωματιδίων** $\text{Ca}(\text{OH})_2$ έτσι ώστε να παρουσιάζουν μορφολογική συμβατότητα με τα χαρακτηριστικά του ασβεστιτικού συνδετικού υλικού που προορίζονται να αναπληρώσουν. Επίσης, εστίασε στη διερεύνηση της δυνατότητας **χρήσης υδατικού διασπορέα** ώστε να εξασφαλιστεί η φυσική υγρασία που είναι απαραίτητα για τη διενέργεια και ολοκλήρωση της αντίδρασης της ενανθράκωσης. Η σύνθεση η σύνθεση υδατικών νανοδιασπορών υδροξειδίου του ασβεστίου επικεντρώθηκε στη μελέτη :

- ✓ Της επίδραση διαδικασίας σύνθεσης που ακολουθείται (top-down και bottom-up) στα μορφολογικά χαρακτηριστικά των νανοσωματιδίων $\text{Ca}(\text{OH})_2$
- ✓ Της επίδρασης της μείωσης της επιφανειακής τάσης ανάμεσα στα νανοσωματίδια $\text{Ca}(\text{OH})_2$ και το διασπορέα μέσα από διερεύνηση:
 - i. Της δυνατότητας τροποποίησης της επιφάνειας των νανοσωματιδίων $\text{Ca}(\text{OH})_2$ μέσω της χρήσης διαφορετικών επιφανειοδραστικών ουσιών και της επίδρασης αυτών στα μορφολογικά χαρακτηριστικά των νανοσωματιδίων $\text{Ca}(\text{OH})_2$
 - ii. Της επίδραση της καινοτόμας χρήσης νερού εμπλουτισμένου με νανοφυσάλιδες O_2 ως εναλλακτικό μέσο στερεοχημικής τροποποίησης των νανοσωματιδίων $\text{Ca}(\text{OH})_2$
 - iii. Της επίδραση της χρήσης μικτού πολικού διασπορέα νερού/ ισοπροπανόλης ως μέσο στερεοχημικής τροποποίησης των νανοσωματιδίων $\text{Ca}(\text{OH})_2$
- ✓ Της δυνατότητα χημικής τροποποίησης των νανοσωματιδίων $\text{Ca}(\text{OH})_2$ με στόχο τη παραγωγή νανოსύνθετων υλικών Ca-Si

Επιπλέον μελετήθηκε η συσχέτιση μεταξύ των μορφολογικών και ρεολογικών χαρακτηριστικών των νέο-σχηματισμένων νανοδιασπορών $\text{Ca}(\text{OH})_2$. Η μελέτη ολοκληρώθηκε με την εκτίμηση της ικανότητας διείσδυσης των νανοδιασπορών $\text{Ca}(\text{OH})_2$ σε 3 πυριτικά δισκία διαφορετικού αλλά και ομοιόμορφου πορώδους, καθώς και σε τρία υποστρώματα δομικών υλικών που χρησιμοποιούνται κατά κόρον στα αρχιτεκτονικά μνημεία της Μεσογείου: ασβεστόλιθος, πωρόλιθος και ασβεστιτικό κονίαμα.

Αρχικά έγινε συγκριτική μελέτη των δύο κύριων μεθόδων σύνθεσης σε υδατικό διασπορέα. Η μέθοδος **Top-down** αφορά την ετερογενή παραγωγή νανοσωματιδίων $\text{Ca}(\text{OH})_2$ μέσα από τη διάλυση μέσω μηχανικής ανάδευσης και χρήσης λουτρού υπερήχων ωριμασμένου ποτού ασβέστη. Χαρακτηριστικό του αποτελέσματος ήταν η παρουσία μεγάλων συσσωματωμάτων αποτελούμενων από νανοσωματίδια $\text{Ca}(\text{OH})_2$. Αντίθετα, η μέθοδος **Bottom-up** αφορά την απευθείας σύνθεση νανοσωματιδίων $\text{Ca}(\text{OH})_2$, μέσω της αντίδρασης διπλής αντικατάστασης: $\text{CaCl}_2 + 2\text{NaOH} \longrightarrow \text{Ca}(\text{OH})_2 + 2\text{NaCl}$. Η αντίδραση πραγματοποιήθηκε σε περιβάλλον εργαστηρίου, ενώ

χρησιμοποιήθηκε και εδώ το λουτρό υπερήχων. Χαρακτηριστικό του αποτελέσματος ήταν η παρουσία εξαγωγικών και ινωδών σωματιδίων $\text{Ca}(\text{OH})_2$, διαστάσεων που ανήκουν στη μικρο-κλίμακα.

Η πρώτη παράμετρος που τροποποιήθηκε ήταν η **αύξηση της ενέργειας των υπερήχων**. Έτσι έγινε αντικατάσταση του λουτρού των υπερήχων (ακουστικής ισχύος 60 W) με ρύγχος υπερήχων ακουστικής ισχύος 500 W. Η αύξηση της ενέργειας των υπερήχων οδήγησε στην περίπτωση της top-down σε **διάλυση των συσσωματωμάτων**, ενώ στη περίπτωση της bottom-up σε **μείωση των διαστάσεων** των σωματιδίων στη νάνο-κλίμακα και επικράτηση του **πλατόμορφου σχήματος**, κάτι που είναι συνδεδεμένο με αύξηση της ειδικής επιφάνειας των αντίστοιχων νανοσωματιδίων και αύξηση της δραστηριότητάς τους. Ενδιαφέρουσα παρατήρηση αποτελεί ότι τα νανοσωματίδια $\text{Ca}(\text{OH})_2$ που παρήχθησαν με τη μέθοδο **bottom-up** χαρακτηρίστηκαν από **μεγαλύτερη ομοιογένεια** ως προς το μέγεθός τους. Το πλατόμορφο και εξαγωγικό σχήμα το νανοσωματιδίων ενισχύθηκε με τη διεξαγωγή της bottom-up σε **αδρανείς συνθήκες He**. Η θετική επίδραση των παραμέτρων οδήγησε στην υιοθέτησή τους για όλες τις συνθέσεις.

Η δεύτερη παράμετρος αφορούσε τη συγκριτική μελέτη της αποτίμησης της δράσης τριών επιφανειοδραστικών σε υδατικό διασπορέα: των μη-ιονικών **Triton X-100** και **n-octylamine** και της κατιονικής **amylamine**. Στην περίπτωση της **Top-down**, μόνο η χρήση του Triton X-100 φαίνεται να επιφέρει μικρή μείωση του μεγέθους των νανοσωματιδίων. Στην περίπτωση της **Bottom-up** μεθόδου, η προσθήκη των μη-ιονικών επιφανειοδραστικών Triton X-100 και n-octylamine φαίνεται να οδηγεί σε **μείωση των διαστάσεων** των νανοσωματιδίων κάτι που αποδίδεται στη τροποποίηση της επιφάνειας των νανοσωματιδίων μέσω της ανάπτυξης δεσμού -H ανάμεσα στην υδρόφιλη κεφαλή των επιφανειοδραστικών και στο -OH της επιφάνειας των νανοσωματιδίων. Αντίθετα, η προσθήκη της αμυλαμίνης συνοδεύτηκε από αύξηση του μεγέθους και ποικιλία στα ως προς το σχήμα. Επιπροσθέτως, η προσθήκη του Triton X-100 οδήγησε σε μείωση των διαστάσεων των νανοσωματιδίων αλλά και των κρυσταλλιτών, ενώ συνοδεύτηκε από μεγάλη ομοιογένεια στο μέγεθος των πλατόμορφων νανοσωματιδίων. Για αυτό το λόγο και επιλέχθηκε ως **βέλτιστο επιφανειοδραστικό** για την επίτευξη της στερεοχημικής σταθερότητας ανάμεσα στα σωματίδια.

Η τρίτη παράμετρος που μελετήθηκε αφορούσε την **επίδραση της επιλογής υδατικού/μικτού διασπορέα**. Αρχικά δοκιμάστηκε για πρώτη φορά η αντικατάσταση του νερού με **νερό εμπλουτισμένο με νανοφυσαλίδες O_2** , που συντέθηκε στο ΕΚΕΦΕ Δημόκριτος. Η χρήση του συγκεκριμένου υδατικού διασπορέα φάνηκε να λειτουργεί κυρίως στη Bottom-up και οδήγησε στη σύνθεση **εξαγωγικών πλατόμορφων νανοσωματιδίων**, σε **μείωση των διαστάσεών** τους και σε **απουσία συσσωματωμάτων**. Αυτό αποδίδεται στην ρόφηση της νανοφυσαλίδας πάνω στην επιφάνεια, επιτυγχάνοντας έτσι τη στερεοχημική σταθερότητα των νανοσωματιδίων. Από τη σκοπιά της

θερμοδυναμικής, η ρόφηση της ναοφουσαλίδας κατά το στάδιο της της πυρονοποίησης των πρώτων πυρήνων $\text{Ca}(\text{OH})_2$ οδήγησε σε μείωση της επιφανειακής ενέργειας και συνεπώς στη σταθεροποίηση και στον έλεγχο του μεγέθους και του σχήματος των ναοσωματιδίων. Επιπροσθέτως, απέδειξε συμβατότητα ως προς τη κοινή χρήση με το επιφανειοδραστικό Triton X-100 και με την προσθήκη ισοπροπανόλης. Στη συνέχεια, δοκιμάστηκε η προσθήκη διαφορετικών ποσοστών ισοπροπανόλης στον υδατικό διασπορέα. Φάνηκε ότι η προσθήκη ισοπροπανόλης οδηγεί στη δημιουργία σφαιρικών ναοσωματιδίων, αυξημένης ειδικής επιφάνειας και ποικιλίας ως προς το μέγεθος, ιδιαίτερα στην περίπτωση της Top-down.

Επίσης, μελετήθηκε η δυνατότητα σύνθεσης ναοσωματιδίων ασβεστοπυριτικής μήτρας μέσω της διαδικασίας *sol-gel* και της σύνθεσης *janus ναοσωματιδίων* (σωματιδίων με διπλή χημική φύση). Μετά το πέρας 12 μηνών, η σύνθεση ναοσωματιδίων ασβεστοπυριτικής μήτρας διαπιστώθηκε μέσω του εντοπισμού της C-S-H φάσης.

Η επίδραση της τροποποίησης των μορφολογικών χαρακτηριστικών των ναοσωματιδίων μελετήθηκε και στη βάση της εκτίμησης της κινητικής σταθερότητας των αντίστοιχων ναοδιασπορών. Στην περίπτωση της προσθήκης των επιφανειοδραστικών ουσιών σε υδατικές ναοδιασπορές, η προσθήκη των μη-ιονικών Triton X-100 και *n-octylamine* αύξησε την κινητική σταθερότητα των υδατικών ναοδιασπορών για τα πρώτα 60 λεπτά, ενώ η *amylamine* οδήγησε σε μείωση της κινητικής σταθερότητας. Στην περίπτωση της μελέτης του διασπορέα, η προσθήκη ισοπροπανόλης οδήγησε στην αύξηση της σταθερότητας σε σχέση με τις καθαρά υδατικές ναοδιασπορές.

Τέλος, πραγματοποιήθηκαν προκαταρκτικές εφαρμογές των νέο-σύνθετων ναοδιασπορών στα 6 πορώδη υποστρώματά. Στην περίπτωση των δισκίων οι συνθέσεις που δοκιμάστηκαν διείσδυσαν κατά μήκος των δισκίων χωρίς να παρατηρείται διαχωρισμός των φάσεων τους. Στην περίπτωση των δομικών υλικών, μεγαλύτερη διείσδυση παρατηρήθηκε στην περίπτωση του πωρόλιθου, γεγονός που αποδίδεται στην ομοιογένεια του δικτύου των πόρων του. Ενδιαφέρον στοιχείο αποτέλεσε ότι η μεγάλη ικανότητα διείσδυσης των ναοδιασπορών με νερό εμπλουτισμένο με ναοφουσαλίδες O_2 , σε αντίθεση με τη μειωμένη κινητικότητά τους σταθερότητα. Τέλος, με την ολοκλήρωση της ενανθράκωσης παρατηρήθηκε σε όλες τις περιπτώσεις ο σχηματισμός ναοσωματιδίων ασβεστίτη CaCO_3 με συγκεκριμένη διευθέτηση συνοχής και μορφολογικών χαρακτηριστικών (σχήμα και μέγεθος) κοινών με το μικριτικό ασβεστίτη που απαντάται ως συνδετικό υλικό στα δομικά υλικά.

Συνολικά, επιτεύχθηκε η σύνθεση υδατικών ναοδιασπορών $\text{Ca}(\text{OH})_2$ με συγκεκριμένα μορφολογικά χαρακτηριστικά, μέσω του τροποποίησης της επιφάνειάς τους. Τα αποτελέσματα της συγκεκριμένης μελέτης συμβάλλουν στο τομέα της σύνθεσης και ανάπτυξης των ναοδιασπορών. Συγκεκριμένα, οδήγησαν στην επιτυχή

σύνθεση υδατικών νανοδιασπορών επιτυγχάνοντας τη στερεοχημική σταθερότητα ανάμεσα στα νανოსωματίδια με τη χρήση νερού εμπλουτισμένου με νανοφυσάλιδες O₂ χωρίς την αναγκαία προσθήκη επιφανειοδραστικών ή οργανικών διασπορέων.

Συνοπτική περιγραφή

Στο **Κεφάλαιο 1** παρουσιάζεται το ερευνητικό πρόβλημα και αναλύονται οι στόχοι και τα στοιχεία καινοτομίας της διατριβής.

Στο **Κεφάλαιο 2** παρουσιάζεται μια μικρή εισαγωγή στα φαινόμενα φθοράς των δομικών υλικών και η θεωρία γύρω από τις κατεργασίας στερέωσης.

Στο **Κεφάλαιο 3** παρουσιάζεται η σύνθεση και η διασπορά των νανοσωματιδίων $\text{Ca}(\text{OH})_2$. Παρουσιάζονται οι αρχές των διαδικασιών που αφορούν την σύνθεση των νανοσωματιδίων, η θεωρία της σύνθεσης των νανοσωματιδίων υδροξειδίου του ασβεστίου, οι παράμετροι που επιδρούν σε αυτήν καθώς και μια εκτεταμένη ανασκόπηση της βιβλιογραφίας που αφορά τη συγκεκριμένη διασπορά.

Στο **Κεφάλαιο 4** παρουσιάζεται η δομή της πειραματικής διαδικασίας καθώς και οι αναλυτικές μέθοδοι που χρησιμοποιήθηκαν για τη διεξαγωγή του χαρακτηρισμού των συνθέσεων.

Στο **Κεφάλαιο 5** παρουσιάζονται τα αποτελέσματα που αφορούν τη σύνθεση των νανοσωματιδίων υδροξειδίου του ασβεστίου $\text{Ca}(\text{OH})_2$. Συγκεκριμένα παρουσιάζονται τα αποτελέσματα του χαρακτηρισμού της σύνθεσης των νανοσωματιδίων $\text{Ca}(\text{OH})_2$ και της επίδρασης των παραμέτρων στα μορφολογικά τους χαρακτηριστικά. Οι παράμετροι αφορούν τις αλλαγές στην πειραματική διαδικασία, την επιφανειακή τους τροποποίηση μέσω της χρήσης επιφανειοδραστικών ουσιών και της επίδραση της τροποποίησης του διασπορέα έχοντας ως βάση το νερό. Ο χαρακτηρισμός ολοκληρώνεται με την εκτίμηση της επίδρασης των παραμέτρων και στα ρεολογικά χαρακτηριστικά των νανοδιασπορών. Επίσης, παρουσιάζονται και τα αποτελέσματα της χημικής τροποποίησης των νανοσωματιδίων.

Στο **Κεφάλαιο 6**, στη βάση των παρατηρήσεων των πειραματικών διαδικασιών του προηγούμενου κεφαλαίου παρουσιάζεται ο μορφολογικός χαρακτηρισμός των έξι βέλτιστων νανοδιασπορών υδροξειδίου του ασβεστίου $\text{Ca}(\text{OH})_2$. Ο χαρακτηρισμός συνοδεύεται από την εκτίμηση της κινητικής τους σταθερότητας καθώς και της ενανθράκωσή τους.

Στο **Κεφάλαιο 7** παρουσιάζονται αποτελέσματα της ικανότητας διεύδυσης των συγκεκριμένων νανοδιασπορών σε διαφορετικά ανόργανα πορώδη υποστρώματα

Στο **Κεφάλαιο 8** παρουσιάζονται τα γενικά συμπεράσματα καθώς και οι προτάσεις για τη δυνατότητα μελλοντικών ερευνών.

List of publications and conference contributions

Peer-reviewed publications

- Michalopoulou A., Michailidi E., Favvas E., Maravelaki P., Kilikoglou V., Karatasios I. (2020), Comparative evaluation of the morphological characteristics of nanolime dispersions for the consolidation of architectural monuments, *International Journal of Architectural Heritage*, doi: 10.1080/15583058.2020.1745323
- Michalopoulou A., Maravelaki P., Kilikoglou V., Karatasios I., (2020) Morphological characteristics of water-based nanolime dispersions for the conservation of built heritage, *Journal of Cultural Heritage*, *under review*
- Michalopoulou A., Favvas E.P., Mitropoulos A.C., Maravelaki P., Kilikoglou V., Karatasios I. (2018), A comparative evaluation of bottom-up and top-down methodologies for the synthesis of calcium hydroxide nanoparticles for the consolidation of architectural monuments, *Materials Today: Proceedings*, 5:14, p. 27425-27433, doi: 10.1016/j.matpr.2018.09.060
- Karatasios I., Michalopoulou A., Amenta M., Kilikoglou V. (2017), Modification of water transport properties of porous building stones caused by polymerization of silicon-based consolidation products, *Pure and Applied Chemistry*, 89:11, doi: 10.1515/pac-2016-1104

Publications in international peer-reviewed scientific books

- Michalopoulou A., Sioulas D., Amenta M., Kilikoglou V., Karatasios I. (2018) Variable Weathering Response of Architectural Marlstones Against NaCl Crystallization. In: Kouli M., Zezza F., Kouis D. (eds) 10th International Symposium on the Conservation of Monuments in the Mediterranean Basin. MONUBASIN 2017. Springer, Cham

Publications in international scientific conferences with full text crisis

- Michalopoulou A., Michailidi E., Favvas E., Maravelaki P., Kilikoglou V., Karatasios I. (2019), Comparative evaluation of the morphological and rheological characteristics of nanolime dispersions for the consolidation of architectural monuments, 5th Historic Mortars Conference (HMC 2019), June 19-21, Pamplona, Spain
- Μιχαλοπούλου Α., Φάββας Ε.Π., Μητρόπουλος Α.Χ., Μαραβελάκη Π. , Β. Κυλίκου Β. , Καρατάσιος Ι., (2017), Συγκριτική αξιολόγηση επαγωγικών και απαγωγικών μεθόδων σύγκρισης νανο-σωματιδίων υδροξειδίου του ασβεστίου για τη στερέωση των αρχιτεκτονικών μνημείων, 11^ο Πανελλήνιο Συνέδριο Χημικής Μηχανικής, Μάιος 25-27 Μαΐου, Θεσσαλονίκη, Ελλάδα

Publications in international scientific conferences with abstract crisis

- Michalopoulou A., Maravelaki N., Kilikoglou V., Karatasios I. (2019), Evaluation of nano-lime dispersions as swelling inhibitors for the protection of clay-based building materials, 15th European Meeting on Ancient Ceramics (EMAC) (EMAC 2019), September 16-18, Barcelona, Spain
- Καρατάσιος Ι., Μιχαλοπούλου Α., Καλαγρή Α., Ζερλέντης Μ., Αμέντα Μ., Τριανταφυλλίδης Π., Κυλίκογλου Β. (2019), Michalopoulou A., Maravelaki N., Kilikoglou V., Karatasios I. (2019), Πολιτισμικές και τεχνολογικές επιρροές στην εξέλιξη της οικοδομικής τεχνολογίας στα Δωδεκάνησα και το Βόρειο Αιγαίο, Τεχνολογίες Αιχμής στην Αρχαία Ελλάδα II: Τα Δωδεκάνησα κάτω από το Μικροσκόπιο, Ιανουάριος 11-13, Ρόδος, Ελλάδα
- Michalopoulou A., Bonazza A., Kilikoglou V., Karatasios I. (2018), Evaluation of the morphological characteristics of different consolidation nanomaterials for cultural heritage conservation, 5th Symposium Archaeological Research & New Technologies (5th ARCH_RNT), October 4-5, Kalamata, Greece
- Μιχαλοπούλου Α., Bonazza A., Κυλίκογλου Β., Καρατάσιος Ι. (2015), Αποτίμηση της στερεωτικής δράσης υλικών νανο-τεχνολογίας σε φυσικούς λίθους, Η συντήρηση της πολιτιστικής κληρονομιάς: προκλήσεις και επαναπροσδιορισμοί, Μαΐος 25-29, Αθήνα, Ελλάδα

Educational work

- Μιχαλοπούλου Α. (2018), Σύθεση, ιδιότητες και αξιολόγηση νανο-υλικών για εφαρμογές συντήρησης μνημείων, 2ωρο διδακτικό έργο στο πλαίσιο του μαθήματος Προηγμένα υλικά και μέθοδοι συντήρησης του ΠΜΣ: Συντήρηση της Πολιτιστικής Κληρονομιάς του Πανεπιστημίου Δυτικής Αττικής, 29 Νοεμβρίου 2018, Αθήνα, Ελλάδα
- Μιχαλοπούλου Α. (2017), Πως γερνούν τα αγάλματα, θερινό σχολείο της Ένωσης Ελλήνων Φυσικών Προσκεκλημένη ομιλία στο θερινό σχολείο της Ένωσης Ελλήνων Φυσικών, 24-27/07/2017, Ερέτρια, Ελλάδα

Workshops, courses and seminars attended

- Σχεδιασμός και διαχείριση ευρωπαϊκών προγραμμάτων, National and Kapodistrian University of Athens, E-Learning (ECVET: 5,42 points) (25/10/2019-)
- Days of Spectroscopy, seminar, INN, NCSR DEMOKRITOS, Athens, Greece (9/05/2019-13/06/2019)
- 2nd InHeriT Local Seminar, Promoting Cultural Heritage as a generator for sustainable development, Pafos, Cyprus (22/01/2018- 26/01/ 2018)
- Design and Optimization of Zero Energy Consumption Buildings, National and Kapodistrian University of Athens, E-Learning (ECVET: 12,5 points) (23/09/2016-08/05/2017)

- LabView, seminar, INN, NCSR DEMOKRITOS, Athens, Greece (24/1/2017)
- Viaduct (Diadrasis): scientific analysis seminar, two-day seminar for heritage specialists, Athens, Greece (30/11/2015-1/2/2015)
- Schematic representation and restoration of historic buildings, I.K.E.T.E.M. T.E.E. Athens, Greece (14/10/2015-6/11/2015)
- OPTO-CH 2015 Workshop (IESL-FORTH): Non- invasive optical analytical methods, Herakleion, Greece (04/05/2015-10/05/2015)

Honors and awards

- Scholarship for the funding of doctoral research: action "HUMAN RESEARCH POTENTIAL STRENGTHENING BY DOCTORAL RESEARCH" of the Operational Program "Human Resources Development, Education and Lifelong Learning", NSRF 2014-2020 with the co-financing of the European Social Fund and the European Social Fund of the Greek State
- Successful candidate for the Scholarship for the funding of doctoral research for the first action for "Supporting Research Enhancing Foundation Hellenic" financing of the Hellenic Foundation for Research

Table of Contents

Acknowledgments	iv
Abstract.....	vi
Περίληψη διδακτορικής διατριβής	viii
Συνοπτική περιγραφή.....	xiii
List of publications and conference contributions	xiv
Table of Contents	xvii
Chapter 1 – Introduction.....	1
1.1 Context.....	1
1.1.1. Nanomaterials in Consolidation	2
1.1.2 Recent approaches in consolidation materials.....	5
1.2 Aims and Research Objectives.....	6
Chapter 2 – Weathering and consolidation of porous building materials	9
2.1 Weathering of porous building materials.....	9
2.2 Consolidation of porous building materials	11
2.2.1 Parameters affecting the consolidation procedure and the result of the treatment	11
2.3 Short review of traditional consolidation materials	13
2.4 Evaluation of consolidation treatments.....	17
Chapter 3 – Synthesis and dispersion of Ca(OH) ₂ nanoparticles	20
3.1 Nanotechnology and Consolidation.....	20
3.1.1 Nucleation in dispersions	20
3.1.1.1 Homogenous nucleation.....	21
3.1.1.2 Heterogenous nucleation.....	22
3.1.2 Nucleation and nanoparticle growth	23
3.2 Calcium hydroxide nanoparticles: synthesis and dispersion process	25
3.2.1 From lime to nanolime.....	25
3.2.2 Synthetic procedures	26
3.2.3 Dispersion process.....	27
3.2.3.1 Dispersion medium (water, short chain aliphatic alcohols, nanobubbles)	33
3.2.3.2 Ultrasounds.....	34
3.2.3 Carbonation process.....	36

3.4 Surface functionalization	38
3.4.1 Surfactants	38
3.4.2 Non-ionic surfactants.....	41
3.5 State of the art in the synthesis of calcium hydroxide particles.....	44
3.5.1 Current experience on the top-down route	44
3.5.2 Current experience on the bottom-up synthetic route.....	45
3.5.3 Interaction between $\text{Ca}(\text{OH})_2$ and silicate products.....	49
Chapter 4 - Materials and Methods.....	50
4.1 Introduction.....	50
4.2 Synthetic routes of $\text{Ca}(\text{OH})_2$ nanoparticles (module M1).....	51
4.2.1 Top-down route	51
4.2.2 Bottom-up synthetic route.....	53
4.2.3 Synthesis of Ca-Si nanocomposites.....	56
4.3 Analytical Methods.....	59
4.3.1 Scanning and Transmitting Electron Microscopy (SEM-TEM).....	59
4.3.2 Dynamic Light Scattering (DLS)	61
4.3.3 Specific Surface Area calculation (BET).....	62
4.3.4 X-ray powder diffraction (XRD).....	64
4.3.5 Fourier Transform Infrared Spectroscopy (FTIR)	65
4.3.6 Raman Spectroscopy	66
4.3.7 Ultraviolet/ Visible light spectrophotometry (UV-VIS).....	66
4.3.8 Stereomicroscope	67
Chapter 5 - Synthesis and characterization of $\text{Ca}(\text{OH})_2$ nanodispersions.....	68
5.1 Introduction.....	68
5.2 Production of $\text{Ca}(\text{OH})_2$ nanodispersions	70
5.2.1 The basic top-down synthetic route.....	70
5.2.2 The basic bottom-up synthetic route.....	71
5.2.3 Implementation of the bottom-up synthetic route with anionic resin.....	74
5.3 Modifications of the basic synthetic routes	76
5.3.1 Sonication energy effect.....	76
5.3.2 The effect of inert atmosphere (He-atmosphere).....	80
5.4 Use of surfactants for nanoparticles functionalization	84
5.4.1 Addition of Triton X-100	84

5.4.2 Addition of n-Octylamine.....	90
5.4.3 Addition of Amylamine	95
5.4.4 Comparative evaluation of the surfactants effect in the bottom-up synthetic route	98
5.5 Modification of the dispersion medium	102
5.5.1 Use of O ₂ nanobubbles enriched aqueous solution	102
5.5.2 Use of mixed polar dispersion medium.....	110
5.6 Colloidal stability of Ca(OH) ₂ nano-dispersions	116
5.6.1 Effect of the addition of surfactants	116
5.6.2 Effect of modification of the dispersion medium.....	117
5.6.2.1 Effect of the use of O ₂ nanobubbles enriched aqueous solution	117
5.6.2.2 Effect of modification of the dispersion medium.....	118
5.7 Development of the Si-Ca(OH) ₂ nanocomposites	120
5.7.1 Sol-gel methodology.....	120
5.7.2 Development of Janus nanoparticles	124
5.7.3 Development of Si-Ca(OH) ₂ nanocomposites through the Stöber reaction	130
Chapter 6- Optimized dispersions of Ca(OH)₂ nanoparticles.....	133
6.1 Introduction.....	133
6.2 Characterization of Ca(OH) ₂ nanoparticles	135
6.2.1 Morphological characterization of Ca(OH) ₂ nanoparticles.....	135
6.2.2 Mineralogical and chemical characterization of Ca(OH) ₂ nanoparticles.....	143
6.3 Colloidal stability of Ca(OH) ₂ nanodispersions.....	146
6.4 Carbonation.....	147
6.4.1 The effect of Relative Humidity on the carbonation process.....	147
6.4.2 Carbonation of the six optimum dispersions of Ca(OH) ₂ nanoparticles	154
Chapter 7- Trial application of nanolime dispersions on porous substrates	160
7.1 Application methodology	160
7.2 Application results.....	167
7.2.1 Application results on glass filter discs of various porosity	167
7.2.2 Application results on porous building materials.....	170
Chapter 8 – Conclusions	179
8.1 Conclusions	179
8.1.1 Morphological characteristics of the Ca(OH) ₂ nanoparticles	179
8.1.2 Development of Si-Ca(OH) ₂ nanocomposites:.....	182

8.1.3 Colloidal stability of the dispersions Ca(OH) ₂ nanoparticles (Module 2).....	183
8.1.4 Carbonation monitoring.....	183
8.2 Future Research.....	185
Appendix	186
A Presentation of all dispersions of Ca(OH) ₂ nanoparticles.....	186
B Summary of the modified parameters of the synthetic procedures and their effect on the morphological characteristics of the Ca(OH) ₂ nanoparticles	189
C. Time period for subjection on ultrasound probe	191
D. Addition of Triton X-100	192
E. Dowex resin-testing	193
F. Deposition and carbonation of the Ca(OH) ₂ nanoparticles on the three porous building materials (limestone, sandstone and mortar)	195
References.....	199

Chapter 1 – Introduction

1.1 Context

It is a staggeringly small world that is below

“There’s Plenty of Room” at the Bottom, Richard P. Feynman, 1959

Nowadays, a key point to the scientific and technological achievements is the research on the fields of Nanoscience and Nanotechnology.

Nanoscience is the study of phenomena and manipulation of materials at atomic, molecular and macromolecular scales, where properties differ significantly from those at a larger scale, whereas **Nanotechnology** includes the design, characterization, production and application of structures, devices and systems by controlling shape and size at nanometer scale [1].

The increase on the progress on this field began when scientists started to have the ability to control the structure of the materials to smaller scales [2]. The importance of this ability is evident, in the area in the nano scale between 100 nm down to atomic level, where the materials have different and/or enhanced properties when compared with the same materials at a larger scale [2-6]. This is due to:

- The increased surface area: The increase of the surface area (per unit mass) results a related increase of the chemical reactivity (Fig. 1.1)
- The dominant role of the quantum effects: In nano-scale, quantum effects can modify the optical, magnetic or electrical properties of the material.

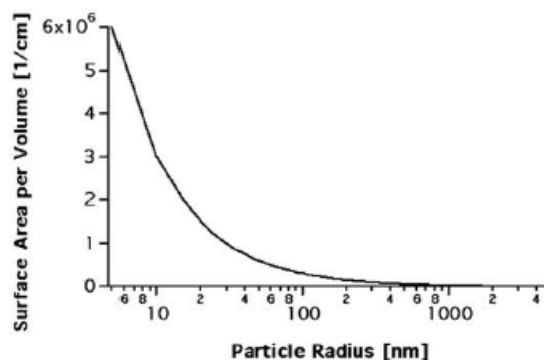


Fig. 1.1 Correlation between surface area per volume to particle radius [4]

The modified functional properties of nanomaterials concern super-plasticity, low-temperature sintering, enhanced diffusivity and dielectric properties, and tribological properties. Nanotechnology can also lead to the synthesis of materials characterized by important properties, like ultra high-strength, improved wear resistance, higher density and enhanced hardness. Furthermore, from the chemical point of view, the increased surface

area improves the chemical reactivity of the nanoparticle, gas absorbency and catalyst activity [3-5].

Finally, nowadays, the scientific research is focused on the synthesis and production of new nanomaterials characterized by:

- lower size heterogeneity
- high level of crystallinity
- improved purity and stability of the final product [2], [5-6].

1.1.1. [Nanomaterials in Consolidation](#)

A breakthrough point on the preservation of cultural heritage and the potential materials science in the consolidation and protection field was the introduction of nanotechnology in the synthesis and development of new materials [7-9].

The dominant parameter in consolidation on the nano scale is the elevated surface area. At nano scale, the surface is characterized by different physico-chemical properties, compared to the bulk phases. The higher surface- to -volume ratio enhances the surface properties of the matter rather than the bulk. The importance of this concept lies on its application to a sequence of crystalline solid phases, where the fine division of the material provides a large surface area [10-13]. Finally, this is the basic principle, that encompasses the application of nanoscience in consolidation [14].

The second most important parameter in understanding the application of nanoscience in the field of consolidation, is the strict definition of the chemical nature of the materials used. [2],[4],[15].

The main advantages of the application of nanotechnology in the field of consolidation can be summarized as following:

- The reduced size of the nanoparticles that enables penetration inside the porous substrate of archaeological materials [16-19]
- The increased surface to volume ratio that provides the enhanced reactivity of the active component [20-22]
- The ability to modify the nanoparticles during the synthetic procedures [16-17]
- The increased concentration of the active component, compared to the traditional materials [16-25]

During the past 20 years, the application of nanotechnology for the development of nanocomposites for consolidation of building materials was primarily focused on the study of two inorganic materials: a) calcium hydroxide and b) ethyl-silicate based nanoparticles [26-30]. Those two inorganic materials have been widely used on the consolidation of building materials mainly due to their physicochemical compatibility with the calcareous or calcareous/siliceous substrates [28] and the absence of the drawbacks caused by the application of organic polymers materials such as acrylic and epoxy resins [31-32].

Nanolime and nanosilica dispersions were primarily used in order to address the reported drawbacks of the poor penetration ability and extensive use of water in the case of lime-water [4],[14] and the presence of cracks at the silica gel, in the case of the ethyl-silicate-based consolidants [26,33].

Nanolime: In nanolime dispersions, the active component is calcium hydroxide ($\text{Ca}(\text{OH})_2$) particles of dimension between 50 to 600 nm dispersed in acoholic or water-alcoholic solutions. Depending on the product, nanoparticles have also different shapes, ranging from well-defined hexagonal plate-like to rounded and spherical and even undefined shape [34-37]. The consolidation action of nanolime relies on the lime technology. The replacement of water by alcohol has improved the colloidal stability and the penetration ability of the dispersions of $\text{Ca}(\text{OH})_2$, but, it has been shown to introduce limitations on the consolidation efficiency through the incompleteness of the carbonation reaction and the migration of the $\text{Ca}(\text{OH})_2$ nanoparticles to the layers of the substrate that are close to the surface during the fast evaporation of the short-chain alcohol [37-38].

The consolidation action of nanolime involves the penetration and deposition of $\text{Ca}(\text{OH})_2$ nanoparticles in the pores of the calcareous substrate, the evaporation of the dispersion medium and their subsequent carbonation (under humidity condition) resulting to the formation of calcitic aggregates of similar physiochemical characteristics with the calcareous substrate [25], [35], [39] (Fig. 1.2).

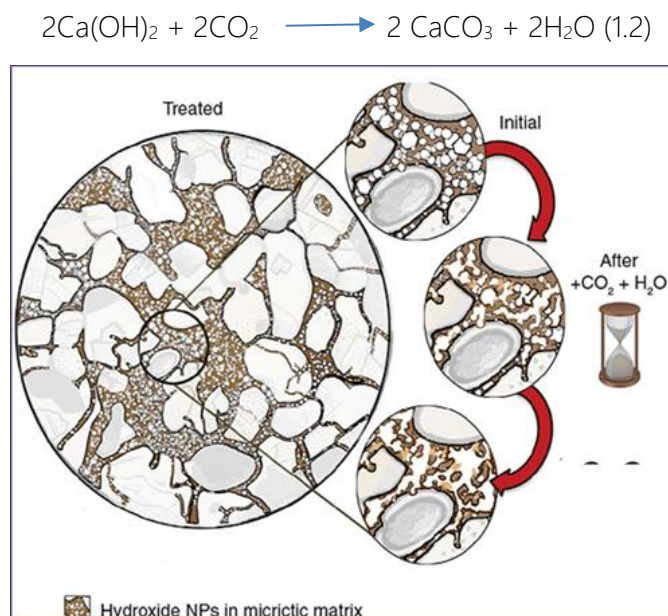


Fig. 1.2 Schematic representation of the deposition of the $\text{Ca}(\text{OH})_2$ on the calcareous binding medium [40]

The morphological characteristics of the $\text{Ca}(\text{OH})_2$ nanoparticles (size and shape) have a strong impact on:

- i) the penetration ability of the nanodispersions [2]
- ii) the reactivity of the nanoparticles, due to the modified physicochemical properties of the materials in the nanoscale [15]
- iii) the compatibility in terms of particles size with the type of the binding medium (micritic or sparry calcite) in sedimentary rocks (e.g. limestone, sparritic limestones, sandstones, lithic limestones) [41]

Besides the advantages of chemical affinity of the active component and kinetic stability of the alcoholic dispersions, still the application of calcium hydroxide nanodispersions undergoes some **disadvantages during application** such as:

- conglomeration on and near under the surface of the substrate [9], due to the partial migration of nanoparticles during the evaporation of the dispersion medium and the phase separation between the dispersion medium and the active component when dispersions are not stable [37], [42]
- lack of chemical affinity in cases of natural stones of calcareous-silicatic component (e.g. sandstones) [43]
- the use of organic solvents as dispersion medium removes humidity from the pore structure which may lead to incomplete carbonation, and consequent reduction of consolidation potential [44].

Nanosilica: is an aqueous dispersion of nanostructured colloidal silica (10-20 nm). The consolidation action includes the aggregation of the nanosilica particles resulting the formation of the amorphous silica gel, after the evaporation of water [30]. Under very humid environmental conditions, the application of nanosilica reduce the open porosity and the water saturation values due to the filling of the pores with the silica gel and the simultaneous increase of the size of the nanoparticles and the reduction of the interparticle distances, causing the re-generation of microporosity [45-46].

The basic advantage of the nanosilica lies the reduction of the potential cracks formation at the final product [48]. Nanosilica can be applied both in dry and wet conditions [23],[30].

However, several disadvantages have been reported concerning the application method [47] and the diffusion of the nanosilica inside the porous substrates [48-50]. Specifically, the application of nanosilica often presents poor penetration ability [51], strong dependence from the environmental condition [45] and reduced efficacy towards the reduction of water absorption, chloride migration and durability performance [52-53].

1.1.2 Recent approaches in consolidation materials

An alternative approach for consolidation is the use of **calcium alkoxides** [54]. Calcium alkoxides are synthesized through the reaction between metallic Ca and an alcohol. The final product of the carbonation reaction is CaCO_3 by either a CO_2 insertion into Ca-O bond of Ca (OR)₂ species with formation of a methyl carbonate derivative, subsequently transformed into CaCO_3 through R-OH elimination (Synthesis of $\text{Ca}(\text{OCH}_3)_2$) or, the hydrolysis of $\text{Ca}(\text{OR})_2$ to $\text{Ca}(\text{OH})_2$, followed by carbonation to CaCO_3 [54-56]. When applied to the calcareous substrate, calcium alkoxides tend to fill the micro-cracks and re-establish the initial cohesion [55]. Therefore, they can be applied to carbonate stones, plasters and wall paintings [57-59]. However, calcium alkoxides have been proven to alter the aesthetic appearance of the wall paintings, underlying the need of further study of their consolidation efficacy [55].

Another promising consolidant is based on the formation of **hydroxyapatite** ($\text{Ca}_{10}(\text{PO}_4)_6(\text{OH})_2$) inside the pores of limestones [60-61]. When compared to the silicate treatments, hydroxyapatite has proven not to alter the pore size distribution and the transport properties of the stone, reaching consolidation efficacy [60-61]. Nevertheless, this specific treatment hasn't yet been tested in terms of durability towards weathering processes and compatibility with the calcareous substrates [62].

The possibility of the improvement of the consolidating action of the nanomaterials is still under scientific investigation.

A promising alternative is the investigation of the possible combined action of a consolidant with a nanometric consolidant of the same chemical nature like the addition of **nanosilica** and **polysiloxane** treatment or **TEOS** that reduces the capillary forces developed during the drying of the gel [63-64]. This approach led to the enhancement of the hydrophobicity of the stone surfaces, leading to their protection, although, it has not proven to be effective as consolidation agent [64].

An innovative approach on the synthesis of a biomimetic nanomaterials for consolidation, composed by particles of **amorphous silica** and **calcium oxalates**, led to the synthesis and development of a strengthening agent with a partial protective effect [43], [65-66]. The alkoxy silane gels doped with the Ca-oxalate amorphous nanoparticles presented enhanced performance for the protection of stone substrates and at the same time address the issue of cracks formation at the final product [67]. However, the evaluation of the performance of these treatments is still an on-going process [67].

The combination of **TiO₂-SiO₂ nanoparticles** led to the formation of a nanomaterial that provides an effective adhesive and crack-free surface layer with self-cleaning properties to the stones and presents an ability for a deep penetration and effective resistance to salt crystallization [47], [68-69].

A different approach concerns the use of CaCO_3 nanoparticles either in aqueous dispersions [70]. The application of CaCO_3 nanoparticles has led to the reduction of the open porosity, but there are no indications concerning the improvement of the mechanical strength or the formation of chemical bonds between the CaCO_3 nanoparticles and the calcareous or silicatic substrates [70].

The synthesis of hybrid $\text{PMMA/SiO}_2/\text{ZrO}_2$ via the sol gel method has proven to enhance the resistance to weathering for sandstones [71]. Finally, the synthesis of dispersions of Ca(OH)_2 nanoparticles doped with ZnO with the addition of APTMS proved to have good penetration ability and lesser presence of the white haze after the application on the surface of the stone substrate [72].

1.2 Aims and Research Objectives

Based on the current consolidation approaches and the literature review, the use of Calcium Hydroxide as consolidation material is always an attractive field for research, providing several open issues for further improvement of the consolidation effect.

Still today, the use of Ca(OH)_2 nano-dispersions in consolidation faces several problems mainly related to the rheological properties and dispersion stability such as:

- ✓ The phase separation between the dispersion medium and nanoparticles during application, attributed both to the reduced colloidal stability of the aqueous dispersions and to the fast evaporation rate of the alcoholic dispersion mediums leading to the partial migration of the nanoparticles to the layers close to the surface.
- ✓ The limitation of the carbonation process, due to the use of alcoholic dispersion media.
- ✓ The reduced penetration ability of the dispersions.
- ✓ The aggregation phenomena and the consequent appearance of the whitening effect on the treated surfaces.
- ✓ The lack of chemical affinity in cases of calcareous stones that are rich in siliceous phases.
- ✓ The use of alcohol a dispersion medium initiates the increase of the volatile compounds emissions (VOCs) that can be harmful both to the human health and to the environment [4], [37], [58], [73].

The above issues underline a research gap between the synthesis of the nanolime materials and their application on the stone substrates. In order to make further steps in the optimization of the consolidation action, the establishment and the control of the interactions between those two stages of the application procedure is essential (e.g. the

study of the interaction between the surface tension and the porosity of the substrate in order to improve the penetration ability of the consolidation treatment).

Aiming to contribute in this field, this research project focuses on the development of water-based nanolime dispersions and the study of the synthetic parameters that affect the morphological characteristics of $\text{Ca}(\text{OH})_2$ nanoparticles,

More specifically, the following parameters are studied:

- The effect of the synthetic procedure followed (top-down vs bottom-up) on the morphological characteristics of nanolime particles
- The potential of functionalization of the nanoparticle's surface by different surfactants on their size and morphological characteristics
- The effect of the modification of the the surface tension between the aqueous dispersions medium and the active component on the colloidal stability and penetration ability of the dispersions
- The effect of O_2 nanobubbles enriched water as an alternative aqueous medium for promoting the steric stabilization between $\text{Ca}(\text{OH})_2$ nanoparticles
- The potential of chemical modification of lime-nanoparticles with the synthesis of Ca-Si nano-composites.

Also, the effect of those parameters on the rheological characteristics of the resulted $\text{Ca}(\text{OH})_2$ nano-dispersions, is being studied, aiming to improve their penetration ability and consolidation effectiveness. Furthermore, the correlation between the morphological and rheological characteristics of the newly formed dispersions of $\text{Ca}(\text{OH})_2$ nanoparticles and the microstructural characteristics of three porous building materials is also studied, by evaluating the penetration ability and deposition results of six laboratory developed nanolime dispersions in three types of porous substrates.

The key **innovation elements** of the present research project are:

✓ The study towards the synthesis and development of aqueous dispersions. This is an important element both for the development of the dispersions and for their effective consolidation action, as the presence of high moisture content is an essential element for the completion of the carbonation process and the efficacy of the consolidation action. In addition to this, the study of aqueous dispersions can lead to the formation of an eco-friendly consolidation treatment.

✓ The introduction of the aqueous solution enriched with O_2 nanobubbles as dispersion medium. This dispersion medium is tested as a mean for the implementation of the steric stabilization without the addition of surfactants or organic dispersion media.

✓ The evaluation of the results is implemented on three modules: the morphological characteristics of the $\text{Ca}(\text{OH})_2$ nanoparticles, the colloidal stability of the dispersions and the penetration/diffusion ability and deposition of the active component inside the substrates.

In this way, the discussion and evaluation of the experimental part is carried out on the basis of the examination of the nanoparticles-dispersion-substrate system as a whole.

The exploitation of the results derived from this doctoral dissertation will create the conditions for further development and scale up of aqueous dispersions, the facilitation of pilot application of these products in the field, in both architectural monuments and modern constructions, creating further prospects for the collaboration of academic institutions with industry, commercial exploitation and research results.

Chapter 2 – Weathering and consolidation of porous building materials

2.1 Weathering of porous building materials

Porous building materials like stone, brick, concrete, mortar suffer from natural decay phenomena caused by physical, chemical, mechanical and biological processes. The identification of the decay mechanisms is a subject of an interdisciplinary study since decay is a polyparametric process and it is affected by intrinsic and extrinsic characteristics of the porous building materials. Especially for the stones, a useful tool for the description of the stone is the ICOMOS-ISCS Illustrated Glossary on Stone Deterioration Patterns [74].

The raw materials that can be found in nature are at an equilibrium state, since they have already interacted with the physical environment [75]. The processing of those raw materials into building materials lead to an upgraded energy state [76]. Therefore, a higher processing degree corresponds to a more intense variation of the material in interaction with the environment and to the presence of intense decay patterns [75-76].

According to the 2nd law of thermodynamics, all physical phenomena are characterized by an automatic trend to a lower state of free energy ($\Delta F < 0$), of free enthalpy ($G < 0$), of chemical potential ($\mu < 0$), and to higher state of entropy ($\Delta S > 0$). The consequent submission to the 2nd law of thermodynamics imposes energy degradation of the materials to an equilibrium state or to more stable chemical compounds [77-78].

Consequently, even in the state of quarrying of natural stones, due to the mechanical procedures, the surface of the natural stones can be characterized as damaged. In particular, the surface is characterized by the presence of different and multiple “active centers”, which include both macroscopic and microscopic irregularities [75],[78]. The presence of those active centers is attributed to defects of the crystal lattice and are characterized as energy upgraded, since they are dominated by the asymmetry of the cohesion forces. Following the 2nd law of thermodynamics, the need of the energy degradation of the active centers facilitates the activation of the different decay patterns [78].

The mechanism of the main decay processes are briefly described in the next paragraphs.

a) *Physical Deterioration Processes*: The physical deterioration processes are closely related to the action of water, accompanied by other agents. This is the cause of structural disintegration of the building materials. Also, it doesn't affect the mineralogical or chemical composition of the stone [75]. This category includes:

- Capillary rise phenomena
- Frost action

- Salt crystallization phenomena [80-81]

b) *Chemical Deterioration Processes*: The processes involve in this category cause severe alteration to the material itself. This is mainly due to the fact that all the chemical deterioration processes are controlled by strong and active reactions like: hydrolysis, oxidation and dissolution. The result is the modification of the material mineralogical and chemical composition. Moreover, a key point to this category is the effect of air pollution [80-81]. This category includes:

- Acid corrosion
- Oxalate patina
- Sandstones and the leaching process
- Wet deposition (rain) on calcareous material
- Wet deposition (rain) on volcanic stones and sandstones
- Dry deposition (dew) [80-82]

c) *Mechanical Deterioration Processes*: Porous building materials like stone, mortars and plasters, can be characterized as rather rigid and brittle. This is due to the fact that they are composed of atoms connected by strong covalent bonds with a certain ionic character [75]. So, the bonds are directional and do not allow the plastic deformation of the crystals. This category includes:

- Tensile stress caused by static load
- Thermal expansion
- Traffic vibrations
- Human actions [83-86]

d) *Biological processes*: The effect of biological processes on building materials is variable, as it can be both beneficial and detrimental. Roots of creepers plants like ivy and other plants and detritals usually cause serious mechanical and chemical damage to constructions under a relatively short period of time [86].

Generally, the most common weathering processes that can be detected on the porous building materials of architectural monuments are the chemical processes, followed by the mechanical, electro-chemical and biological processes [75], [76] [80].

The on-going weathering processes lead eventually to the loss of the internal cohesion of the material, creating the need for consolidation action.

2.2 Consolidation of porous building materials

Consolidation is performed when natural stone loses the initial cohesion due to weathering, the material collapses and different decay patterns appear until a certain depth. The main goal of consolidation is therefore to restore the initial mechanical properties of the material (as a process of strengthening and reinforcing) and to reduce the rate of the decay [87] This is the reason why consolidation is considered of major importance among conservation interventions in the area of architectural and archaeological conservation [88].

Consolidation is a process that encompasses different parameters. The variety of parameters to be analyzed include the intrinsic stone properties, the extent of the decay phenomena on the stone (loss of material, enhanced roughness and increased porosity), the availability, compatibility, durability and reversibility of the consolidation treatments This is the reason why before assessing to the evaluation process of the consolidation treatment, it is important to understand the parameters which may affect the final result [76], [79].

2.2.1 Parameters affecting the consolidation procedure and the result of the treatment

1) *Application method*: The method of application affects the amount of the consolidant actually applied on the specimen, the penetration depth and the distribution of the material. In addition to that, the application method is closely related to other factors as: the physical state of the consolidants, the type of the solvent, the mechanism of deposition, the curation time of the treatment and the final number of applications [89-90]. As far as the actual method of application is concerned, in consolidants are usually applied by brush (mainly), spraying or long-term contact with the stone [91]. But, in the laboratory, there are many additional application methods: natural capillary absorption, poulticing total immersion, and vacuum or pressure impregnation [89]. Other attempts of improving the application include, the use of a "pocket system" that holds the consolidant against the stone, the use of "intravenous" tubes that lead to a rather slow drop- to-drop application to the stone surface and the development of a low pressure application technique that enhances the capillary absorption [79].

In the case of nanolime, several authors suggest the covering of the treated surface with the use alcoholic hydroxypropyl cellulose gels, cellulose poultice soaked with water or damp cloths, in order to diminish the evaporation of the dispersion medium [92-93]. In addition to this, the consequent defect of the whitening effect on the surface of the substrates, the residue nanolime must be removed from the surface with the use of sponge [24].

2) *Consolidation process*: From the chemical point of view, the difference among the consolidation treatments, exists on the basis of the consolidation mechanism:

- chemical reaction

- precipitation
- evaporation of the solvent
- polymerization
- hydrolysis
- condensation mechanisms [94-98]

The effectiveness of the consolidation is controlled by the type and properties of the final product of the consolidation action, deposited after the consolidation treatment. In particular it is controlled by the chemical compatibility of the final product with the stone's mineralogical composition, and by the level of strength of the bonds formed by the final product of consolidation and the substrate of the stone [96-99].

3) *Pore structure (pore size distribution, absorption coefficient, capillarity, permeability, drying, and adsorption) and condition of the stone substrate:* The condition of the substrate of the stone has a direct impact on the effectiveness of consolidation treatment, since the pore-structure affects the physical-chemical properties of the stones and the stone's sensitivity to weathering [95], [100]. The extent of the decay phenomena, affect directly the physical-chemical characteristics of the stone and indirectly the effectiveness of the application of the treatment, the penetration depth etc. Also, factors like the soluble salts, biological growth and deposition of air-born particles contribute to the reduction of the effectiveness of the consolidation treatment [81], [95], [101].

4) *Environmental setting:* The environmental setting (humidity, fluctuations of temperature, winds, micro-organisms) has a strong effect on the consolidation process, since it controls the actual application of the consolidation treatments (specifically, the evaporation of the solvent or the deposition rate of the material). In addition to that, it can alter the chemical compatibility of the consolidant (through intensive fluctuations of the temperature) or the service life of an organic material (through the process of photochemical degradation) [95], [102]. Finally, nowadays, special attention on the eco-friendly character of the consolidation treatments is required [79].

The above parameters highlight the complexity that characterizes the consolidation treatment, as well as the fact that there is no preferred consolidating treatment. In contrast, there is a constant need for the evaluation of different consolidation approaches that should be based on the systematic monitoring of quantitative and objective properties of treated specimens. However, in each case of stone consolidation, there are specific requirements that every consolidant must fulfill [88], [91], [95].

The requirements of a consolidation treatment are summarized and listed below [29], [75], [88], [91], [103-105]:

Physicochemical Compatibility	Chemical Stability
Mechanical Strength	Depth of Penetration
Ease of Application	Durability of the treatment
Cost	Time required for the application
Health and Safety Issues	Biological Resistance
Effect on liquid water and vapor permeability	Sensitivity to temperature and humidity during the application
No creation of whitening effect	No film creation on the surface
Aesthetic Compatibility- No intensive changes in color, texture and reflectivity	

2.3 Short review of traditional consolidation materials

Apart from the traditional materials used historically in conservation interventions (milk, egg white and natural glues), the ancestors of the modern consolidation treatments appeared in the late 19th century, with the use of flourides and fluorisilicatic compounds (such as HF). The use of those compounds on the restoration of the Cathedral of Bamberg in Germany, caused the acceleration of wear and the final destruction of the sculptures [106].

In 1823 the silicon tetrachloride $\text{Si}(\text{Cl})_4$ was synthesized by Berzelius, a substance that is still used for the production of TEOS. The main disadvantage is based on the difference between of the thermal expansion coefficient between the SiO_2 and the CaCO_3 of the calcareous substrates causing the formation of both superficial and inner cracks [102].

Finally, the famous water-glass or liquid glass dispersion of SiO_2 appeared in 1818 (by Fuchs with NaOH as a solvent) and in 1847 (by Kulmann with KOH as a solvent). The first application of water glass was made by Kulman in 1873 on many important monuments like the Notre Dame and the Louvre. The drawbacks of the deposition on the surface of salts of amorphous silica and K_2CO_3 or Na_2CO_3 , produced by the natural carbonation process, are still matter of interest along with the high cost of the production of water glass) [94],[102]. Furthermore, lithium water glass has been tested, since the produced LiCO_3 is much less soluble than the salts mentioned above [102].

Inorganic materials

During the 20th century, due to the lack of a single treatment universally accepted, a vast range of materials has been used for stone consolidation purposes. One of the most frequently group of materials used in consolidation actions are inorganic consolidants. This includes chemical compounds, with consequent precipitation of inorganic molecules that promote the bonding of the loose particles of the decayed stone [29]. In this way, the improvement of the cohesion properties of the stone is enhanced. The inorganic consolidants include limewater, barium hydroxide, sodium and potassium silicates, fluorosilicates and aluminates. The consolidation action of inorganic consolidants includes the precipitation of alkalis and alkaline earth cations that promote the bonding of the loose particles of the decayed stone [101]. Theoretically, inorganic consolidants have high potentials due to the chemical similarity between the decayed material and the bonding agent [101]. The main advantage of the inorganic consolidants is the fact that their action is mainly based on the environmentally friendly water-based systems, rather than on organic solvents [29], while their main limitation is the low penetration capacity and the formation of superficial to the stone surface layers [91]. Water is the most important activator of long-term deterioration processes in building materials [101].

Among the inorganic consolidants, **calcium hydroxide or limewater** is one of the most frequently used materials. The most preferable inorganic treatment through the years has been the saturated solution of $\text{Ca}(\text{OH})_2$ due to the chemical compatibility between the calcareous stone matrix and the precipitated material, thus leading to a consolidation action of high efficiency [4]. The lime technique includes the penetration of a saturated solution of calcium hydroxide (slaked lime, $\text{Ca}(\text{OH})_2$) and the subsequent evaporation of the solution. The result of this action will be the deposition of calcium hydroxide within the stone. In turn, calcium hydroxide will react with carbon dioxide (CO_2) in the air to produce calcium carbonate (CaCO_3) [35], [101], [107].

Theoretically, the chemical compatibility between the calcareous stone mass and the precipitated material provides high efficiency to this method. This is the reason why lime water is characterized as the most preferable inorganic treatment. Also, it is proposed that the effect of this method on closure of the pores prohibits the colonization of the stone by the microorganisms [79], [88].

Some of the basic drawbacks of this method are:

- Due to the low solubility of $\text{Ca}(\text{OH})_2$, the total amount of deposited CaCO_3 is characterized as rather low
- Limited penetration depth
- The end product of the consolidation action is not characterized by sufficient level of mechanical strength, hardness and adhesion to the substrate
- The carbonation reaction is usually not fully implemented
- Possible mobilization of soluble salts (due to the presence of water) and additional stress from the weight of the water

- Possible dissolution and re-crystallization of carbonates through the chemical and physical action of water

Due to the high alkalinity of limewater (pH=11), there is also a possibility of mobilization of the soluble iron compounds, that may lead to brownish discolorations. Moreover, the alkaline environment increases the rate of deposition of acidic air pollutants (NO_x and SO₂) which may lead to the dissolution of the nearly formed crystals of calcite [29], [105-106].

The in-situ evaluation of the consolidation action with the use of limewater underlined the reduced concentration of active component due to the low solubility of Ca(OH)₂ in water (1.65 g L⁻¹ at 20 °C) [107]. An alternative approach was the performance of more than 160 successive applications, in order for the consolidation level to be characterized as acceptable [106]. This kind of approach in consolidation actions, usually contains the risk of inducing large quantities of the dispersion medium inside the porous building material. In the specific case, the introduction of large quantities of water is directly connected with the presence of weathering phenomena such as : dissolution, discoloration, clay-swelling (in cases of sandstones of high clay content), mobilization of salts or freeze-thaw damage [44], [106].

A great part of the research is directed towards the improvement of the lime technique, since it is the most common inorganic consolidation treatment. In particular, the research focuses on the parameters mentioned below:

- ✓ Control of depth of penetration
- ✓ Crystallization parameters (required morphology and size)
- ✓ Carbonation (rate and effect on crystal growth)
- ✓ Calcium carbonate polymorphs
- ✓ Alternative dispersion media [4], [37], [58], [73], [108-112]

Silane based materials

Another category of materials used in consolidation actions are the alkoxy silanes and alkyl alkoxy silanes or silanes. The basic form of silane is a tetraalkoxy silane, where all four groups attached at the central silicon, can form cross-links with other silane molecules [113-114]. The main compounds in this category are: the methyltrimethoxysilane (MTMOS) and the tetra-ethoxysilane (TEOS). Those two compounds are not only easily found commercially, but they are also the synthetic basis of a number of proprietary products. In addition to that, there have been attempts to modify a number of silanes have also been tried, usually involving substitution of the methyl group with alkyl (methyltributoxysilane) or acryl groups (γ- methacryloxypropyl-trimethoxysilane) [89],[113].

The consolidation action of the silane-based materials is based on the formation and deposition of the amorphous silica gel. In particular, this process is composed by two reactions that act simultaneously. The first reaction is the hydrolysis of silanes by water in order to form the stable intermediate chemical compound, silanols (-Si-OH). This reaction

can be enhanced either by acidic or alkaline catalysis or by a tin-organic or lead compound catalyst already admixed to the majority of the ready commercial products presently available in the market. The second reaction is the condensation of the silanols and with the resulted formation of silica gel, which attributes to required strength to the stone [114-115] The water involved can be either from the atmosphere or from the stone itself or can even be added [88] (in which case, a solvent a solvent may be required in order to make the mixture miscible). In addition, an important characteristic is that the condensation reaction, and often the hydrolysis reaction also, takes place after the consolidation materials have been absorbed by the porous substrate. The main advantage is the hydrogen bonds that are developed between the silanol groups of the TEOS molecule and the hydroxide groups covering the surface of the minerals of the stone (quartz or feldspar) creating strong adhesion between the substrate and the end-up product of the polymerization reaction [43], [101], [113]. The main drawbacks that have been reported are the incomplete condensation reaction due to the rigidity of the structure and the distance between the silanol groups and the formation of cracks and the silica gel during shrinkage and drying [65],[116].

Acrylic resins

Generally, acrylic resins are derived from either acrylates or meth-acrylates. In addition to that, depending on whether they are cross-linked or not, acrylic resins can be thermoplastic or thermosetting. Usually their performance varies and depends on stone characteristics. As far as the actual consolidation action is concerned, the acrylic polymer molecules are deposited into the pore surface, through the evaporation of water. Theoretically, a continuous film is formed through the filling of the empty spaces between stone particles. Eventually, the loose cohesion of the stone is improved [80],[88].

From the chemical point of view, all acrylic compounds are esters from acrylic acid and any alcohol. They can be applied either as macromolecules dissolved in organic solvents or as aqueous dispersions (mainly as additives for mortars or repair mortars). Among the acrylates, the most known product among is polymethyl methacrylate (PMMA) [117]. PMMA is obtained through the polymerization of methyl methacrylate. But the most commonly used acrylate is Paraloid B 72. In fact, it is used for consolidating disintegrating stone surfaces, ceramic and metallic archaeological finds, wall paintings and many other objects. Also, it presents excellent adhesion properties [79],[94]. Furthermore, there have been various attempts for the synthesis of a mixture through which the consolidation effect of the acrylates and a hydrophobic ability would be combined. This is achieved by the synthesis of acrylic-silicone mixture, commonly known as Bologna Cocktail (BC). Bologna Cocktail is composed by a copolymer of methylacrylate and ethyl methacrylate (Paraloid B72, Rohm and Haas) and a partially pre-polymerized methyl siloxane (Dri Film 104, General Electric) in a solvent mixture. Theoretically, it is characterized by good penetration ability and good

stability towards photo-oxidative deterioration and to acid action due to atmospheric pollution [118],[119].

Epoxy resins

The action of most of the epoxy resins is based on the bisphenol-A epoxy resin which is the product of the reaction of bisphenol-A (a divalent alcohol) and epichlorhydrin [94],[120]. In particular, the bisphenol-A epoxy resin needs to be crosslinked to form a solid epoxy. This is achieved by the addition of a curing agent such as an amine. Amines (of primary, secondary and tertiary form), are hardeners that induce different types of crosslinking bonds that will influence the properties of the cured epoxy. Theoretically, epoxy resins cause a greater increase in mechanical strength than silanes or acrylic consolidants [75]. Also, they can present good adhesion properties. But, their use on the stone consolidation field, is generally avoided because their application lacks reversibility, and is characterized by excessive color changes, brittleness and viscosity. It must be noticed that a key point on the application of epoxy resins is the choice of solvent, the means of application, and post application procedures [79].

2.4 Evaluation of consolidation treatments

In general, the aim of consolidation treatment is to strengthen the micro structural and mechanical characteristics of stones, in order to in their weathering rate and prohibit further decay of the stone monuments, enhancing the cohesion between the materials grains [103]. However, there is not a clear-cut path for the assessment of the consolidation effectiveness, because the degree of success of the consolidation treatment greatly depends on the nature and the condition of the stone. Even when research protocols of the published literature are used, the comparison of different tests applied in different case studies is sometimes futile and ineffective [91], [112]. This is the reason why the evaluation process of the applied consolidation treatment must have an interdisciplinary character; primarily through laboratory tests, which assess the durability, effectiveness and potential harmfulness. This, along with the systematic study of the deterioration mechanisms and the set of a particular framework ethical restrictions, may eventually lead to an effective evaluation of the consolidation action [92],[95].

Nowadays, this is achieved through the calculation and estimation of specific parameters, which are listed below.

- *Internal cohesion*: This is one of the basic parameters in the evaluation process, since it represents the basic goal of the consolidation treatments. This is the reason why, theoretically, the set of values for calculating internal cohesion, is usually the main parameter to characterize the consolidation treatment [75]. The set of parameters encompasses both characteristics for the surface and for the bulk of the porous substrate. In particular, the surface can be characterized by surface hardness through scratch test, micro hardness, rebound test or abrasion resistance. In addition to that, the bulk stone can be defined

through the following tests: dynamic modulus of elasticity (E), velocity of the ultrasound propagation, pull out test, tensile strength (σ_t), compressive strength (σ_c), three-point bending strength (σ_b) etc. Among these, the ratio of dynamic modulus of elasticity over the flexural test (E/σ_f) can be used as a quantitative estimation of the crack sensitivity; in fact higher values of this ratio indicate higher crack sensitivity [75], [95], [102], [121-122].

- *Penetration depth*: is a crucial parameter for the evaluation of the consolidation treatment since is directly related to the action of the consolidant. The impregnation of the consolidant at an insufficient depth may cause the formation of a surface crust [95]. Moreover, penetration depth depends on the application method, the viscosity of the consolidant and on the characteristic properties of the stone: surface tension and pore structure (in particular on effective porosity and permeability) [106]. Furthermore, it can be defined through the use of a microscope, ultrasonic velocity tests and micro drilling techniques. Also, the use of a marker or of the method of UV fluorescence could be combined with a microscopic technique [88].

- *Pore structure*: As far as consolidation is concerned, the parameters of real density, open or effective porosity and pore size distribution are affected by a possible conservation action [75]. This is due to the fact that those parameters are related with durability of the substrate, the mechanical and surface properties, absorption and water transport. In addition to that, pore size distribution is used in order to make estimations on the treatments effect on durability, and also as a tool for the creation of the unique fingerprint of the micro-structure of the stone [95]. There are both direct and indirect techniques to assess the pore structure [88], [94].

- *Absorption and evaporation of water*: The presence of water on the stone is closely related with the decay phenomena: frost damage, thixotropy, biological growth, acid attack, salt crystallization and dissolution phenomena [95], [103], [123]. Apart from the tests based on the five hygroscopic properties, additional test, both direct (gravimetric methods, chemical analysis of water) and indirect (neutron image, contact angle of water drop) can be used to define this crucial property [124].

- *Durability against accelerated aging tests*: In order to ensure the durability of the stone, a primary goal is to diminish the deterioration rate. So, this includes the thorough study of both the chemical and mineralogical aspect of the stone and the study of the deterioration agent. In addition to that, the study of the deterioration agents is mainly done through the performance of artificial weathering aging tests (salt crystallization, freeze thaw cycles, frost resistance), along with additional tests for the estimation of the effect of air pollutant or biological organisms [95], [103].

A key point of conservation ethics is the following: as far as the deterioration mechanisms are concerned, both treated and untreated substrates should be characterized by the same rate of deterioration, same deteriorating agents, and by the same weathering patterns [94].

- *Aesthetic issues*: Theoretically, consolidation treatments should not cause any alterations to the color of the stone (which is usually affected by environmental conditions) [124]. In addition, a close relation between the color variation and the surface roughness has been established [124]. So, it is evident that possible color changes must be identified. This is accomplished through the use of CIE-lab system, accompanied by measurements concerning the surface roughness (roughness tests, image analysis techniques) [95], [124].

Chapter 3 – Synthesis and dispersion of $\text{Ca}(\text{OH})_2$ nanoparticles

3.1 Nanotechnology and Consolidation

In the field consolidation the materials involving nanotechnology are in the form of dispersions with nanoparticles being the stable phase and dispersion medium being a continuous phase. "Dispersions are materials comprising more than one phase where at least one of the phases consists of finely divided phase domains" (IUPAC definition). Dispersions can be categorized also in terms of the size of the nanoparticles of the dispersed phase, the presence of Brownian motion and the occurrence of precipitation [4], [125-126]. The materials, which are mainly used in the conservation field, are colloidal dispersions, micro emulsions, micelle solutions and gels [4].

Colloidal dispersions are two-phase systems composed by the dispersed materials (small particles, droplets or bubbles) in a dispersion medium (or dispersed phase). The size of the particles is between 1 nm and 1 μm (the upper limitation may be extended). Nanoscience includes organized structures in the area lower than 100 nm [126-127].

Micro emulsions are colloidal dispersions (usually composed of particles of $10\text{nm} < d < 50\text{nm}$), where a liquid is dispersed in a continuous liquid phase of different composition. Micro emulsions are thermodynamically stable systems, composed by water, oil and surfactant. Furthermore, in the conservation field, micellar solutions and gels (a non fluid colloidal or polymer network) are also used [128].

The two main synthetic routes for the synthesis of colloidal dispersions are:

- The top-down procedure: a material, whose features are not in nano scale, is altered in order to produce a nano-structured material
- The bottom-up procedure: the nanomaterial is built atom by atom [4],[19]

3.1.1 Nucleation in dispersions

Nucleation can be characterized as a discrete thermodynamic new phase. It describes the presence of the nucleus (an ensemble of atoms) and its ability to irreversibly grow into a larger nucleus inside the metastable primary (parent) phase [129].

The study of the nucleation is based on the classical nucleation theory (CNT), that was developed by Becker and Döring. The CNT is based on the macroscopic Gibbs capillary effect and imposes the categorization of nucleation into homogenous and heterogenous nucleation. Homogenous or primary nucleation refers to the random and spontaneous nucleation, under supercritical conditions (ex. supersaturation of the solution), whereas heterogenous or secondary nucleation refers to the nucleation occurring on the surface of particles that are characterized by the presence of nucleation site (structural inhomogeneities of the surface of the particle such as dislocations and impurities) [129-133].

3.1.1.1 Homogenous nucleation

In terms of thermodynamics, the Gibbs total free energy (ΔG) of a nanoparticle corresponds to the sum of the surface free energy (γ) and the bulk (crystal) free energy (ΔG_v). The bulk (crystal) free energy (ΔG_v) is negative and describes the energy of a favorable bonding between two monomers that leads to a lower state of the Gibbs energy. It depends on the parameters of temperature T , Boltzmann's constant k_B , the supersaturation of the solution S , and its molar volume, v . The surface free energy (γ) is positive describes the energy of an un-favorable bonding between two monomers that leads to a higher state of the Gibbs energy [129-130], [133].

So, for a spherical nanoparticles of radius r , the total free energy can be calculated according to (3.1) [129] :

$$\Delta G = -\frac{4}{3}\pi r^3 |\Delta G_v| + 4\pi^2 \gamma \quad (3.1)$$

As it can be observed in Fig. 3.1 the cluster Gibbs free energy presents a maximum point that is determined by the energy barrier of the activation energy ΔG_c and the corresponding critical radius r_c . The critical radius r_c represented the critical limit of the size of the clusters. For clusters of radius smaller than r_c , the dissolution of the clusters is more favorable than their growth.[133]

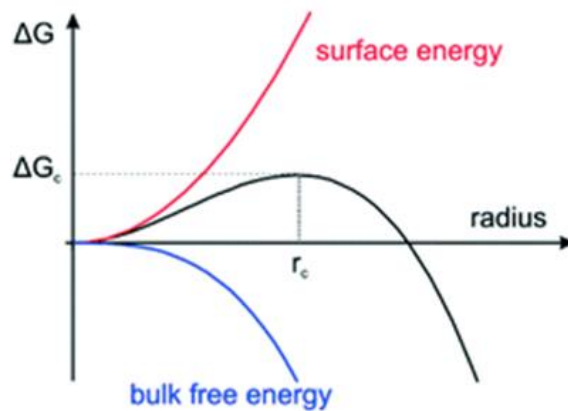


Fig. 3.1 Diagram of Gibbs free energy in relation with the particle radius

The critical radius r_c can be calculated by (3.2) [129]:

$$r_c = \frac{2\gamma}{|\Delta G_v|} \quad (3.2)$$

The critical Gibbs total free energy that is necessary for a nucleus to have in order to proceed to the formation of a stable nucleus can be calculated by (3.3):

$$\Delta G_{\text{crit}} = \frac{4}{3}\pi \gamma r_{\text{crit}}^2 = \Delta G_{\text{crit}}^{\text{homo}} \quad (3.3)$$

3.1.1.2 Heterogenous nucleation

In terms of thermodynamics, the lower effective surface free energy presented at the nucleation sites (such as impurities, nanobubbles, structural defects, phase and grains boundaries), directly decrease the critical Gibbs total free energy. So, contrary to the homogenous nucleation, the nuclei are formed on the surface of a foreign body. Therefore, the spherical shape is replaced by a cap-shaped forming a contact angle θ with the substrate (Fig. 3.3). If $\theta < \pi$, the nuclei and the nucleation site present high affinity and consequently, the surface free energy (γ) decrease. [129],[133]

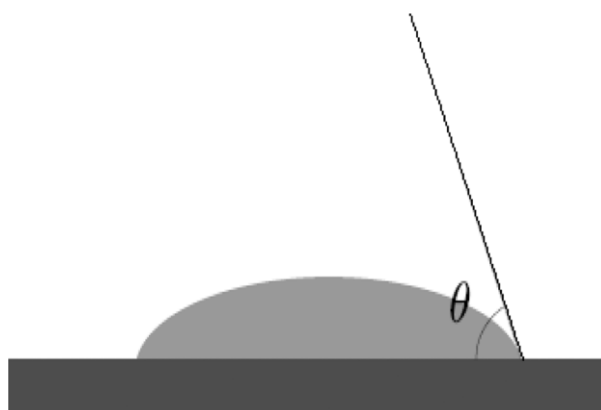


Fig. 3.3 A liquid phase immersed in a fluid (gas or liquid) wets a solid surface, defining the contact angle [129]

Consequently, a new term is introduced in the law of the primary homogenous nucleation (3.4):

$$\Delta G_{\text{crit}}^{\text{hetero}} = \phi \Delta G_{\text{crit}}^{\text{homo}} \quad (3.4)$$

that is depended on the contact angle between the nuclei and the substrate (3.5):

$$\phi = \frac{(2 + \cos \theta)(1 - \cos \theta)^2}{4} \quad (3.5)$$

In general, in the field of the synthesis of nanoparticle, heterogenous nucleation is connected with the seed-mediated growth of the nanoparticles and its occurrence is most probably expected, compared with the homogenous nucleation. But in reality, both nucleation types occur at the same time [129-130]. A key point to control the shape of the nanoparticles, in terms of thermodynamics, is the reduction of the surface free energy [131].

3.1.2 Nucleation and nanoparticle growth

There are five main theories concerning the nucleation and growth of nanoparticles based on the description of the different processes/mechanisms. A brief description of the main theories follows [4], [129].

a. LaMer Mechanism

The basis of the LaMer's mechanism of (sulfur) nucleation is the conceptual separation of the nucleation and nanoparticle growth in different stages (Fig. 3.4). The (theoretical) qualitative curve describes the monomer concentration as a function of time.

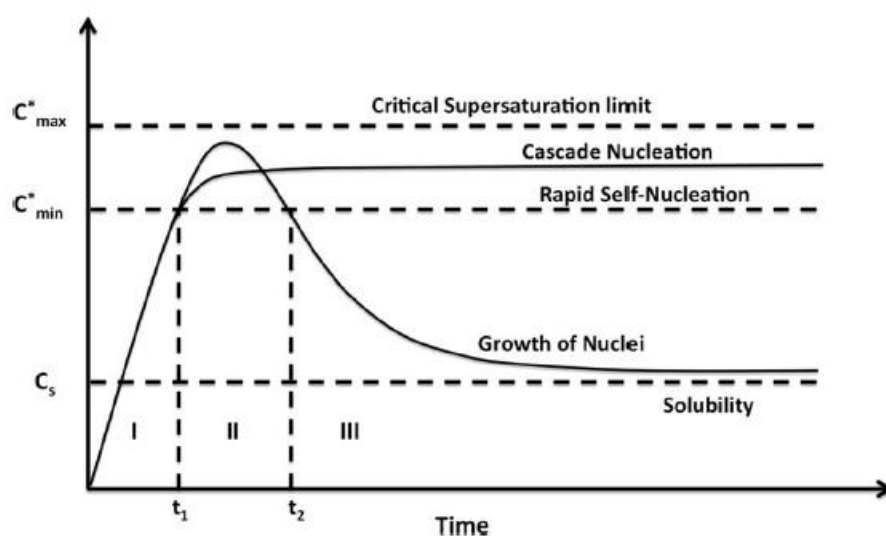


Fig. 3.4 La Mer diagram. The supersaturation phase (phase I), the nucleation phase (phase II) and the growth phase (phase III) are indicated, as well as two different pathways leading to particles with different polydispersity [4]

As it can be observed in fig. the first part (I) concerns the rapid increase of the concentration of the monomer and reaches the critical supersaturation level (C_s), where the realization of the homogenous nucleation can be described as possible to occur but “effectively realized” (supersaturation phase); the second part (II) concerns the so called burst nucleation, where rapid self-nucleation can be occur due to the increase of the saturation level up to C_{\min} at which the activation energy as an energy barrier can be overcome (nucleation phase); and the third part (III) concerns the absence of any homogenous nucleation (self-nucleation) due to the low concentration of monomers and the consequent occurrence of the growth of nanoparticles (growth phase). Often the third part is related with the presence of heterogenous nucleation. Overall, the LaMer model can successfully describe the process of the nucleation and growth of a stable nuclei but can be used for the prediction of the evolution of the nanoparticle’s size distribution [4], [129-130], [133]. Both nucleation and growth phases can be influenced by rate of production and consumption of the primary nuclei [131].

b. Ostwald and Digestive Ripening

According to the Ostwald ripening theory or coarsening procedure [131], the nanoparticles growth occurs in the case of the simultaneous action of the increase of solubility of the nanoparticles and the reduction of their size. The nanoparticles tend to dissolve and consequently, the size of the larger nanoparticles is further increased [129]. On the contrary to the Ostwald ripening, Digestive ripening suggests due to the surface free energy of the nanoparticles, the larger nanoparticles are dissolved and thus the number of the smaller nanoparticles is increased [129], [134].

c. Finke-Watzky Two Step Mechanism

The basis of the Finke-Watzky two step mechanism is the concurrent realization of both nucleation and growth processes [129]. The first step concerns the realization of a slow continuous nucleation, whereas the second step concerns the realization of the autocatalytic surface growth. Although this theory differs from the CNT, both theories are based on the crucial role of the critical nanoparticle's size [129], [135].

d. Coalescence and Orientated attachment

This theory attributed the growth of the nanoparticle's size to the phenomena of coalescence and orientated attachment of smaller nanoparticles [129]. The difference between these two phenomena stand on the different orientation of the crystal lattice at grain boundary. In the case of the occurrence of coalescence, no orientation is needed. In the case of the, the attachment must follow a common crystallographic alignment [136].

e. Intraparticle Growth

According to Peng et al.[137], intraparticle growth takes place when a difference occurs between the surface free energy of the different crystal facets of the nanoparticle. This is attributed in the case where the surface free energy of the monomer's present lower values in respect with the surface free energy of the crystal facets, leading to the dissolution of the high energy facets, the growth of the lower ones and the consequent appearance of the intraparticle diffusion phenomenon [129], [137].

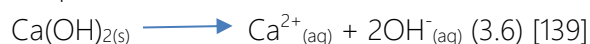
Finally, mathematical models using rate equations are used as alternative approaches in order to describe the evolution and growth of the size of the nanoparticles.

3.2 Calcium hydroxide nanoparticles: synthesis and dispersion process

3.2.1 From lime to nanolime

In order to overcome the previously mentioned disadvantages of limewater, in the last two decades, research has focused on the application of colloid and surface science in the field of consolidation materials. One of the most promising materials appears to be nanolime. Nanolimes are colloidal dispersions of calcium hydroxide nanoparticles and their effectivity is due to the physical and chemical compatibility with the calcareous substrate and the elevated concentration of the active component, especially when compared with the traditional limewater [35], [37-38],[138].

In the case of the limewater, calcium hydroxide forms a saturated solution of Ca^{2+} ions, where the calcium content is limited by the solubility constant of calcium hydroxide and the temperature of the solution [35], [37-38],[138].:



In the case of the synthesis of nanolime via the bottom up synthetic route, the synthesis is based on the assemblage of atoms and the consequent precipitation of the solid product. The synthesis is realized via the homogenous reaction of [4], [139]:



Full-shell Clusters		Total Number of Atoms	Surface Atoms (%)
1 Shell		13	92
2 Shells		55	76
3 Shells		147	63
4 Shells		309	52
5 Shells		561	45
7 Shells		1415	35

Fig. 3.5 Total number of atoms and % of surface atoms in clusters of nanoparticles consisting of one to seven full shells. [4]

As it can be observed in Fig. 3.5, the reduction of the particles size involves the assemblage of a smaller number of atoms. The incorporation of nanoparticles may result therefore the development of a $\text{Ca}(\text{OH})_2$ nano-dispersion, where the content of the active component (nano-lime particles) can be adjusted to much higher values (0,1-20 % wt) [4],[139].

In addition to this, the increased surface area of nanoparticles, enhances the consolidation potential and increases of the reactivity of the nanoparticles [14].

The first attempts to overcome the limitations of limewater through the application of nanotechnology, were implemented back in the early 2000s by Ambrosi and Giorgi [8]. Giorgi et al. 2000 [140] studied the synthesis of dispersions of $\text{Ca}(\text{OH})_2$ nanoparticles through the use of the heterogeneous synthetic route (following the slaking of quicklime), whereas Ambrosi et al. 2001 [8] studied through the use of the homogeneous synthetic route. In both cases, apart from the **synthetic route**, a major parameter was the **selection of the appropriate dispersion medium**, in specific between water and short chain aliphatic alcohols. The selection criteria of the dispersion medium were connected with the stability of the final dispersion, the sorptivity and penetration ability with the porous substrate. The final result was characterized as polydisperse in terms of the size of the nanoparticles, since both nano- and micro-particles of $\text{Ca}(\text{OH})_2$ were present, along with the presence of aggregates. Baglioni et al. 2006 [2] was the first to produce nanolime dispersions, with the synthesis of $\text{Ca}(\text{OH})_2$ nanoparticles of dimensions below 500 nm. The size limit of the nanoparticles according to nanotechnology is below 100 nm, however, due to the need for the resemblance of the end up product of the consolidation action with the sparry calcite, the increase of the desired limit was necessary. Those studies were the primary steps for the study and development of nanolimes as effective consolidation product.

Nowadays the application of nanotechnology in cultural heritage involves the optimization of the development of colloidal dispersions., the development of a colloidal system involves two basic steps:

- ✓ The synthetic process
- ✓ The dispersion process

3.2.2 Synthetic procedures

The two basic synthetic routes for obtaining the calcium hydroxide nanoparticles are the "top-down" and the "bottom-up" synthetic route.

The "top-down" synthetic route involves the breaking down of bulk solids, the decreasing of the particle's size either by grinding them into smaller particles (mechanical synthesis) or by thermal decomposition into molecular or atom size. The use of grinding technique is the most common [2],[4],[14]. It can be characterized as an heterogeneous method. However, it

presents two main drawbacks: a) the limitation of the achieved particle size because of the particles' tendency of aggregation (limiting the particle size to micron scale) and b) the susceptibility of the particles' surface to contamination either by atmospheric gases or by the mill [2].

The “**bottom-up**” synthetic route involves the building up of the particles to a desired size by the external collection of ions or atoms, following either the solid-state sintering route and the realization of a reaction or the precipitation and growth of crystals from liquid (mainly) or vapor phase [4], [14]. A common application of the bottom-up synthetic route concerns the realization of the homogenous phase reaction between two or more solutions, in the case of the synthesis of inorganic nanoparticles that present low solubility (Ca(OH)_2 in aqueous dispersion medium). In this case, the size of the newly synthesized inorganic nanoparticles is determined by the high degree of saturation, a parameter that can be controlled by pressure or temperature [14].

3.2.3 Dispersion process

The second part of the procedure for the development of a colloidal system involves the creation of stable dispersions, through the dispersion of the particles in the dispersion medium (or continuous phase) [14], involving the use of ultra-homogenizer systems and ultrasonic baths [9]. Nanoparticle dispersions do not need stabilizers, since they exhibit a high kinetic stability. The major parameter in this stage is the selection of the appropriate dispersion medium, mainly affected by the **surface tension** of the dispersion medium [4], [17]. According to the relevant literature, for alkaline-earth metal hydroxide nanoparticles (like Ca, Mg etc), short chain aliphatic alcohols tend to be appropriate dispersion mediums, because the dispersion mediums' low surface tension provides quickly and easily the wetting of the substrates' matrix, providing a high penetration ability [4], [17], [141]. Also, the addition of Ca(OH)_2 increases the surface tension of the dispersion medium [4], [142].

In general, a dispersion medium used in stone consolidation treatments must be characterized [14],[37],[42]:

<i>Volatility</i>	The dispersion medium must be characterized by an appropriate degree of volatility that will enable the diffusion and penetration inside the porous substrate and not the fast evaporation of the dispersion medium forcing the nanoparticles to remain on the surface of the porous substrate in the form of agglomerates
<i>Hydrogen Bonding System</i>	In the cases of calcareous porous substrates like natural stones and mortars, the penetration ability of the nanodispersion is enhanced by the selection of the appropriate dispersion medium that forms hydrogen bonds with the substrate
<i>Action</i>	In the cases of calcareous porous substrates like natural stones and mortars, the penetration ability of the nanodispersion is enhanced by the selection of the appropriate dispersion medium that forms hydrogen bonds with the substrate

A key point in the optimization of the development of the dispersions of $\text{Ca}(\text{OH})_2$ nanoparticles is **the understanding of the transportation mechanism**. During the diffusion and absorption phase, nanolime penetrates easily the stone substrate, but during the drying phase, when the dispersion medium moves back to the drying surface, nanolime particles are deposited, causing the appearance of accumulation phenomena in the layers very close to the surface [37],[42],[143-144]. In order to have a good penetration during the consolidation action, the evaluation of the application procedure must be examined in relation to the whole system of nanodispersion and porous substrate, since is favorable when the solid air surface energy is higher than the solid/liquid surface energy [144].

Apart from the transportation mechanism, the size of the nanoparticles and the microstructural characteristics of the porous substrates also define the efficiency of the consolidation action [145]. In particular, the deposition of the $\text{Ca}(\text{OH})_2$ nanoparticles is affected by the size of the nanoparticles. During the penetration of the nanodispersion inside the porous substrate, and the evaporation of the dispersion medium, the nanoparticles of smaller size (30 nm to 60 nm) migrate back to the layers close to surface, whereas the nanoparticles of larger size (70 nm to 400 nm) are precipitated inside the substrate. In addition to this, in the case of coarse natural stones, the fast rate of diffusion, penetration and evaporation of the dispersion medium can lead to phase separation of the nanodispersion, with the consequent effect of the accumulation of the $\text{Ca}(\text{OH})_2$ nanoparticles on the surface and to the layers close to the surface. So, in order to improve the penetration ability, the parameters that affect the transportation and deposition mechanisms must be defined and modified, [34-35] [37], [42], [143], [146-47].

The selection transportation and deposition mechanisms are primarily affected selection the appropriate dispersion medium. A dispersion medium with slower drying rate and higher

dielectric constant might be used to favor nanoparticle/dispersion medium phase separation and induce nanoparticle deposition in depth. A slowing drying rate could be achieved by altering mechanically or chemically the kinetic stability of the dispersion medium or mechanically. But at the same time, the phase separation has proven to prohibit the penetration of the nanodispersions in finer porous substrates [4], [17], [147].

Therefore, the selection and modification of the appropriate dispersion medium must fulfill the synthesis of stable nanodispersions that promote a homogeneous nanoparticles distribution inside the porous substrate during the consolidation action [4].

The stability of the nanodispersions is directly connected with the absence of aggregation phenomena during the synthesis of the nanoparticles and the absence of agglomeration phenomena during the drying stage of the application procedure (according to Smoluchovski's model) [148], [149]. The presence of aggregation phenomenon is connected with the domination of the attractive Van der Waals interactions to electrostatic interactions. In addition to this, the presence of agglomeration phenomenon during the last stages of drying is favored by capillary forces. The morphological characteristics can also contribute to the irreversibility of the agglomeration between the $\text{Ca}(\text{OH})_2$ nanoparticles [148]. It is reported that the crystallographically oriented (epitaxial) attachment between the nanoparticles promotes the interparticle structural continuity minimizing the energy state, thus, prohibiting the regain of the original colloidal stability of the nanoparticles [149].

The synthesis of stable nanodispersions requires the formation of an energy barrier that will prohibit the domination of the attractive Van der Waals interactions. In the case of dispersions of $\text{Ca}(\text{OH})_2$ nanoparticles, the use of polar dispersion medium results in the adsorption of negative charged ions (OH^-) on the surface of the $\text{Ca}(\text{OH})_2$ nanoparticles. This negatively charge ion (OH^-) may attract a positive counterion (Ca^{2+}) of the dispersion [139]. The interaction between the nanoparticles can be explained with the use of the electric double layer [4]. As shown in Fig. 3.6 the term electric double layer describes the layer surrounding the nanoparticle, the ions that are adsorbed on surface of the nanoparticle, and the film of the countercharged dispersion medium. It is consisted of three parts:

1. *Surface charge*: which includes the charged ions that are adsorbed on the surface of the nanoparticle
2. *Stern layer*: which includes the counterions (charged opposite to the surface charge), that are attracted to the surface of the nanoparticle and are attached to this layer by electrostatic force. It represents the minimum distance to the nanoparticle's surface approachable by counterions
3. *Diffuse layer*: which includes a film of the dispersion medium adjacent to the particle. The diffuse layer contains free ions and a larger concentration of the counterions. The ions of the diffuse layer are affected by the electrostatic force of the charged surface of

the nanoparticle. The double layer thickness is a function of the concentration and the valence of ions in the dispersion. [4], [150-151]

The electrical potential within the electric double layer presents a maximum value on the surface of the nanoparticle. The value of the electrical potential is reduced as the distance from the surface is increased, reaching 0 on the boundary of the electric double layer. As the nanoparticles move in the dispersion medium, a layer of the surrounding medium remains adsorbed on the surface of the nanoparticle. The boundary of this additional layer is called slipping plane (shear plane) and the electric potential that is present at the slipping plane is called zeta potential [4],[151].

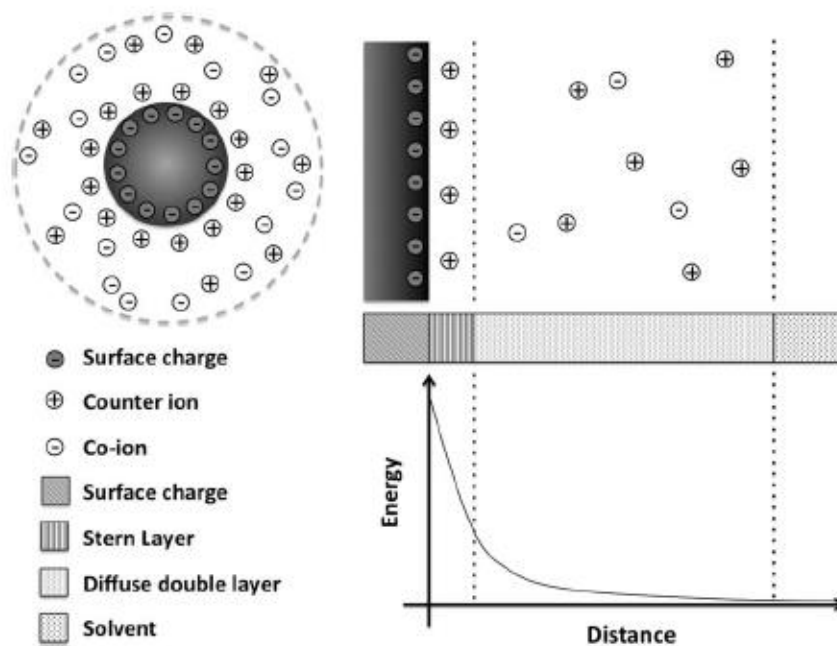


Fig. 3.6 Sketch of a negatively charged nanoparticle in a polar solvent. Surface charges, counter ions and co-ions are indicated, as well as the Stern layer and the diffuse double layer [4]

According to the DLVO (Derjaguin, Landau, Verwey and Overbeek) theory, the interaction of two nanoparticles is defined by the electrostatic forces that are developed due to the overlapping of their electric double layer in the interlayer of the dispersion medium. In particular, the potential energy interaction (Φ_T) between two nanoparticles can be characterized as the result of the combination of the potential energy interaction due to the Van der Waals forces (Φ_A) and the potential energy due to and the electric repulsion interaction (Φ_R) [4], [152-153].

The use of the DLVO theory for the prediction of the interactions between the nanoparticles can be characterized as reliable when:

1. The density of the surface charge is uniform
2. The electric potential of the surface charge remains constant

3. The concentration of the ions that are adsorbed on the surface of the nanoparticle and the concentration of the counterions remain constant
4. There is no chemical interaction between the nanoparticles and the dispersions medium [152-153].

Since the charging of the surface of the nanoparticle is attributed to the adsorption of the ions from the dispersion medium and the entropy contribution to the free energy of the system is independent from the concentration of the adsorbed ions, the electric potential that will occur on the boundary is constant.[4], [152-153].

The simplest model consists of two spherical nanoparticles of equal radius (Fig. 3.7)

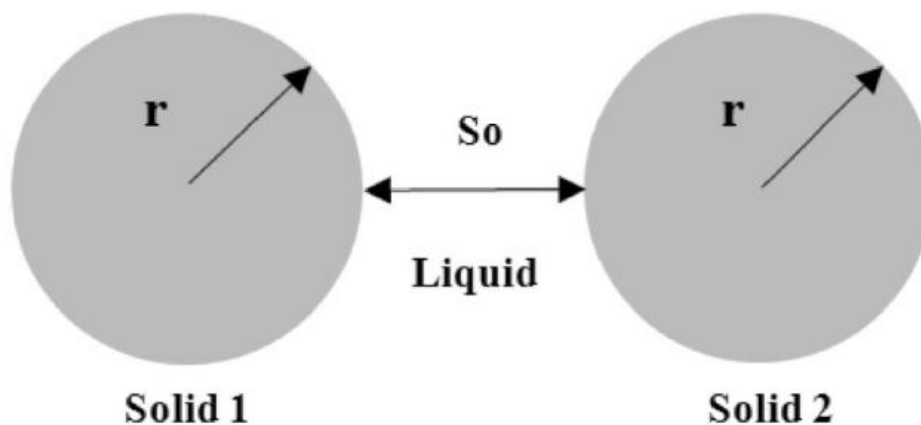


Fig. 3.7 Sketch of a negatively charged nanoparticle in a polar solvent. Surface charges, counter ions and co-ions are indicated, as well as the Stern layer and the diffuse double layer [4]

When the separation distance is significantly smaller than the particle radius, the simplest estimation of the Wan der Walls energy is (Fig. 3.8):

$$\Phi A = -\frac{Ar}{12S} \quad (3.8)$$

Where: A= Hamacker constant of the compound (10^{-20} J), r=the radius (m) and S the distance between the nanoparticles (m)

Particles	Φ_A
Two spheres of equal radius, r^*	$-\frac{Ar}{12S}$
Two spheres of unequal radii, r_1 and r_2^*	$-\frac{Ar_1r_2}{6S(r_1 + r_2)}$
Two parallel plates, with thickness of δ , interaction per unit area	$-\frac{A}{12\pi(S^{-2} + (2\delta + S)^{-2} + (\delta + S)^{-2})}$
Two blocks, interaction per unit area	$-\frac{A}{12\pi S^2}$

* r, r_1 and $r_2 \gg S$.

Fig. 3.8 Determination of Wan der Walls energy (Φ_A) [152]

Also, the electric repulsive potential energy can be estimated by:

$$VR = 2\pi\epsilon\epsilon_0rz2e^{-kx}(3.9) [4]$$

where, ϵ =the dielectric constant of the solvent, ϵ_0 =vacuum permittivity, z =zeta potential, and k = function of the ionic concentration (k^{-1} is the characteristic length of the Electric Double Layer).

As showed at Fig.3.9 the minimum of the potential energy determines the separation distance between two nanoparticles that corresponds to their stable equilibrium. The maximum energy barrier of the potential energy corresponds to the point when the electrostatic repulsive forces dominate the Wan der Walls forces. Thus, the two major parameters are a) the thickness of the electric double layer and b) the value of zeta potential. [129]

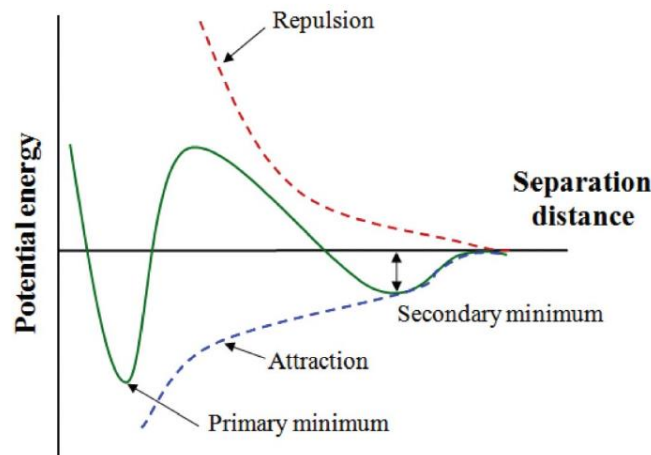


Fig. 3.9 Correlation between the potential energy and separation distance between two nanoparticles [129]

On the basis of the DLVO theory, there are two approaches for the synthesis of a stable colloidal dispersion: a) **the electrostatic stabilization** and b) **the steric stabilization**. **The electrostatic stabilization** involves the use of polar dispersions medium that lead to an uneven distribution of counterions (at a low level of concentration) and the consequent charging at the level of the electrical double layer. When two nanoparticles approach each

other, the electrostatic (repulsive) forces dominate over the Van der Waals (attractive) forces leading to the formation of an energy barrier that prevents the agglomeration phenomenon and leads to the effective stabilization of the dispersion. The **steric stabilization** usually addition of non-ionic surfactants and/or polymers in the nanodispersion. The compounds are adsorbed on the surfaces of the nanoparticles enhancing the repulsion between the two nanoparticles due to the steric hindrance of the non-ionic surfactant/ polymer [4], [129], [152-153].

3.2.3.1 Dispersion medium (water, short chain aliphatic alcohols, nanobubbles)

According to the DLVO theory mentioned above, the colloidal stability of the dispersion can be obtained by following two paths: a) the electrostatic stabilization and b) steric stabilization. Those two paths are also applied in the cases of dispersions of $\text{Ca}(\text{OH})_2$ nanoparticles [4].

Following the electrostatic stabilization, a common practice is the effective charging of the surface of the nanoparticle by the use of a polar dispersion medium (such as water and short chain aliphatic alcohols) [39]. The interpretation of the effect of the addition of the different polar dispersion mediums highlighted the simultaneous realization of the electrostatic and steric stabilization. The molecules of the dispersion medium are adsorbed on the surface of the nanoparticles [149], [154].

This can be interpreted with the use of the interfacial surface tension $\gamma_{1,2}$ as the force that operates inwards from the boundaries between two immiscible phases as the force that operates inwards from the boundaries of a surface perpendicular to each phase, tending to minimize the area of the interface. The presence of interfacial tension can also be attributed to the net differences between intermolecular forces acting at the interfaces. Therefore, the phenomena that occur near the interface are dominated by the intermolecular interactions [4], [129].

The energy required to overcome the adhesive forces can be estimated by:

$$W_{1,2}^A = \Delta G^A = \gamma_{\text{final}} - \gamma_{\text{initial}} = \gamma_2 + \gamma_1 - \gamma_{1,2} \quad (3.10) \quad [4]$$

$W_{1,2}^A$ is the work of adhesion and the various γ_2, γ_1 and $\gamma_{1,2}$ represent the corresponding surfaces and interfacial surface. According to this approach two surfaces that are characterized by high values of energy tension are likely to cohere strongly. Consequently, the adsorption of molecules of lower surface tension values contribute to the reduction of the interfacial tension and attribute to the enhancement of the colloidal stability of the nanoparticles with the absence of agglomeration and aggregation phenomena [4].

It is reported that in aqueous suspensions of nanolime are kinetically unstable and settled rapidly. Consequently, along with the higher values of surface tension and contact angle, the higher viscosity of water and the limited sorptivity, the penetration is inhibited causing the creation of the white glazing effect on the surface. It has been reported that the use of water as dispersion medium often leads to the presence of aggregation and agglomeration

phenomena during the synthetic procedures. The low surface tension of the short chain aliphatic alcohols (fourfolded in respect with the surface tension of pure water Table 3.1) provides high penetration ability and increased kinetic stability (due to the reported reduction of the sedimentation rate of the nanoparticles), whereas the low dielectric constant of alcohols has proven to have no effect on the agglomeration phenomena [39],[154]. The lower sedimentation rates and the higher stability of the alcoholic dispersion medium lead to the improvement of the reactivity degree and the reduction of the superficial phenomenon of the white glazing. However, the use of alcohols doesn't prohibit the phase separation during the drying stage [148].

Dispersion medium	Surface Tension (n/m) at 25°C	Boiling point (°C)
<i>Water</i>	72,1	100
<i>Methanol</i>	22,1	65
<i>Ethanol</i>	21,97	78,2
<i>1-propanol</i>	23,75	97,3
<i>2-propanol</i>	20,93	82,3
<i>Acetone</i>	23	56,1
<i>Butanol</i>	24,93	117,7

Table 3.1 Surface tension and boiling point of different polar dispersion mediums

3.2.3.2 Ultrasounds

The use of ultrasounds has been widely adopted over the years. Their application is designed based on the phenomenon of cavitation. At high intensities, the sound waves that propagate the liquid media, result in a constant change in between low-pressure (compression) and high-pressure (rarefaction) cycles. The rate of the alteration depends on the frequency of the sound waves. During the cycle of low-pressure, the high intensity ultrasonic waves tend to create small vacuum bubbles in the liquid. During the cycle of high-pressure, when these bubbles reach the point where the energy can no longer be absorbed, they tend to collapse violently, thus creating the phenomenon of cavitation collapse. The ultrasonic irradiation is generated also, by the generation of high velocity interparticle collisions and jets of liquids striking onto the surfaces of the particles. [155-157].

There are both direct and indirect sonication configurations for generating ultrasonic waves (Fig. 3.10). The direct sonication concerns the immersion of an ultrasound probe (transducer horn) into the suspension/dispersion and the indirect sonication concerns the introduction of the sample container into a liquid where the propagation of ultrasonic waves is realized [158]. When compared to the indirect sonication, direct sonication is characterized by the higher effective energy impact on the liquid sample, due to the elimination of the physical barriers to wave propagation.

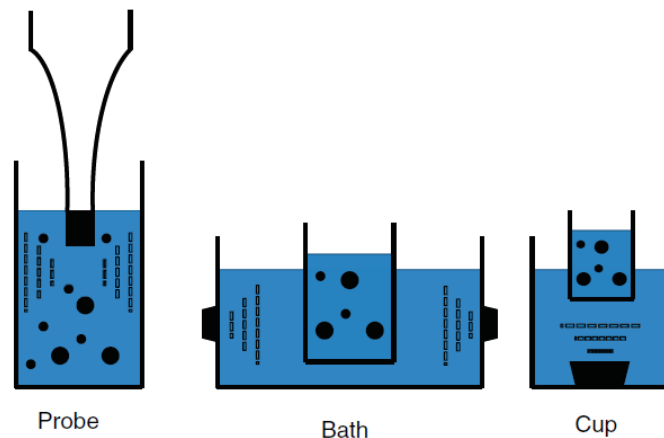


Fig. 3.10 Schematic illustration of direct (left) and indirect (middle and right) sonication configurations [158]

Cavitation can be initiated by high-pressure nozzles, rotor-stator mixers, or ultrasonic processors. In all cases, the ultrasonic device transforms electrical power into vibrational energy by means of a piezoelectric transducer that changes its dimensions in response to an applied electric field. The input energy can be transformed into friction, turbulences, waves and cavitation. The part of the input energy that is transformed to cavitation collapses depends on the movement that is generated by the selected equipment. The main parameter is the intensity of acceleration. Higher acceleration increases in the differences between the low-pressure and the high-pressure leading to the production of a higher amount of bubbles [155],[158].

$$P = \frac{1}{2} \rho c A^2 (2\pi f)^2 a \quad (3.11)$$

Where: P = the acoustic power (W) of the ultrasound source, a = the 'emission area' (m²), which is the surface area of the emitting ultrasound source, ρ = the liquid density (kg m⁻³), A = the amplitude (m) of oscillation of the ultrasound probe, c = the speed of the acoustic wave in the liquid medium (m s⁻¹) and f = the vibration frequency (Hz).

Ultrasonic cavitation has been already applied in many physico-chemical processes. In specific, it has been successfully applied in the case of production of emulsions or stable dispersions of particles that belong to the micro- or nanoscale [158].

Both low-intensity and high-intensity ultrasounds have been used for analysis, imaging and to non-destructive techniques. In addition to this, high-intensity ultrasounds are commonly used during the processing of liquids, such as in cases of mixing, emulsifying, milling, dispersing or de-agglomeration (Fig. 3.11). In the field of nanotechnology, they are usually used in the top-down route for the production of nanoparticles [155]. Also, it can be applied for the inhibition of agglomeration during crystallization. The successful application of this

technique during the crystallization stage led to the reduction of the metastable zone width, to a narrower particle size distribution and homogeneous crystal morphology [159].

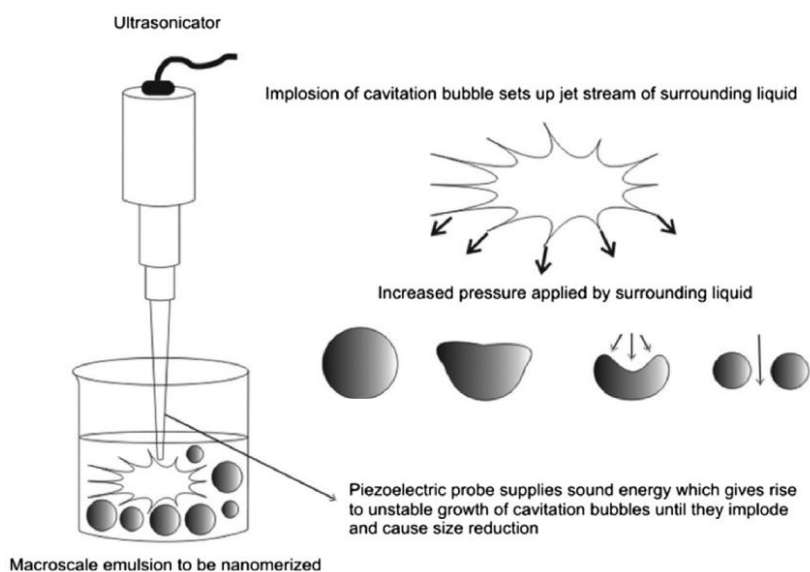


Fig. 3.11 Schematic illustration of the cavitation phenomenon [159]

3.3.3 Carbonation process

As mentioned above, the carbonation process can be characterized as a rather complex reaction that controls the end-up product of the consolidation action. The carbonation reactions within the pore network or at neutral substrates have not been studied systematically so far [160].

The overall equations is:



This reaction (3.12) can be realized either under standard atmospheric conditions (room T and atmospheric pCO_2 of $10^{-3.5}$ atm) via a dissolution-precipitation method [160] or under high temperature via a solid-state mechanism [161]. In both cases, the presence of water is critical for the realization of the carbonation process through the dissolution of Ca(OH)_2 crystals and the atmospheric CO_2 .

According to Rodriguez-Navarro et al. 2016 [160], the realization of the carbonation reaction is complete at three stages:

- a) The first stage concerns the dissolution of Ca(OH)_2 in adsorbed or pore water and the consequent releasing of $\text{Ca}^{2+} + \text{OH}^-$



- b) The second stage concerns the dissolution of atmospheric CO_2 as a loosely hydrated aqueous form which
 - i) At higher pH values is rapidly dissociated at CO_3^{2-}



- ii) At lower pH values is hydrated to H_2CO_3 , which dissociated into HCO_3^- and CO_3^{2-}



- c) The third and final stage concerns the reaction between the ions Ca^{2+} and CO_3^{2-} and the consequent formation of CaCO_3 :



According to Rodriguez Navarro et al. 2017 [25], the rate of the realization of the carbonation process is controlled by the dissolution of $\text{Ca}(\text{OH})_2$ to $\text{Ca}^{2+} + \text{OH}^-$ (3.13). The dissolution of $\text{Ca}(\text{OH})_2$ results in the formation of an alkaline environment, under which the hydration of CO_2 can be realized at a higher rate via the reaction [162]:



There are several parameters that affect the kinetics of carbonation and the supersaturation of the system, thus controlling the nucleation density and the phase of evolution of the final product of the carbonation reaction [160]. In specific, the parameters are the relative humidity RH, the temperature T, the surface area of the reactant, the hydration rate and the partial pressure of CO_2 and the addition of impurities/additives such as Mg ions or organic additives [25].

In general, carbonation is an exothermic reaction depending on the diffusion of the atmospheric CO_2 gas into the pore structure and on the chemical reaction between the dissolved CO_2 and $\text{Ca}(\text{OH})_2$ [162-163]. As mentioned before, the shape of the particles, in particular the hexagonal nanoprism shape, is generally preferred in cases of consolidation that involve the reaction of natural carbonation, since a better carbonation reaction is achieved due to water retention among the hexagons inter-layers [164]. It has been reported that during the initial stage of the realization of the carbonation reaction, a porous CaCO_3 surface layer is formed. During the carbonation reaction, this layer acts like a passivating layer inhibiting the carbonation of the core of the $\text{Ca}(\text{OH})_2$ nanoparticle. Also, the study of the carbonation reaction has revealed that, in the case of $\text{Ca}(\text{OH})_2$ crystals of larger size (in mm), the difference in the molar volume between the reactant phase ($\text{Ca}(\text{OH})_2$) and the product phase (CaCO_3) creates stress that lead to the formation of cracks along the basal planes [165]. This underlines that carbonation yield is connected with both the size, shape and thickness of the $\text{Ca}(\text{OH})_2$ nanoparticles [25].

Another important aspect is the ambiguous role of the moisture. On the one hand, is necessary and can accelerate the carbonation process [112]. Also, it is evident that the residual water content (along with the concentration of the nanolime) affects the

carbonation process efficiency (yield) (Daniele 2010). On the other hand, a high moisture content may act as an inhibitor for the penetration of the consolidant (in this case, in order to reduce the moisture content, it is necessary to pre-wet the material with ethanol). Depending on the environmental conditions (humidity, possibility of CO₂ migration) and the amount of nanolime, the carbonation process may last from days to weeks [112]. The addition of carbonate sources through the addition of baking soda [44] or the realization of yeast fermentation [106] has been also investigated.

During the field application of dispersions of Ca(OH)₂ nanoparticles, the temperature can be characterized as rather low. So, the relative humidity RH% can control the end-up product of the carbonation reaction [93], [106], [166]. It has been reported that under the condition of RH<30%, an adsorbed water film on the surface of the Ca(OH)₂ nanoparticles was realized, leading to the dissolution of CO₂ and Ca(OH)₂ and to the initiation of the carbonation process [106], [166]. The increase of the values of RH% has been linked directly to an increase in the rate of the carbonation reaction and to an increase of the carbonation yield [167-169]. The conditions of RH% have been associated with the presence of metastable phases of CaCO₃. Recent studies have revealed that Amorphous calcium carbonate (ACC, CaCO₃.nH₂O) is the dominant phase during the initial stage of the carbonation reaction at room T, via the dissolution of Ca(OH)₂. At RH<75%, the formation of primary nanoparticles of vaterite and aragonite via the heterogenous nucleation on the ACC and their consequent aggregation to iso-oriented structures, was observed. Both metastable phases dissolve and precipitate into calcite form, following the Ostwald's step rule [39], [160]. It has been reported that the nucleation and kinetic stabilization of the metastable phases is favored by the presence of short chain alcohols (like ethanol and 2-propanol) used as dispersion medium [170].

3.4 Surface functionalization

3.4.1 Surfactants

The term surfactant concerns amphiphile molecules that are characterized by a specific molecular structure/architecture. They are consisted of a lyophobic group and a lyophilic group that interact in different ways with the dispersion medium. They present the ability to be adsorbed onto the surfaces, thus, modifying the surface energy between two immiscible phases [4], [146]. The characteristic molecular structure of the surfactants is responsible for their ability to be adsorbed onto the interfaces, to enhance the solubilization of hydrophobic materials and to form self-assembled particles.

According to Young's equation:

$$\cos\theta = \frac{\gamma_{vs} - \gamma_{vl}}{\gamma_{sl}} \quad (3.18)$$

When the surfactant is adsorbed on an interface, it causes the reduction of the surface tension. So, if the surface tension between liquid-solid or vapor-liquid is decreased (1), the contact angle is reduced, promoting the wetting of the surface [4].

One of the most important characteristics of the surfactants is the concentration value at which they associate and create a micelle, a self-assembled molecular cluster. The critical micelle concentration (CMC) represents the concentration value at which the formation of micelles occurs. The interaction between the micelles and the aqueous dispersion medium is interpreted by the hydrophobic interaction caused by the increase of entropy in the water molecules that interact with the hydrophobic group of the micelles. In specific, when the surfactants are added in water, the water molecules surrounding the hydrophobic group tend to create an iceberg structure causing the reduction of the entropy [4]. As the concentration of the surfactant is increased reaching the CMC, the association of the hydrophobic group leads to the collapse of this iceberg structure, to the release of the water molecules and to the consequent increase of the entropy of water molecules through the freedom of their motion and formation of hydrogen bonds. This extent of energy activates the micellization process. As observed in Fig. 3.12 the addition of surfactants above their solubility limitation, leads to the formation of the adsorption film at the liquid-vapor interface. The further addition of the surfactants leads to the formation of a saturated surface film before reaching the CMC and the consequent presence of micelles [4], [171]

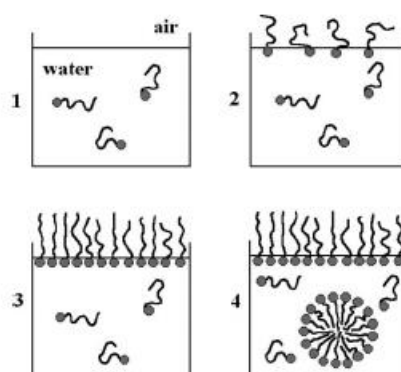


Fig. 3.12 Schematic illustration of the consecutive addition of the surfactant [171]

As it can be observed in Fig. 3.13, under conditions of constant temperature, the increase of the concentration of the surfactant results to the reduction of the surface tension of the interface. But, when the concentration of the surfactant meets the CMC, the surface tension of the interface remains constant and the presence of micelles can be observed.

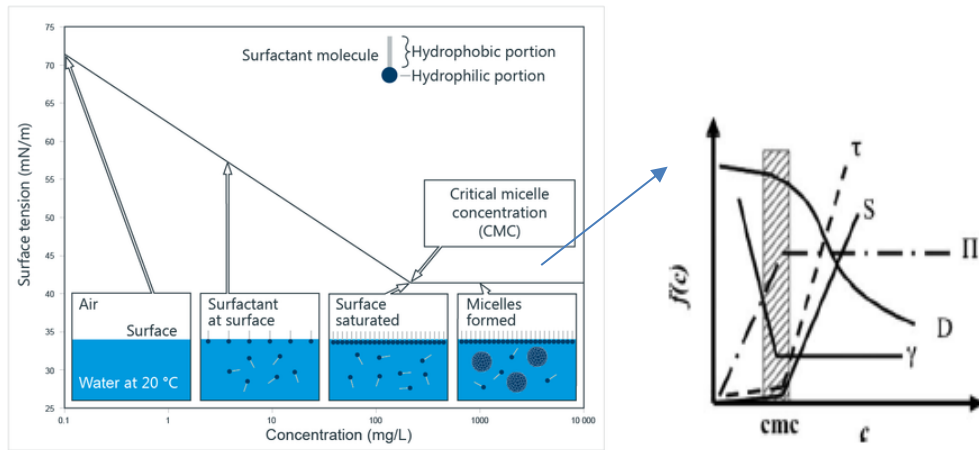


Fig. 3.13 Correlation between surface tension and the concentration of the surfactant [4]

The CMC is determined by different parameters, such as the surface tension of the dispersion medium, the conductance, and/or osmotic pressure. The concentration of the surfactant determines also the shape of the micelles (Fig. 3.14). In aqueous dispersion mediums, the structure of the micelles is spherical in order to prevent the interaction between the polar dispersion medium and the hydrophobic group of the surfactant. As observed in Fig. 3.14, the Kraft point is the triple point triple point of the surfactant monomer's solubility curve, the CMC temperature curve, and the phase transition line (T_c) of hydrated solids to micelles and/or liquid crystal. The formation of micelles is promoted only when the Kraft point is higher than the CMC value [4], [171].

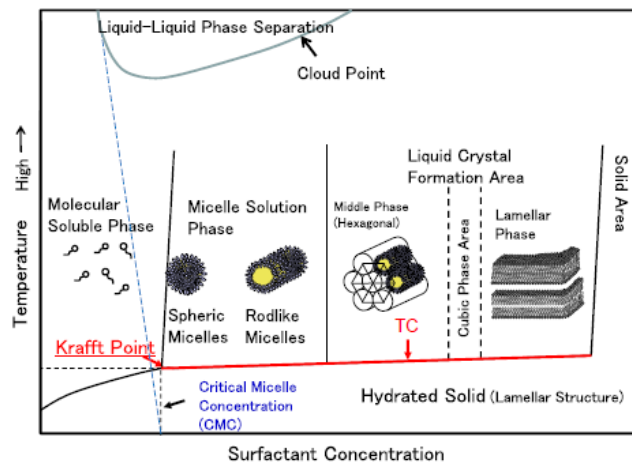


Fig. 3.14 Correlation between the CMC and the shape of the newly formed micelle [171]

For aqueous dispersion medium, the most common classification of the surfactants is based on the chemical nature of the polar (lyophilic group):

1. Anionic Surfactants: In the case of the anionic surfactants, the polar head group contains a carboxylate, sulfate, sulfonate or phosphate group and is negatively charged. Anionic surfactants such as sodium dodecyl sulfate (SDS), and sodium alkyl polyglycoside sulfosuccinates (AGESS), have been applied in the synthesis of

nanostructured cleaning fluids for the removal of detrimental coatings from artistic surfaces.

2. Cationic Surfactants: In the case of the cationic surfactants, the polar head group contains an ammonium residue and is positively charged.
3. Zwitterionic Surfactants: In the case of zwitterionic surfactants, both positive and negative charges are presented in the surface-active portion (ex. Long chain aminoacid), creating zero charge
4. Non-ionic Surfactants: In the case of the non-ionic surfactants, they are formed by neutral head group, usually consisted of alcohol, ethers, carboxylates and amines. [4], [171]

The intermolecular interaction between the surfactants, the nanoparticles and the dispersion medium, depends on the structure of the surfactant. In particular, it can have the form of ion-ion interaction, ion-dipole, dipole, dipole or hydrogen bonding. Generally, in an aqueous dispersion medium, the polar head groups of the surfactant will interact with the water molecules and with the nearby hydrophilic heads, while the hydrophobic chains of the surfactant will experience attractive London interaction with the adjacent lipophilic regions. In the case of a non-ionic surfactants, repulsive steric interactions are formed between the polar head groups, whereas in the case of ionic surfactants the repulsion between the heads is attributed to the formation of coulombic repulsions [4]. As far as the adsorption of surfactant on the surface of a nanoparticle is concerned, ionic surfactants can be adsorbed through ion pairing, ion exchange and polarization of π electrons, whereas non-ionic surfactants can be adsorbed through the formation of Hydrogen bonds. In addition to this, adsorption by dispersion forces and by hydrophobic interaction between the surfactant and the substrate have also been observed [172].

3.4.2 Non-ionic surfactants

Non-ionic surfactants are composed by a neutral head group (often compiled by hydroxyl group) and a hydrophobic body. The addition of the non-ionic surfactant into the polar dispersion medium in the case of nanolimes, promotes the stability of the nanodispersion, since they are adsorbed on the surface of the nanoparticle, forming hydrogen bonds with the nanoparticles, and prohibiting the presence of agglomeration phenomena due to the steric barrier. Along with the absence of dissociation phenomena and the reduction of the surface tension between the nanoparticles and the polar solvent, the addition of non-ionic surfactant generally promotes the steric stabilization of nanodispersions [4], [173].

One of the most commonly used non-ionic surfactants is the **Triton X-100**, a polyoxyethylene-(10)-tert-octylphenyl-ether ($C_{14}H_{22}O(C_2H_4O)_{10}$). It is characterized as a

biodegradable non-ionic surfactant, compatible with anionic cationic and other surfactants and active at a range of low temperatures from 15-45 °C. It has been reported that the high viscosity of the Triton X-100 is responsible for the fact that the depletion effect is not immediately detectable. But, Triton X-100 is also connected with the presence of certain flocculation phenomena [174-175]. It has been applied during the synthesis and functionalization of both hydrophilic and hydrophobic nanoparticles (Fig. 3.15) such as $\text{Ca}(\text{OH})_2$, TiO_2 , Ag, perylene, liquid marbles etc [174-177]. Triton X-100 is also applied in a wide range of processes as a dispersant or wetting agent such as the heavy-duty industry, agrochemical products and gentle detergents [178]

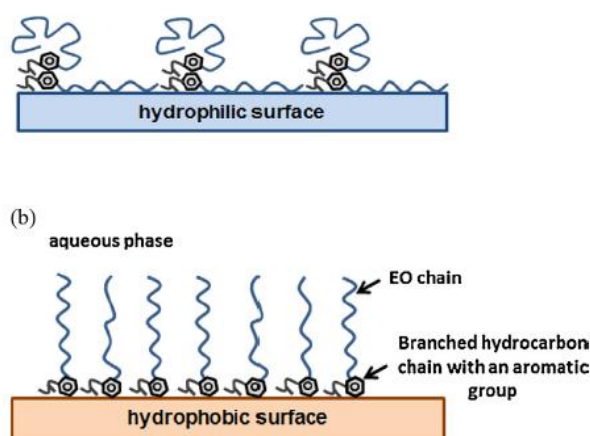


Fig. 3.15 Schematic Illustration of the adsorption of Triton X-100 on hydrophilic and hydrophobic surfaces [4]

A Triton X-100 molecule has a hydrophilic polyethylene oxide chain and an aromatic hydrocarbon hydrophobic group (Fig. 3.16).

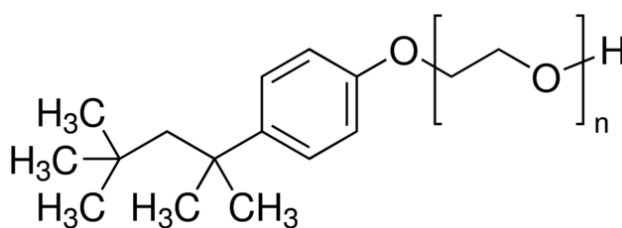


Fig. 3.16 Schematic illustration of a molecule of Triton X-100 [4]

Under low pressure conditions, with the increase of the surfactant concentration, the ethylene oxide groups are gradually displaced from the surface layer to the bulk solution, while the surface layer preferentially accumulates the hydrocarbon chains, for which the increase in surface pressure results in a decreased molar area of the molecules in the adsorption layer [179].

Triton X-100 has been successfully applied on the file of the synthesis of $\text{Ca}(\text{OH})_2$ for the steric stabilization of the dispersion. It has been reported the increase of the amount of Triton X-100 in an aqueous solution (with a change of concentration from 10^{-7} M to 10^{-3} M)

resulted to the reduction of the surface tension from 70 mN/m to 30 mN/m [35], [178]. Triton X-100 is adsorbed on the surface of the $\text{Ca}(\text{OH})_2$ nanoparticles due to the hydrogen bonds between the hydroxyl group (OH^-) and the $-\text{O}$ of the polyoxyethylene group of Triton X-100, forming a steric barrier and thus preventing the agglomeration phenomena. It has been reported that the addition of Triton X-100 on the aqueous solution of the bottom-up process led to the reduction of the size of the $\text{Ca}(\text{OH})_2$ nanoparticles [35],[173]. The reduced size of the nanoparticles can be attributed to the reported interaction between Ca^{2+} and the functional polyoxyethylene group of Triton X-100, that has proven to inhibit the nucleation of the primary nanoparticles and the presence of aggregation phenomena [138], [180].

Another non-ionic surfactant used in the synthesis of nanoparticles is **n-octylamine** (Fig. 3.17). In specific, n-octylamine was used for the synthesis of mesoporous silica nanoparticles via the surfactant-template sol-gel method. Above the CMC concentration of n-octylamine forms ordered structures made up of geometrical arrays of the micelles, acting like true liquid crystals. The addition of an inorganic precursor (TEOS) to the aqueous dispersion medium that surrounds the hydrophilic surface of the micelles results in the realization of the hydrolysis reaction that leads to the formation of a regular array of silica cylinders over the pre-existing template of n-octylamine. In this way the polymerization is topologically driven by the pre-formed ordered template made up of the molecule of the surfactant. The synthesis can be performed either in acidic or basic conditions, and the source of silica can be fumed silica, sodium silicate, tetra-alkyloxide of silane [4]. N-octylamine was selected due to the ability to form mesoporous structures [33] and to be removed by evaporation [181]. The sol gel synthesis is controlled by the formation of hydrogen bonds between the inorganic precursor (TEOS) and the surfactant (n-octylamine). The most recent application of n-octylamine were reported in the synthesis of TiO_2 - SiO_2 nanocomposite photocatalysts for the self-cleaning of stones [64] and to the synthesis of ormosils (modified silanes) for stone restoration [182].

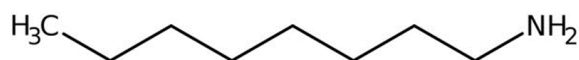


Fig. 3.17 Schematic illustration of a molecule of n-octylamine [4]

For comparison reasons, **amylamine** as a cationic surfactant (Fig. 3.18) is also being studied in this research. Amylamine has been successfully applied on the synthesis of stable foams. In specific, amylamine was adsorbed on the silica nanoparticle surface through electrostatic binding, resulting in the hydrophilization of the silica nanoparticle and to consequent stabilization of the foam [183]. The addition of both n-octylamine and amylamine has been successfully applied on the synthesis of lamellar-shape silver nanoparticles via the surfactant-template sol-gel method [184]. Finally, the addition of amylamine on the sol-gel synthesis of nanosilica particles of uniform size [185]

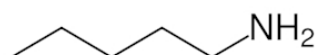


Fig. 3.18 Schematic illustration of a molecule of amylamine [4]

3.5 State of the art in the synthesis of calcium hydroxide particles

As mentioned before, calcium hydroxide $\text{Ca}(\text{OH})_2$ nanoparticles are synthesized using the two fundamental procedures: the top-down synthetic route that involves the thermo-mechanical treatments of slaked lime and the bottom-up synthetic route, which is building up crystals starting from an external collection of atoms or ions [4].

Both nanometric ($\leq 100\text{nm}$) and submicrometric particles ($<1\ \mu\text{m}$) of calcium hydroxide can be obtained by the two synthetic routes.

3.5.1 Current experience on the top-down route

The **top-down route** (thermo-mechanical treatment) was applied by the slaking of quicklime (hydration process) by mixing one part by weight of CaO with about 0.5–0.75 part of water. The advantages of the top-down route are the actual conditions of high temperature and pressure, which prevent the formation of the unwanted passivated surface layer of hydroxide (that could inhibit the completion of the carbonation reaction), by forcing the hydration of the unreacted oxide. The hydration process and consequently the morphological characteristics of the newly formed nanocrystals can be affected by CaO reactivity, oxide/water ratio, slaking water T, vapor- vs liquid-phase hydration, additives (ex. alcohols) and local overheating [4],[39].

The hydration of CaO that is connected to the volume expansion of the crystal, leads to the effective formation of $\text{Ca}(\text{OH})_2$ nanoparticles with the shape of hexagonal platelets and size from 150 nm to 300 nm. The two reported advantages of this synthetic route are the possibility of the synthesis of large amounts of nanoparticles (without any purification procedures required) and the possibility of the synthesis of nanoparticles that follow a bi-modal particle's size distribution [148].

During the application process, the bi-modal particles size distribution involves the presence of two categories $\text{Ca}(\text{OH})_2$ nanoparticles:

- a) of size in between 150 nm -300nm that will penetrate to the sub-micron pores of the porous substrate and
- b) of larger size that could present good adhesion properties with the larger pores, fractures of flakes of the surface of the porous substrate [39].

An alternative to this method that was used in many papers is the mechanical dissolution of aged lime putty. According to the relevant literature, the prismatic crystals that are present in fresh lime putty undergo ripening upon ageing in aqueous solutions, a process that leads to the reduction of the crystal's size and to the overdevelopment of the basal faces.

Eventually, the phenomenon of ripening upon ageing leads to the creation of sub-micrometer crystals of plate – like habit and to the following realization of the secondary nucleation of the plate-like $\text{Ca}(\text{OH})_2$ nanoparticles. It has been reported that aged lime putties are connected with faster carbonation rates, higher water retention, higher dynamic viscosity and workability [186-187]. The produced $\text{Ca}(\text{OH})_2$ nanoparticles are characterized by a high surface/volume ratio, that leads to the increase of their level of reactivity (closely connected with the carbonation rate and dissolution kinetics). Also, the final dispersion presents a high colloidal stability and enhanced rheological properties [39]. The study of this alternative procedure underlined the importance of the shape of the $\text{Ca}(\text{OH})_2$ nanoparticles. In particular, this study revealed that the prismatic $\text{Ca}(\text{OH})_2$ nanoparticles present an high degree of solubility in the aqueous dispersion medium in respect to the hexagonal $\text{Ca}(\text{OH})_2$ nanoparticles. But, overall, the top-down route does not offer the possibility of the modification of the surface of the $\text{Ca}(\text{OH})_2$ nanoparticles [28], [148].

The effect of the temperature and of the addition of 2-propanol on the rheological characteristics has been also studied. In specific, the synthesis of $\text{Ca}(\text{OH})_2$ nanoparticles was achieved by the dissolution of $\text{Ca}(\text{OH})_2$ in de-carbonated water (the insolubilization – precipitation method) following the drop to drop addition of 2-propanol. The higher values in both cases (76°C and 90% 2-propanol content of the dispersions medium) resulted in the production of stable dispersions of hexagonal $\text{Ca}(\text{OH})_2$ nanoparticles [188].

The sol-gel citrate method was also tested. Calcium nitrate CaNO_3 was dissolved in aqueous dispersion medium with the addition of citric acid (as an emulsifier) in order to obtain nanoparticles of CaO of dimensions 100 nm, that were immediately hydrated to $\text{Ca}(\text{OH})_2$ nanoparticles. This method did not require any purification or washing since the by-product NH_3 evaporated from the solution. Due to the small size of the newly synthesized nanoparticles, this method was applied for the consolidation of paper and not for porous building materials [189].

The heterogenous synthetic route of $\text{Ca}(\text{OH})_2$ nanoparticles can be used also in the cases of industrial processes, like the production of paper and acetylene (C_2H_2). In specific, in the case of acetylene production, the by-product of the hydrolysis of Ca_2C is the Carbide lime (CL) (or lime sludge), that leads to the generation of C_2H_2 and CaO [39].

[3.5.2 Current experience on the bottom-up synthetic route](#)

The **bottom-up synthetic route** concerns the synthesis of the desired nanoparticles through a homogeneous phase reaction in in alcoholic or water-alcoholic dispersion media both resulting in the synthesis of nano-sized crystals of calcium hydroxide $\text{Ca}(\text{OH})_2$ nanoparticles with a plate-like shape and cauliflower-like agglomerates, but with several differences concerning the average size of the $\text{Ca}(\text{OH})_2$ nanoparticles and particle size distribution [8-9].

The most commonly used synthetic procedure, according to the literature, includes the mixing drop by drop equal volumes of sodium hydroxide (NaOH)(or NaNO₃) or and calcium chloride (CaCl₂)or Ca(NO₃) aqueous solutions both at a high temperature (90°C) and vigorous stirring. According to the following reaction:



Through this procedure, particles of dimension 200–400 nm or smaller are produced. The size and shape of the particles can be altered depending on the reaction temperature, the concentration of the reactants and their mole ratio. The nucleation rate of the Ca(OH)₂ nanoparticles is favored respect to particle growth due to supersaturation degree, high temperature and slow mixing, thus, promoting the precipitation of Ca(OH)₂ nanoparticles [8-9], [73], [173].

The results of the bottom-up synthetic route can be interpreted also with the use of LaMer diagram (Fig. 3.19). The critical concentration (C_{\min}) regulated the extent of the the first two phases: the supersaturation phase (I) and the nucleation phase (II). In order to proceed to a further reduction of the size of the nanoparticles, the nucleation rate must be favored to nanoparticle's growth. Also, the production of Ca(OH)₂ nanoparticles of homogenous size is promoted when the nucleation phase is as short as possible. So, It is evident, that the bottom-up synthetic route display more possibilities for modification of the process for the optimization of the morphological characteristics of the newly synthesized Ca(OH)₂ nanoparticles [4], [129].

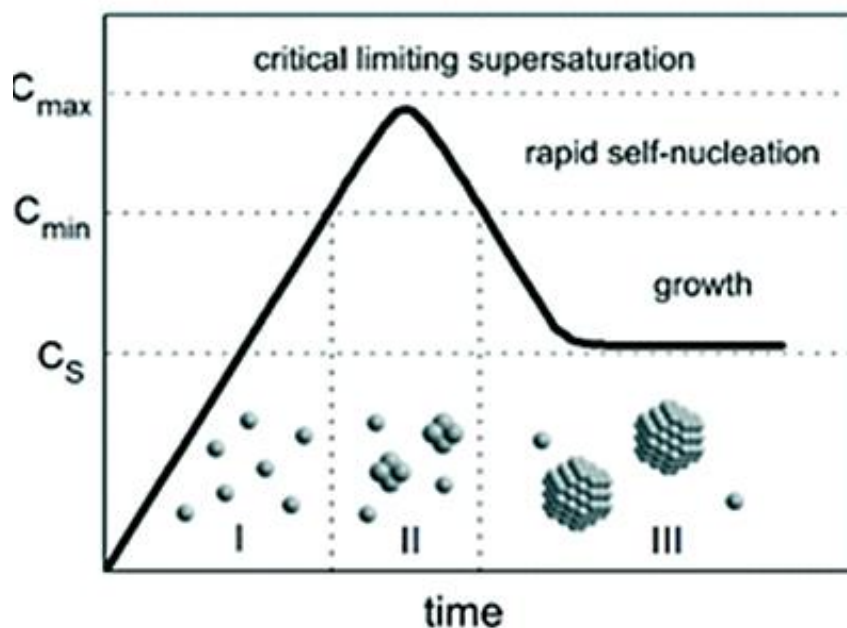


Fig. 3.9 between supersaturation of the dispersion and nucleation of the nanoparticles [133]

One of the main drawbacks of the synthetic procedure is the need for the removal of the NaCl by-product through several washes with deionized water.

The dissolution of the $\text{Ca}(\text{OH})_2$ nanoparticles of dimensions $<100\text{nm}$ is then carried out due to continuous washes. This could be a possible explanation for the size of the $\text{Ca}(\text{OH})_2$ nanoparticles synthesized via the homogenous synthetic route, that has not often been reduced lower of the limitation of 100nm [39]. The first alteration involved the replacement of the aqueous dispersion medium with a mixed polar dispersion medium of 90% alcohol (ethanol or 2-propanol) and 10 % of distilled water, at a desired concentration (e.g., 5 g/L) [8], [173]. Furthermore, the synthetic route of the realization of the homogenous reaction can be characterized as a rather costly and time-consuming method [148].

The main drawbacks of this synthetic route are:

- The slow mixing rates
- The removal of byproducts or undesired phases that could lead to the dissolution of the $\text{Ca}(\text{OH})_2$ nanoparticles
- The low specific yield of $\text{Ca}(\text{OH})_2$ nanoparticles production [73]

The further reduction of the size of the $\text{Ca}(\text{OH})_2$ nanoparticles was attempted though the temperature's increase (up to 175°C), with the **use of ethylene and propylene glycol as reaction dispersion media**, followed by repeated washes of the precipitates with saturated $\text{Ca}(\text{OH})_2$ solution and elimination of excess solution via dialysis. The realization of this modification led to the synthesis of significantly smaller $\text{Ca}(\text{OH})_2$ nanoparticles of dimensions in between 30 nm –60 nm. However, the completion of the synthesis required more than 3 days.

In addition to this, the development of a homogeneous phase reaction in diols that reaches a higher temperature was studied. The procedure involved the hydrolysis of CaCl_2 (or $\text{Ca}(\text{NO}_3)_2$) solution in diols (as the reaction medium) and the consecutive addition of the a NaOH aqueous solution at the temperature of 175°C . The main drawback of this procedure was the presence of agglomeration phenomena due to the adsorbed molecules of diols on the surface of the $\text{Ca}(\text{OH})_2$ nanoparticles. The adsorbed diols were removed with the use of the peptization bath (with the addition of 2-propanol in the ultrasonic bath) after the completion of the synthetic procedure [9], [32], [148].

The **use of the peptization bath** revealed the synthesis of $\text{Ca}(\text{OH})_2$ nanoparticles of average size of 60 nm, characterized by the uniformity of their size and the consequent narrow size distribution. However, this synthetic procedure was characterized as time- consuming and eventually the amount of the freshly synthesized nanoparticles was low [9], [14], [190]. According to the relevant literature, possible alterations could be the addition of a surfactant at the beginning of the reaction or the addition of another experimental stage concerning the microwave treatment (at the microwave chemical reactor MCR-3), followed by filtration and heat treatment at 300°C [141].

The **synthesis of Ca(OH)₂ nanoparticles by means of template** has been also tested by following two approaches: the first approach concerns the use of a water-in-oil microemulsion, formed from a nonionic surfactant resulting at the production of nanoparticles diameter of 5 nm, but generally characterized as extremely time-consuming technique [14], [191] and the second approach by the use of hydro-soluble polymers (PVA and PEG) in order to control the formation of specific structures (ending at the production of particles of size 50–100 nm) [14].

The **H₂ plasma-metal reaction method** was also applied in the field of the synthesis of Ca(OH)₂ nanoparticles. In particular, spherical, spongy Ca(OH)₂ nanoparticles of mean particle size of 100 nm were synthesized via the arc melting of partially oxidized Ca ingot, in a nitrogen/hydrogen atmosphere. The newly synthesized Ca(OH)₂ nanoparticles could be applied in the fields of cultural heritage conservation, flue gas desulfuration and pollutant emission control [192].

The decrease of the required time was achieved by **adding a surfactant agent** in the initial aqueous solutions [173], [193]. In particular, the addition of the non-ionic surfactant Triton X-100 to the CaCl₂ aqueous solution and the consequent mixing with the NaOH aqueous solution, led to the synthesis of hexagonal Ca(OH)₂ nanoparticles of dimensions in between 100 and 300 nm. The time of the completion of the synthetic method was highly reduced. But, the removal of the non-ionic surfactant can be characterized as rather complex [173], [193]. .

The same group suggested a new method based on the **use of an anionic exchange resin** (in OH⁻ form). The synthesis of the nanoparticles was achieved by mixing (under moderate stirring) the anion exchange resin with the aqueous CaCl₂ solution, in room temperature. Following the stirring, the resin was separated from the precipitated Ca(OH)₂ nanoparticles with the use of a sieve during an one step process. The residual chlorides can be reduced by mixing the suspension with a fresh ion exchange resin. This could lead to the formation of lime nanoparticles as well (two steps process). The quick synthetic route led to the production of crystalline, hexagonally plated, and with dimension less than 100 nm, Ca(OH)₂ nanoparticles [13]. The application of the dispersion of Ca(OH)₂ nanoparticles synthesized via this methodology with a pre-treatment of the substrate with a sticky rise was recently studied. The efficiency level of the consolidation action to weathering conditions was rather reduced [194].

Finally, other methodologies for the synthesis of Ca(OH)₂ nanoparticles include the **dissolution of CaCl₂ aqueous solutions in 5-10% sucrose solutions** with the use of magnetic stirring for 4 h under ambient conditions. The size of the nanoparticles was characterized by polydispersity since nanoparticles with a range of size from 25 nm to 600 nm were

detected. The synthesis of $\text{Ca}(\text{OH})_2$ particles at the nano-scale was related to calcium complex formation with less mannitol than sucrose [195].

3.5.3 Interaction between $\text{Ca}(\text{OH})_2$ and silicate products.

The reported lack of chemical affinity between dispersions $\text{Ca}(\text{OH})_2$ and siliceous limestones has been only recently studied. The first attempts concern the synthesis of $\text{Ca}(\text{OH})_2$ -TEOS nanocomposites that can act as a chemical "bridge".

The synthesis of the nanocomposites is based on the previous studies of the interaction of TEOS with calcareous porous substrates (ex. deteriorated concrete) suggested that the polymerization of TEOS may be modified by the possible realization of the reaction between Ca^{2+} ions in the basic medium, possibly inducing the precipitation of a C-S-H gel. The precipitation of the C-S-H gel could enhance the internal cohesion of the damaged concrete [52], [196-197].

At high RH% values, the presence of portlandite has been proven to modify the polymerization of TEOS leading to the formation of the C-S-H gel. This along with the interaction of TEOS with the newly formed C-S-H gel in hydrated cement paste results in the formation of gels of longer chains [196]. The formation of the C-S-H gel has been detected also in the case of the activation of $\text{Ca}(\text{OH})_2$ into nano SiO_2 cements and evaluated as a new type of CaO-SiO_2 cement, as observed in Fig. 3.20. In particular, it has been reported that the activation nano SiO_2 by $\text{Ca}(\text{OH})_2$ is an exothermic reaction, which is attributed to the breakdown of the -Si-O-Si- bonds. The Ca^{2+} offset the charge imbalance and bond to Si-OH and Si-O, forming the C-S-H gel [197].

Finally, the mixing of commercial nanolime dispersion with TEOS at the conditions of high RH%, proved to exhibit great affinity when applied on mortars during a consolidation action [52].

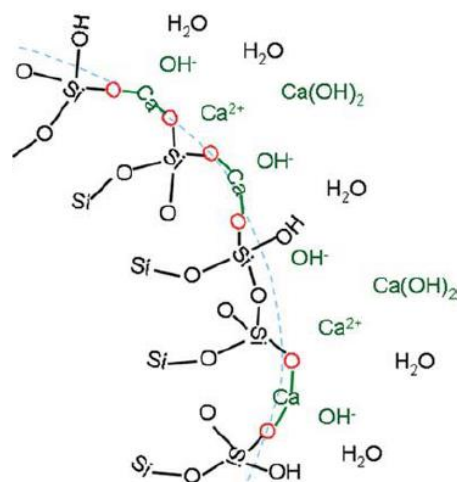


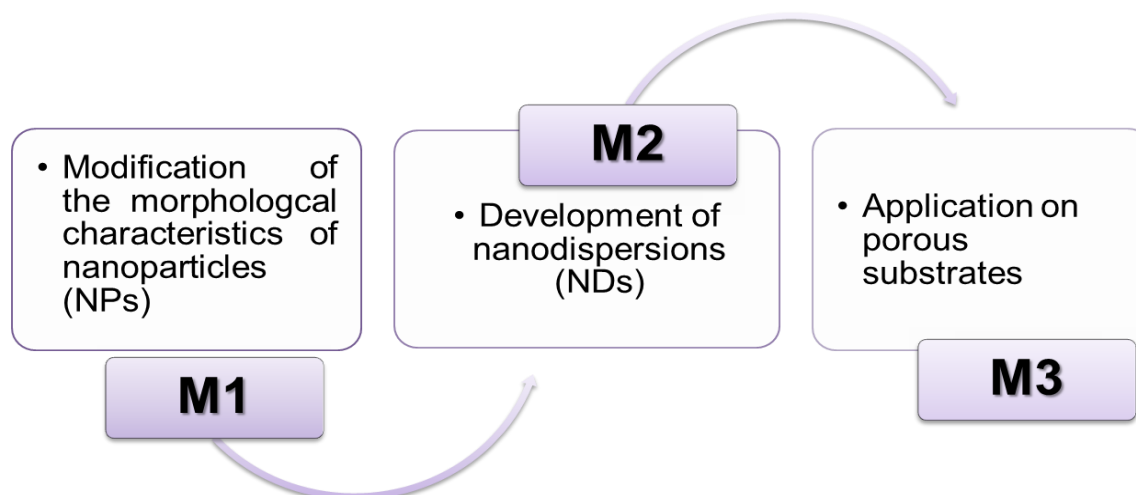
Fig. 3.12 Schematic illustration of the reaction between nanoparticles SiO_2 and $\text{Ca}(\text{OH})_2$ in aqueous solution [196]

Chapter 4 - Materials and Methods

4.1 Introduction

Chapter 4 describes the experimental procedures followed for the optimization of the morphological characteristics of the $\text{Ca}(\text{OH})_2$ nanoparticles and the colloidal stability of the nanodispersions. The **implementation** of the experimental research was based on three main interrelated modules (M_1 , M_2 and M_3):

- M_1 concerned the laboratory synthesis of $\text{Ca}(\text{OH})_2$ nanoparticles and the modification of the parameters affecting their morphological and compositional characteristics, such as sonication energy, the addition of surfactants, the modification of the dispersion medium etc.
- M_2 was focused on the design and laboratory development of $\text{Ca}(\text{OH})_2$ nanodispersions, using different types of dispersion media. The key objective of this module will be the study of the effect of the different modifications of the morphological characteristic of the $\text{Ca}(\text{OH})_2$ nanoparticles on the colloidal stability of the dispersions.
- M_3 addressed the study of the kinetic properties of the $\text{Ca}(\text{OH})_2$ nanodispersions as well as the diffusion and deposition mechanism of the modified $\text{Ca}(\text{OH})_2$ nanoparticles (M_1 and M_2). The later carried out both in standardized inorganic porous substrates (synthetic filter discs), as well as in three (3) representative building materials that exhibit different values of open porosity and pore size distribution (limestone, sandstone and lime-mortar). The application method and the characterization procedures of all substrates are also included in this module (M_3), describing also the relevant analytical methods.



4.2 Synthetic routes of Ca(OH)₂ nanoparticles (module M1)

The synthesis of Ca(OH)₂ nanoparticles was based on two main synthetic procedures: i) **the top-down** and ii) **bottom-up methodologies**. The above methodologies were further modified in order to affect the physical and morphological properties of the nanoparticles synthesized. The main alteration include:

- ✓ modifications of the **synthetic procedure**
- ✓ modification of the **dispersion medium**
- ✓ **functionalization** of Ca(OH)₂ particles' surface
- ✓ **chemical modification** of the Ca(OH)₂ through the synthesis of *Ca-Si* nano-composites

4.2.1 Top-down route

In the main top-down route (T_01), 2,2g of eight years matured lime putty (Ca(OH)₂) for where dissolved in 200 ml of distilled water under continuous stirring for 48 hours. The mixture was subjected to sonication (100W) for 5 hours prior to characterization. The experiment designed on the basis of the effect of the ageing time of the lime putty at the size and morphological characteristics of its [39]

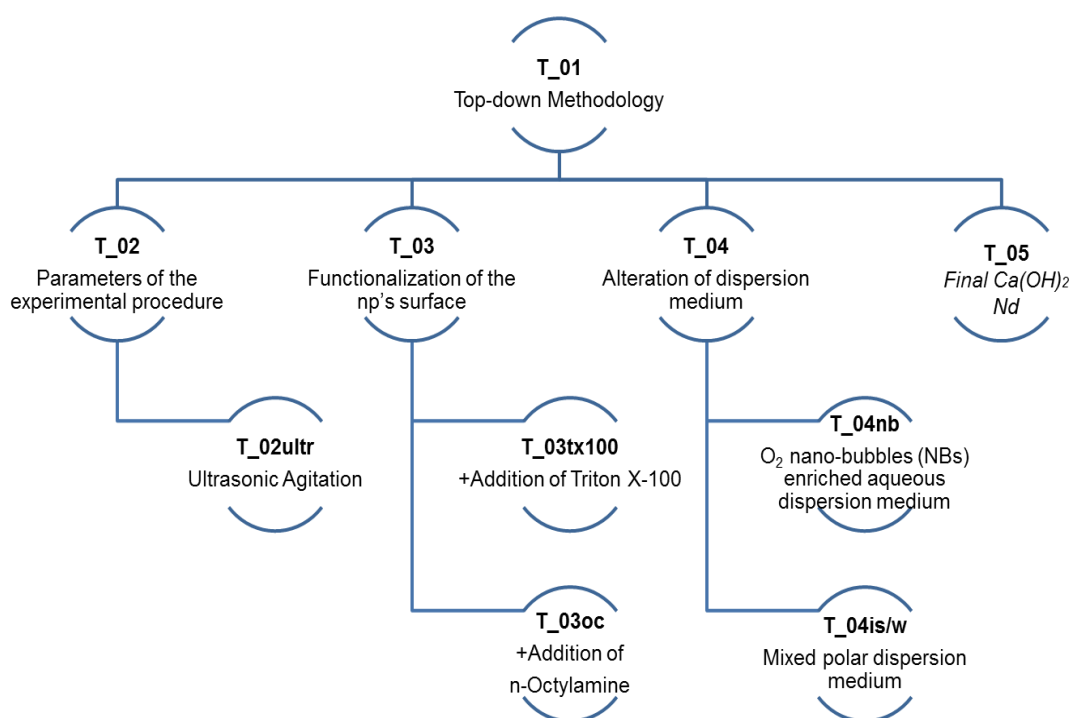


Fig. 4.1 Schematic illustration of experimental synthesis of Ca(OH)₂ via the top-down route

Three modifications of the above synthesis were designed and carried out (T_02-04), in order to investigate the parameters affecting the size and morphology of the of the

produced nano-particles, the functionalization of the surface of the nanoparticles (M1) and the stability of the newly formed $\text{Ca}(\text{OH})_2$ nanodispersions (M2). Figure 4.1 depicts the modifications of the Top-down route:

✓ **T_02:** the first modification concerns the *experimental procedure*, focusing on the sonication energy. The results of the initial top-down route (T_01) indicated that the replacement of ultrasonic bath with higher energy sonicator (UIP 1000 hdTHielser) that induces 500W for 30min (**T_02ultr**) would lead to the disaggregation of any agglomerates formed during the synthetic procedures (Chapter 5.3.1).

✓ **T_03:** the second modification concerns the *parameters affecting the surface functionalization of the newly formed* $\text{Ca}(\text{OH})_2$ nanoparticles. Two non-ionic surfactants were tested for this purpose, in order to study their consequent effect on the morphological characteristics of the produced solid particles. 1g of Triton X-100 (**T_03tx100**) and 1ml of n-octylamine (**T_03oc**) were added in the initial lime-water mixture for the reduction of the surface tension between the nanoparticles and the dispersion medium. The amount of the two surfactants was selected according to the relevant literature [173]

Both surfactants are characterized as non-ionic. Non-ionic surfactants are composed by a neutral head group (often compiled by hydroxyl group) and a hydrophobic body. They are adsorbed on the surface of the $\text{Ca}(\text{OH})_2$ nanoparticles forming hydrogen bonds, leading to the repulsion between the nanoparticles through the steric hindrance of the surfactant (steric stabilization). The selection of Triton X-100 was based on its ability to be adsorbed on the surface of the $\text{Ca}(\text{OH})_2$ nanoparticles due to the hydrogen bonds between the hydroxyl group (OH-) and the -O of the polyoxyethylene group of Triton X-100, forming a steric barrier, thus reducing the surface tension between the nanoparticle and the dispersion medium. Similarly, the selection of n-octylamine was based on its ability to reduce the surface tension between the nanoparticle and the dispersion medium, to successfully form mesoporous structures and to its ability to be removed through evaporation.

✓ **T_04:** the third modification concerns two alterations of the dispersion medium of the $\text{Ca}(\text{OH})_2$ nanodispersions and their consequent effects on the morphological characteristics of the $\text{Ca}(\text{OH})_2$ nanoparticles and the stability of the $\text{Ca}(\text{OH})_2$ nanodispersions. The distilled water was replaced with an aqueous solvent enriched with oxygen (O_2) nanobubbles of average dimension c.a. 800 nm (**T_04nb**) and with a mixed polar dispersion medium, using different 2-propanol and water ratios (**T_04is/w**).

All three dispersion mediums (distilled water, aqueous solvent enriched with oxygen (O_2) nanobubbles and 2-propanol) are characterized as polar media, thus, promoting the electrostatic stabilization between the $\text{Ca}(\text{OH})_2$ nanoparticles and the dispersion medium, in order to avoid the aggregation between the newly formed nanoparticles. The selection of the aqueous dispersion medium enriched with oxygen (O_2) nanobubbles was based on the ability of the stable bulk oxygen (O_2) nanobubbles to interact with the $\text{Ca}(\text{OH})_2$ nanoparticles

through their adsorbent and re-nucleation of the surface of the nanoparticles, forming a steric barrier and thus, inhibit the aggregation of the nanoparticles [146]. Finally, among the short-chain aliphatic alcohols, 2-propanol presents the lowest surface tension and higher boiling point. The selection of 2-propanol was based on the characteristic low surface tension and its ability to be adsorbed on the surface of the nanoparticles, forming a steric barrier. In this way, the presence of 2-propanol promotes the deagglomeration of the newly formed $\text{Ca}(\text{OH})_2$ nanoparticles and the formation of stable dispersions [4], [39].

The optimum $\text{Ca}(\text{OH})_2$ nanodispersion in terms of morphological characteristics and stability of the nanodispersions, were chosen for the application on the six inorganic substrates (presented in Chapter 7).

4.2.2 Bottom-up synthetic route

The bottom-up synthesis of $\text{Ca}(\text{OH})_2$ nanoparticles was based on the displacement reaction between calcium chloride CaCl_2 and sodium hydroxide NaOH in aqueous solutions. The reaction products are the solid calcium hydroxide nanoparticles $\text{Ca}(\text{OH})_2$ and the water-soluble sodium chloride NaCl (as by-product), according to the reaction:



100ml of NaOH (0.6mol/L) was added drop to drop in 100ml of $\text{CaCl}_2 \cdot \text{H}_2\text{O}$ solution (0.3 mol/L). Aiming to diminish the dissolution of the calcium hydroxide, the temperature of the reactants and of the final solution were maintained constant at 90 °C throughout the experimental procedure, using a thermal bath. Aiming to support the formation of portlandite particles at the nanoscale, a slow mixing rate (drop to drop) and high temperature conditions were selected, in order to favor the nucleation rate and not the particle growth [73]. At the end of the synthesis, the NaCl by-product was removed by continuous washings using distilled water at 90 °C, in order to minimize the solubility of $\text{Ca}(\text{OH})_2$ in water and thus the potential dissolution of smaller nanoparticles in it. The synthetic route led to the production of nanolime dispersions of concentration of 1% w/v. (B_01).

Contrary to the common practice [173], at the end of the washing procedure the water was not replaced by the mixed polar dispersion medium, but with distilled water.

Four modifications of the above synthesis were designed and carried out, in order to investigate the parameters affecting the size and morphology of the of the produced nanoparticles, the functionalization of their surface (M1) and the stability of the newly formed $\text{Ca}(\text{OH})_2$ nano-dispersions (M2). Figure 4.2 illustrates the modifications of the bottom-up synthetic route:

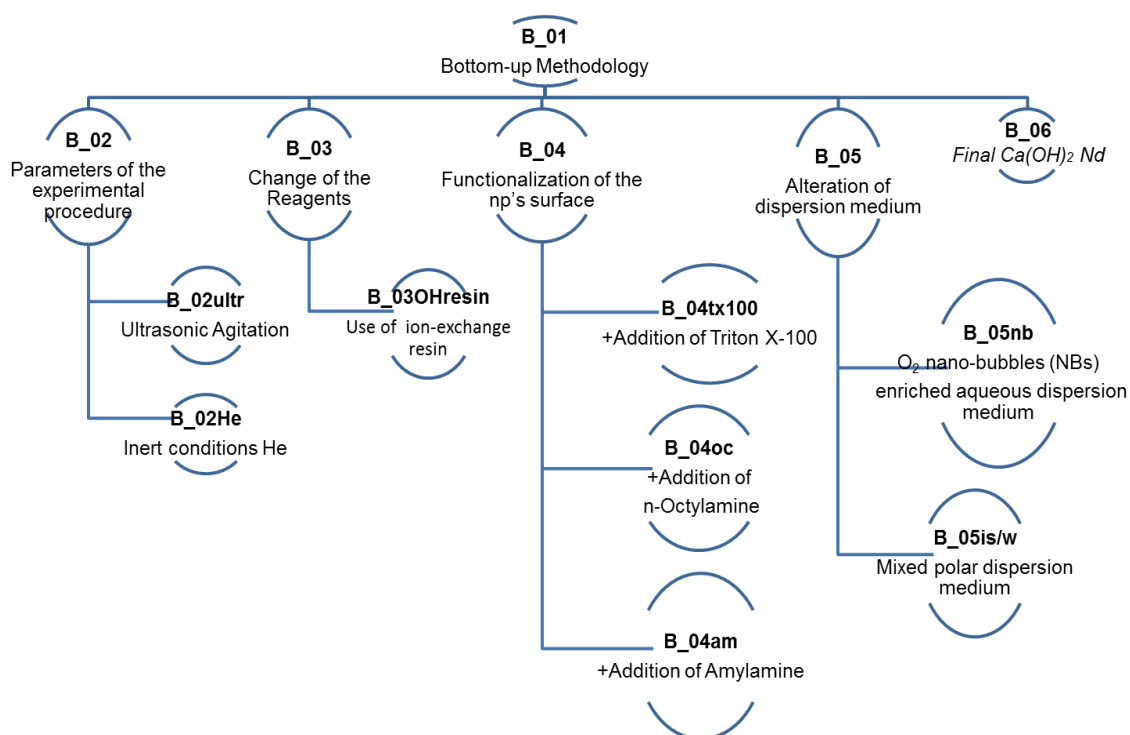


Fig. 4.2 Schematic illustration of experimental synthesis of $\text{Ca}(\text{OH})_2$ via the bottom-up synthetic route

- ✓ **B_02:** the first modification concerns the *experimental procedure*, focusing again on the sonication energy. The preliminary results of the main bottom-up synthetic route (B_01) indicated that the replacement of ultrasonic bath with UIP 1000 hdThieler (Fig. 4.3) of higher energy that induces 500W for 30min (B_02ult) would lead to the disaggregation of any agglomerates formed during the synthetic procedures (Chapter 5.3.1).



Fig. 4.3 The ultrasonic agitation unit (UIP 1000 hdThieler) used for sonication the $\text{Ca}(\text{OH})_2$ nano-dispersions.

The monitoring of the carbonation rate during the first trials of the synthetic procedure indicated the need for the investigation of the implementation of the experimental procedure under inert conditions. The He atmosphere was selected for this purpose [38] (B_02He)



Fig. 4.4 Reactor for the synthesis of Ca(OH)_2 nanoparticles under inert conditions (He atmosphere)

✓ **B_03:** the second modification concerns the *replacement of the reagents* and the replacement of NaOH with an ion-exchange resin. An ion-exchange resin (DowexMonosphere 550 A (OH^-)) was added (115ml of anionic resin solution) into $\text{CaCl}_2 \cdot \text{H}_2\text{O}$ (100ml of 0.1 M solution) at room temperature, under moderate stirring for 60 minutes. At the end of the experimental procedure, the resin was removed, and the solid product was collected for characterization

✓ **B_04:** the third modification concerns the *parameters affecting functionalization of the surface* during the synthesis Ca(OH)_2 nanoparticles. It consists on the addition of three non-ionic surfactants during the synthetic procedure, in order to study their consequent effect on the size, morphology and mineralogy of the produced solid particles. 1g of Triton X-100 (**B_04tx100**), 1ml of n-octylamine (**B_04oc**) and 1ml of amylamine (**B_04am**) were added on the 100ml solution $\text{CaCl}_2 \cdot \text{H}_2\text{O}$. The amount of the three surfactants was selected according to the relevant literature (Daniele et al. 2012). Further to the two non-

ionicsurfactants already used (Triton X-100 nd n-octylamine) the use of amylamine was based on its beneficial ability to successfully form stable foams and to be removed through evaporation.

✓ **B_05:** the fourth modification concerns two alterations of the dispersion medium and their consequent effects on the morphological characteristics of $\text{Ca}(\text{OH})_2$ nanoparticles and the stability of the nano-dispersions derived. the distilled water was replaced by an aqueous solvent enriched with oxygen (O_2) nanobubbles of average dimension c.a. 800 nm (**B_05nb**) and by a mixed polar dispersion medium, using different 2-propanol and water ratios(**B_05is/w**).

The five optimum $\text{Ca}(\text{OH})_2$ nano-dispersions in terms of the morphological characteristics and stability of the nanodispersions, was chosen for the application on the six inorganic substrates (presented in Chapter 7).

4.2.3 Synthesis of Ca-Si nanocomposites

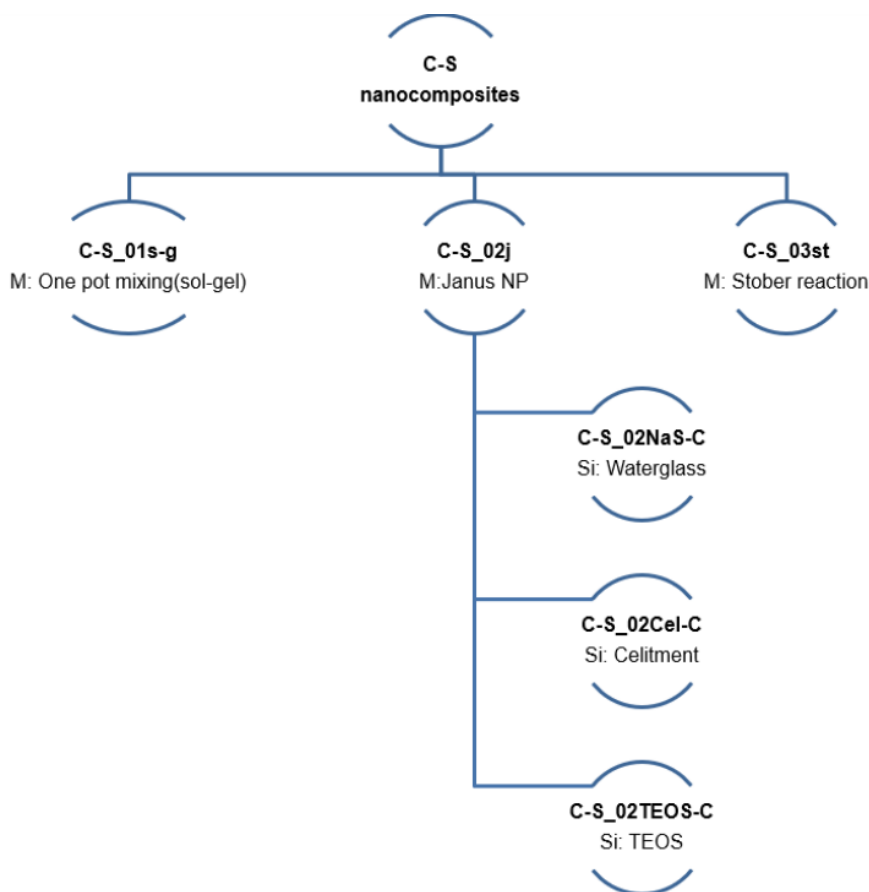


Fig. 4.5 Schematic illustration of experimental synthesis of Ca-Si nanocomposites

Three modifications were implemented for the potential interaction of Ca-OH and Si-O to form a C-S-H phase, corresponding to the synthesis of Ca-Si nanocomposites:

✓ **C-S_01s-g:** The mixing of $\text{Ca}(\text{OH})_2$ nanoparticles in TEOS was realized in one pot synthesis via the sol-gel method. This synthetic route was focused on the on the formation of C-S-H phase based on amorphous silica and calcium hydroxide (Veganelaki et al. 2015), aiming to enhance the electrostatic interactions between the nanocomposite and the lithic substrate. The selection of the two components (TEOS and calcium hydroxide) was based on the significant role of the end-up products (amorphous silica and calcium hydroxide) on the biomineralization and consolidation actions [65]. The two initial mixing solutions were prepared (stage A) by:

a) a nanolime dispersion made of a 5-year aged putty ($\text{Ca}(\text{OH})_2$), diluted in a mixture of 2-propanol and water (4:1 v/v), stirred for 120 min and subjected to ultrasonic agitation for 5 min

b) a TEOS solution diluted in 2-propanol, with molar ratio of TEOS/2-propanol of 1/3, left for 120 min under magnetic stirring.

The two batches (a+b) were mixed simultaneously (stage B) and the resulting mixture remained for 20 hours under magnetic stirring (stage C). Finally, the mixture was diluted with 2-propanol and kept under magnetic stirring at room temperature for 3 days (stage D) (fig. 4.6).

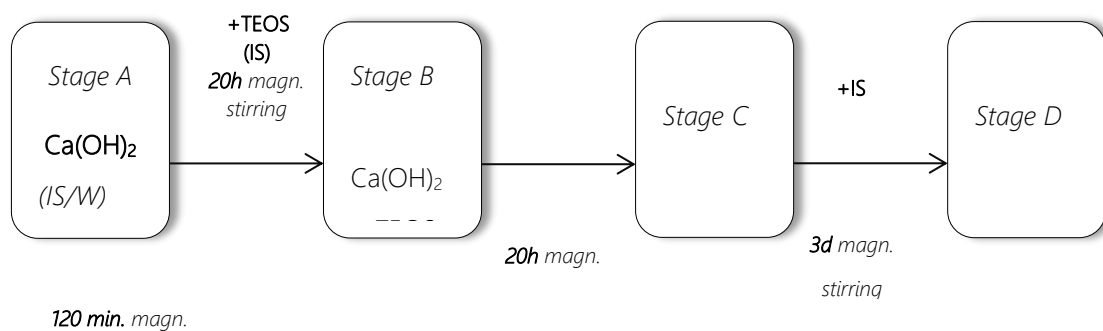


Fig. 4.6 Schematic illustration of experimental synthesis of one-pot synthesis of Ca-Si nanocomposites via the sol-gel methodology

✓ **C-S_02j:** the second approach is based on the synthesis of Janus nanoparticles. 3 gr of $\text{Ca}(\text{OH})_2$ and 3gr of silicate were added homogeneously dispersed in isopropanol/water (6%, w/w) solution and heated at 65 °C (stage A). 1 g of wax was then added to the particles suspension. After the wax melting, the mixture was subjected to vigorous stirring for 80s (stage B). Then 1g of the non- ionic surfactant of Triton X-100 is added and then the suspension is subjected to vigorous stirring for 5 min. (stage C). Finally, turpentine was added for the removal of the wax (stage D) (Fig. 4.7).

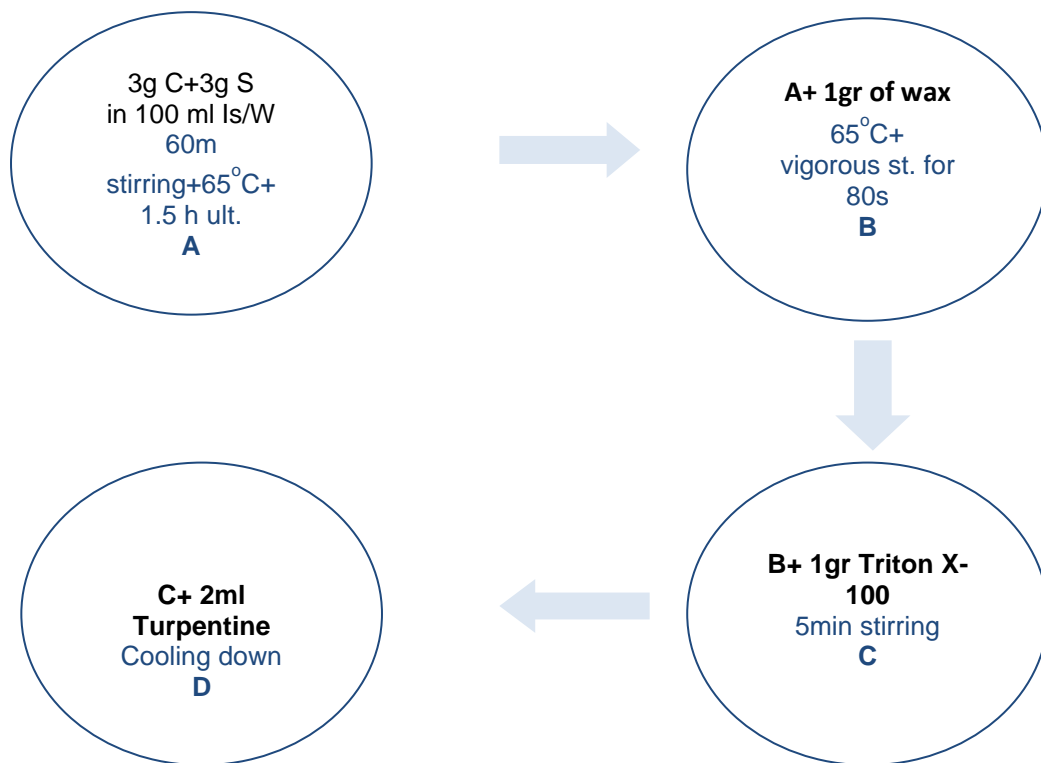


Fig. 4.7 Schematic illustration of experimental synthesis of Ca-Si nanocomposites via the synthesis of janus nanocomposites

Three modifications of the above process were realized, changing the chemical composition of the Si-compound. The first trial was based on the use of waterglass (C-S02NaS-C). The second trial involved the use of the commercial product Celitment, an innovative hydraulic binder(C-S02Cel-C). The third trial incorporated the use of TEOS (C-S02TEOS-C).

✓ **C-S_03st:** the third modification of the synthetic approach for Ca-Si nanoparticles was based on the simultaneous realization of the Stöber reaction for the synthesis of Si-spheres and the incorporation of the Ca(OH)₂ nanoparticles. In this approach, Si-spheres were synthesized via an 100ml ethano suspension with the addition of 11ml of Ca(OH)₂nanodispersion (T01), 6ml of TEOS and 8ml of NH₃. The suspension was placed under vigorous stirring at 50°C. After 30min., the suspension was subjected three times to centrifugation at 12000 rpm for 8min. Then the gel was collected and was re-dispersed in ethanol [99].

4.3 Analytical Methods

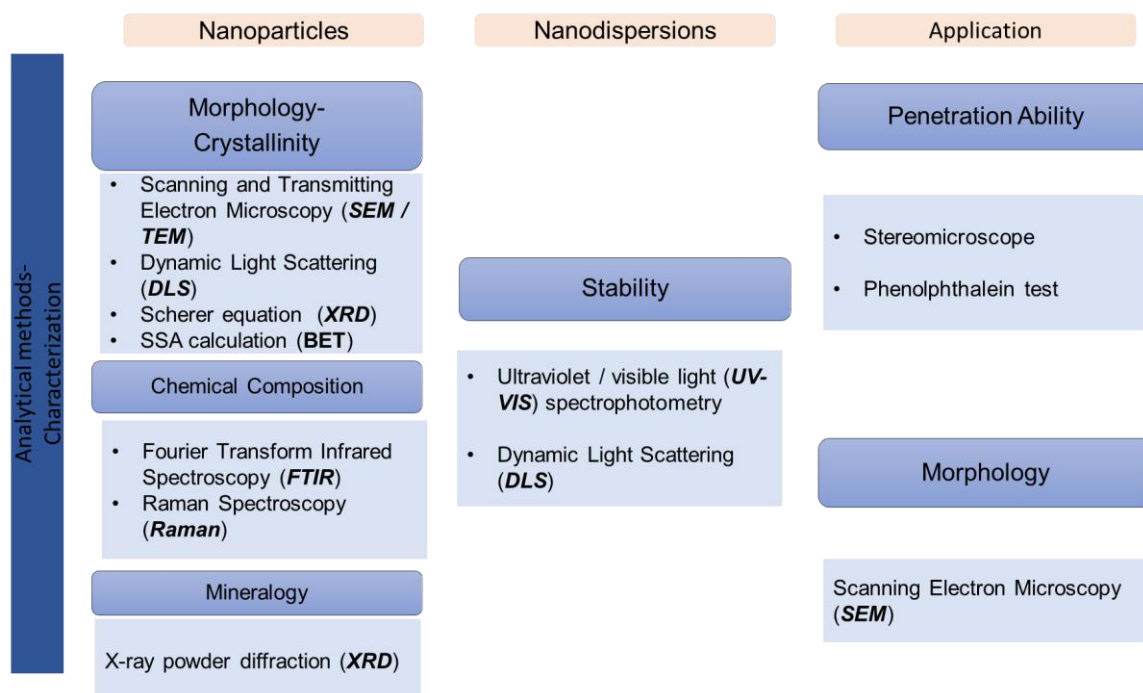


Fig. 4.8 Layout of the analytical methods

4.3.1 Scanning and Transmitting Electron Microscopy (SEM-TEM)

The use of SEM and TEM lead to the determination of the morphological characteristics of the newly synthesized $\text{Ca}(\text{OH})_2$ nanoparticles. During the SEM analysis, the exploitation of the secondary electrons will result in the determination of the size (diameter) and shape of the nanoparticles. The use of TEM will lead to the further investigation and determination of the nanoparticles in reduced scaling and will provide an estimation concerning the crystallinity of the nanoparticles via the SAED analysis.

The principle of the method is based on the interaction of the sample with a high energy electron beam, characterized by a very short wavelength (about 0.1nm). The electron beam is produced by thermal emission from a heated tungsten filament and then is accelerated by a constant voltage value 1- 50 kV, thus obtaining a specific wavelength. Magnetic lenses focus the beam to another beam of small diameter, which is scanned on the sample surface. Moreover, the entire assembly is under vacuum [200]

The primary electrons interact with the sample and generate the:

- Backscattered electrons (backscattered): They derived from the elastic collisions of primary electrons and the atoms of the sample surface (to a depth of 100 nm) and they have high energies (up to 50 keV). Furthermore, the intensity of the generated sample depends on the atomic number of interface elements as well, and crystallographic

orientation. Still, the contrast caused is much greater in respect with the one caused by secondary electrons (category b). So, this enables the collection of information concerning the microstructure and the surface topography.

b) Secondary electrons (secondary): They are characterized as low-energy electrons (with a value of up to 50 eV) and derived from the inelastic collisions (ionization) of individuals sampled from the primary electrons. An important characteristic is that the sample micro-topography represented on the screen as bright or dark areas, because of the number of emitted (from the sample) secondary electrons is proportional to the angle of the incidence of the beam.

c) X-Ray: Production of the surface layer of the specimen (at a depth of 1 micron). The characteristic spectrum of the sample is recorded using X-ray spectrometer. Indeed, X-rays from a particular sample component, can be displayed on the screen as bright spots in the test area, giving the local concentration of this element (element mapping). Generally, the X-ray spectrum gives the intensity of the lines as a function of energy and the analysis results in chemical surface analysis (X-ray microanalysis method dispersion energy, energy dispersive analysis EDS). Finally, the constraining element of conventional X-ray spectrometers, is that it can detect elements with atomic number $z > 11$ [200] (Fig.4.19).

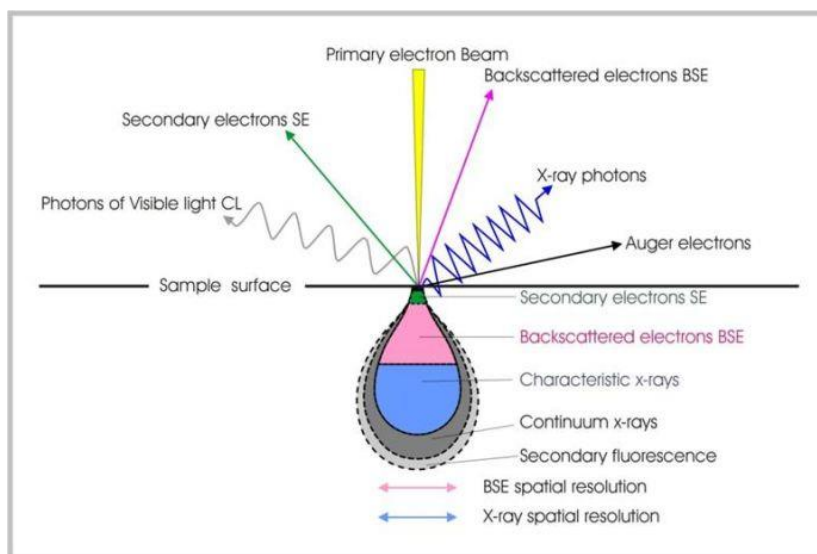


Fig. 4.9 Interaction between electrons and the substrate of the specimen in SEM [201]

To sum up, the scanning electron microscope (SEM) provides access to the investigation of specimens, with a resolution narrowed down to nanometer scale. This method enables the identification of the consolidation treatment inside the stone specimens. Consequently, this is a crucial method for estimating the depth of penetration and determining the filling of the pores [200].

In the case of transmission electron microscope (TEM) electron beams, generated from an electron gun, focus on the specimen by metal apertures and electromagnetic lens in the

column of the microscope. The mechanism of the focusing phenomenon of electrons is based on the wavelike character of electrons as they behave as negatively charged particles, then deflected by magnetic or electric fields. During this procedure, electrons only within a small range of energy could pass through, leading to a well-defined energy electron beam. Then, the transmitted electrons are applied to the specimen in the column of a TEM, which is placed onto the sample holder (or called TEM grid, consisting of metal frame and carbon-based film) equipped with a mechanical arm for controlling the position and holding the specimen. The thickness of a TEM specimen usually should be within 100 nm for electrons to pass through. Many factors of the specimens could have an impact on the transmission of electron beam, such as density or composition of a specimen. The main difference between SEM and TEM is the operation of the electron beam. In the case of SEM, the image is constructed by the reflected electrons, whereas in the case of TEM the electron beam is transmitted through the specimen and the image is constructed by the refracted beam [202].

4.3.2 Dynamic Light Scattering (DLS)

The DLS method provided the characterization of the size of the newly formed $\text{Ca}(\text{OH})_2$ nanoparticles through the determination of the hydrodynamic diameter of the nanoparticles. Also, the determination of the particle size distribution curves will underling the uniformity or polydispersity of the size of the nanoparticles. Finally, the determination of the ζ -potential of the nanodispersions will indicate the tendency of the nanoparticles to form aggregates.

The operation of the dynamic light scattering (DLS) method is based on the application of a laser beam on the dispersion and on the consequent production of scattered light from the nanoparticles (Tyndall effect) (Fig. 4.10). In specific, when a monochromatic beam interacts with nanoparticles, the light scatters in all directions as a function of the morphological characteristics (size and shape) of the nanoparticles. The interpretation of the results using different mathematical models results on the determination of the size and pore size distribution of the nanoparticles, the temperature and pH dependence, the ζ -potential, the molecular weight etc [203]. The measurements are based on the Stokes Einstein equation (4.2)

$$D_o = \frac{kT}{6\pi\eta R} \quad (4.2)$$

Where: D_o =is the diffusion coefficient, k = is the Boltzman constant, T =is the absolute temperature, η =is the dynamic viscosity of the dispersion and R = the radius of the nanoparticle.

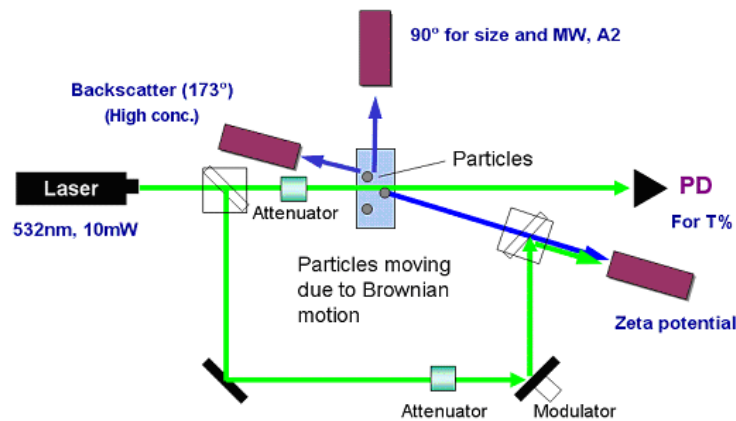


Fig. 4.10 Schematic illustration of the working principals for the determination of the particle size distribution and the ζ -potential of the nanoparticles

[204]

4.3.3 Specific Surface Area calculation (BET)

The determination of the specific surface area of the newly synthesized $\text{Ca}(\text{OH})_2$ nanoparticles will indicate the effect of the modification of the different parameters on the size of the nanoparticles in terms of the S/V ratio and thus the effect on their reactivity.

The basis of this method is the evaluation of the quantity of gas being adsorbed on the surface of the material in relation to the applied partial pressure. The interpretation of the results with the BET (Brunauer, Emmett, and Teller) results in the determination of the specific surface area. For the application of the BET mode, it is assumed that a monomolecular layer of N_2 is adsorbed on the surface of the sample in accordance with (4.3):

$$1/(v[(P/P_o) - 1]) = (c - 1)/vm (P/P_o) + 1/vm \quad (4.3)$$

Where: v =is the adsorbed gas volume, P = is the applied pressure, P_o = is the saturation pressure, v_m = is the gas volume needed to create a monomolecular layer of nitrogen and c =is the BET equation constant.

The selection of the gas is based on the affinity with the selected sample. The results from the BET method are represented to graphs of isotherms (Fig. 4.11) and hysteresis (Fig. 4.12). *Type I adsorption isotherm* is characteristic of microporous solids (pore size > 2nm). The relatively small uptake is determined by the volume of the micropores. Type I depicts a monolayer adsorption, when $P/P_o < 0$ and $c > 1$ in the BET equation 4.3. *Type II adsorption isotherm* is characteristic of non-porous or macroporous solid (pore size < 50 nm). Type II represents the unrestricted monolayer multilayer adsorption. Point B at the linear middle section is an indication of the completion of the monolayer adsorption and the beginning of the multilayer adsorption. *Type III* also represents the process of the formation of an unrestricted multilayer. The formation of the multilayer is attributed to the interactions between the adsorbed molecules and their stronger effect compared to the interactions between the surface sample and the adsorbed molecules. *Type IV adsorption isotherm* and

type *V adsorption isotherm* are characteristic adsorption isotherms for the process of the adsorption of mesoporous solids via multilayer adsorption followed by capillary condensation. The formation of the multilayer in type *V* is attributed to the interactions between the adsorbed molecules and their stronger effect compared to the interactions between the surface sample and the adsorbed molecules (pore size in between 2nm and 50 nm). *Type VI* represents the stepwise multilayer adsorption on a uniform nonporous surface. The height of the step represents the monolayer capacity of the adsorbed layer and its sharpness depends on the temperature and the whole system (Fig. 4.11) [205-206]

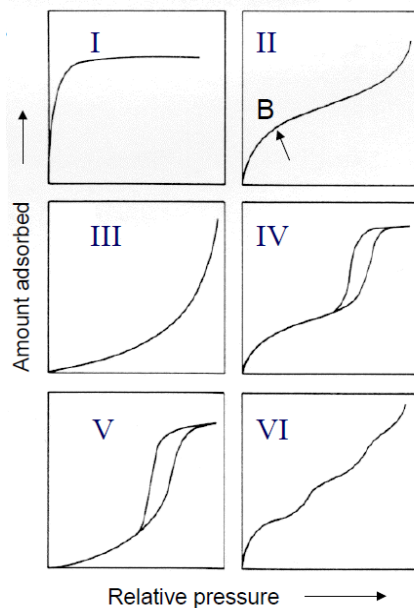


Fig. 4.11 Schematic illustration of the adsorption isotherms [206]

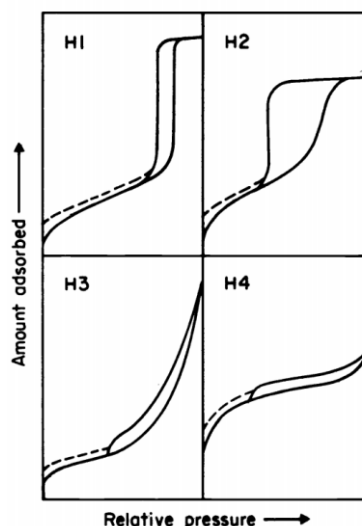


Fig. 4.12 Schematic illustration of the adsorption isotherms ([207])

The phenomenon of hysteresis is attributed to either thermodynamic or network effects or to the combination of these two effects. As it can be observed in Fig. 4.12, the steepness of the

isotherms decreases from H1 to H4. *Hysteresis H1* indicates a relatively high degree of uniformity of the size of the pores and a connected pore network. It is indicative of a cylindrical geometry of the pores. Hysteresis H1 is attributed to the uniform arrangement of the agglomerates of the spherical particles of the adsorbed gas. *Hysteresis H2* indicates a relatively uniform pore network and the presence of ink-bottle pores. Hysteresis H2 is attributed to the domination of the pore network effect. *Hysteresis H3* is attributed to the formation of slit-like pores by the agglomeration of plate-like particles. Finally, *Hysteresis H4* is attributed to the synergetic effect of the presence of narrow slit-like pores, particles with internal pores of irregular shape and broad size distribution and to hollow spheres with walls consisted of ordered mesoporous silica nanoparticles [207]

4.3.4 X-ray powder diffraction (XRD)

The XRD method will present the mineralogical characterization of the newly formed nanoparticles and the monitoring of the carbonation procedure. Also, the application of the Scherrer equation will lead to the determination of the crystallite size.

X-ray diffraction is used for the study of crystal structures and atomic spacing. The phenomenon of diffraction occurs when the light is scattered due to a periodic array with long-range order. The scattering of light produces constructive interferences at specific angles. The atoms of a crystal can scatter the light with intensity proportional to the number of e^- surrounding it. The atoms of a crystal are arranged in a periodic array and thus have the ability to diffract the monochromatic X-rays. The wavelength of the X-rays is similar to the distance between the atoms. The scattering of X-rays from the atoms produces a diffraction pattern, which contains information about the atomic arrangement within the crystal. A key component of all diffraction methods is the angle between the incident and diffracted rays.

These X-rays are generated by a cathode ray tube, filtered to produce monochromatic radiation, collimated to concentrate, and directed toward the sample. The diffraction of the X-rays is realized when the conditions satisfy the Bragg's law (4.4):

$$n\lambda = 2d\sin\theta \quad (4.4)$$

Where: λ =is the wavelength of the x-ray, d = is the spacing of the crystal layers (path difference), θ =is the incident angle (the angle between incident ray and the scatter plane) and n =is an integer.

The Bragg law relates the wavelength of electromagnetic radiation to the diffraction angle and the lattice spacing in a crystalline sample. The scanning of the sample through a range of 2θ angles, enables the detection of all possible diffraction directions of the lattice. The detection of the characteristic d -spacing of each mineral is realized through the conversion of the diffraction peaks to d -spacing. The results are presented in a X-ray diffractogram. The size and the symmetry of the unit cell determine the positions of the peak. The position

of the atoms inside the unit cell determine the intensity of the peaks. Finally, the widths of the peaks are affected by the size/strain of the crystallites [208].

4.3.5 Fourier Transform Infrared Spectroscopy (FTIR)

The FTIR analysis provide the chemical characterization of the nanoparticles. In this way, the detection of the carbonation effect and the C-S-H phase were implemented.

The molecular absorption/transmission of the electromagnetic radiation in the infrared region promotes the transitions between the vibrational and rotantional energy levels of the lowest electronic energy state (Fig. 4.13). This transition can be converted and expressed to an infrared spectrum. The frequency of the absorption/transmission peaks is determined by the vibrational and rotantional energy gap. The intensity of the peaks is related to the change of dipole moment and the possibility of the transition of energy levels. Therefore, by analyzing the infrared spectrum, the structure of the molecules can be analyzed. The samples can be analyzed in gas, liquid and solid state, except from the gases of as O₂, N₂ and Cl₂ due to the zero dipole change in the vibration and rotation of these molecules. The common region for infrared absorption spectroscopy is 4000 ~ 400 cm⁻¹ because the absorption/transmission radiation of most organic compounds and inorganic ions is within this region.

FTIR spectrometers prevents several advantages when compared to the previous infrared spectrometers:

- The signal-to-noise ratio of spectrum is significantly higher than the previous generation infrared spectrometers
- The accuracy of wavenumber can be characterized as rather high. The error is within the range of $\pm 0.01 \text{ cm}^{-1}$
- The scan time of all frequencies is short (approximately 1 s)
- The resolution is characterized as high ($0.1 \sim 0.005 \text{ cm}^{-1}$)
- The scan range is wide ($1000 \sim 10 \text{ cm}^{-1}$) [209-210]

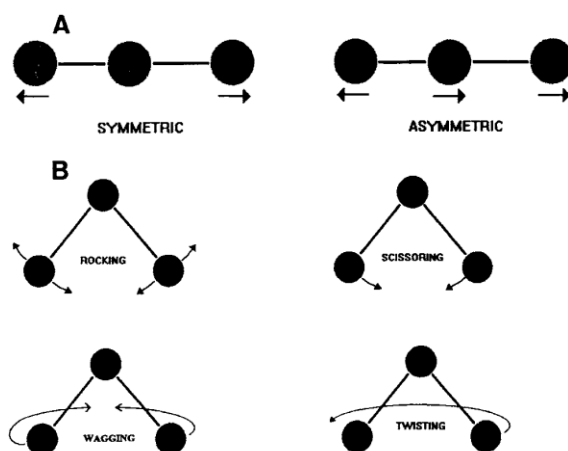


Fig. 4.13 Schematic illustration of the molecular vibrations: a) Stretching vibrations and b) bending vibrations [210]

4.3.6 Raman Spectroscopy

The use of Raman analysis provided further information about the effect of the carbonation procedure via the chemical characterization of the products.

The Raman spectroscopy is a scattering technique. Samples are illuminated with a monochromatic laser beam which interacts with the molecules and originated a scattered light. It is based on the interaction of the inelastic scattering of the incident radiation with the vibrating molecules. The incident radiation and the molecules of the sample interact through the inelastic collision. The scattering radiation that is characterized by the same frequency with the incident radiation constitutes the Rayleigh scattering. The portion of the scattering radiation that exhibits a different frequency constitutes the Raman scattering.

The Raman scattering depends on wavelength of incident radiation. In order to obtain a Raman spectrum, a modification of the polarizability during molecular vibration is essential. Raman active normal modes usually occur in the range of the 4000 cm⁻¹ to 400 cm⁻¹ ([211]

4.3.7 Ultraviolet/ Visible light spectrophotometry (UV-VIS)

The use of the UV-VIS spectroscopy led to the determination of the colloidal stability of the newly produced nanodispersions.

The UV-VIS spectrophotometry is based on the Beer-Lambert law (4.5):

$$A = \log\left(\frac{I_0}{I}\right) = \epsilon CL \quad (4.5)$$

Where: A= is the absorbance, I₀=is the incident intensity, I= is the transmitted intensity, C= is the concentration of the solute (mol/m⁻³), L= is the of the solution that light passes through (m) and ε= is the molar absorption coefficient.

According to the Beer-Lambert law, the decrease of the intensity of the transmitted light beam depend on the concentration of the solution. [212]

Based on the application of the UV-VIS spectrophotometry, the kinetic stability (KS) of a dispersion can be estimated by turbidity measurements, determining the absorbance at λ= 600 nm in respect to time (upon 4 hours) intervals by UV/VIS spectrometer. The turbidity of the dispersions is considered to be proportional to the absorbance at 600 nm, and its decrease over time is related with the occurrence of particle agglomeration and settling. The relative kinetic stability (KS %) is estimated according to the formula (4.6):

$$KS \% = \left\{1 - \frac{(A_0 - A_t)}{A_t}\right\} \times 100 \quad (4.6)$$

Where A₀ is the starting absorbance and A_t the t time interval [37]

4.3.8 Stereomicroscope

The use of stereomicroscope will lead to the determination of the extent of the penetration ability of the nanodispersions.

Stereomicroscope (or dissecting microscope), is an optical microscope, the use of which is based on the idea of using the reflected light, rather than the transmitted one. The principle of this analytical method is the production of two slightly different optical angles for each eye, causing the production of a three-dimensional visualization of the sample. This is realized through the use of two separate optical paths with two objectives and eyepieces (Fig. 4.17) [213].

So, the main advantage of the stereomicroscope is the examination of samples characterized by complex surface topography. Finally, on the basis of the principle of their design, stereomicroscopes can be divided into two categories:

- a) Designed according to the Greenough principle design
- b) Designed according to the telescope principle (which is the newest design principle) [213].

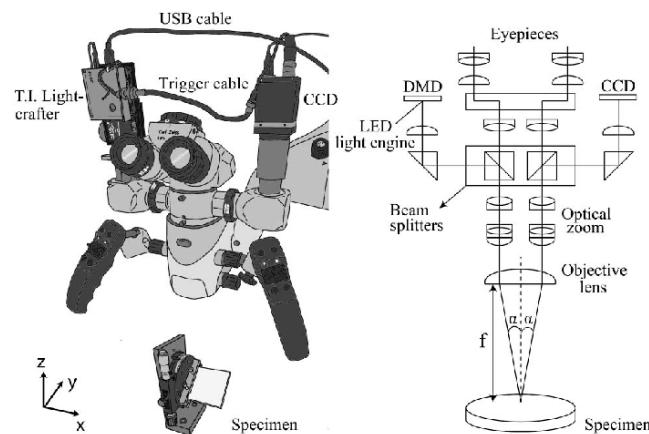


Fig. 4.14 Schematic illustration of the operation of a stereomicroscope [213]

Chapter 5 - Synthesis and characterization of Ca(OH)₂ nanodispersions

5.1 Introduction

In chapter five, the characterization results of the newly synthesized dispersions of Ca(OH)₂ nanoparticles are presented. The characterization concerns the chemical, mineralogical and morphological characterization of Ca(OH)₂ nanoparticles as well as the kinetic stability of the dispersions. The presentation and interpretation of the results are organized on the basis of the parameter that is modified in each experiment.

The first part concerns the results of the two basic synthetic routes: the top-down (T01) and the bottom-up (B01), without any modification of the basic procedure. The next chapters contain the results obtained after **modification of different parameters in both processes** such as, the effect of:

- replacement of NaOH reagent by an ions exchange (-OH) resin (B_03OHresin),
- sonication energy (ultrasonic agitation) (T_02ultr and B_02ultr),
- synthetic conditions, i.e open-air or static inert atmosphere (B_02He),
- functionalization of the nanoparticles surface through the addition of surfactants and
- modifications of the polar dispersion medium.

The three surfactants studied include: i) the non-ionic surfactant Triton X-100 (T_03tx100 and B_04tx100), ii) the non-ionic surfactant n-octylamine (T_03oc and B_04oc) and iii) the cationic surfactant amylamine (B_04am).

In the case of the dispersion medium, de-ionized water was replaced by i) O₂ nanobubbles (nbs) enriched water (T_04nb and B_05nb), ii) 2-propanol and iii) mixtures of the above in different ratios, providing a wide range of dispersion media (T_04is/w and B_05is/w).

Finally, the synthesis of Ca-Si nanocomposites was studied through three synthetic routes:

- incorporation of Ca(OH)₂ nanoparticles in TEOS, in one pot synthesis via the sol-gel method (CaSi_01s-g),
- synthesis of Janus Ca-Si nanocomposites. The silicate agents tested were: i) water-glass (CaSi_02NaS-C), ii) a novel hydraulic binder (Celitement, CaSi_02Cel-C), and iii) TEOS (CaSi_02TEOS-C).
- incorporation of Ca(OH)₂ nanoparticles in TEOS via the Stober reaction (CaSi_03st).

Rationale on SEM results

The images obtained during SEM examination of the newly formed Ca(OH)₂ nanoparticles concerns the material deposited on the stub surface, as loosely-bonded clusters of Ca(OH)₂

nanoparticles. This is attributed to the evaporation of the dispersion medium during the sample preparation procedure. During the evaporation stage, the agglomeration of the nanoparticles is favored by capillary forces, which eventually overcome the electrostatic repulsion [149]. Consequently, the nanoparticles form larger agglomerates and are deposited as a solid material (Fig. 5.1), thus imitating the morphology of the material deposited inside the pore matrix of the building materials during consolidation. Therefore, the morphological characteristics observed in SEM are related to the characteristics of the dispersion medium used each time and the surface tension between the surfactant/dispersion-medium/nanoparticles system during the evaporation of the liquid phase [146].

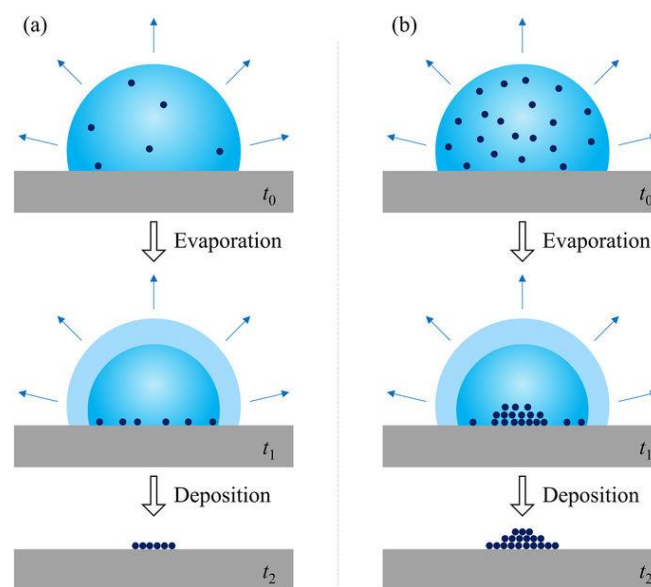


Fig. 5.1 Schematic illustration of the evaporation of the dispersion medium and deposition of the nanoparticles.

Therefore, the characterization of dispersions presented in the following chapters encompasses the size of the hexagonal portlandite crystallites based on the XRD results, the morphology of the nanoparticles in TEM and the morphology of the clusters of the nanoparticles in SEM, after evaporation of the dispersion medium, condensation and deposition of the solid fraction. Moreover, the use of DLS was selected for the characterization of the hydraulic diameter/size of the produced nanoparticles when dispersed in the dispersion medium.

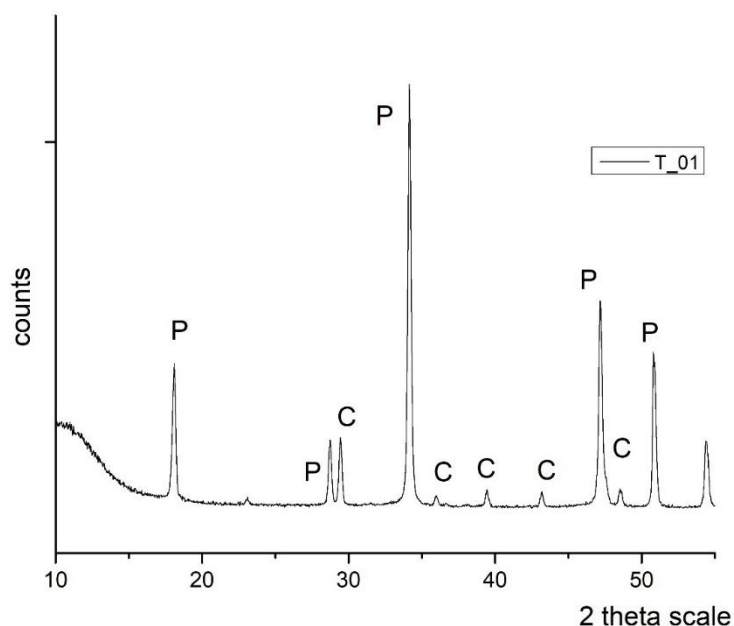
5.2 Production of Ca(OH)₂ nanodispersions

5.3.1 The basic top-down synthetic route

Mineralogical characterization - XRD results

The mineralogical characterization results of T₀₁ dispersion were characterized by the dominant presence of portlandite Ca(OH)₂ (Graph 5.1). Specifically, the presence of the major peaks 18,01°, 28,5°, 34,1°, 46,9° and 50,8° [214] along with the sharpness of the peaks, contributed to the identification of portlandite particles of hexagonal crystals. Other minor phase identified was the one of calcite (CaCO₃) of trigonal crystals [215]. The presence of calcite could be attributed to the partial carbonation of the samples, due to the CO₂ dissolved in water during drying.

The average crystallite dimensions of portlandite were determined, using the Scherer equation [44], [216] T₀₁ resulted in the formation of portlandite nanoparticles with average crystallite size of 33 nm. The difference between the crystallite size (domain structure) and the size of the Ca(OH)₂ nanoparticles indicated a multi-domain structure.



Graph 5.1 X-ray Diffraction pattern of the produced nanoparticles (T₀₁)

Morphological characterization - SEM results

The examination of Ca(OH)₂ particles developed by the implementation of the top-down route (heterogeneous reaction) (T₀₁) in SEM, revealed the formation of conglomerates, consisted of Ca(OH)₂ particle clusters in the range of 140 nm to 1.8 μm (Fig. 5.2). Calcite particles were also evident in SEM examination, having the characteristic form of peanut-like aggregates [217] (Fig. 5.2a). The above results indicate that the aging of lime putty was accompanied by the reduction of the particles size (of initial particle size belonging to the

micro-scale) and the transformation of portlandite particles from prismatic to plate-like [4], [35], [218]

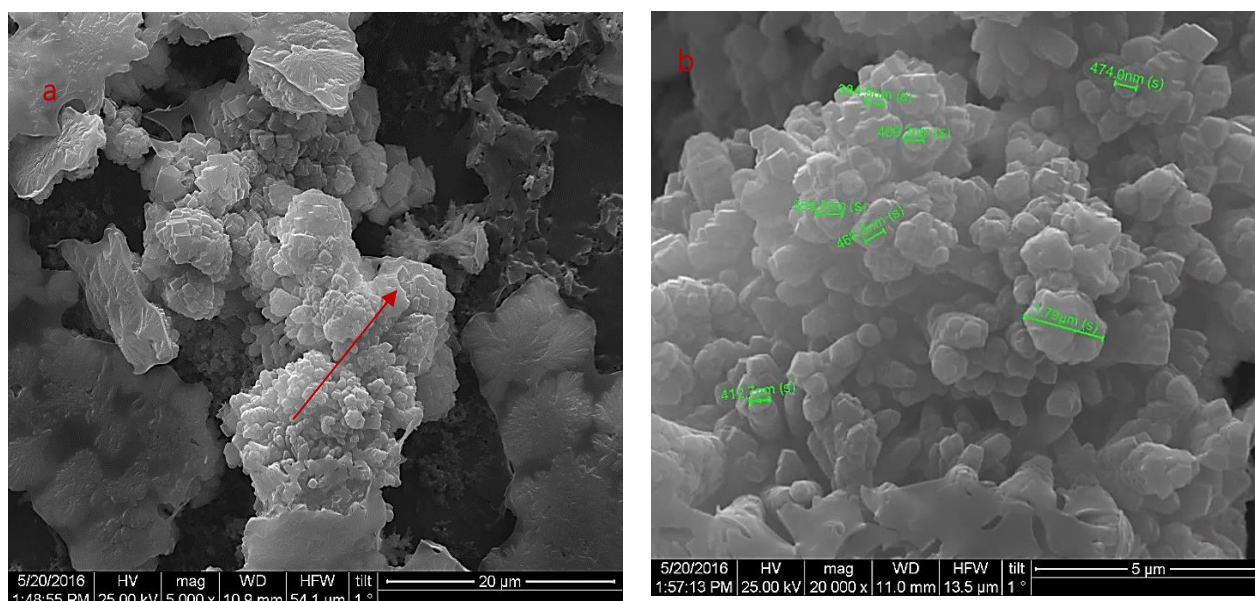


Figure 5.2 (a) $\text{Ca}(\text{OH})_2$ nanoparticle clusters forming larger conglomerates and $\text{Ca}(\text{CO}_3)$ particles (scale bar at 20 μm) and (b) $\text{Ca}(\text{OH})_2$ nanoparticle clusters, of dimensions in between 400 nm- 1.8 μm , forming larger conglomerates (scale bar at 5 μm)

The presence of large agglomerates underlined the need of the use of high intensity ultrasounds that could induce higher energy amounts and thus breaking the Van der Waals forces that keep the nanoparticles together as agglomerates.

5.2.2 The basic bottom-up synthetic route

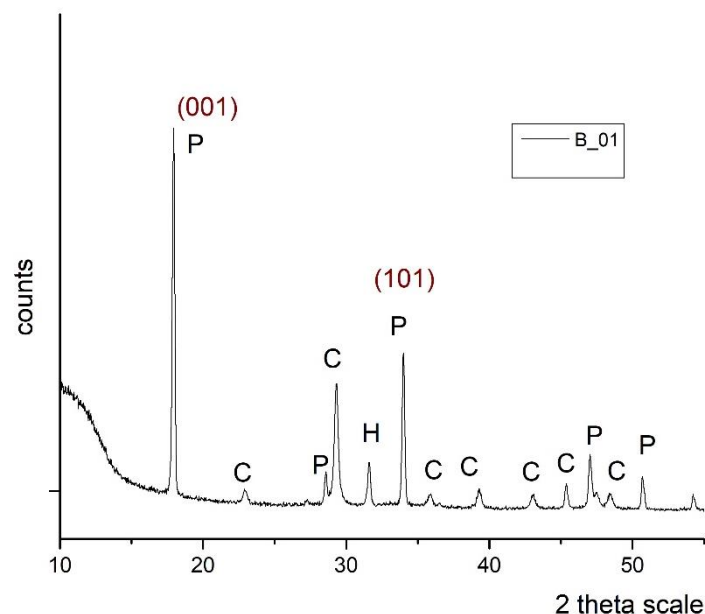
Mineralogical characterization - XRD results

The mineralogical analysis of the nanoparticles produced by the bottom-up synthetic route (B_01) were characterized by the presence of hexagonal structure portlandite particles, with the main peaks 18,0°, 28,5°, 34,12°, 47,0° and 50,8° corresponding to the XRD pattern of 44-1481 (Graph 5.2). B_01 resulted in the formation of portlandite crystals of 38 nm average crystallite size.

The peaks of portlandite were well-defined, indicating high crystallinity of the produced nanoparticles. The interpretation of the results indicated an increase of the I(001)/I(101) index. The increase of the I(001)/I(101) was linked with the alignment of the portlandite nanoparticles in a preferential direction of the {001} plane/ hexagon base [9], [219] (Fig 5.3b).

Minor content of trigonal calcite and cubic halite (NaCl) of cubic crystals were also detected. The presence of the calcite was attributed to the fast initiation of the carbonation process during the samples drying. Regardless the CO_2 free experimental conditions, the use of water as dispersion medium promoted the dissolution of CO_2 during drying and the partial carbonation of the nanoparticles close to the surface of the water film [39], [42] [160], [163]).

Finally, the presence of halite is related to the incomplete removal of the by-product of the bottom-up synthetic route.



Graph 5.2 X-ray Diffraction pattern of the produced nanoparticles (B_01)

Morphological characterization - SEM results

The shape of the initial crystallites formed during $\text{Ca}(\text{OH})_2$ synthesis is hexagonal and it is confirmed by the XRD patterns (Graph 5.2). After washing the initial batch and replacement of water by the final dispersion medium, the agglomeration and aggregation of the initial nanoparticles resulted in the formation of the shapes and morphologies examined in SEM (clusters of $\text{Ca}(\text{OH})_2$ nanoparticles). The examination of the calcium hydroxide particles synthesized by the bottom-up synthetic route (B01) in SEM, resulted in the production of hexagonal $\text{Ca}(\text{OH})_2$ particles characterized by a wide range of dimensions, mainly concentrated in the micro-scale. The presence of nanoparticles of undetermined shape was also detected, together with several fiber-like cluster formations (Fig. 5.3a). Moreover, the presence of a preferential alignment at the basal phase that was indicated by XRD was also detected (Fig. 5.4b). Elemental analysis (EDAX) was used for the chemical characterization of the fiber-like particles and other formations. The elemental ratio of Ca/C was used as an indicator for characterizing the fiber-like particles as $\text{Ca}(\text{OH})_2$ (Fig. 5.4).

The results indicated that the particle growth was promoted, resulting in the formation of hexagonal micro-particles.

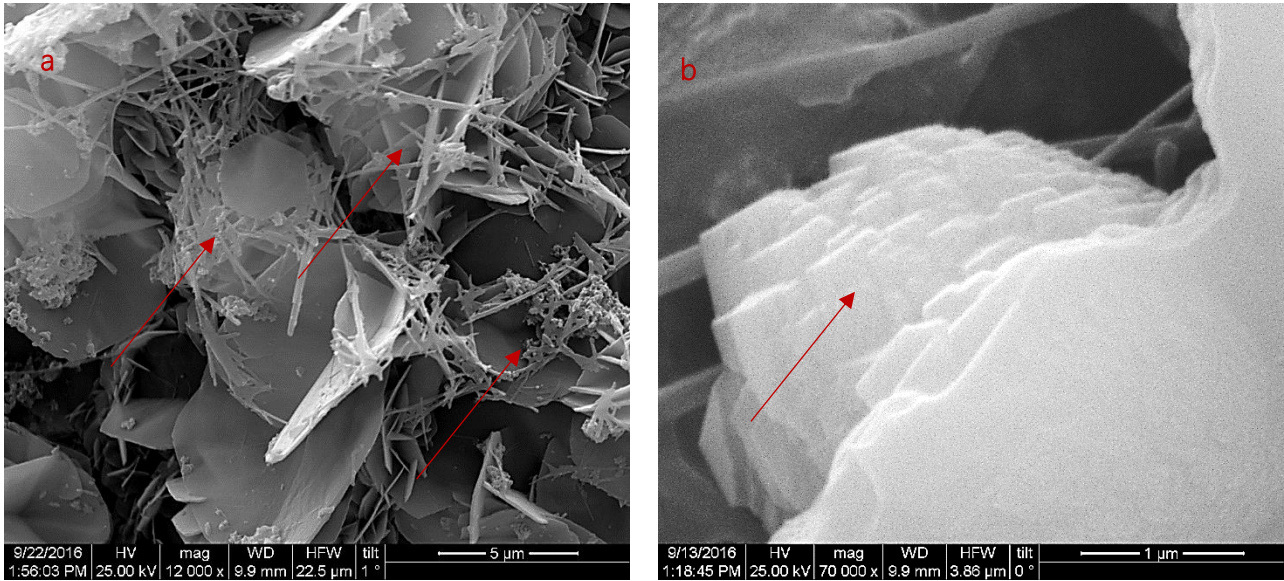


Figure 5.3 Clusters of: (a) Hexagonal Ca(OH)_2 particles of size in between $2\mu\text{m}$ and $8\mu\text{m}$, fiber like nanoparticles and Ca(OH)_2 nanoparticles of undetermined shape (scale bar at $5\mu\text{m}$); (b) Preferential alignment along the hexagon base of the hexagonal Ca(OH)_2 particles (scale bar at $1\mu\text{m}$).

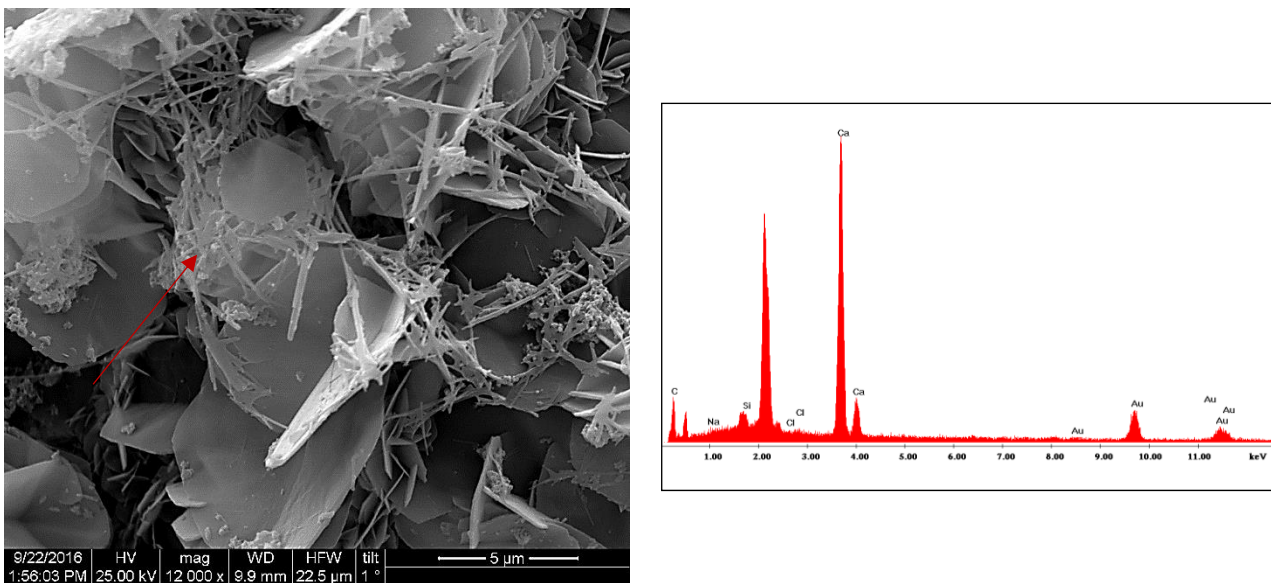


Figure 5.4 EDAX analysis of the fiber-like clusters identified as Ca(OH)_2

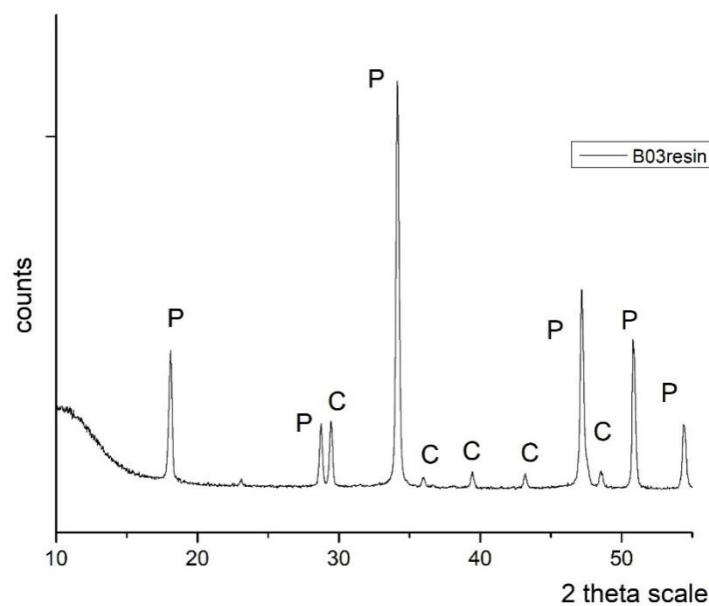
The comparison of the top-down (T_01) and bottom-up (B_01) results underlined the difference between the morphological characteristics of the newly synthesized Ca(OH)_2 nanoparticle and the drawbacks of each synthetic route:

- The implementation of the top-down route led to the formation of agglomerated $\text{Ca}(\text{OH})_2$ nanoparticles, underlining the need of a more efficient way of ultrasonic agitation, while the presence of $\text{Ca}(\text{OH})_2$ nanoparticles of small crystallite size was attributed to the aging procedure of the lime putty that was used.
- The implementation of the bottom-up synthetic route led to the formation of hexagonal $\text{Ca}(\text{OH})_2$ particles and of $\text{Ca}(\text{OH})_2$ nanoparticles of undetermined shape. The size of the hexagonal particles underlined the need of modification of the parameters of the experimental procedure.

5.2.3 Implementation of the bottom-up synthetic route with anionic resin

Mineralogical characterization - XRD results

The mineralogical characterization of the B_03OHresin particles didn't show any difference compared to the previous experiments. The particles were characterized by the dominant presence of portlandite $\text{Ca}(\text{OH})_2$ (Graph 5.3). Specifically, the presence of the major peaks $18,0^\circ$, $28,5^\circ$, $34,12^\circ$, $47,0^\circ$ and $50,8^\circ$ indicated the formation of portlandite of typical hexagonal crystals corresponding to the XRD pattern of 44-1481. Other minor phase identified was that of calcite (CaCO_3) of trigonal crystals corresponding to the XRD pattern of 5-586. The average crystallite size of the portlandite crystals was 32,7 nm.



Graph 5.3 X-ray Diffraction pattern of the produced nanoparticles (B03resin)

Morphological characterization - SEM results

The use of the anionic resin (**B3OHresin**) for replacing the NaOH reagent resulted in the production of particles with a broad range of morphological characteristics and dimensions in the range of micro-scale. The main shapes of the nanoparticle clusters identified in SEM examination were these of hexagonal, prismatic, fiber-like and of undetermined shape particles, exhibiting a high tendency to form large conglomerates (Fig. 5.5a). The increase of the experimental period for ions exchange from 60 to 90 min of under magnetic stirring did not present any improvements of the morphological characteristics of the particles, in terms of particles size and absence of agglomerates (Fig. 5.5b). The results did not come in accordance with the results reported by other researchers that were using the anionic resin [73].

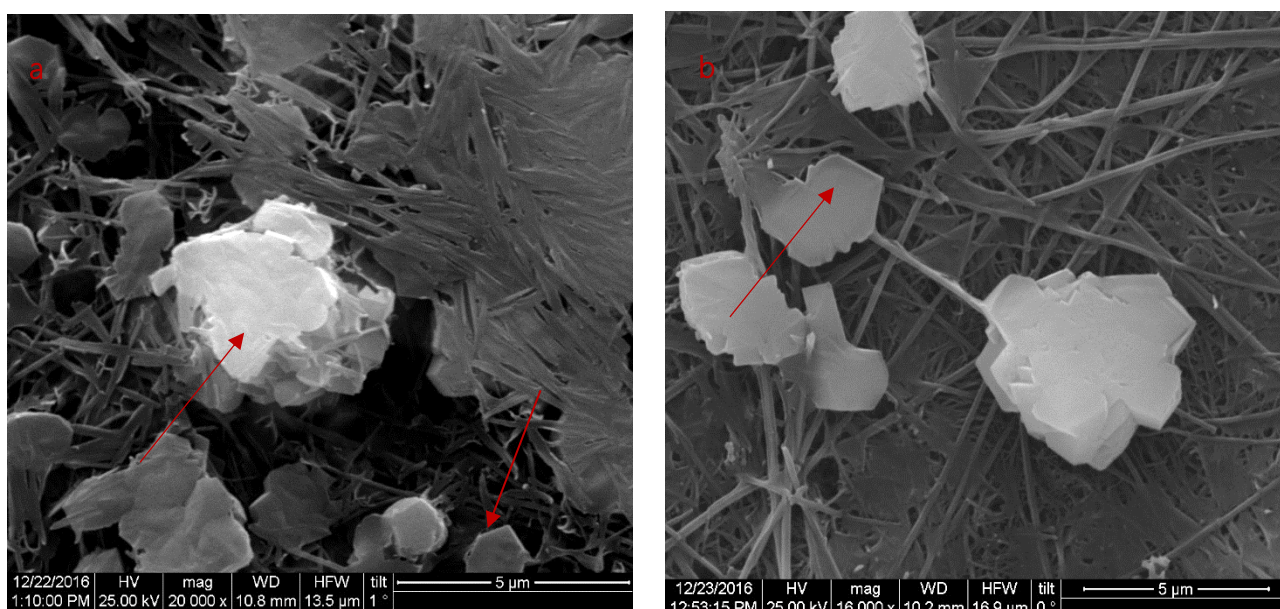


Figure 5.5 Clusters of: (a) Agglomerates of hexagonal, prismatic, fiber-like and of undetermined shape Ca(OH)_2 particles, 60 min magn. Stirring (scale bar at 5 μm); (b) Agglomerates of hexagonal, prismatic, fiber-like and of undetermined shape Ca(OH)_2 particles, 90 min magnetic stirring(scale bar at 5 μm).

5.3 Modifications of the basic synthetic routes

The following chapters contain the results of the different modification parameters implemented in the basic synthetic routes for examining their effect on the morphological characteristics of the $\text{Ca}(\text{OH})_2$ nanoparticles.

5.3.1 Sonication energy effect

The results of the two basic synthetic routes were characterized by the presence of several agglomerates. Aiming to overcome the agglomeration phenomenon, the use of probe sonication (UIP 1000 hdTHielsler of 1.0kW and 20kHz) was tested on both synthetic routes, instead of the ultrasonic bath.

The results showed that the use of probe sonication had a direct effect on the morphological characteristics of the $\text{Ca}(\text{OH})_2$ nanoparticles. The morphological characteristics of portlandite were studied by SEM and DLS, while the potential effect on mineralogical synthesis was studied by XRD.

Morphological characterization - SEM results

In the case of the top-down route (T02ultr), the use of the ultrasound probe resulted in the production of rounded, needle like and of undetermined shape $\text{Ca}(\text{OH})_2$ nanoparticles (Fig. 5.6). When compared to the initial results of the top-down route (T_01) in Fig. 5.2, the newly formed $\text{Ca}(\text{OH})_2$ nanoparticles were characterized by a large variation in terms of size (160 nm to 800 nm) and shape (from undetermined shape to more angular shape) and by the absence of larger agglomerates.

In the case of the bottom-up synthetic route (B02ultr), the use of the ultrasound probe resulted in the presence of plate-like $\text{Ca}(\text{OH})_2$ nanoparticles of regular shape (Fig. 5.7a). The plate-like shape of the nanoparticles was connected with the increase of the specific surface area and so to the increase of their reactivity [187]. The nanoparticle clusters were characterized by a uniform shape and their dimensions vary between 150 nm and 400 nm. Also, they presented a preferential alignment after the deposition and the evaporation of the aqueous dispersion medium (Fig. 5.7). When compared to the results of the original bottom-up synthetic route (B_01) in Fig. 5.3, the newly formed $\text{Ca}(\text{OH})_2$ nanoparticles were characterized by the reduction of size and the uniform shape.

The effect of sonication in the two synthetic routes was different: in the case of top-down route (T02ultr) $\text{Ca}(\text{OH})_2$ nanoparticles were characterized by polydispersity in terms of size and shapes, whereas in the case of the bottom-up synthetic route (B02ultr) the $\text{Ca}(\text{OH})_2$ nanoparticles were characterized by sorted particles size range and better uniformity in terms of their morphological characteristics

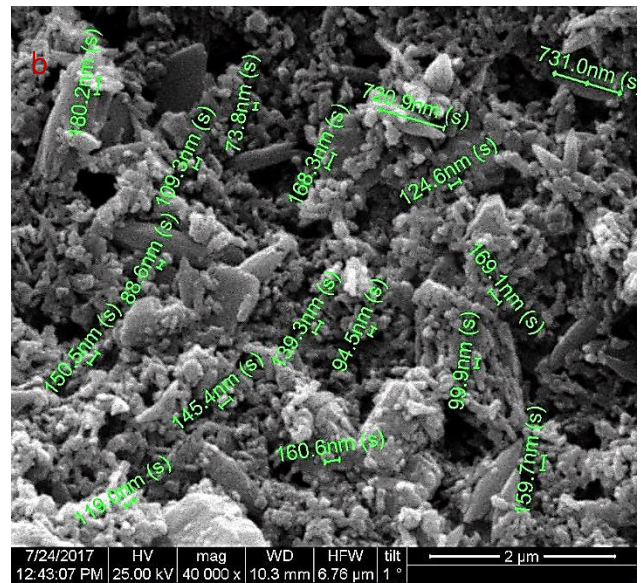
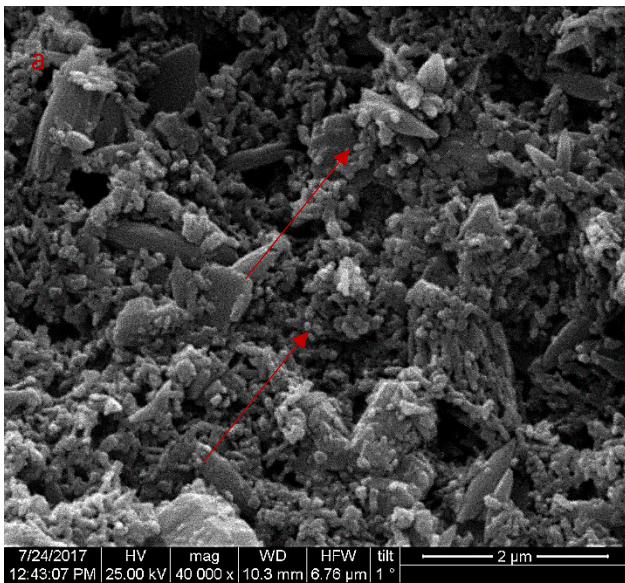


Figure 5.6 Clusters: (a) Rounded, needle like and of undetermined shape Ca(OH)_2 nanoparticles (scale bar at $2\mu\text{m}$); (b) Rounded, needle like and of undetermined shape Ca(OH)_2 nanoparticles of dimensions between 160 nm to 800 nm (T02ultr)(scale bar at $2\mu\text{m}$).

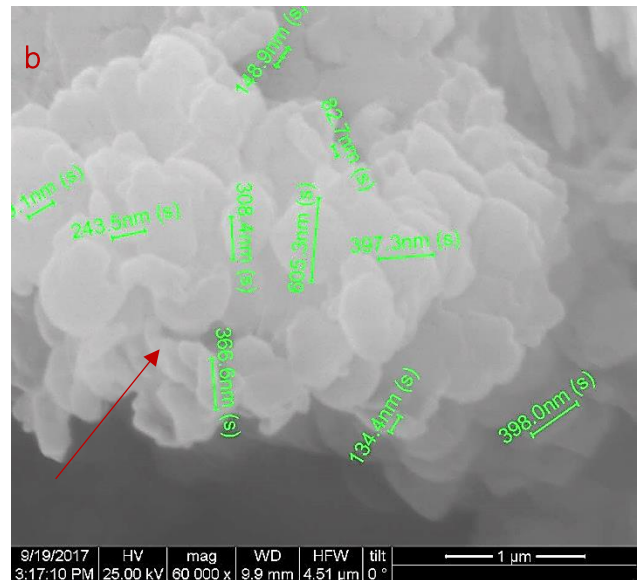
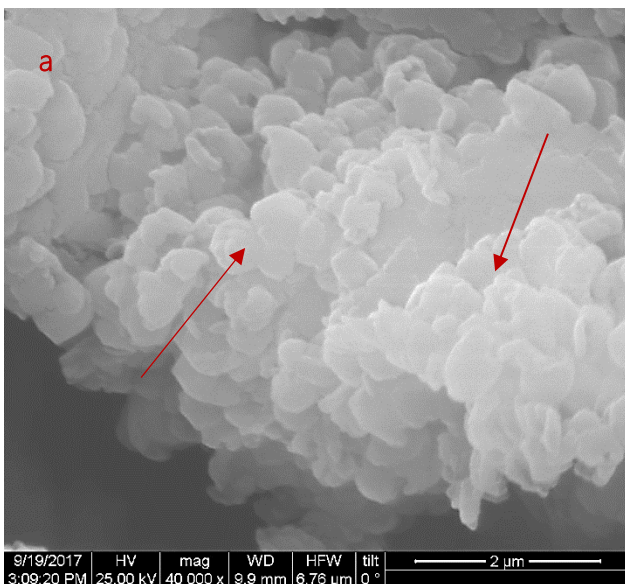
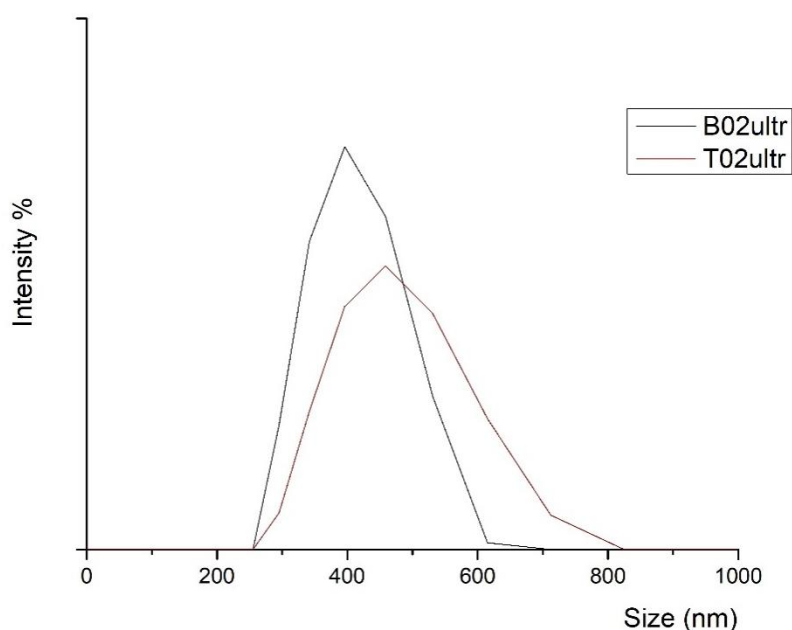


Figure 5.7 Clusters: (a) Plate-like Ca(OH)_2 nanoparticles of regular shape Ca(OH)_2 particles (scale bar at $2\mu\text{m}$); (b) Plate-like Ca(OH)_2 nanoparticles of regular shape Ca(OH)_2 particles of dimensions between 82 to 600 nm (scale bar at $1\mu\text{m}$).

Morphological characterization - DLS results

In the results of the DLS analysis, the **top-down route** (T02ultr) resulted in the formation of $\text{Ca}(\text{OH})_2$ nanoparticles of average size of 440 nm, contrary to the bottom-up synthetic route (B02ultr) that resulted in nanoparticles of 380 nm average size.

In addition, the particle size distribution curve (Graph 5.4) corresponding to **the bottom-up synthetic route** (B02ultr) presented a narrower shape, indicating the homogeneity of the produced $\text{Ca}(\text{OH})_2$ nanoparticles in terms of size. Contrary to this, the wider curve of the top-down route (T02ultr) confirmed the polydispersity of the produced $\text{Ca}(\text{OH})_2$ nanoparticles.

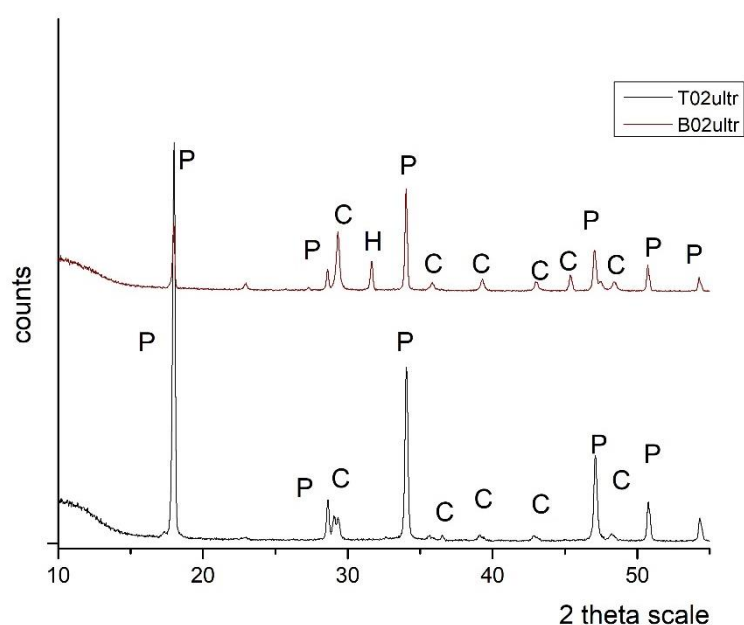


Graph 5.4 Particle size distribution by DLS of the main of the produced $\text{Ca}(\text{OH})_2$ nanoparticles T02ultr and B02ultr

Compared to the results of the morphological characterization of the original synthetic routes, the application of the ultrasonic probe in both cases proved to have a direct effect on the morphological characteristics of the $\text{Ca}(\text{OH})_2$ nanoparticles. The sonication had a direct effect on the shape of the nanoparticles, due to the high intensity of the acceleration induced by the probe that led to the increase of the difference between the low-pressure and the high-pressure leading to the production of a higher amount of bubbles. So, the cavitation phenomenon increased, leading to the transfer of higher amounts of energy on the nanoparticles during the cavitation collapses. In this way, the weak Van der Waals bonds of the agglomerates broke apart. Also, the intensity of the energy that was transferred had a direct effect on the morphological characteristics of the nanoparticles.

Mineralogical characterization - XRD results

The results of the mineralogical characterization of the T02ultr and B02ultr were characterized by the dominant presence of portlandite $\text{Ca}(\text{OH})_2$, as indicated in the XRD diffractogram (Graph 5.5). Specifically, the presence of the major peaks $17,9^\circ$, $28,4^\circ$, $34,1^\circ$, $46,8^\circ$ and $50,6^\circ$ and $18,0^\circ$, $28,5^\circ$, $34,2^\circ$, $47,0^\circ$ and $50,8^\circ$ respectively, of portlandite of typical hexagonal crystals corresponding to the XRD pattern of 44-1481. Other minor phase identified was that of calcite (CaCO_3) of trigonal crystals corresponding to the XRD pattern of 5-586. The average crystallite size of the portlandite crystals was determined with the Scherer equation in the case of T02ultr was 37,5 nm and in the case of B02ultr was 43,29 nm. The application of the ultrasound probe in the vase of the bottom-up synthetic route was characterized by a slight increase of the average crystallite size in the case of the bottom,-up synthetic route (B02ultr).



Graph 5.5 X-ray Diffraction pattern of the produced nanoparticles T02ultr and B02ultr

- The intensity of the energy that was transferred had a direct effect on the morphological characteristics of the nanoparticles
- In the case of the top-down route (T02ultr) sonication resulted in the de-agglomeration of the particles, while in the case of the bottom-up synthetic route (B02ultr) resulted in the reduction of the size of nanoparticles. , the intensity of the energy that was transferred had a direct effect on the morphological characteristics of the nanoparticles.

[5.3.2 The effect of inert atmosphere \(He-atmosphere\)](#)

As mentioned in Chapter 4, a basic modification of the experimental procedure was the implementation of the bottom-up experiment under inert helium (He) conditions of (B02He).

The morphological characteristics of the developed nanoparticles were examined by electron microscopy (SEM, TEM), their size by DLS and the specific surface area of the nanoparticles was determined using the BET method. The mineralogy of the newly synthesized nanoparticles was characterized by XRD.

Morphological characterization - SEM results

The inert He conditions resulted production of hexagonal, rounded, needle like and of undetermined shape Ca(OH)_2 nanoparticles (Fig. 5.8). The size of the nanoparticles varies from 150 nm to 400 nm. When compared to the results of the original bottom-up synthetic route (Fig. 5.3), the change of the experimental conditions proved to have a direct effect on the shape of the Ca(OH)_2 nanoparticles. Also, the width of the nanoparticles was increased.

Morphological characterization - TEM results

The TEM examination revealed the development of hexagonal (2-D) and rounded Ca(OH)_2 nanoparticles of dimensions between 100 nm and 300 nm relatively low thickness were observed (Fig. 5.9a). According to Lanzon et al. [38], the low thickness of the hexagonal 2-D nanoparticles could be attributed to the split of the Ca(OH)_2 along the 0001 cleavage planes due to the sonication and the weakness. In addition to this, rounded nanoparticles of dimensions less than 100 nm were detected, indicating that there were always present but not seen in SEM. The rounded nanoparticles could be characterized as 0-D(Fig.5.9b).

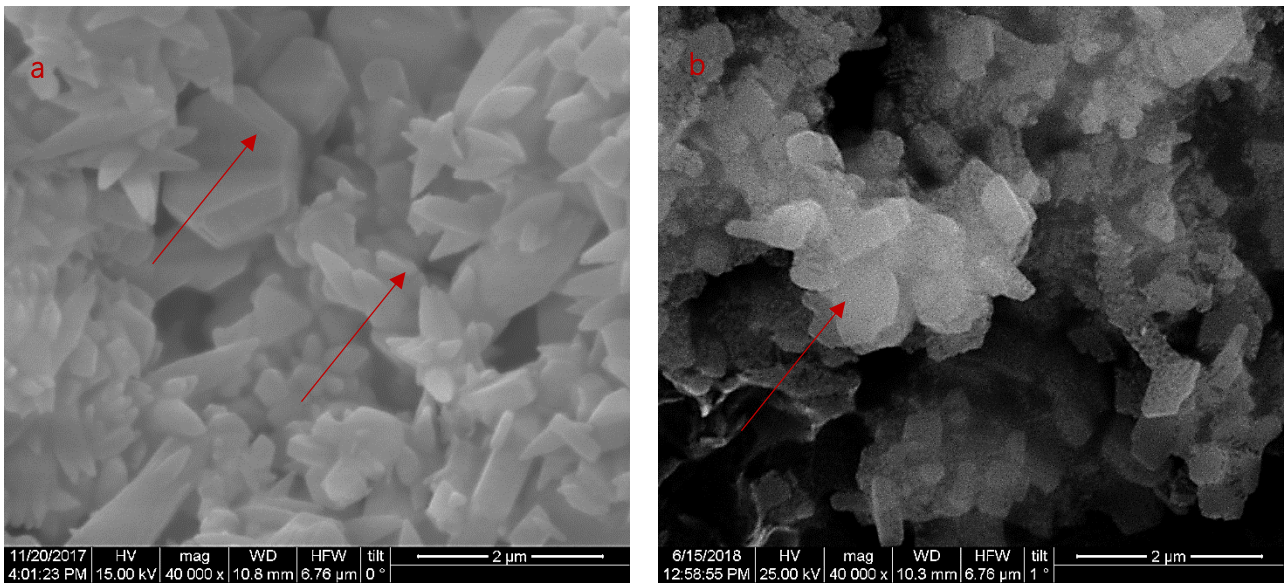


Figure 5.8 Clusters of : (a) Hexagonal, rounded, needle like and of undetermined shape $\text{Ca}(\text{OH})_2$ nanoparticles (scale bar at $2\mu\text{m}$); (b) $\text{Ca}(\text{OH})_2$ nanoparticles of dimensions between 150 nm to 400 nm (B02He)(scale bar at $2\mu\text{m}$).

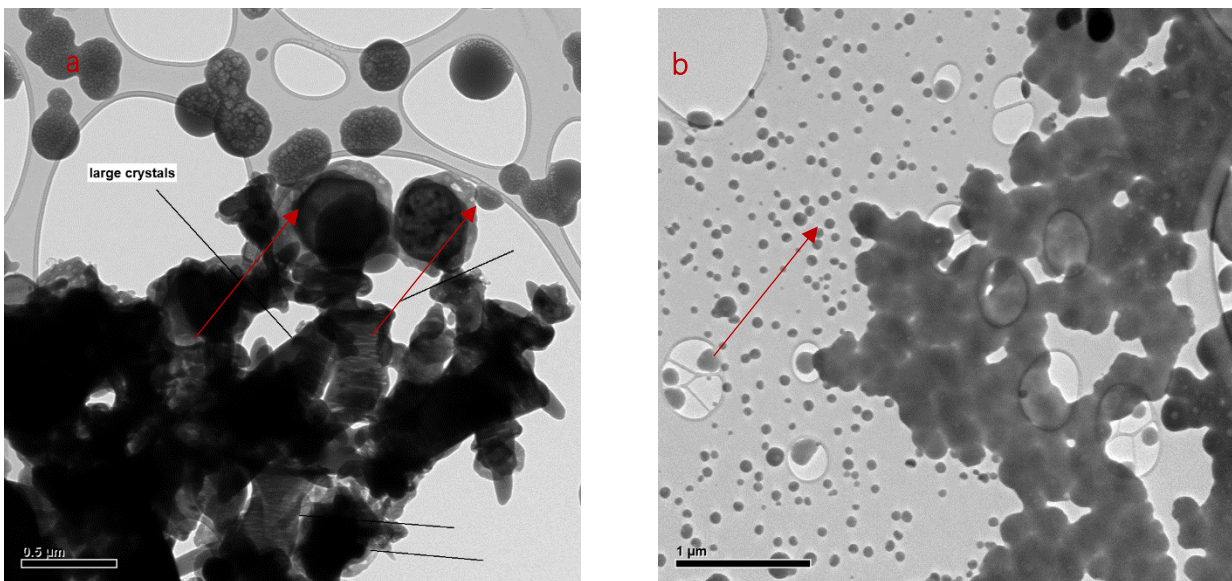


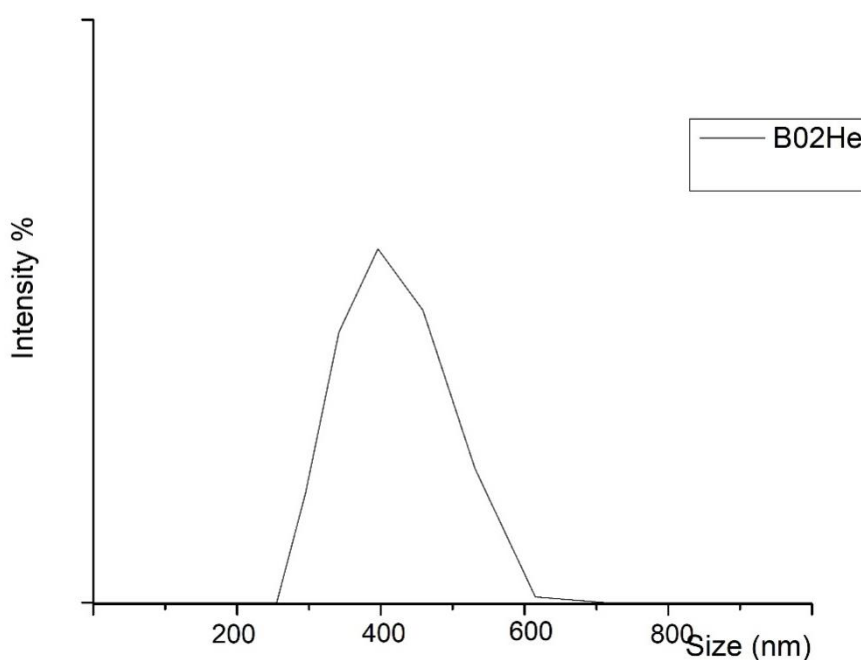
Figure 5.9 (a) Hexagonal and rounded $\text{Ca}(\text{OH})_2$ nanoparticles of dimensions between 100 nm and 300 nm (scale bar at 200 nm); (b) Rounded shape $\text{Ca}(\text{OH})_2$ nanoparticles of dimensions below 100 nm (B02He)(scale bar at $2\mu\text{m}$).

Morphological characterization - DLS results

DLS analysis of B02He resulted in the formation of $\text{Ca}(\text{OH})_2$ nanoparticles of average size of 400 nm. The corresponding particle size distribution curve (Graph 5.6) presented a wider

shape, indicating polydispersity of the shape of the produced $\text{Ca}(\text{OH})_2$. The specific surface area was determined at $3.9 \text{ m}^2/\text{g}$, which is an indication of a rather low reactivity.

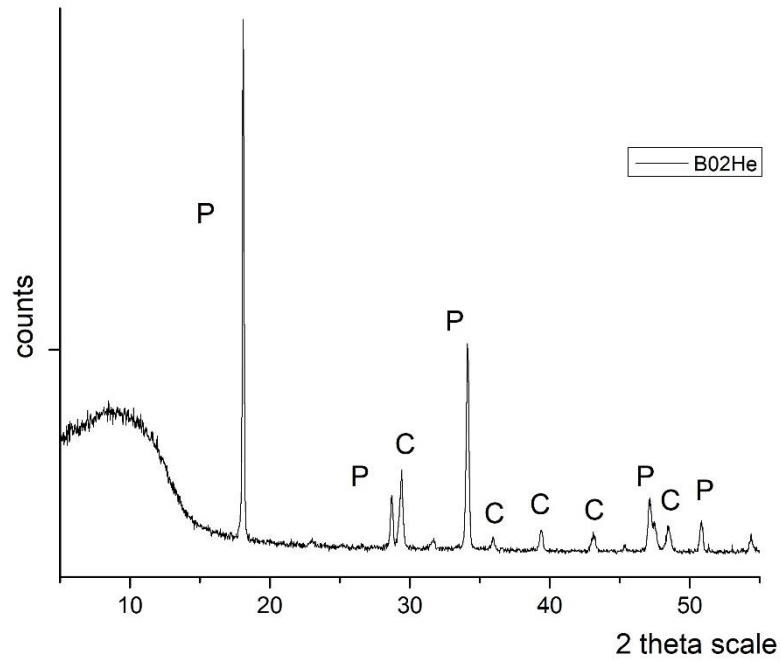
The modification of the experimental equipment led to the development of a system similar to a batch reactor. In this way, the implementation of the bottom-up synthetic route was realized under conditions of constant temperature of 90°C favouring the realization of the reaction. The replacement of air with an inert gas like He, did not affect the concentrations of the reactants or the partial pressure of the solution, and thus did not alter the equilibrium of the replacement reaction. The use of He, seemed to create an inert environment where He did not react with the reactants.



Graph 5.6 Particle size distribution by DLS of the main of the produced $\text{Ca}(\text{OH})_2$ nanoparticles B02He

Mineralogical characterization - XRD results

The results of the mineralogical characterization of the B02He were characterized by the dominant presence of portlandite $\text{Ca}(\text{OH})_2$, as indicated in the XRD diffractogram (Graph 5.7). Specifically, the presence of the major peaks $17,9^\circ$, $28,4^\circ$, $34,1^\circ$, $46,8^\circ$ and $50,6^\circ$ of portlandite of *t* hexagonal crystals corresponding to the XRD pattern of 44-1481. Other minor phase identified was that of calcite (CaCO_3) of trigonal crystals corresponding to the XRD pattern of 5-586. The average crystallite size was determined with the Scherrer equation was $45,45 \text{ nm}$. When compared to the previous results of the bottom-up synthetic route, average crystallite size is increased in the case of B02He.



Graph 5.7 X-ray Diffraction pattern of the produced nanoparticles B02He

Overall:

The use of ultrasonic probe:

- In the top-down route (T02ultr) resulted in the de-agglomeration of the particles
- In the bottom-up synthetic route (B02ultr) resulted in the reduction of the size of the nanoparticles and to the synthesis of plate-like $\text{Ca}(\text{OH})_2$ nanoparticles of homogeneity in terms of size and shape.

Moreover, based on the advancements resulted by the He-inert atmosphere, this parameter was introduced in all experiments implemented therefore by the bottom-up synthetic route.

5.4 Use of surfactants for nanoparticles functionalization

5.4.1 Addition of Triton X-100

Morphological Characterization - SEM results

In the case of the top-down route (T03tx100), the use of Triton X-100 non-ionic surfactant resulted in the production of rounded and of undetermined shape $\text{Ca}(\text{OH})_2$ nanoparticles, of dimensions in between 98 nm and 180 nm (Fig. 5.10a). When compared to the original results of the top-down route (T_01 and T_02ultr) in Fig. 5.2 and Fig. 5.6, the newly formed $\text{Ca}(\text{OH})_2$ nanoparticles were characterized by the reduction of their size, by the homogeneity of shape and by the absence of agglomerates.

In the case of the bottom-up synthetic route (B04tx100a), the addition of Triton X-100 resulted in the synthesis of $\text{Ca}(\text{OH})_2$ nanoparticles of regular and angular shape (Fig. 5.10b). The nanoparticles were characterized by a uniform shape and their dimensions vary between 200 nm to 270 nm. (Fig. 5.10b). When compared to the results of the original bottom-up synthetic route (B_01) in Fig. 5.3, the newly formed $\text{Ca}(\text{OH})_2$ nanoparticles were characterized by the reduction of size to the nano-scale and by the uniformity in terms of shape.

The comparative evaluation of the two main synthetic routes revealed that the addition of Triton X-100 resulted in size reduction of $\text{Ca}(\text{OH})_2$ nanoparticles, uniformity of their shape and absence of agglomerates and aggregates (in the case of the bottom-up synthetic route).

Another modification of the bottom-up synthetic route was implemented, in order to improve the nucleation rate in respect to the particle growth. Therefore, the addition of the CaCl_2 and Triton X-100 aqueous solution to NaOH was realized **drop to drop and not immediately** (B04tx100b) leading to the reduction of the nanoparticle size and to the modification of the shape of the nanoparticles contributing to the relevant literature [73], [173]. Moreover, with this modification, presence of high local concentrations of the surfactants that could cause phenomena of particle flocculation was avoided [183].

The examination of the reaction product in SEM revealed that very slow mixing rate along with probe sonication, resulted in the production of plate-like of hexagonal habit $\text{Ca}(\text{OH})_2$ nanoparticles of dimensions between 100 nm to 280 nm (Fig. 5.11a). The plate-like shape of the nanoparticles is connected with the increase of the specific surface area and so to the increase of their reactivity [187]. The nanoparticles presented smaller size, enhanced width and more angular shape, compared to the main bottom-up method results, without the addition of the surfactant. In addition to this the slow mixing rate and the high temperature seemed the nucleation rate of the $\text{Ca}(\text{OH})_2$ to the particle growth, promoting the formation of $\text{Ca}(\text{OH})_2$ nanoparticles [73].

Moreover, an alignment of the $\text{Ca}(\text{OH})_2$ nanoparticle clusters in a preferential direction was clearly observed (Fig. 5.11a) during the examination of the samples in SEM.

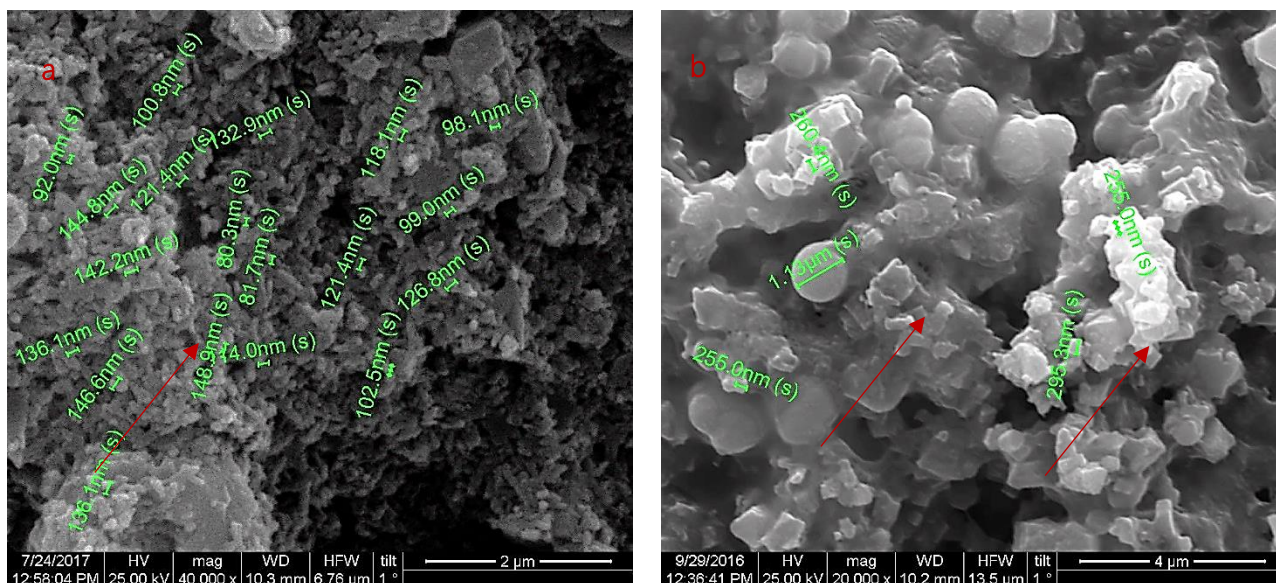


Figure 5.10 Clusters of: (a) Rounded and undetermined shape $\text{Ca}(\text{OH})_2$ nanoparticles, of dimensions in between 98 nm and 180 nm (T03x100)(scale bar at 2 μm); (b) Regular and angular $\text{Ca}(\text{OH})_2$ nanoparticles of dimensions between 200 nm to 270 nm.(B04x100a)(scale bar at 4 μm).

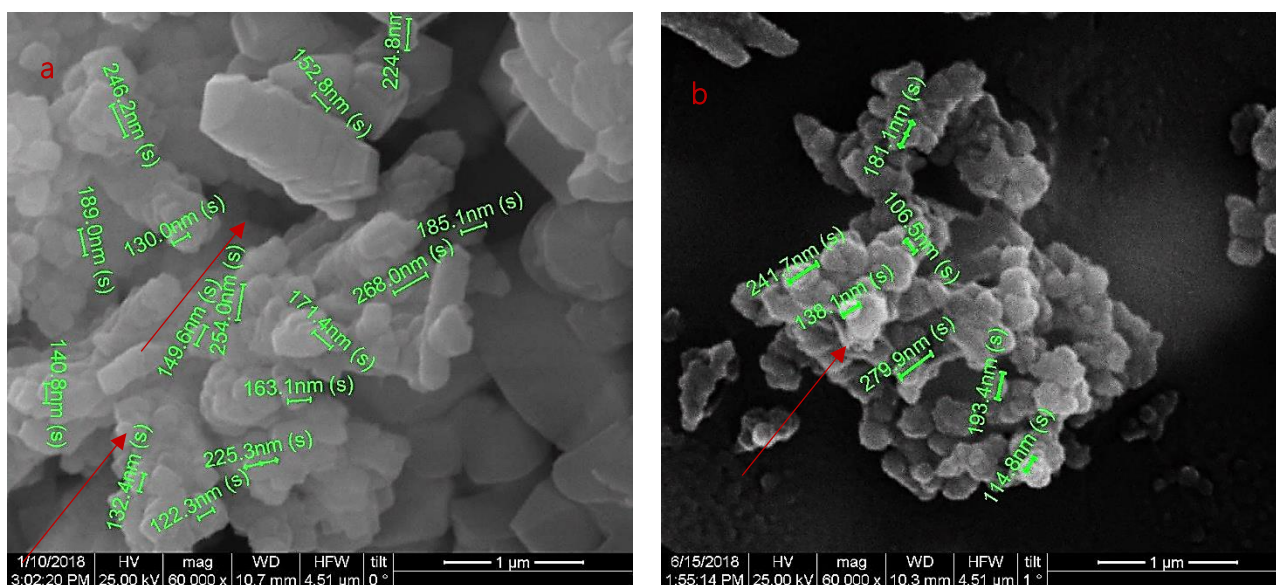


Figure 5.11 Clusters of: (a) Plate-like of hexagonal habit $\text{Ca}(\text{OH})_2$ nanoparticles of dimensions between 100 nm to 280 nm (B04TX100b)(scale bar at 1 μm); (b) Plate-like $\text{Ca}(\text{OH})_2$ nanoparticles of dimensions between 115 nm to 280 nm (B04x100c)(scale bar at 1 μm).

The implementation of the same experiment under He inert atmosphere, revealed very similar results and the production of plate-like of hexagonal habit $\text{Ca}(\text{OH})_2$ nanoparticles of dimensions between 115 nm to 280 nm (Fig. 5.11b). The nanoparticles presented smaller size and of plate-like shape, compared with the larger particles of regular size obtained main bottom-up method without the addition of the surfactant.

Morphological characterization - TEM results

The TEM analysis of the B04tx100c confirmed observations concerning the smaller size and plate-like shape of hexagonal habit obtained with the use of SEM. In specific, hexagonal $\text{Ca}(\text{OH})_2$ nanoparticles of dimensions between 100 nm and 300 nm were observed. In addition to this, the $\text{Ca}(\text{OH})_2$ nanoparticles can be characterized as 3-D (3- dimensional) and relatively well crystallized (Fig.5.12).

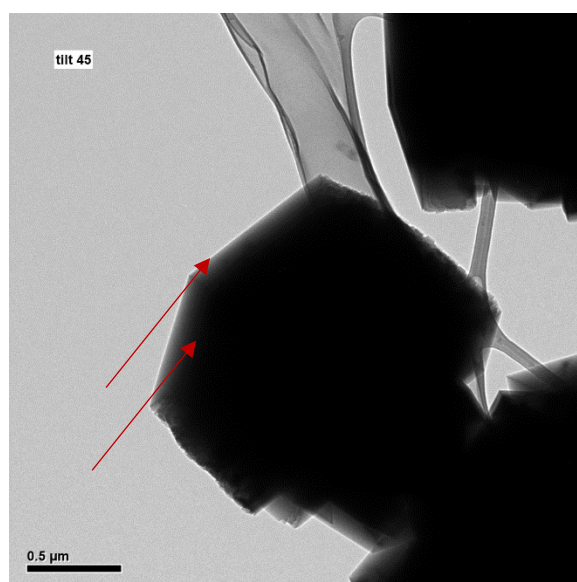
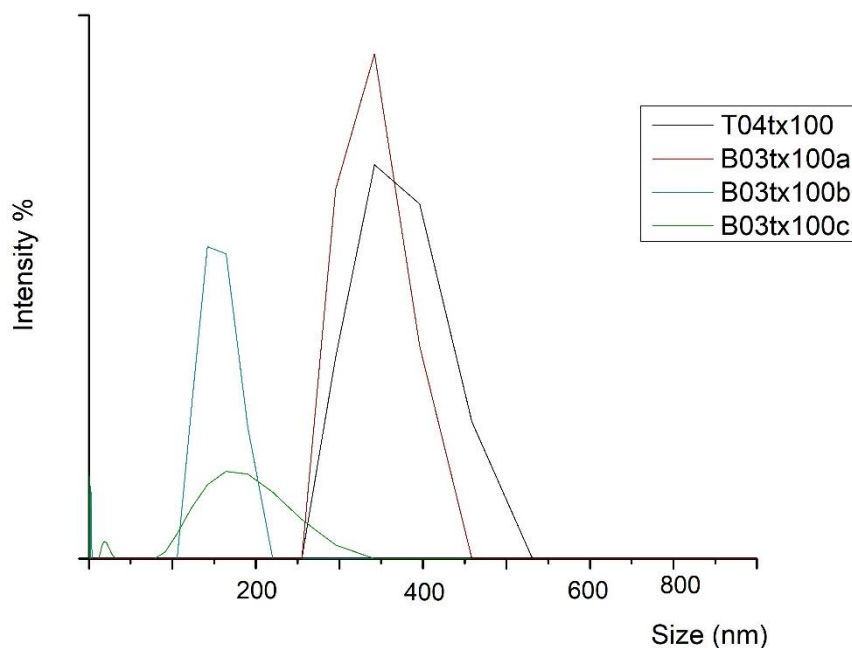


Figure 5.12 3-D $\text{Ca}(\text{OH})_2$ nanoparticles (B03tx100c)(scale bar at 500 nm).

Morphological characterization - DLS results

The size of $\text{Ca}(\text{OH})_2$ nanoparticles was additionally studied by DLS, calculating the average size, the particle size distribution and the ζ -potential. **According to DLS results**, the addition of the non-ionic surfactant of Triton X-100 in the top-down route (T03tx100) resulted in the formation of $\text{Ca}(\text{OH})_2$ nanoparticles of average size of 365 nm. In addition, the corresponding particle size distribution curve (Graph 5.8) presented a wider shape, indicating polydispersity of the shape of the produced $\text{Ca}(\text{OH})_2$ nanoparticles. The addition of the non-ionic surfactant of Triton X-100 in the bottom-up synthetic route (B04tx100A) resulted in the formation of $\text{Ca}(\text{OH})_2$ nanoparticles of average size of 293 nm. In addition, the corresponding particle size distribution curve (Graph 5.8) presented a wider shape, indicating polydispersity of the shape of the produced $\text{Ca}(\text{OH})_2$ nanoparticles.



Graph 5.8 Particle size distribution by DLS of the synthesis implemented with the addition of the non-ionic surfactant Triton X-100

The interpretation of DLS results indicates that the implementation of the bottom-up synthetic route by mixing the reactants drop to drop (B03tx100b) resulted in the formation of $\text{Ca}(\text{OH})_2$ nanoparticles of average size of 153 nm. In addition, the corresponding particle size distribution curve (Graph 5.8) presented a narrower shape, indicating homogeneity of the shape of the produced $\text{Ca}(\text{OH})_2$ nanoparticles. Finally, the implementation of the previous experimental procedure under inert conditions of He (B04tx100c) resulted in the formation of $\text{Ca}(\text{OH})_2$ nanoparticles of average size of 176 nm. The corresponding particle size distribution curve (Graph 5.8) presented a wider shape, indicating polydispersity of the shape of the produced $\text{Ca}(\text{OH})_2$ nanoparticles. The DLS results confirmed the reduction of the size of $\text{Ca}(\text{OH})_2$ nanoparticles by the addition of the non-ionic surfactant Triton X-100 for both synthetic routes. Moreover, the drop to drop implementation of the bottom-up synthetic route proved to have a direct effect on the further reduction of the size of the nanoparticles.

With the use of the DLS methodology, the ζ -potential of the three alterations of the bottom-up synthetic route was determined. The ζ -potential provided an estimation of the tendency of the newly formed $\text{Ca}(\text{OH})_2$ nanoparticles towards aggregation. The B03tx100a has a ζ -potential at -3,6mV, the B03tx100b at -14,8mV and the B04tx100c -1,9mV.

The comparative evaluation of the three alterations proved that in the case of the drop to drop mixing of the reagents (B04tx100b) the newly formed $\text{Ca}(\text{OH})_2$ nanoparticles show a reduced tendency to aggregation, in respect with the other two alterations (B04tx100a and B43tx100c).

During the nucleation stage, the non-ionic surfactant Triton X-100 is adsorbed on the surface of the primary $\text{Ca}(\text{OH})_2$ nanoparticles (nuclei) due to the hydrogen bonds between the hydroxyl group (OH^-) and the $-\text{O}$ of the polyoxyethylene group of Triton X-100 (Fig. 5.13), forming a steric barrier by reducing the surface tension of the solid-liquid interface and thus reducing the total surface energy (γ) closer to the critical energy barrier (ΔG_c). The critical energy barrier corresponds to the critical radius (r_c) for the formation of $\text{Ca}(\text{OH})_2$ nuclei (primary particles) and the absence of dissociation phenomena [129]. This causes the creation of thermodynamically stable nanoparticles, preventing the consequent crystal growth [133]. In this way, the growth and polydispersity of the nanoparticles is limited, and the hexagonal shape is preserved [138].

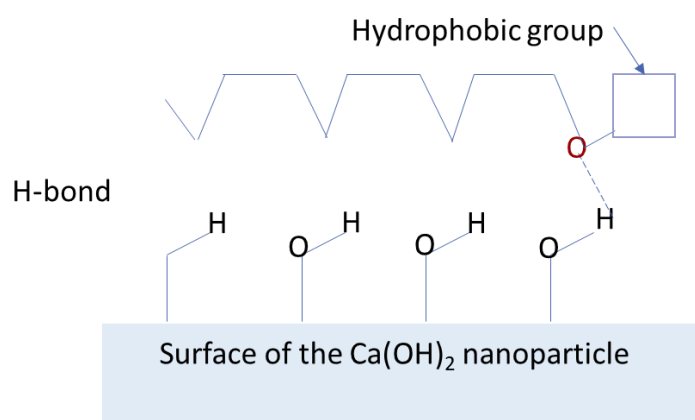
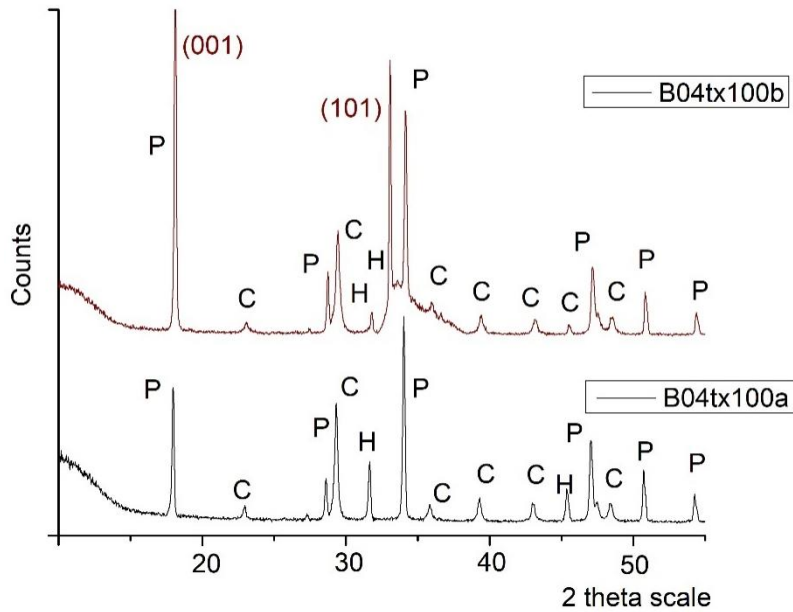


Figure 5.13 H-bonding between the non-ion surfactant Triton X-100 and the $\text{Ca}(\text{OH})_2$ nanoparticle's surface

Mineralogical characterization - XRD results

The results of the mineralogical characterization of the all four synthetic procedures were characterized by the dominant presence of portlandite $\text{Ca}(\text{OH})_2$, as indicated in the XRD diffractogram (Graph 5.9). Specifically, the presence of the major peaks $17,9^\circ$, $28,4^\circ$, $34,1^\circ$, $46,8^\circ$ and $50,6^\circ$ of portlandite of hexagonal crystals corresponding to the XRD pattern of 44-1481. Other minor phase identified was that of calcite (CaCO_3) of trigonal rhombohedral crystals corresponding to the XRD pattern of 5-586.

The mineralogical analysis of the nanoparticles produced by the bottom-up methodology with the drop to drop addition of the reactants containing the non-ionic surfactant Triton X-100 indicated an increase of the $I_{(001)}/I_{(101)}$ index (Fig. 5.14). The increase of the $I_{(001)}/I_{(101)}$ was linked with the alignment of the portlandite nanoparticles in a preferential direction of the $\{001\}$ plane/ hexagon base, which was verified by the morphological appearance of produced particles (Fig. 5.11 a and b) of the bottom-up methodology.



Graph 5.9 X-ray Diffraction pattern of the produced nanoparticles B04tx100a and B04TX100b

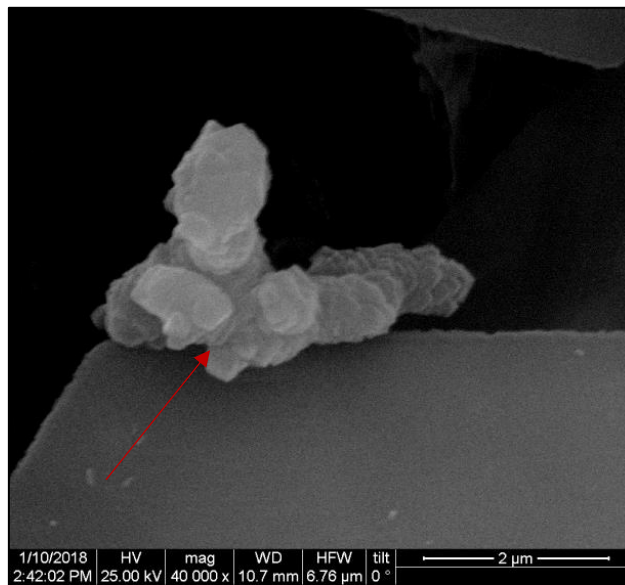


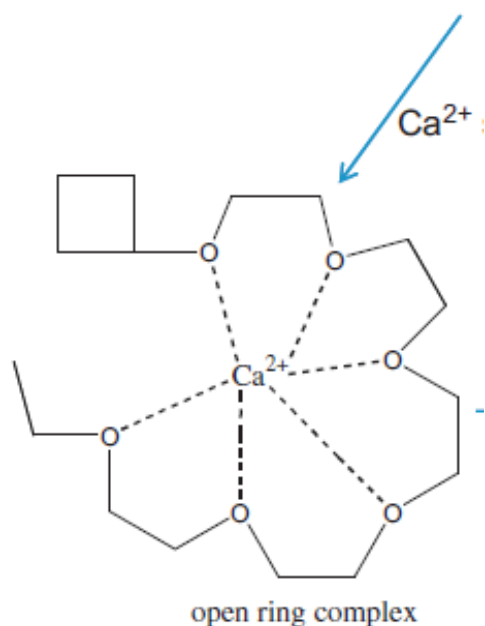
Figure 5.14 Preferential alignment along the hexagon base of the hexagonal Ca(OH)_2 particles (scale bar at $2\mu\text{m}$);

The average crystallite size for all four synthesis was determined with the Scherer equation. The average crystallite size for the top-down route (T03TX100) was 38 nm. When compared to the results of the basic top-down route, the average crystallite size was not altered. The average crystallite size for the alterations of the bottom-up synthetic route was estimate at:

- a) 38 nm for the first alteration (B04tx100a),
- b) 37 nm for the second alteration (B04tx100b)
- c) 39 nm for the third alteration(B04tx100c).

When compared to the results obtained by the original bottom-up synthetic route (average crystallite size of 43 nm), the addition of the Triton X-100 led to a decrease of the average crystallite size.

Overall, the addition of the Triton X-100, led to a significant decrease of the size of the newly formed $\text{Ca}(\text{OH})_2$ nanoparticles for both synthetic routes. Also, it led to the absence of agglomeration and aggregation phenomena. The reduced size of the nanoparticles can be attributed to the reported interaction between Ca^{2+} and the functional group polyoxyethylene group of Triton X-100, that has proven to inhibit the nucleation of the primary particles and the presence of aggregation phenomena [174],[180]. This was reflected to the reduction of both the size of the nanoparticles and the average crystallite size of the results of the bottom-up synthetic route. The addition of Triton X-100 on the top-down route resulted in the reduction of the size of the nanoparticles and to absence of agglomerates due to the adsorption of the polar head of the Triton X-100 onto the surface of the $\text{Ca}(\text{OH})_2$ nanoparticles through the formation of H-bonds.



[180]

[5.4.2 Addition of n-Octylamine](#)

Morphological characterization - SEM results

In the case of the **top-down route (T03oc)**, the use of the ultrasound probe resulted in the production of rounded and of undetermined shape $\text{Ca}(\text{OH})_2$ nanoparticles, of dimensions in between 60 nm and 460 nm (Fig. 5.15.a). When compared to the original results of the top-down route (T_01 and T_02ultr) in Fig. 5.2 and Fig. 5.6, the newly formed $\text{Ca}(\text{OH})_2$ nanoparticles were characterized by the reduction of their size and by the homogeneity of shape. But, the results were characterized by the presence of additional agglomerates.

In the case of the **bottom-up synthetic route (B04oc)**, the addition of n-octylamine resulted in the synthesis of hexagonal and regular shape Ca(OH)_2 nanoparticles (Fig. 5.15b). The nanoparticles were characterized by a uniform shape and their dimensions vary between 200 nm to 450 nm. (Fig 5.15b). In addition to this, the newly formed Ca(OH)_2 nanoparticles presented a characteristic width. When compared to the results of the original bottom-up synthetic route (B_01) in Fig. 5.3, the newly formed Ca(OH)_2 nanoparticles were characterized by the reduction of size to the nano-scale and by the uniformity in terms of shape. The **drop to drop mixing** along with probe sonication, resulted in the production of plate-like of hexagonal habit Ca(OH)_2 nanoparticles of dimensions between 128 nm to 800 nm (Fig. 5.15c). The nanoparticles presented smaller size, enhanced width and more angular shape, compared with the main bottom-up method without the addition of the surfactant. Moreover, an alignment of the Ca(OH)_2 nanoparticles in a preferential direction was clearly observed (Fig. 5.15c).

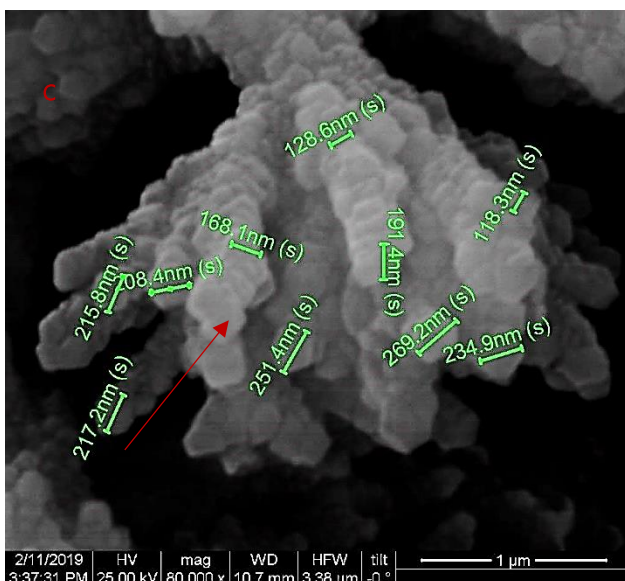
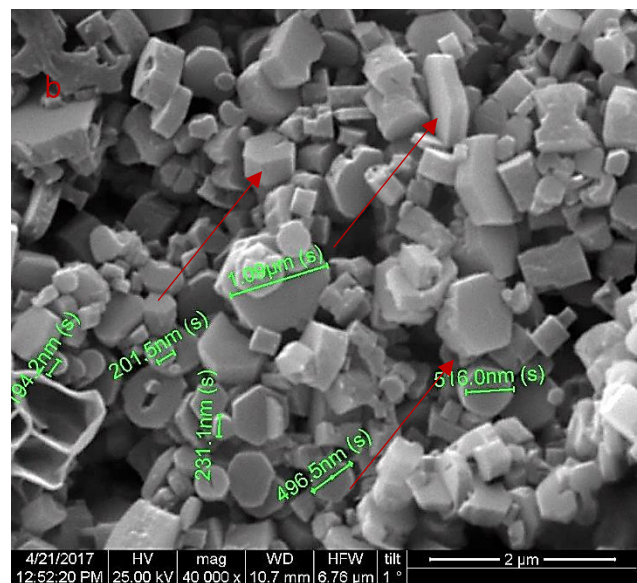
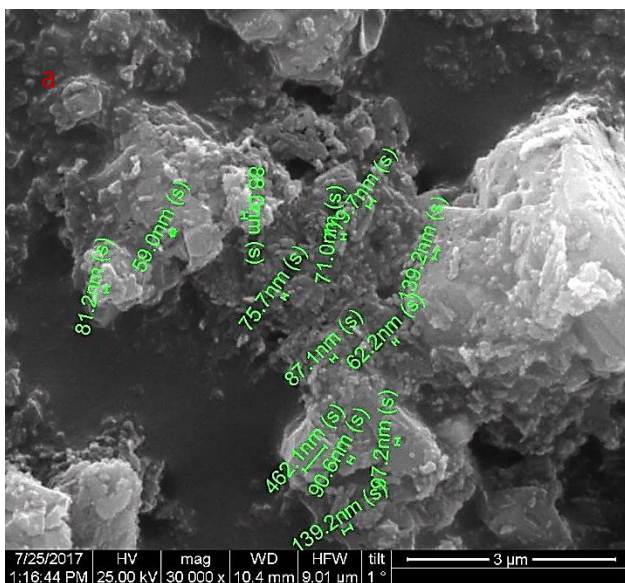
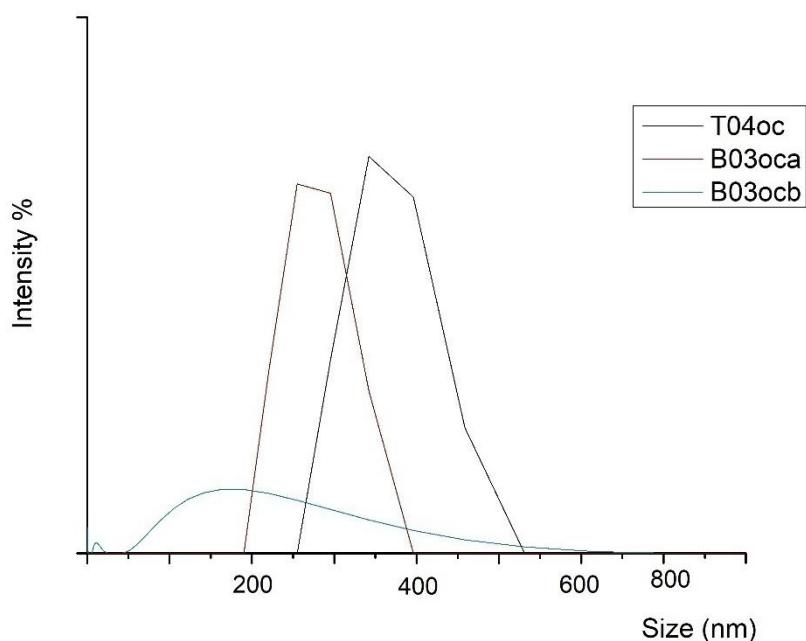


Figure 5.15 Clusters of: (a) Rounded and of undetermined shape $\text{Ca}(\text{OH})_2$ nanoparticles, of dimensions in between 60 nm and 460 nm (T03oc) (scale bar at $3\mu\text{m}$); (b) Hexagonal $\text{Ca}(\text{OH})_2$ nanoparticles of dimensions between 200 nm to 450 nm (B04oca) (scale bar at $2\mu\text{m}$) and (c) Plate-like $\text{Ca}(\text{OH})_2$ nanoparticles of hexagonal habit. Their dimensions vary between 200 nm to 450 nm (B04oca) (scale bar at $1\mu\text{m}$).

Morphological characterization - DLS results

The size of $\text{Ca}(\text{OH})_2$ nanoparticles was additionally studied by DLS, calculating the average size, the particle size distribution and the ζ -potential. The addition of the non-ionic surfactant of n-octylamine in the top-down route (T03oc) resulted in the formation of $\text{Ca}(\text{OH})_2$ nanoparticles of average size of 365 nm. In addition, the corresponding particle size distribution curve (Graph 5.10) presented a wider shape, indicating polydispersity of the shape of the produced $\text{Ca}(\text{OH})_2$ nanoparticles. The addition of the non-ionic surfactant of n-octylamine in the bottom-up synthetic route (B04oca) resulted in the formation of $\text{Ca}(\text{OH})_2$ nanoparticles of average size of 275 nm. In addition, the corresponding particle size distribution curve (Graph 5.10) presented a wider shape, indicating polydispersity of the shape of the produced $\text{Ca}(\text{OH})_2$ nanoparticles.



Graph 5.10 Particle size distribution by DLS of the synthesis implemented with the addition of the non-ionic surfactant n-octylamine

The implementation of the bottom-up synthetic route by the mixing of the reactants by drop to drop (B04oc) resulted in the formation of $\text{Ca}(\text{OH})_2$ nanoparticles of average size of 197 nm. The corresponding particle size distribution curve (Graph 5.10) presented a wider shape, indicating polydispersity of the shape of the produced $\text{Ca}(\text{OH})_2$ nanoparticles. The DLS measurements confirmed the reduction of the size of $\text{Ca}(\text{OH})_2$ nanoparticles by the addition of the non-ionic surfactant n-octylamine for both synthetic route. Moreover, the

drop to drop implementation of the bottom-up synthetic route proved to have a direct effect on the further reduction of the size of the nanoparticles.

With the use of the DLS methodology, the ζ -potential of the three alterations of the bottom-up synthetic route was determined: for the B03oca the ζ -potential was estimated at $-4,8\text{mV}$, and for the B03ocb the ζ -potential was estimated at $-14,7\text{mV}$. The ζ -potential provided an estimation of the tendency of the newly formed $\text{Ca}(\text{OH})_2$ nanoparticles towards aggregation. The comparative evaluation of the two alterations proved that in the case of the drop to drop mixing of the reagents (B03ocb) the newly formed $\text{Ca}(\text{OH})_2$ nanoparticles show the lesser tendency to aggregation, in respect with the original experimental procedure (B03oca).

During the nucleation stage, the non-ionic surfactant n-octylamine is adsorbed on the surface of the primary $\text{Ca}(\text{OH})_2$ nanoparticles (nuclei) due to the hydrogen bonds between the hydroxyl group (OH^-) and the polar amine group (Fig. 5.16), forming a steric barrier by reducing the surface tension of the solid-liquid interface and thus reducing the total surface energy (γ) closer to the critical energy barrier (ΔG_c). The critical energy barrier corresponds to the critical radius (r_c) for the formation of $\text{Ca}(\text{OH})_2$ nuclei (primary particles) and the absence of dissociation phenomena [129]. This causes the creation of thermodynamically stable nanoparticles, preventing the consequent crystal growth [133]. In this way, the growth and polydispersity of the nanoparticles is limited, and the hexagonal shape is preserved [138].

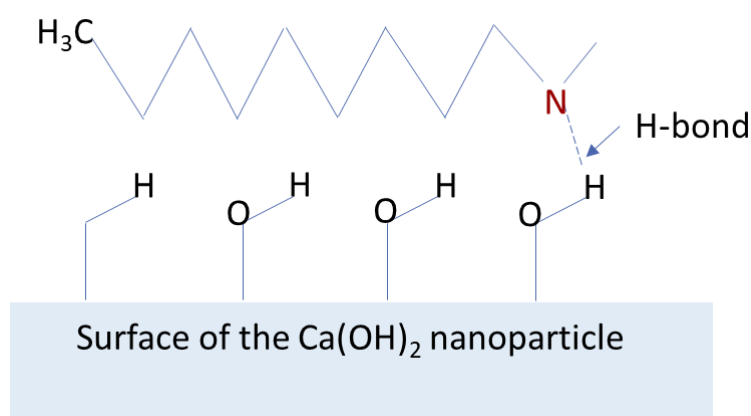
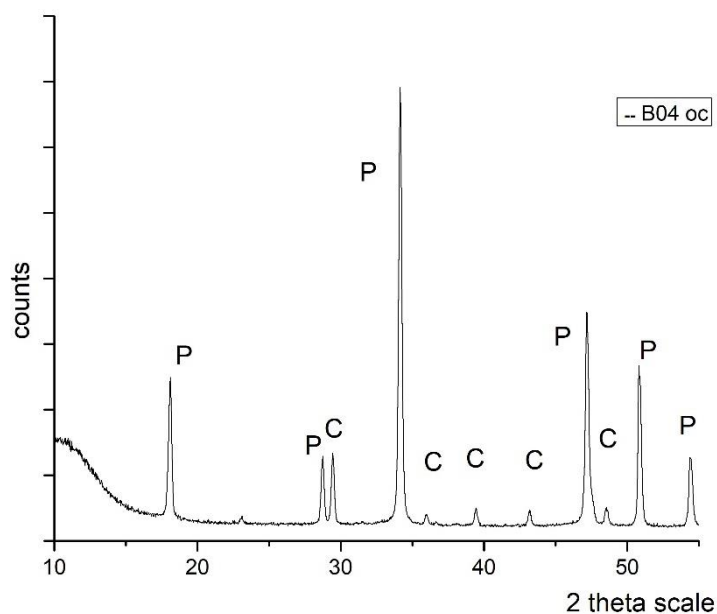


Figure 5.16 H-bonding between the non-ion surfactant n-octylamine and the $\text{Ca}(\text{OH})_2$ nanoparticle's surface

Mineralogical characterization - XRD results

The results of the mineralogical characterization of the all four synthetic procedures were characterized by the dominant presence of portlandite $\text{Ca}(\text{OH})_2$, as indicated in the XRD diffractogram (Graph 5.11). Specifically, the presence of the major peaks $17,9^\circ$, $28,4^\circ$, $34,1^\circ$, $46,8^\circ$ and $50,6^\circ$ of portlandite of hexagonal crystals corresponding to the XRD pattern of

44-1481. Other minor phase identified was that of calcite (CaCO_3) of trigonal crystals corresponding to the XRD pattern of 5-586.



Graph 5.11 Representative X-ray Diffraction pattern of the produced nanoparticles of the T04oc and B04oc

The average crystallite size for all three synthesis was determined with the Scherer equation. The average crystallite size for the top-down route (T03oc) was 38 nm. When compared to the original results of the top-down route, the average crystallite size was not altered. The average crystallite size for the alterations of the bottom-up synthetic route was estimate at: a) 46 nm for the first alteration (B04oca) and b) 50 nm for the second alteration (B04ocb), When compared to the results obtained by the original bottom-up synthetic route (average crystallite size of 43 nm), the addition of the n-octylamine led to a increase of the average crystallite size.

Overall, the addition of n-octylamine led to a decrease of the size of the newly formed $\text{Ca}(\text{OH})_2$ nanoparticles for both synthetic routes.

Compared to both basic synthetic routes, the addition of n-octylamine resulted in the reduction of the size of the nanoparticles due to the adsorption of the polar head of the n-octylamine onto the surface of the $\text{Ca}(\text{OH})_2$ nanoparticles through the formation of H-bonds.

5.4.3 Addition of Amylamine

The third surfactant that was tested was the **amylamine cationic surfactant** (B04am), following the previously adopted methodology of the drop to drop addition of the reactants.

Morphological characterization - SEM results

The addition of amylamine resulted in a notable increase of the nanoparticles thickness and diversity in their shape and size (Fig. 5.17). SEM examination resulted in the formation of prismatic, hexagonal and spike-like $\text{Ca}(\text{OH})_2$ nanoparticles, with dimensions between 170 nm to 1 μm (Fig. 5.17).

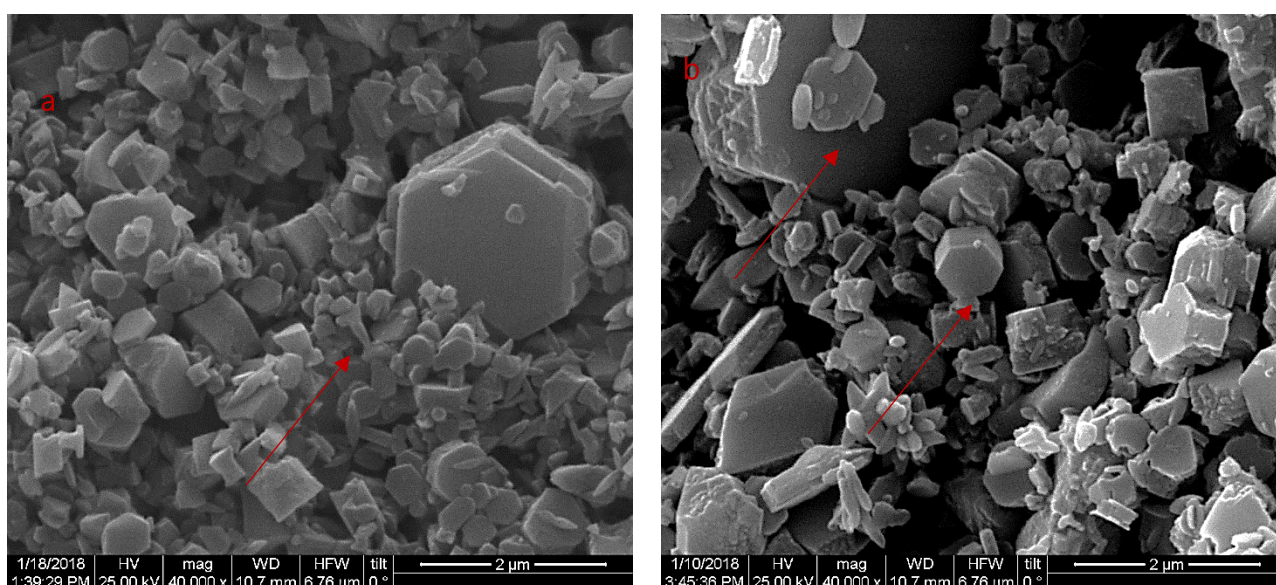
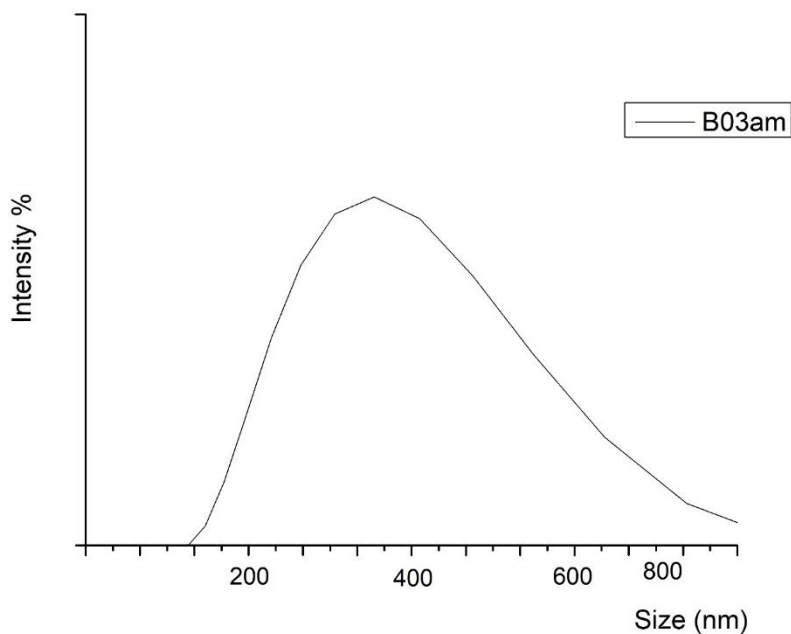


Figure 5.17 Clusters of: (a) Hexagonal and spike-like $\text{Ca}(\text{OH})_2$ nanoparticles, of dimensions in between 170 nm and 1 μm (scale bar at μm) and (b) Hexagonal $\text{Ca}(\text{OH})_2$ nanoparticles (B04am) (scale bar at 2 μm)

Morphological characterization - DLS results

The size of $\text{Ca}(\text{OH})_2$ nanoparticles studied by DLS indicated the formation of $\text{Ca}(\text{OH})_2$ nanoparticles of average size of 531 nm. In addition, the corresponding particle size distribution curve (Graph 5.13) presented a wider shape, indicating polydispersity of the shape of the produced $\text{Ca}(\text{OH})_2$ nanoparticles.



Graph 5.12 Particle size distribution by DLS of the synthesis implemented with the addition of the cationic surfactant of amylamine

During the nucleation stage, the cationic surfactant amylamine is adsorbed on the surface of the primary $\text{Ca}(\text{OH})_2$ nanoparticles (nuclei) due to the electrostatic interactions between the anion hydroxyl and the cation amine (Fig. 5.18), forming a steric barrier. In the case of amylamine, the interpretation of the results revealed that the surface tension is not sufficiently reduced, thus allowing the crystal growth. This underlined the fact that the use of cationic surfactants is not recommended for the implementation of steric stabilization for the synthesis of $\text{Ca}(\text{OH})_2$ nanoparticles.

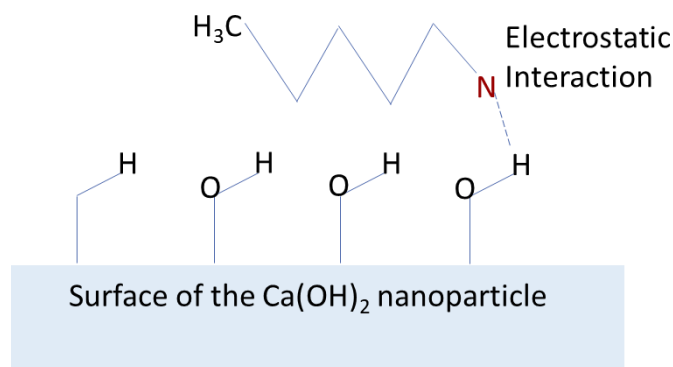
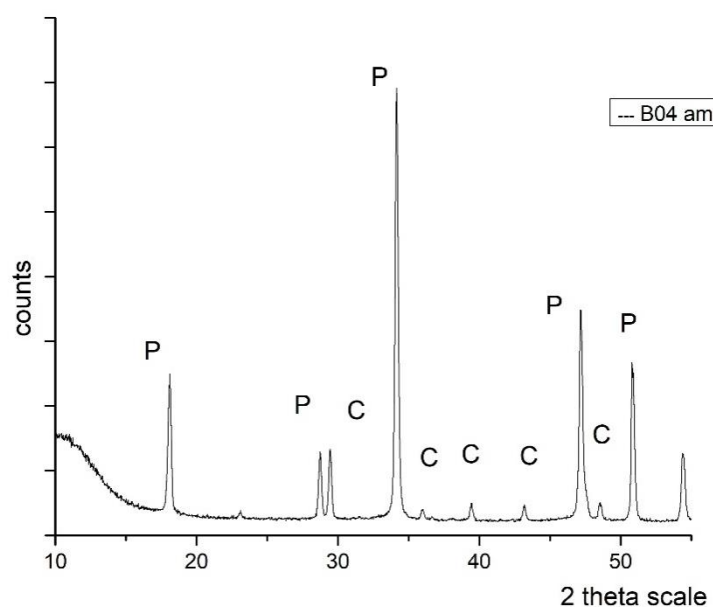


Figure 5.18 H-bonding between the non-ion surfactant n-octylamine and the $\text{Ca}(\text{OH})_2$ nanoparticle's surface

Mineralogical Characterization - XRD results

The results of the mineralogical characterization of the all four synthetic procedures were characterized by the dominant presence of portlandite Ca(OH)_2 , as indicated in the XRD diffractogram (Graph 5.13). Specifically the presence of the major peaks $17,9^\circ$, $28,4^\circ$, $34,1^\circ$, $46,8^\circ$ and $50,6^\circ$ of portlandite of hexagonal crystals. corresponding to the XRD pattern of 44-1481. Other minor phase identified was that of calcite (CaCO_3) of trigonal crystals corresponding to the XRD pattern of 5-586. The average crystallite size for the bottom-up synthetic route with the addition of amylamine (B04am) was 32 nm. When compared to the original results of the bottom-up synthetic route, the average crystallite size was decreased.



Graph 5.13 X-ray Diffraction pattern of the produced nanoparticles of B04am

Overall, the addition of amylamine led to a decrease of the size of the newly formed Ca(OH)_2 nanoparticles when compared to the results of the original bottom-up synthetic route. However, the results characterized by a large variety of different dimensions of Ca(OH)_2 nanoparticles. The reported reduction of the average crystallite size was not observed on the size of the Ca(OH)_2 nanoparticles. The reported modifications were attributed to the adsorption of amylamine through the electrostatic interactions between amylamine and the surface of the Ca(OH)_2 nanoparticle.

5.4.4 Comparative evaluation of the surfactants effect in the bottom-up synthetic route

The addition of all three surfactants had a direct effect on the morphological characteristics of the Ca(OH)_2 nanoparticles:

- Triton X-100 resulted in the production of plate-like of hexagonal habit Ca(OH)_2 nanoparticles (Fig. 5.19b). The nanoparticles presented smaller size, enhanced width and more angular shape, compared with the main bottom-up method without the addition of the surfactant (Fig. 5.19a). Moreover, an alignment of the Ca(OH)_2 nanoparticles in a preferential direction was clearly observed (Fig. 5.19b).
- n-octylamine resulted in plate-like and spherical Ca(OH)_2 particles (Fig. 5.20a). Compared to the previous synthesis, the nanoparticles were characterized by diversity and variation in terms of size and random orientation. Finally,
- amylamine resulted in the formation of prismatic, hexagonal and spike-like Ca(OH)_2 nanoparticles (Fig. 5.20b). The addition of amylamine resulted in diversity in terms of shape and size of the nanoparticles, compared to the uniformity of the nanoparticles in the case of the results obtained by the initial bottom-up methodology and the addition of Triton X-100. Also, amylamine resulted a notable increase of nanoparticles thickness.

It is worth noting that Ca(OH)_2 nanoparticles resulted from the initial bottom-up methodology and the addition of Triton X-100 presented an alignment in a preferential direction of the hexagon base. In contrast, those obtained by n-octylamine and amylamine experiments were clearly characterized by a random placement of the nanoparticles. This phenomenon has been observed by other researchers as well [9],[219] and it is connected to the inhibition of the colloidal characteristic of the dispersion.

Table 5.1 summarizes the quantitative results obtained by different methods concerning the dimensions of nanolime particles. The addition of Triton X-100 and n-octylamine resulted in the reduction of the average size of the Ca(OH)_2 nanoparticles (Table 5.1). However, the comparative evaluation between the dimensions of the nanoparticles (Table 5.1) and the size of the corresponding crystallites (section 4.1) underlines that **the reduction of the crystallites' size -when compared to the basic bottom-up route- is reflected only to the reduction of the size of the Ca(OH)_2 nanoparticles due to the addition of Triton X-100.** The addition of n-octylamine resulted in the reduction of the size of the Ca(OH)_2 nanoparticles but didn't inhibit the presence of aggregation phenomena. This could be attributed to the stronger H-bonding formed in the case of the adsorption of Trin X-100 onto the surface of th primary Ca(OH)_2 nanoparticles during the nucleation stage, when compared to the n-octylamine. Finally, the addition amylamine proved to be less sufficient to act as a steric barrier, thus, resulting in the increase of the size of the nanoparticles.

Table 5.1 Average size of portlandite crystallites, nanoparticles and clusters determined by different analytical techniques

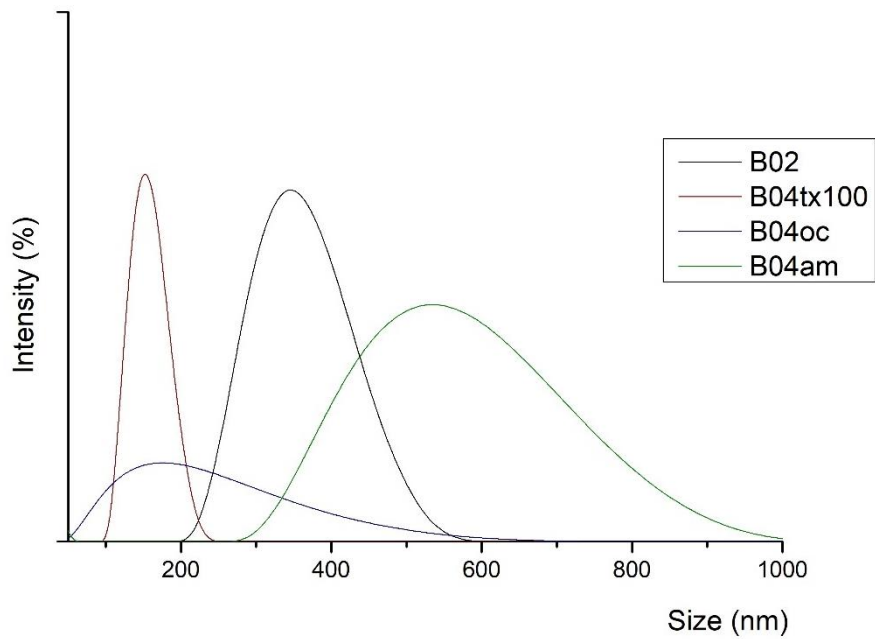
<i>Alteration</i>	Nanoparticle clusters' size (nm)	Mean values of the nanoparticle's size (nm)	Crystallite size (nm)
	<i>SEM</i>	<i>DLS</i>	<i>XRD</i>
B02	150 – 450	348	43
Triton X-100 (B04tx100)	100 – 300	153	37
N-octylamine (B04oc)	150 – 800	197	50
Amylamine (B04am)	170 – 1000	531	32

Moreover, in the particle size distribution curve (Graph 5.14) that corresponds to Triton X-100, a narrower shape is observed, indicating the homogeneity of the produced $\text{Ca}(\text{OH})_2$ nanoparticles in terms of size. Contrary to this, the wider shape of the curves that corresponds to n-octylamine and amylamine confirm the polydispersity of the produced $\text{Ca}(\text{OH})_2$ nanoparticles.

The use of non-ionic surfactants in the bottom-up synthetic route (homogenous reaction) and the exposure of the nanodispersions to the ultrasonic probe, seemed to favor the hexagonal plate-like shape of the nanoparticles and nanoparticle cluster.

Similar to the results reported in literature [34],[173],[217], the modifications on the size and shape of $\text{Ca}(\text{OH})_2$ nanoparticles, are attributed to the presence of the two non-ionic surfactants (Triton X-100 and n-octylamine) during the nucleation stage of the $\text{Ca}(\text{OH})_2$ nanoparticles. The non-ionic surfactants are adsorbed on the surface of the $\text{Ca}(\text{OH})_2$ primary nanoparticles particles through the formation of hydrogen bonds. In terms of thermodynamics, this causes the reduction of the surface free energy (γ) of water to values closer to the critical energy barrier (ΔG_c) which corresponds to the critical radius (r_c) for the formation of $\text{Ca}(\text{OH})_2$ nuclei (primary particles) and the absence of dissociation phenomena [144]. This causes the creation of thermodynamically stable nanoparticles, preventing the consequent crystal growth [129],[131]. Thus, the growth of the nanoparticles is limited, and the hexagonal shape is preserved [133]. In the case of the amylamine, the results reflect the absence of the electrostatic interactions that would lead to the adsorption of amylamine onto the surface of the $\text{Ca}(\text{OH})_2$ primary nanoparticles [138]. In terms of potential consolidation applications, the dimensions of the produced $\text{Ca}(\text{OH})_2$ nanoparticles coincide with the dimensions of the micritic calcite. The hexagonal plate-like shape of crystallites

could be beneficial since their preferential alignment along the basal plane (001) of the hexagonal $\text{Ca}(\text{OH})_2$ nanoparticles promote the increase of the total surface area in relation to the total volume. The increased total surface area along with the reduced size of the $\text{Ca}(\text{OH})_2$ nanoparticles could promote the carbonation reaction after the deposition of the nanoparticles on the porous substrate, since it enhances the reactivity and the ability of the formation of an adsorbed water film on the surface of nanoparticles.



Graph 5.14 Particle size distribution by DLS of the main of the produced particles of the bottom-up methodology and the alteration with the three surfactant

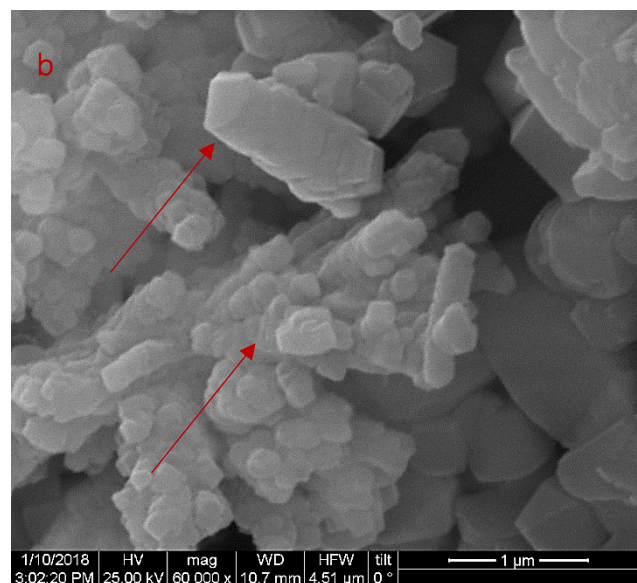
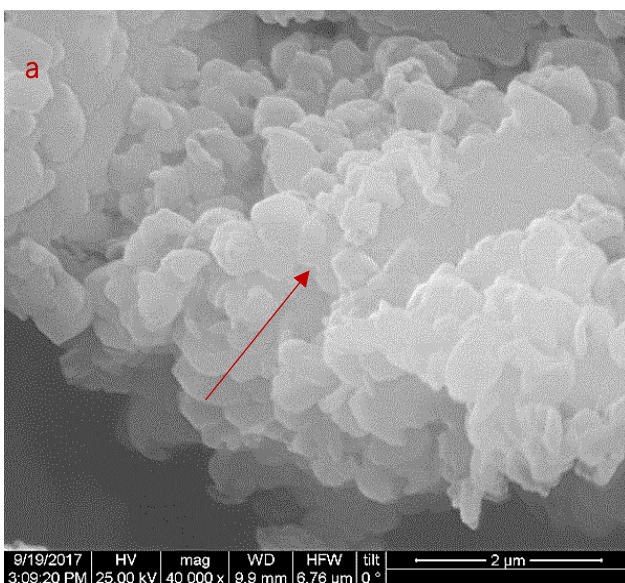


Figure 5.19 Clusters of: (a) Plate-like nanoparticles of $\text{Ca}(\text{OH})_2$ particles of undetermined shape of dimensions between 150 nm to 400 nm (B02)(scale bar at $2\mu\text{m}$); (b) Plate-like of hexagonal habit $\text{Ca}(\text{OH})_2$ nanoparticles of dimensions between 100 nm to 300 nm.(B04tx100b)(scale bar at $4\mu\text{m}$).

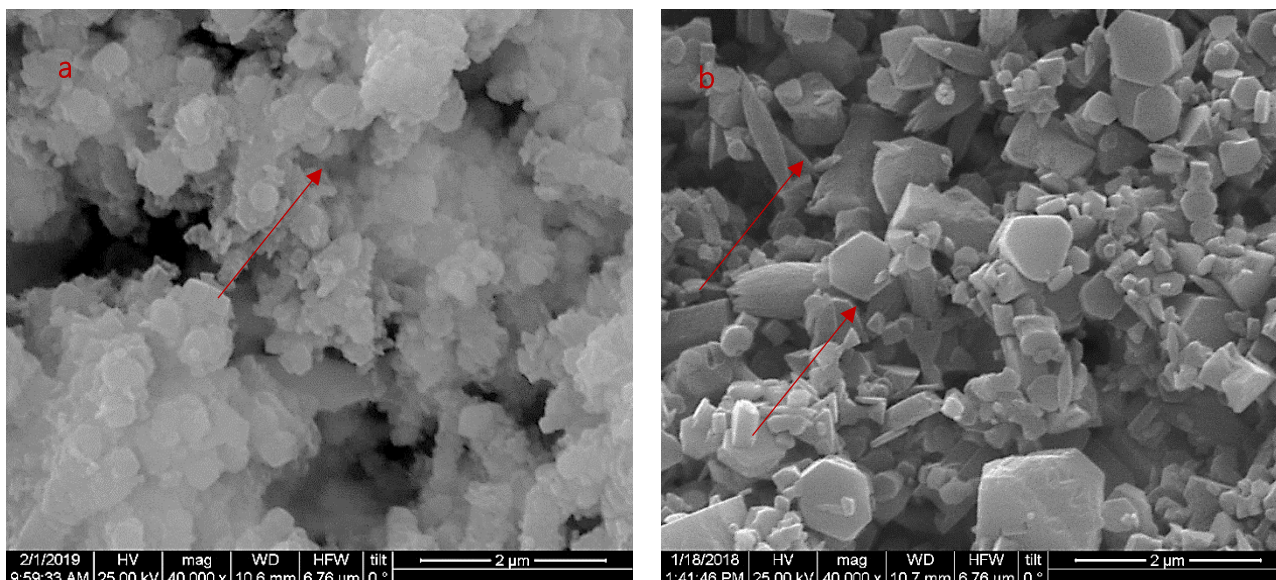


Figure 5.20 Clusters of: (a) Plate-like of hexagonal habit and spherical $\text{Ca}(\text{OH})_2$ nanoparticles, with dimensions between 150 nm to 800 nm resulted from the addition of n-octylamine (B04oc) (scale bar at $2\mu\text{m}$); (b) Hexagonal, prismatic and spike-like $\text{Ca}(\text{OH})_2$ nanoparticles, with dimensions between 170 nm to $1.10\mu\text{m}$ (B04am) (scale bar at $22\mu\text{m}$).

Overall, the addition of Triton X-100 was selected as the parameter for the functionalization of the surface of the $\text{Ca}(\text{OH})_2$ nanoparticles on the basis of:

- ✓ Effective reduction of the size of the $\text{Ca}(\text{OH})_2$ nanoparticle
- ✓ Direct effect in the formation of plate-like $\text{Ca}(\text{OH})_2$ nanoparticle of hexagonal habit
- ✓ In terms of potential consolidation applications, the dimensions of the produced $\text{Ca}(\text{OH})_2$ nanoparticles coincide with the dimensions of the micritic calcite

Moreover, based on the advancements resulted by addition of drop to drop of the two initial reagents, this parameter was introduced in all experiments implemented therefore by the bottom-up synthetic route.

5.5 Modification of the dispersion medium

One of the major parameters that affects both the morphological characteristics of $\text{Ca}(\text{OH})_2$ nanoparticles and the colloidal stability of the dispersions is the selection of the appropriate dispersion medium. During this research two polar dispersion medium were tested: a) an innovative O_2 nanobubbles (nbs) enriched aqueous solution and b) a polar dispersion medium consisted of a short chain alcohol and water.

5.5.1 Use of O_2 nanobubbles enriched aqueous solution

The morphological characteristics of the $\text{Ca}(\text{OH})_2$ nanoparticles developed by incorporating O_2 nanobubbles (nbs) enriched water was implemented by SEM, TEM and DLS. Also, the newly synthesized nanoparticles were characterized mineralogically through XRD.

Morphological characterization - SEM results

In the **top-down route (T04nb)**, the use of O_2 nanobubbles (nbs) enriched water resulted in the production of rounded and of undetermined shape $\text{Ca}(\text{OH})_2$ nanoparticles, of dimensions in between 200 nm and 500 nm (Fig. 5.21a). When compared to the results of the basic top-down route (T_01) (Fig. 5.2). The newly formed $\text{Ca}(\text{OH})_2$ nanoparticles were characterized by the evident presence of agglomerates.

In the case of the **bottom-up synthetic route (B05nba)**, the use of O_2 nanobubbles (nbs) enriched aqueous solution both the synthetic process and the washings resulted in the synthesis of $\text{Ca}(\text{OH})_2$ nanoparticles of hexagonal, regular and angular shape (Fig. 5.21b). The nanoparticles were characterized by a uniform shape and their dimensions vary between 200 nm to 450 nm. (Fig. 5.21b). When compared to the results of the basic bottom-up synthetic route (B_01) in Fig. 5.3, the newly formed $\text{Ca}(\text{OH})_2$ nanoparticles were characterized by the reduction of size to the nano-scale and by the polydispersity in terms of shape.

The comparative evaluation of the two main synthetic routes revealed that use of the O_2 nanobubbles (nbs) enriched water as dispersion medium proved to be effective only in the case of the bottom-up synthetic route.

On the basis of the results obtained in chapter 5.4, two further alterations of the B05nba experimental procedure were implemented: the addition of the non-ionic surfactants Triton X-100 (B05nbtX100a) and n-octylamine (B05nboca) (Fig. 5.22 a and b respectively).

The addition of Triton X-100 (B05nbtX100a) resulted in the formation of hexagonal $\text{Ca}(\text{OH})_2$ nanoparticles, of dimensions in between 175 nm and 350 nm. The newly formed $\text{Ca}(\text{OH})_2$ nanoparticles presented also a certain width observed with the use of SEM (Fig. 5.22a).

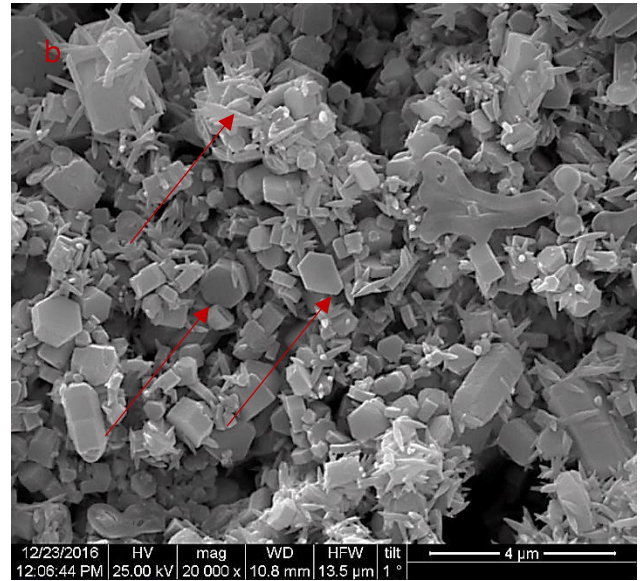
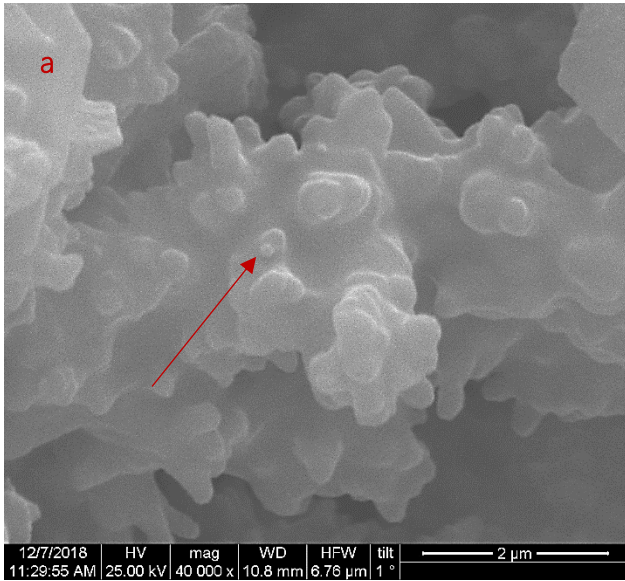


Figure 5.21 Clusters of: (a) Rounded and of undetermined shape $\text{Ca}(\text{OH})_2$ nanoparticles, of dimensions in between 200 nm to 500 nm , as parts of agglomerates (T04nb) (scale bar at 2 μm); (b) Hexagonal, regular and angular shape $\text{Ca}(\text{OH})_2$ nanoparticles of dimensions in between 200 nm to 450 nm. (B05nba) (scale bar at 4 μm).

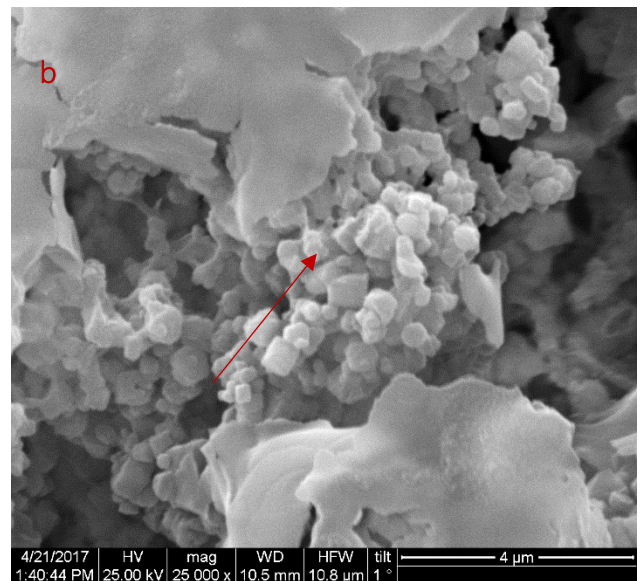
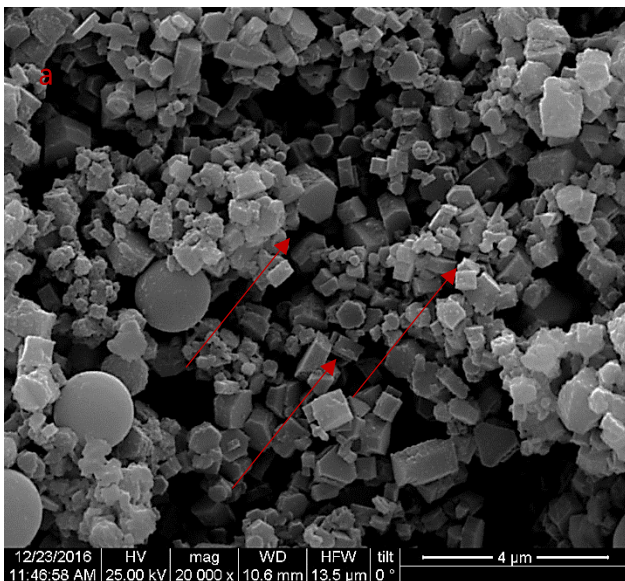


Figure 5.22 Clusters of: (a) Hexagonal $\text{Ca}(\text{OH})_2$ nanoparticles, of dimensions in between 200 nm and 350 nm. (B505tx100a) (scale bar at 4 μm); (b) Hexagonal $\text{Ca}(\text{OH})_2$ nanoparticles, of dimensions in between 200 nm and 350 nm. (B505tx100a) (scale bar at 4 μm).

The addition of *n*-octylamine (B05nboca) resulted also in the formation of hexagonal $\text{Ca}(\text{OH})_2$ nanoparticles, of dimensions in between 200 nm and 350 nm. (Fig. 5.22b). However, due to the presence of larger parts of conglomerates, the addition of *n*-octylamine could not be characterized as effective.

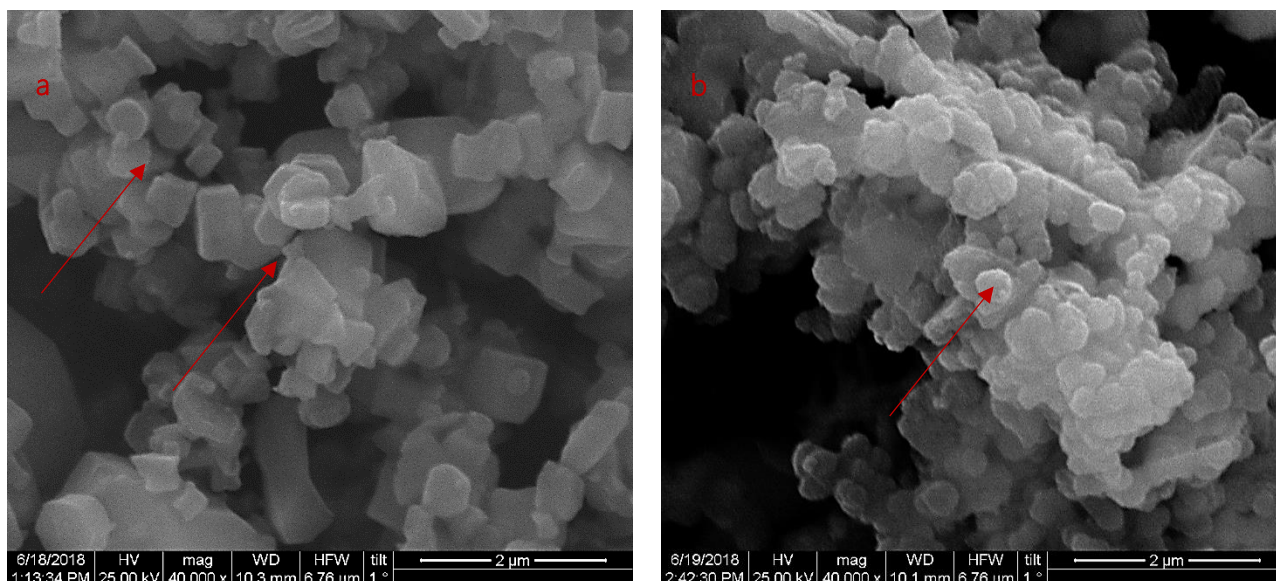


Figure 5.23 Clusters of: (a) Hexagonal $\text{Ca}(\text{OH})_2$ nanoparticles, of dimensions in between 100 nm and 300 nm (B05nb) scale bar at $1\ \mu\text{m}$; (b) Hexagonal and plate-like $\text{Ca}(\text{OH})_2$ nanoparticles, of dimensions in between 100 nm and 300 nm (B05nbt100) (scale bar at $2\ \mu\text{m}$).

The use of O_2 nanobubbles (nbs) enriched water as dispersion medium proved to be effective in the case of the bottom-up synthetic route. On this basis, two further alterations of the bottom-up synthetic route were implemented. The implementation of the bottom-up synthetic route using the O_2 nanobubbles (nbs) enriched water as dispersion medium (B05nb) a) in inert He-conditions and b) by drop to drop addition of the non-ionic surfactant Triton X-100 (B05nbt100).

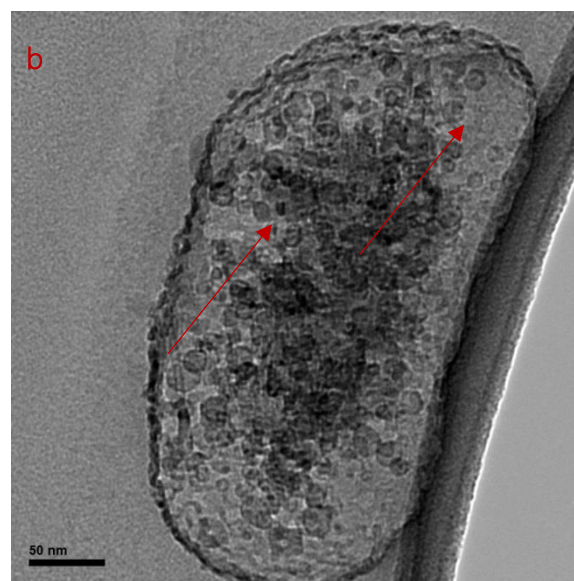
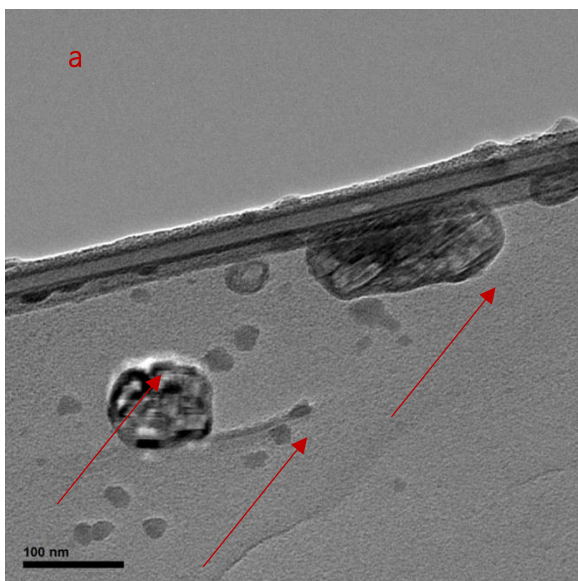
The first modification of the bottom-up synthetic route (B05nb) resulted in the production of hexagonal $\text{Ca}(\text{OH})_2$ nanoparticles, of dimensions in between 130 nm and 300 nm. The newly formed $\text{Ca}(\text{OH})_2$ nanoparticles were characterized by high homogeneity in terms of shape (Fig. 5.23a).

The addition of Triton X-100 resulted in the reduction of the size of the $\text{Ca}(\text{OH})_2$ nanoparticles. In specific, the addition of Triton X-100 resulted (B05nbt100) in the production of hexagonal and plate-like $\text{Ca}(\text{OH})_2$ nanoparticles, of dimensions in between 100 nm and 300 nm (Fig. 5.23c). The newly formed $\text{Ca}(\text{OH})_2$ nanoparticles were characterized by high homogeneity in terms of size and shape.

Morphological characterization - TEM results

The TEM analysis expanded the information obtained by SEM. In specific, in both experimental procedures hexagonal and plate-like 2-D $\text{Ca}(\text{OH})_2$ nanoparticles of dimensions between 50 nm to 150 nm were observed (Fig. 5.24 a and b). The plate-like shape of the nanoparticle was connected with the increase of the specific surface area and so to the increase of their reactivity [187]. However, in the main bottom-up synthetic route

B05nb (Fig. 5.24a) the plate like nanoparticle seemed to be composed by a single nanoparticle. Contrary to this, the results of the second alteration B05nbt100 revealed that the plate-like $\text{Ca}(\text{OH})_2$ nanoparticles were composed by many smaller ones (Fig. 5.24b). This could be an indication about the nucleation-growth process of the $\text{Ca}(\text{OH})_2$ nanoparticles. According to the relevant literature [165], the synthesis of hexagonal and plate-like 2-D $\text{Ca}(\text{OH})_2$ nanoparticles is characterized by a layer by layer growth mechanism, initiated by screw-dislocations or 2-dimensional nucleation. But, in the case B05nbt100 the detection of plate-like $\text{Ca}(\text{OH})_2$ nanoparticles composed by many smaller ones, could be attributed to the implementation of a non-classical nucleation growth mechanism, where the plate-like nanoparticles were composed by the recrystallization of smaller spherical primary $\text{Ca}(\text{OH})_2$ nanoparticles to a single one. The SAED analysis confirmed that the $\text{Ca}(\text{OH})_2$ nanoparticles were monocrystalline (Fig. 5.24c).



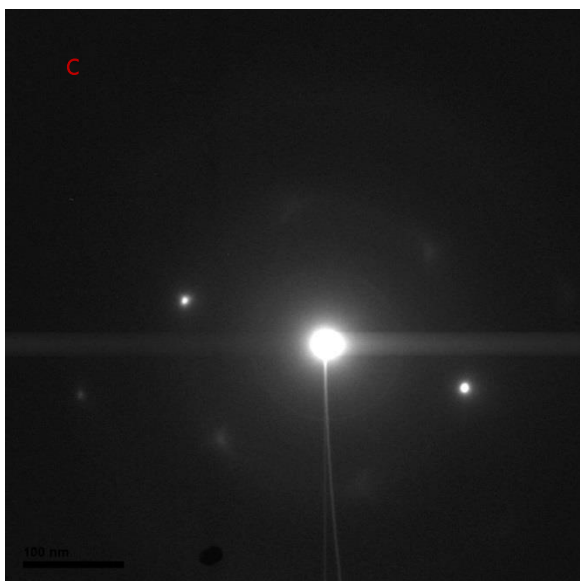
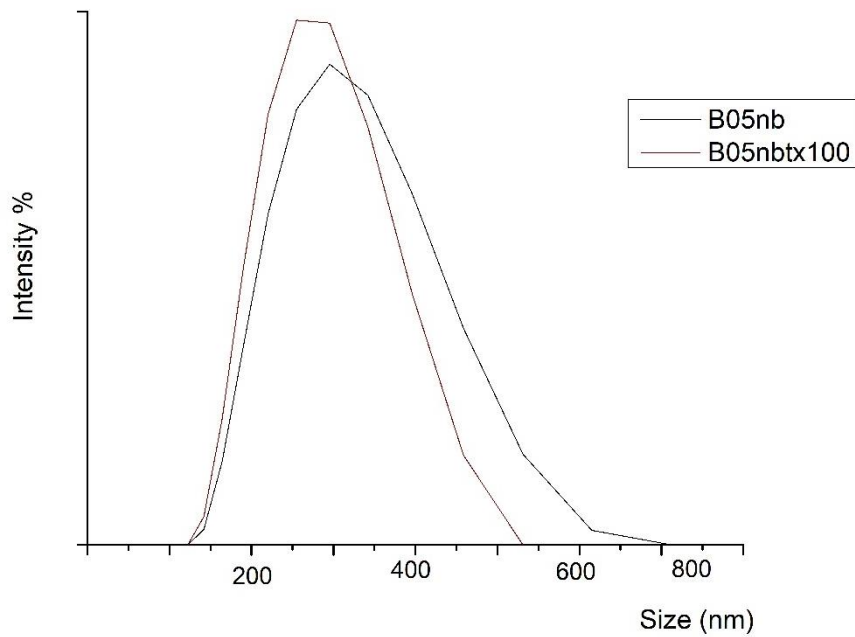


Figure 5.24 (a) Hexagonal $\text{Ca}(\text{OH})_2$ and plate-like nanoparticles (B05nb) (scale bar at 100 nm); (b) Plate-like $\text{Ca}(\text{OH})_2$ nanoparticle composed by smaller ones (B05nbtx100) (scale bar at 50 nm) and (c) SAED analysis

Morphological characterization - DLS results

The size of $\text{Ca}(\text{OH})_2$ nanoparticles was additionally studied by DLS, calculating the average size, the particle size distribution and the ζ -potential. The use of O_2 nanobubbles (nbs) enriched water as dispersion medium at the bottom-up synthetic route (B05nb) resulted in the formation of $\text{Ca}(\text{OH})_2$ nanoparticles of average size of 310 nm. The addition of Triton X-100 non-ionic surfactant (B05nbtx100) resulted in the formation of $\text{Ca}(\text{OH})_2$ nanoparticles of average size of 278 nm. Both corresponding particle size distribution curves (Graph 5.15) presented a narrower shape, indicating homogeneity of the shape of the produced $\text{Ca}(\text{OH})_2$ nanoparticles.

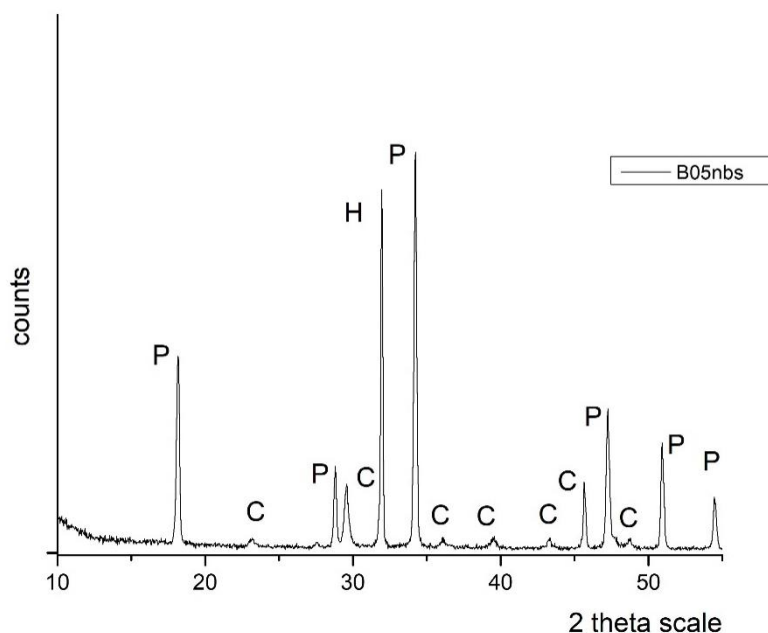


Graph 5.15 Particle size distribution of the two nanodispersions

With the use of the DLS methodology, the ζ -potential of the two alterations of the bottom-up synthetic route was determined: for the B05nb the ζ -potential was estimated at -11mV and for the B05nbtX100 the ζ -potential was estimated at -12mV. The ζ -potential provided an estimation of the tendency of the newly formed $\text{Ca}(\text{OH})_2$ nanoparticles towards aggregation. The comparative evaluation of the two modifications proved that in both cases the newly formed $\text{Ca}(\text{OH})_2$ nanoparticles showed lesser tendency to aggregation.

Mineralogical characterization - XRD results

The results of the mineralogical characterization of the all four synthetic procedures were characterized by the dominant presence of portlandite $\text{Ca}(\text{OH})_2$, as indicated in the XRD diffractogram (Graph 5.16). Specifically, the presence of the major peaks $18,1^\circ$, $28,5^\circ$, $34,1^\circ$, $46,7^\circ$ and $50,7^\circ$ of portlandite of hexagonal crystals corresponding to the XRD pattern of 44-1481. Other minor phase identified was that of calcite (CaCO_3) of trigonal crystals corresponding to the XRD pattern of 5-586.



Graph 5.16 X-ray Diffraction pattern of the B05nb and nanoparticles

The average crystallite size for two synthesis was determined with the Scherer equation. The use of O_2 nanobubbles (nbs) enriched aqueous solution as dispersion medium at the bottom-up synthetic route (B05nb) resulted in the formation of $Ca(OH)_2$ nanoparticles of average crystallite size of 35 nm. The addition of the non-ionic surfactant of Triton X-100 (B05nbtX100) resulted in the formation of $Ca(OH)_2$ nanoparticles of average crystallite size of 36 nm. In both cases, the use of O_2 nanobubbles (nbs) enriched aqueous solution as dispersion medium resulted in the reduction of the average crystallite size in respect with the original bottom-up synthetic procedure.

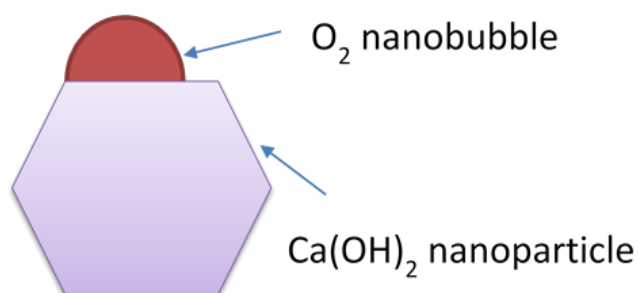
According to the relevant literature, the characteristic higher conductivity ($2\mu S$ instead of $1.7\mu S$) of enriched with oxygen NBs water compared to the distilled water can be attributed to the excess of hydroxyl ions (OH^-) relative to hydrogen ions (H^+) at the gas-water interface [220-221]. Thus charging is also responsible for the electrophoretic mobility of the O_2 nanobubbles resulting in the negative values of ζ -potential of water enriched with O_2 nanobubbles [146],[222]. Because of this interface, gas-water, charging the gaseous cavities (in our case O_2) can be formatted and remained into the water phase as bulk NBs [223-224]. In our case the diameter of the produced bulk NBs is around 350 nm, whereas the NBs are presenting high stability, longevity and ability of adsorption mainly to the hydrophobic surfaces.

The longevity of the O_2 nanobubbles is attributed in the presence of H-bridges between the nanobubbles and the dispersion medium (distilled water) that reduces the diffusivity of the gas (O_2) and creates an energy barrier against the rupture of the nanobubbles for a long period of time. The stability of the specific dispersion medium lies on the innovative methodology of production of O_2 nanobubbles in the liquid phase through hydrodynamic

cavitation and the use of a venture tube. When the two-phase mixture (water-gas) passes through the venture tube the pressure fluctuation results in the formation of the nanobubbles [146],[225-228]

Overall, the use of O_2 nanobubbles (nbs) enriched aqueous solution as dispersion medium at the bottom- up synthetic route led to a significant decrease of the size of the newly formed $Ca(OH)_2$ nanoparticles, clusters and of the corresponding crystallites.

This modification led to the formation of hexagonal and plate-like crystals of $Ca(OH)_2$ and clusters, and to the absence of agglomeration and aggregation phenomena. Considering the presence of O_2 -nanobubbles in both the reactant and the dispersion medium, a potential explanation of their role could be their behavior as a "physical barrier" between $Ca(OH)_2$ nanoparticles. The modifications of the morphological characteristics of the newly formed nanoparticles were attributed to the nucleation of the nanobubbles on the surface of the nanoparticles, forming a new homogenous population of nanoparticles of a diameter in between the diameter of the original nanoparticles and the O_2 -nanobubbles. In this way, the phenomenon of steric stabilization was implemented. The consequent reduction of the surface tension between the $Ca(OH)_2$ nanoparticles and the dispersion medium led to the modifications of their morphological characteristics and a slight decrease of the colloidal stability of the newly formed dispersions. The realization of this phenomenon depends on the size of the original nanoparticle. In specific, this cannot be applied in the case of nanoparticles of diameter below 100nm. Since the above mechanism takes place during the nucleation stage, the presence of O_2 nanobubbles - in terms of thermodynamics - reduces the surface free energy (γ) of water, leading to values closer to the critical energy barrier (ΔG_c) which corresponds to the critical radius (r_c) for the formation of $Ca(OH)_2$ nuclei (primary particles) [144]. Therefore, the reduction of the surface energy close to the critical energy barrier creates thermodynamically stable nuclei and prevents the crystal growth [129],[131]. Thus, the growth of $Ca(OH)_2$ nanoparticles was limited, resulting in the smaller average particles size among the bottom-up samples, while their hexagonal shape was preserved [133], [146]. Finally, nanobubbles could promote the electrostatic stabilization of the dispersion, since they present negative electric charge.



5.5.2 Use of mixed polar dispersion medium

The effect of mixed polar dispersion media (Table 5.2) on the morphological characteristics of Ca(OH)₂ nanoparticles was implemented by the use of SEM and TEM, while their mineralogy was studied by XRD.

Table 5.2 Description of the eight dispersions of Ca(OH)₂ nanoparticles of mixed polar dispersion medium

Sample I.D.	Description				
	Method	Water (% v/v)	2-propanol (% v/v)	Ethanol (% v/v)	Acetone (% v/v)
T04_100w	Top-down	100	0	0	0
T04_80w20isp	Top-down	80	20	0	0
T04_50w50isp	Top-down	50	50	0	0
T04_20w40isp40ac	Top-down	20	40	0	40
T04_20w80eth	Top-down	20	0	80	0
T04_20w80isp	Top-down	20	80	0	0
T04_10w90isp	Top-down	10	90	0	0
B05_10w90isp	Bottom-up	10	90	0	0

Morphological characterization - SEM results

The study of mixed polar dispersion medium was implemented through the characterization of the dispersions of Ca(OH)₂ nanoparticles synthesized through eight experimental procedures. The addition of the non-ionic surfactant Triton X-100 was common in all eight experimental procedures.

In the case of the top-down route (T04_100w):

- the use of 100% distilled water resulted in the production of rounded, angular and of undetermined shape Ca(OH)₂ nanoparticles, of dimensions in between 120 nm and 300 nm (Fig. 5.25a).

- The reduction of the aqueous part to 80% and the addition of 20% of 2-propanol (T04_80w20isp) resulted in the production of rounded and undetermined shape Ca(OH)_2 nanoparticles, of dimensions in between 140 nm and 310 nm (Fig. 5.25b).
- The use of a 1:1 distilled water and 2-propanol (T04_50w50isp), resulted in the production of rounded and undetermined shape Ca(OH)_2 nanoparticles, of dimensions in between 214 nm and 300 nm (Fig. 5.26a).
- Further reduction of the aqueous part to 20% and the addition of 40% of 2-propanol and 40% of acetone (T04_20w40isp40ac) resulted in the production of angular, rounded and of undetermined shape Ca(OH)_2 nanoparticles.

The comparative evaluation of the morphological characteristics of the newly formed Ca(OH)_2 nanoparticles led to the distinction of the effect of 2-propanol and acetone on the shape of the Ca(OH)_2 nanoparticles. Specifically,

- the synthesis of rounded and undetermined shape Ca(OH)_2 nanoparticles, of dimensions in between 214 nm and 300 nm was attributed to the presence of 2-propanol, whereas the presence of larger aggregates consisted of angular Ca(OH)_2 nanoparticles, of dimensions in between 200 nm and 400 nm was attributed to the presence of acetone (Fig. 5.26b).
- The addition of 80% of ethanol along with 20% of distilled water (T04_20w80eth) led to the presence of larger agglomerates consisted of rounded and undetermined shape Ca(OH)_2 nanoparticles, of dimensions in between 170 nm and 300 nm (Fig. 5.27a).
- The replacement of ethanol by 2-propanol at the same percentage (T04_20w80isp) led to the synthesis of rounded and undetermined shape Ca(OH)_2 nanoparticles, of dimensions in between 120 nm and 200 nm (Fig. 5.27b).
- The increase of the percentage of 2-propanol to 90% with the addition of 10% of distilled water (T04_10w90isp) led to the presence of aggregates of rounded and of undetermined shape Ca(OH)_2 nanoparticles, of dimensions in between 120 nm and 250 nm (Fig. 5.28a).

Finally, the the use of the same mixed polar dispersion medium (90% 2-propanol and 10% distilled water) on the bottom-up synthetic route (B05_10w90isp) led to the synthesis of spherical and hexagonal Ca(OH)_2 nanoparticles, of dimensions in between 100 nm and 350 nm (Fig. 5.28b).

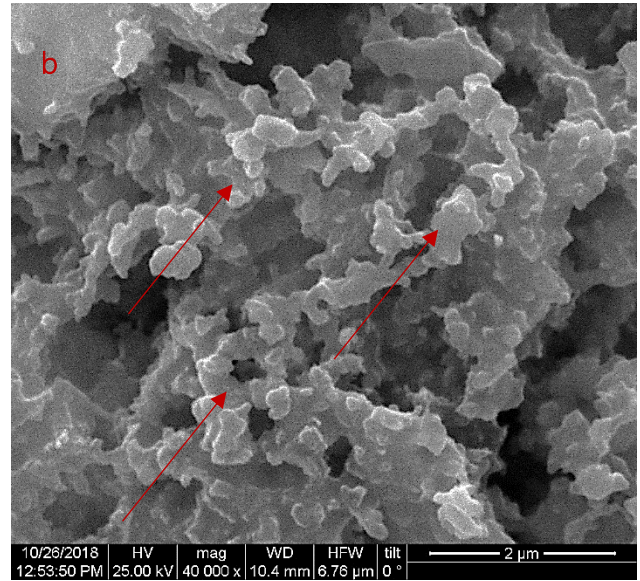
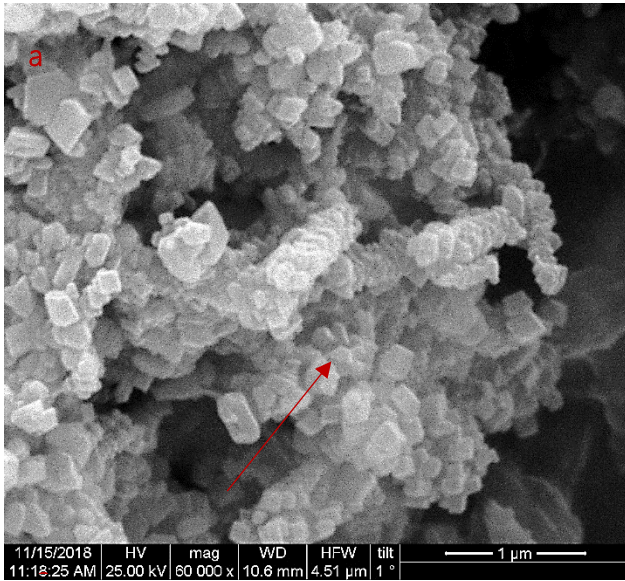


Figure 5.25 Clusters of: (a) Rounded, angular and of undetermined shape Ca(OH)_2 nanoparticles, of dimensions in between 120 nm and 300 nm (T04_100w) (scale bar at 1 μm); (b) Rounded and of undetermined shape Ca(OH)_2 nanoparticles, of dimensions in between 140 nm and 310 nm (T04_80w20isp) (scale bar at 2 μm).

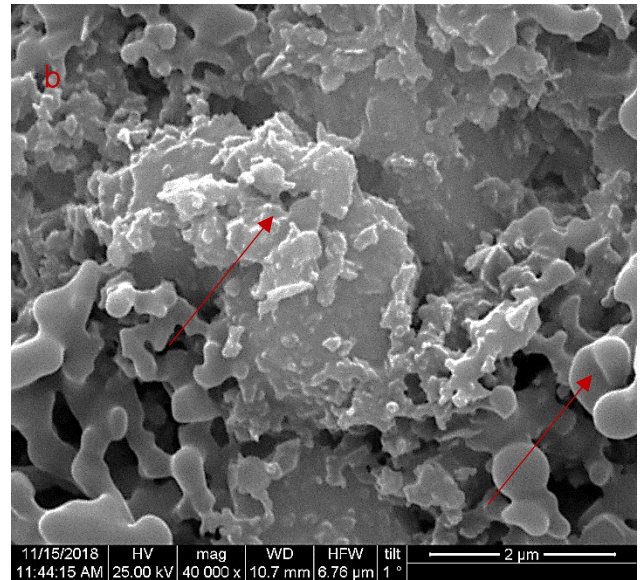
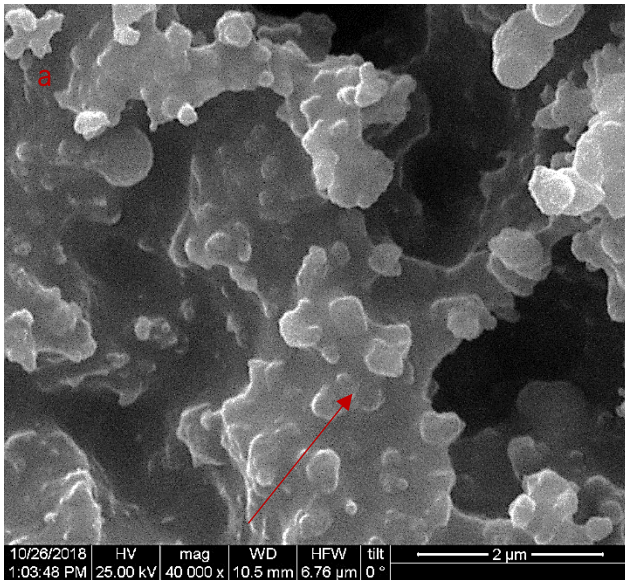


Figure 5.26 Clusters of: (a) Rounded and of undetermined shape Ca(OH)_2 nanoparticles, of dimensions in between 214 nm and 300 nm (T04_50w50isp) (scale bar at 2 μm); (b) Angular, rounded and of undetermined shape Ca(OH)_2 nanoparticles (T04_20w40isp40ac) (scale bar at 2 μm).

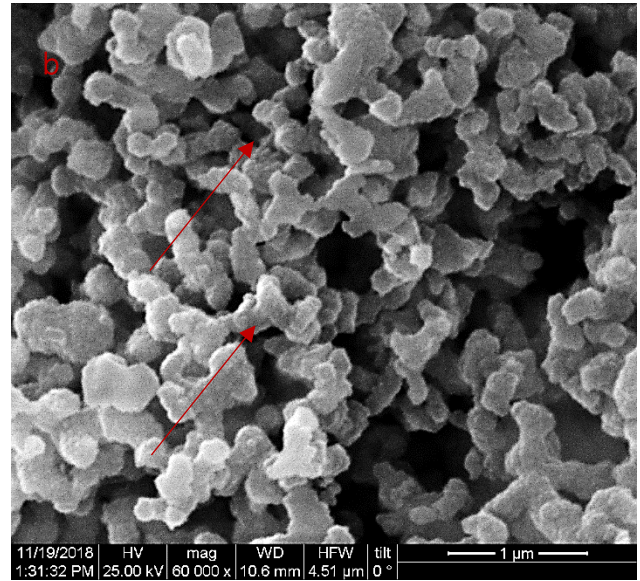
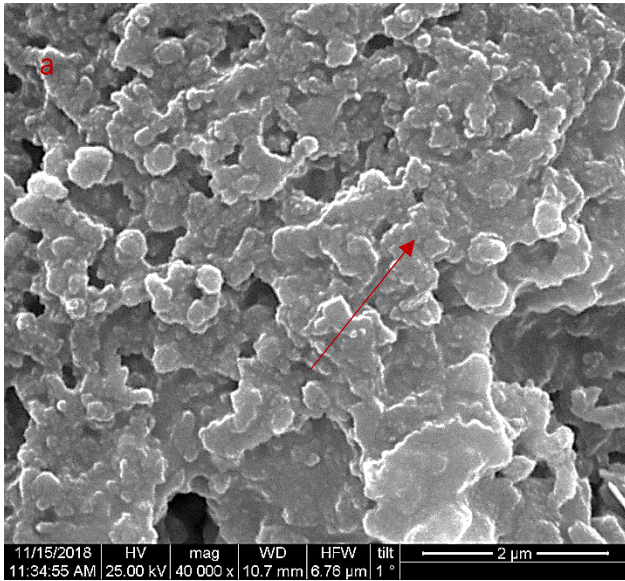


Figure 5.27 Clusters of: (a) Agglomerates consisted of rounded and undetermined shape Ca(OH)_2 nanoparticle clusters, of dimensions in between 170 nm and 300 nm (T04_20w80eth) (scale bar at 2 μm); (b) Rounded and of undetermined shape Ca(OH)_2 nanoparticles, of dimensions in between 120 nm and 200 nm (T04_20w80isp) (scale bar at 1 μm).

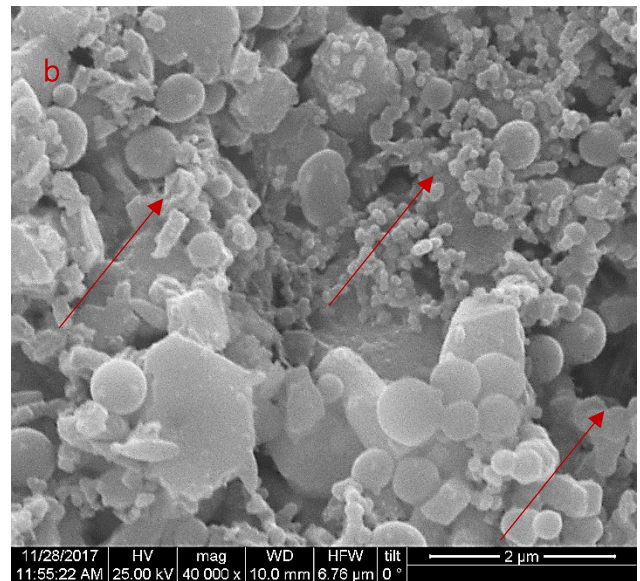
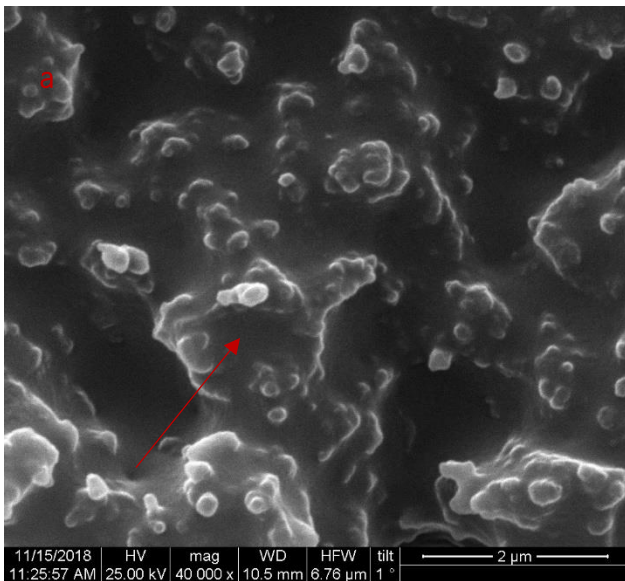


Figure 5.28 Clusters of: (a) Agglomerates of rounded and undetermined shape Ca(OH)_2 nanoparticle clusters, of dimensions in between 120 nm and 250 nm (T04_10w90isp) (scale bar at 2 μm); (b) Spherical and hexagonal Ca(OH)_2 nanoparticles, of dimensions in between 100 nm and 350 nm (B05_10w90isp) (scale bar at 2 μm).

The use of mixed polar dispersion mediums proved to be effective in the case of the top-down route.

- The addition and gradual increase of 2-propanol percentage resulted in the development of rounded Ca(OH)_2 nanoparticles.

- The addition of acetone and ethanol resulted in the presence of agglomerates. Finally,
- the addition 2-propanol in the case of the bottom-up synthetic route presented a direct effect on the shape of the $\text{Ca}(\text{OH})_2$ nanoparticles. Specifically, the addition of 2-propanol led to the synthesis of rounded and hexagonal $\text{Ca}(\text{OH})_2$ nanoparticles

Morphological characterization - TEM results

The TEM analysis expanded the information obtained by SEM. In specific, in the case of bottom-up synthetic route (B05_10w90isp), hexagonal 2-D $\text{Ca}(\text{OH})_2$ nanoparticles of dimensions between 120 nm to 200 nm were observed (Fig. 5.29 a and b). Also, possible microstructural changes were detected at the edge of the hexagonal $\text{Ca}(\text{OH})_2$ nanoparticle (Fig. 29a).

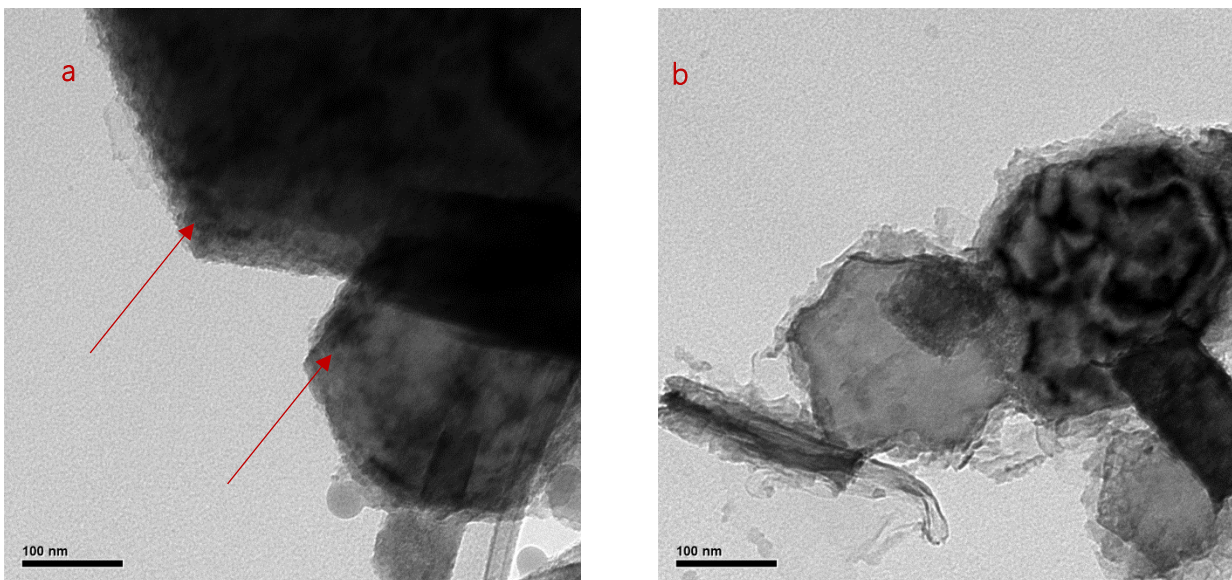
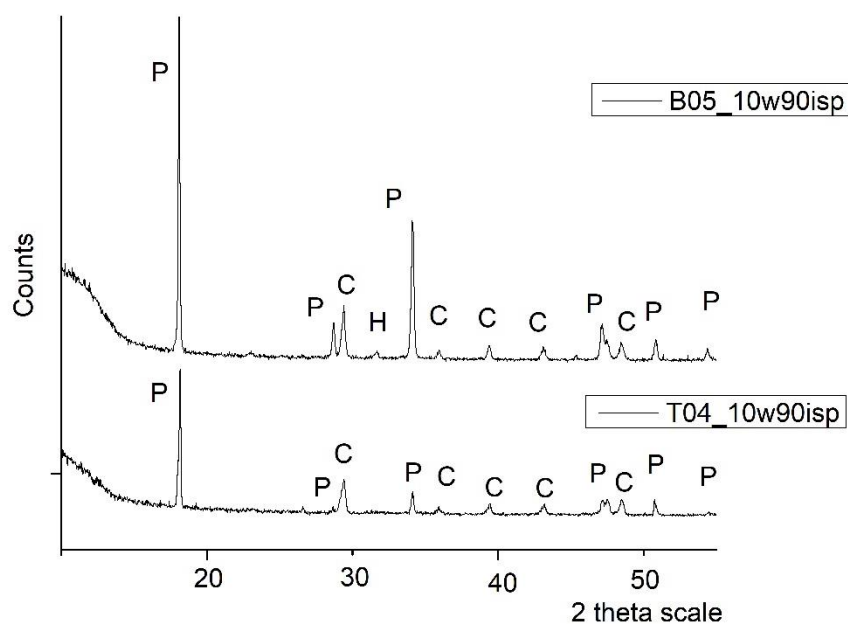


Figure 5.29 (a) Hexagonal $\text{Ca}(\text{OH})_2$ (B05_10w90isp) (scale bar at 100 nm); (b)Physisorption of the molecules of 2-propanol on to the surface of the hexagonal $\text{Ca}(\text{OH})_2$ nanoparticles (B05_10w90isp)(scale bar at 100nm)

Mineralogical characterization - XRD results

The results of the mineralogical characterization of the all four synthetic procedures were characterized by the dominant presence of portlandite $\text{Ca}(\text{OH})_2$, as indicated in the XRD diffractogram (Graph 5.17). Specifically, the presence of the major peaks $17,9^\circ$, $28,4^\circ$, $34,1^\circ$, $46,8^\circ$ and $50,6^\circ$ of portlandite of hexagonal crystals corresponding to the XRD pattern of 44-1481. Other minor phase identified was that of calcite (CaCO_3) of trigonal crystals corresponding to the XRD pattern of 5-586.



Graph 5.17 X-ray Diffraction pattern of the produced nanoparticles $\text{Ca}(\text{OH})_2$ of T04_10w90isp and B05_10w90isp

The average crystallite size for two synthesis was determined with the Scherer equation. In the case of the top-down route (T04_100w):

- the use of 100% distilled water resulted in the formation of $\text{Ca}(\text{OH})_2$ nanoparticles of average crystallite size of 37.5 nm.
- The reduction of the aqueous part to 80% distilled water and 20% of 2-propanol (T04_80w20isp) resulted in the formation of $\text{Ca}(\text{OH})_2$ nanoparticles of average crystallite size of 37.1 nm.
- The use of a 1:1 distilled water and 2-propanol (T04_50w50isp) resulted in the formation of $\text{Ca}(\text{OH})_2$ nanoparticles of average crystallite size of 41.3 nm.
- The reduction of the aqueous part to 20% distilled water and the addition of 40% of 2-propanol and 40% of acetone (T04_20w40isp40ac) resulted in the formation of $\text{Ca}(\text{OH})_2$ nanoparticles of average crystallite size of 39 nm.
- The addition of 80% of ethanol along with 20% of distilled water (T04_20w80eth) resulted in the formation of $\text{Ca}(\text{OH})_2$ nanoparticles of average crystallite size of 37.5 nm. The replacement of ethanol with 2-propanol at the same percentage (T04_20w80isp) resulted in the formation of $\text{Ca}(\text{OH})_2$ nanoparticles of average crystallite size of 37 nm.
- The increase of the percentage of 2-propanol to 90% with the addition of 10% of distilled water (T04_10w90isp) resulted in the formation of $\text{Ca}(\text{OH})_2$ nanoparticles of average crystallite size of 39.9 nm. Finally,

- the use of the same mixed polar dispersion medium (90% 2-propanol and 10% distilled water) on the bottom-up synthetic route (B05_10w90isp) resulted in the formation of Ca(OH)₂ nanoparticles of average crystallite size of 45.3 nm.

Overall, the use of mixed polar dispersion medium through the addition of 2-propanol led to the modification of the morphological characteristics of the Ca(OH)₂ nanoparticles.

The addition of 2-propanol led to the formation of rounded Ca(OH)₂ nanoparticles clusters of reduced dimensions. This was attributed to the adsorption of the molecules of 2-propanol on the surface of the Ca(OH)₂ nanoparticles forming a steric barrier.

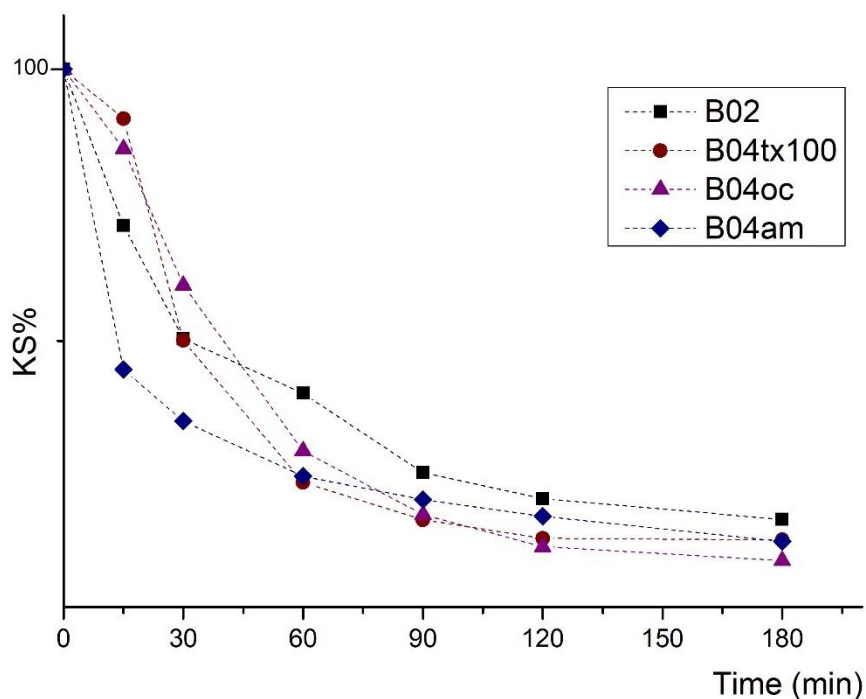
The comparative evaluation between the average crystallite size of the newly formed of the eight synthetic procedures led to the conclusion that only in the case of the bottom-up synthetic route the addition of 2-propanol had a direct effect on the average crystallite size. This could be attributed to the effect of the adsorption of the molecules of 2-propanol on the surface of the nanoparticles.

The comparative evaluation between the top-down route and the bottom-up synthetic route revealed that in the case of the bottom-up synthetic route the addition of 2-propanol led to the absence of aggregation phenomena.

5.6 Colloidal stability of Ca(OH)₂ nano-dispersions

5.6.1 Effect of the addition of surfactants

The colloidal stability of the four dispersions of Ca(OH)₂ nanoparticles was determined through the use of UV-VIS spectroscopy. As observed in Graph 5.18, there was not any notable difference in the colloidal stability between the four Ca(OH)₂ dispersions. The addition of the non-ionic surfactants of Triton x-100 (B04trx100) and n-octylamine (B04oc) resulted to an increase of the colloidal stability of the dispersions for the first 45 min, in respect to the colloidal stability of the original bottom-up synthetic route. This was attributed to the steric stabilization of the dispersions through the adsorption of the molecules onto the surface of the Ca(OH)₂ nanoparticles and the inhibition of agglomeration phenomena. This can be explained through the reported reduction of the surface tension between the Ca(OH)₂ nanoparticles and the aqueous medium. However, after this time period, the three dispersions did not present any significant difference in terms of their colloidal stability. The addition of amylamine seemed to reduce the colloidal stability of the dispersion.



Graph 5.18 KS% of the four dispersions of Ca(OH)₂ nanoparticles

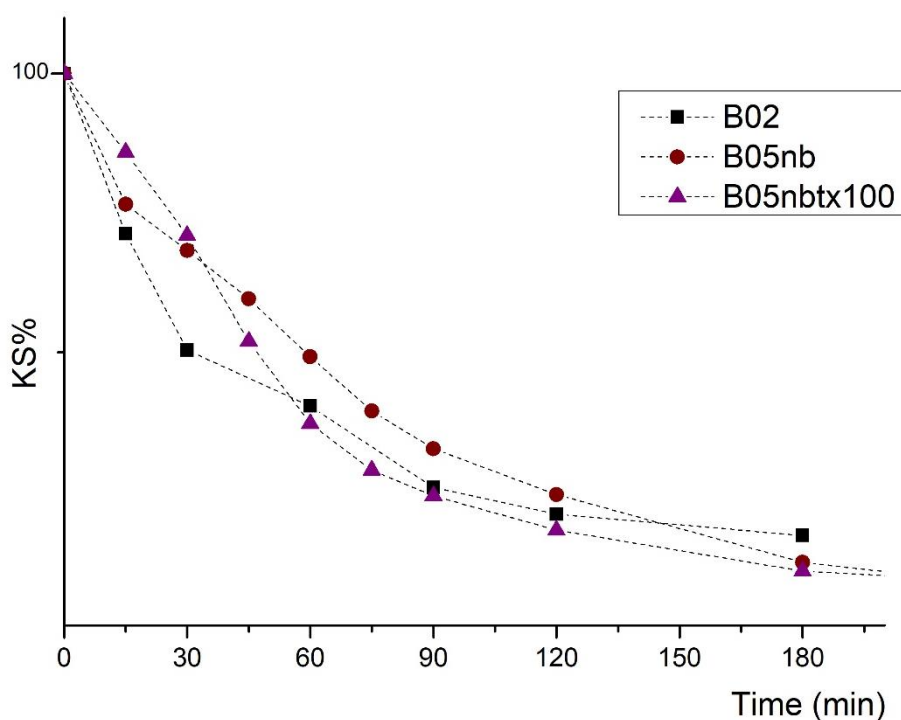
Overall, the addition of Triton X-100 proved to lead to the enhancement of the colloidal stability of the nanodispersion though the absence of agglomerates

5.6.2 Effect of modification of the dispersion medium

5.6.2.1 Effect of the use of O₂ nanobubbles enriched aqueous solution

The effect of the use of O₂ nanobubbles enriched aqueous solution on the colloidal stability of the final dispersion was implemented through the comparison of the colloidal stability of the two modifications B05nb and B05nbtx100 to the colloidal stability of the B02 of the original bottom-up synthetic route.

The use of O₂ nanobubbles (nbs) enriched water as dispersion medium in the bottom-up synthetic route (B05nb) and the addition of the non-ionic surfactant of Triton X-100 (b05nbTX100) **resulted to an increase of the colloidal stability of the dispersions for the first 45 min** in respect to the colloidal stability of the original bottom-up synthetic route (Graph 5.19). This was attributed to the steric stabilization of the dispersion medium and the inhibition of agglomeration phenomena. This can be interpreted though the reported reduction [4] of the surface tension between the Ca(OH)₂ nanoparticles and the aqueous medium. But after this time period, the three dispersions did not present any significant difference in terms of their colloidal stability.



Graph 5.19 KS% of the three dispersions of $\text{Ca}(\text{OH})_2$ nanoparticles B02, B05nb and B05nbt100

5.6.2.2 Effect of modification of the dispersion medium

The effect of the modification of the dispersion medium on the colloidal stability of the final dispersion was implemented through the comparative evaluation of the colloidal stability of the eight dispersions of T04_100w, T04_80w20isp, T04_50w50isp, T04_20w40isp40ac, T04_20w80eth, T04_20w80isp, T04_10w90isp and B05_10w90isp.

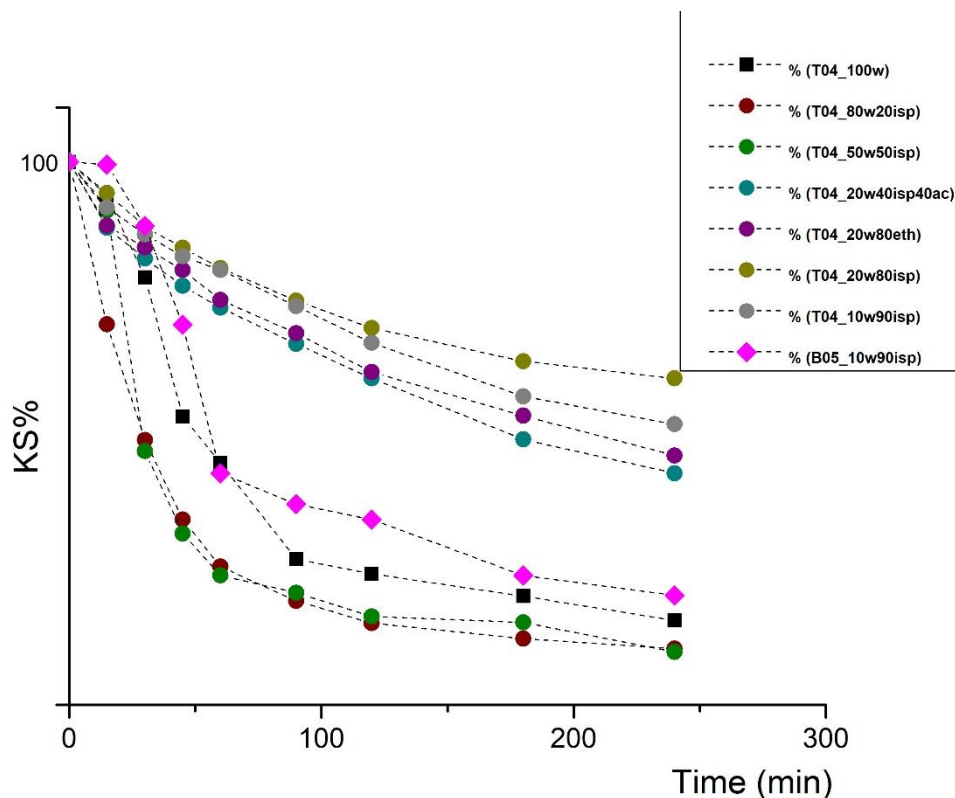
As observed in Graph 5.20, the addition and gradual increase of the 2-propanol percentage in the cases of T04_20w40isp40ac, T04_20w80eth, T04_20w80isp, T04_10w90isp led to the increase of the colloidal stability of the dispersions of $\text{Ca}(\text{OH})_2$ nanoparticles, in respect with the original aqueous dispersion T04_100w.

The comparative analysis among the four dispersions revealed that the use of a mixed polar dispersion medium of 20% water and 80% 2-propanol led to the higher increase of the colloidal stability of the dispersion. This was attributed to the steric stabilization of the dispersion medium and the inhibition of agglomeration phenomena. This can be attributed to the reported reduction of the surface tension between the $\text{Ca}(\text{OH})_2$ nanoparticles and the polar dispersion medium.

The use of ethanol and acetone did not lead to an enhancement of the colloidal stability of the dispersion, in relation with the effect of 2-propanol. In the case of the top-down route, the small reduction of the percentage of water and the addition of 2-propanol, in the cases of T04_80w20isp, T04_50w50isp led to the reduction of the colloidal stability of the

dispersions of $\text{Ca}(\text{OH})_2$ nanoparticles. This is considered as an indication that the small percentage of 2-propanol was not sufficient to increase the steric stabilization of the dispersion.

Finally, the use of a mixed polar dispersion medium of 10% water and 90% between the top-down route (T04_10w90isp) and the bottom-up synthetic route (B05_10w90isp), underlined the higher colloidal stability of the dispersions of $\text{Ca}(\text{OH})_2$ nanoparticles produced through the top-down route.



Graph 5.20 KS% of the eight dispersions of $\text{Ca}(\text{OH})_2$ nanoparticles

Overall, the addition of 2-propanol in relation with the addition of distilled water, acetone and ethanol had a direct effect on the increase of the colloidal stability of the dispersions of the $\text{Ca}(\text{OH})_2$ nanoparticles. In specific, the adsorption of the molecules of 2-propanol on the surface of the newly formed $\text{Ca}(\text{OH})_2$ nanoparticles led to the realization of the steric stabilization of the dispersions and the absence of agglomeration phenomena.

5.7 Development of the Si-Ca(OH)₂ nanocomposites

5.7.1 Sol-gel methodology

The Ca(OH)₂ nanoparticles produced by the top-down synthesis was incorporated in the TEOS matrix by the one pot synthesis. The study of mixing process during the one pot synthesis via the sol-gel method was focused on the morphological characteristics of the produced composite. The results showed that only at the fourth stage of the synthetic route (C-S_01s-g stage d) there was an obvious change related to the mixing of the calcium hydroxide nanoparticles in TEOS (Fig. 5.30b-d).

Morphological characterization - SEM analysis

At the beginning of the incorporating procedure, the presence of spherical particles was attributed to the silicatic component (Fig 5.30b), following the comparison with the morphological characteristics of nanolime obtained by the top-down methodology presented in Fig.5.27a. The absence of those spherical particles (Fig. 5.30c) and the presence of film that covers the conglomerated of the Ca(OH)₂ (Fig. 5.30d) was attributed to the polymerization reaction of TEOS. The mixing was closely connected with the activation of the stage of hydrolysis of the polymerization reaction of TEOS in the basic environment. Finally, the observation of the results after a time period of two years revealed the morphological characteristics of the final product. In specific, the final product of the experimental procedure was consisted of spherical nanoparticles of dimensions between 102 nm and 140 nm (Fig. 5.30e).

Mineralogical characterization - XRD results

Regarding the incorporation of Ca(OH)₂ into TEOS, the X-ray diffraction analysis indicated (Graph 5.21a) the reduction of portlandite peaks through the three stages of the one pot process, until the elimination of portlandite and the weak appearance of calcite. The detection of the potential reaction products between Ca(OH)₂ and TEOS by XRD was difficult, due to the lack of ordered structures, the presence of calcite at the end of fourth day (final stage) of the reaction (C-S_01s-g stage d) underlined the realization of the carbonation reaction. In fact, the realization of the carbonation reaction proved to be favored, instead of the potential formation of calcium-silicate-hydrate (C-S-H) phases. The reduced intensity of the peaks was connected to the hydrolysis and polymerization of TEOS, thus the formation of a solid phase around the calcite nanoparticles. The mineralogical analysis of final product of the experimental procedure after two years revealed the calcium-silicate-hydrate (C-S-H) phase. In addition to this, the intensity of the peaks could be an indication of the crystallinity of the C-S-H phase (Graph 5.21b).

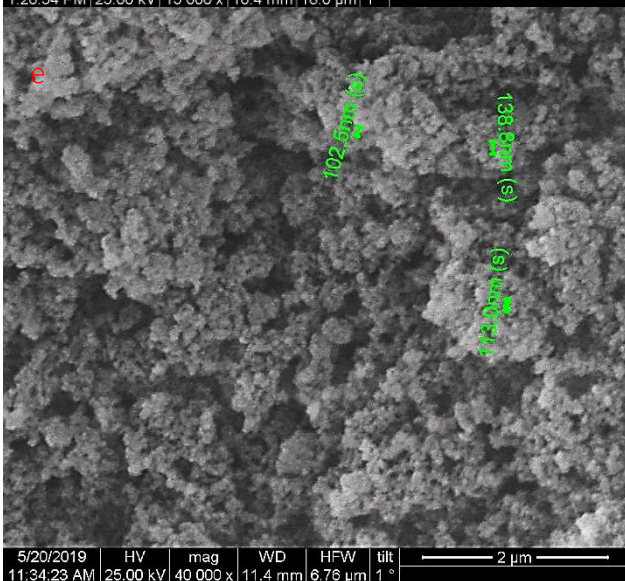
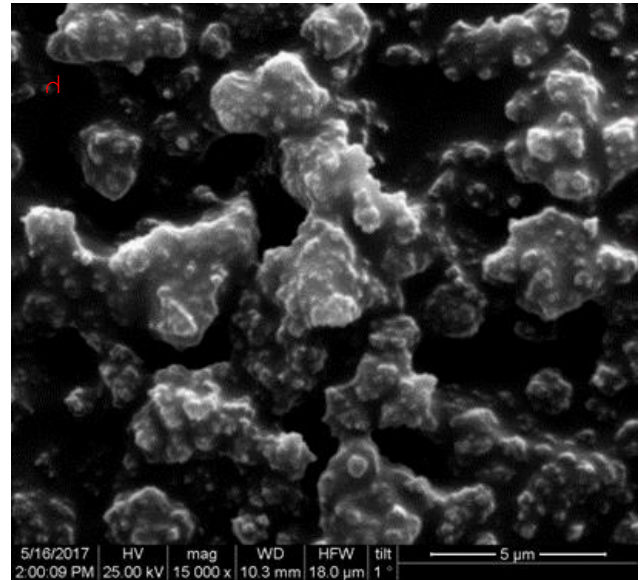
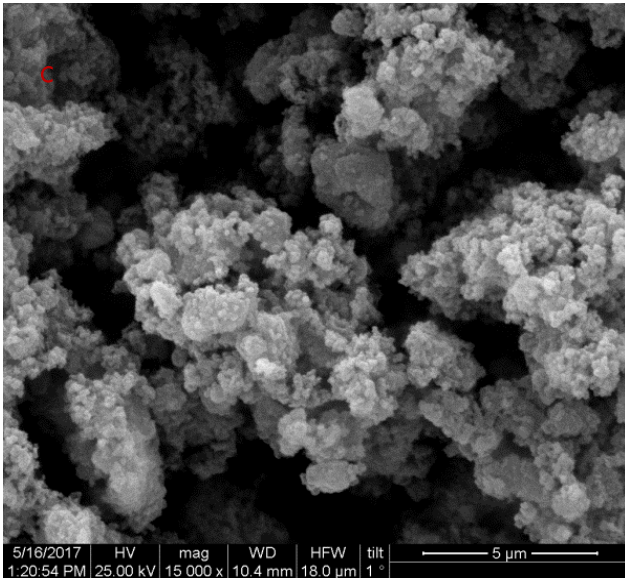
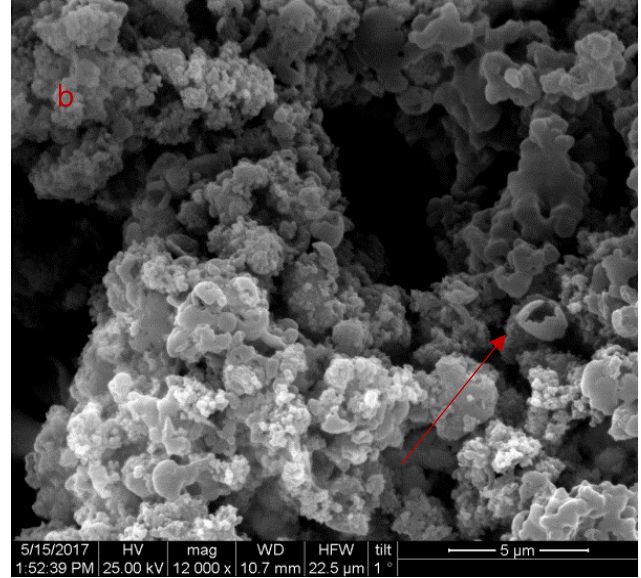
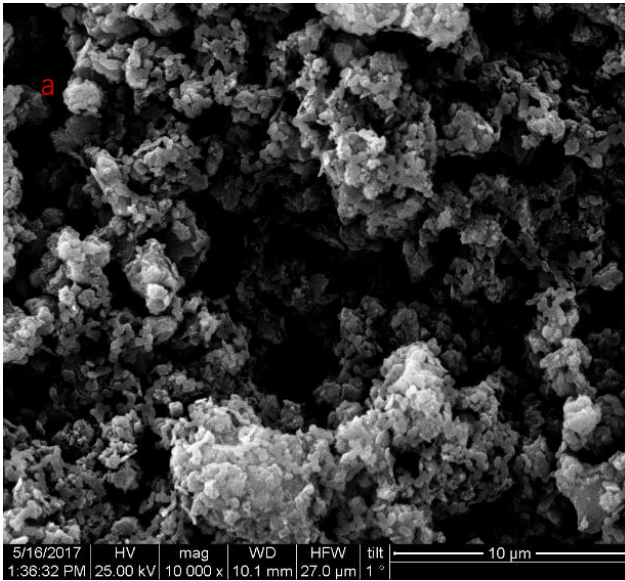
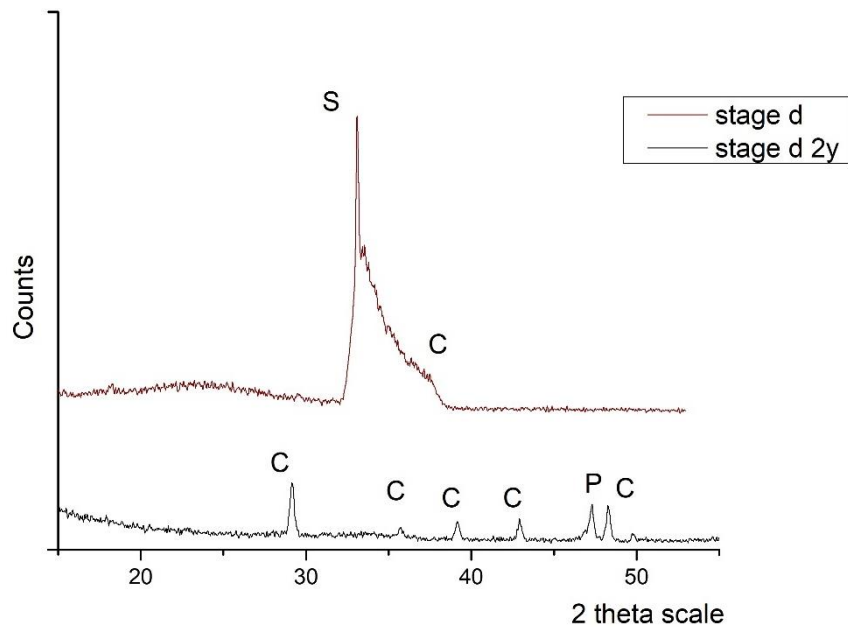
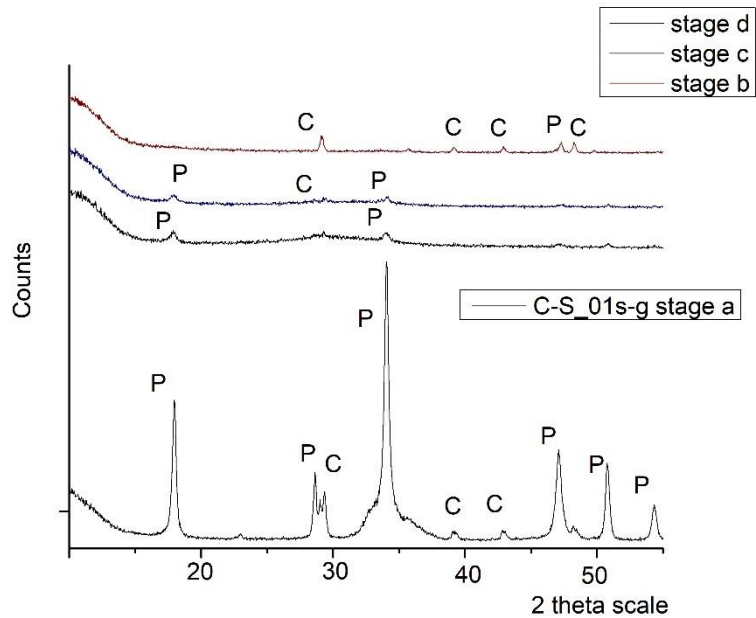


Fig. 5.27 Clusters of: (a) $\text{Ca}(\text{OH})_2$ nanoparticles resulted from the top-down methodology (C-S_01s-g stage a)(scale bar at $10\mu\text{m}$); (b) Conglomerates of nanoparticle of calcium hydroxide nanoparticles of regular, rounded and angular shape and spherical particles of silicate nature (C-S_01s-g stage b) (scale bar at $5\mu\text{m}$); (c) Conglomerates of nanoparticles of calcium hydroxide nanoparticles of undetermined shape (C-S_01s-g stage c) (scale bar at $5\mu\text{m}$); (d) Conglomerates of calcium hydroxide nanoparticles with hydrolyzed TEOS (C-S_01s-g stage d) (scale bar at $5\mu\text{m}$); and (e) Spherical nanoparticles of dimensions between 102 nm and 140 nm (C-S_01s-g stage e) (scale bar at $2\mu\text{m}$)



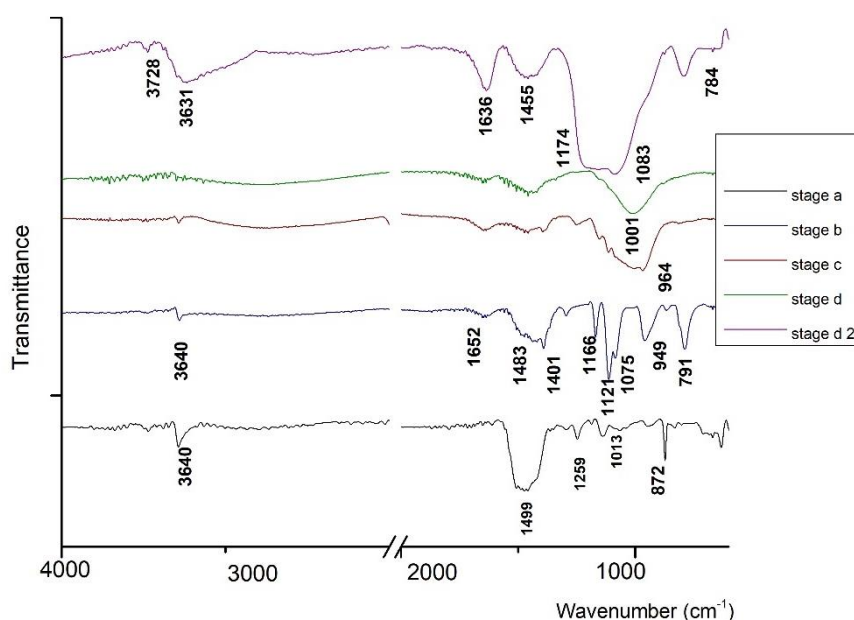
Graph 5.21 (a).Representative X-ray Diffraction pattern of the produced particles of the top-down methodology and comparative analysis of the X-ray Diffraction pattern of the three stages $\text{Ca}(\text{OH})_2$ nanoparticles incorporated in TEOS and (b) Comparative evaluation of the final product after a time period of two years

Chemical Characterization - FTIR results

The FTIR spectrum of nanoparticles produced through the top-down methodology (Graph 5.22) verified the presence of portlandite and calcite already identified in mineralogical analysis. In particular, FTIR spectrum (Graph 5.23) presented a strong and sharp band at 3640 cm^{-1} corresponding to the OH^- stretching modes. The band was characteristic of portlandite. The presence of calcite was verified by the broad band centered at 1499 cm^{-1} , corresponding to the ν_2 symmetric deformation of the carbonates $-\text{CO}_3^{2-}$, 872 cm^{-1} and 791 cm^{-1} , corresponding to the ν_3 asymmetric stretching of the carbonates $-\text{CO}_3^{2-}$.

The bands at 1166 , 1121 and 1075 cm^{-1} corresponding to the stretching of the Si-O-Si bond, along with the bands 949 and 791 cm^{-1} (corresponding to the stretching of the Si-O bond) were attributed to the presence of TEOS [196]. The bands at 1652 cm^{-1} , 1483 cm^{-1} and 1401 cm^{-1} were attributed to isopropanol. The gradual reduction until disappearance of the band at 3640 cm^{-1} at the final stage and the simultaneous disappearance of the characteristic band of TEOS at 1121 , 11075 and 949 cm^{-1} was an indication of the mixing of $\text{Ca}(\text{OH})_2$ in the silica gel [196].

After a time period of two years, the presence of the C-S-H was also verified by the interpretation of the FTIR spectra. In specific, the widening of the Si-O asymmetric stretching vibrations in the C-S-H gel at 1174 and 1083 cm^{-1} and the absence of the 964 cm^{-1} band of the silanol group indicated the formation of the C-S-H gel [196].



Graph 5.22 Comparative analysis of the FTIR spectra of the $\text{Ca}(\text{OH})_2$ nanoparticles and the three stages of $\text{Ca}(\text{OH})_2$ nanoparticles incorporated in tetraethoxysilane (TEOS)

5.7.2 Development of Janus nanoparticles

The second experimental procedure involved an attempt for the development of Janus nanoparticles of Ca-Si composition. The non-ionic surfactant Triton X-100 was added for the functionalization of the produced nanocomposites. Three modifications were realized, based on the chemical composition of the Si-compound. The first modification (C-S02NaS-C) concerned the use of sodium silicate (waterglass). The second modification (C-S02Cel-C) concerned the use of Celitment, an innovative commercially available hydraulic binder made of . The third modification (C-S02TEOS-C) concerned the use of TEOS.

Morphological characterization - SEM results

The monitoring of the first alteration (C-S02NaS-C) revealed the domination of the flower-like morphology attributed to the use of the waterglass. Inside this formation $\text{Ca}(\text{OH})_2$ nanoparticles were observed (Fig. 5.31 a and b). After one year the presence of flower-like morphology was reduced and the presence of conglomerates was evident (Fig. 5.31c).

The monitoring of the second alteration (C-S02Cel-C) revealed the presence of large conglomerates consisted of $\text{Ca}(\text{OH})_2$ nanoparticles of dimension between 120 nm and 250 nm. The presence of film that covered the conglomerates of the $\text{Ca}(\text{OH})_2$ (Fig. 5.32a) was attributed to the hydration procedure of celitement (Fig. 5.32 a and b). After one year the presence of compact material consisted of flake -like formations and $\text{Ca}(\text{OH})_2$ nanoparticles was evident (Fig. 5.32c).

Finally, the monitoring of the third alteration (C-S02TEOS-C) revealed the presence of large conglomerates consisted of $\text{Ca}(\text{OH})_2$ nanoparticles of dimension between 88 nm and 180 nm, as two separate phases (Fig. 5.33 a and b). *After one year* the presence of flower-like morphology was evident (Fig. 5.33c).

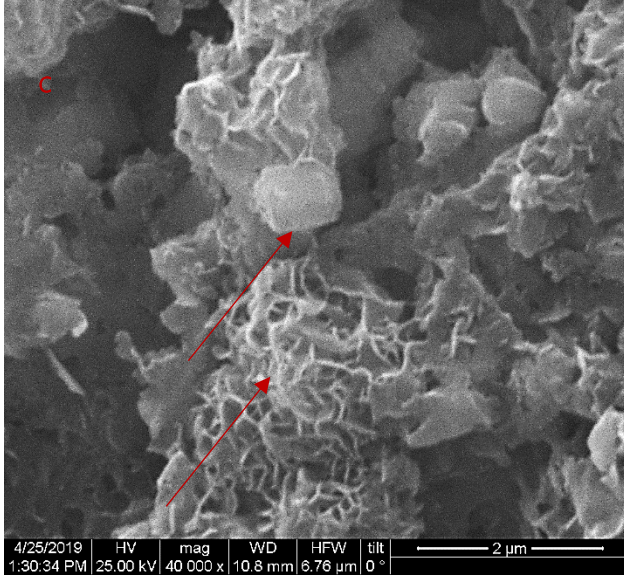
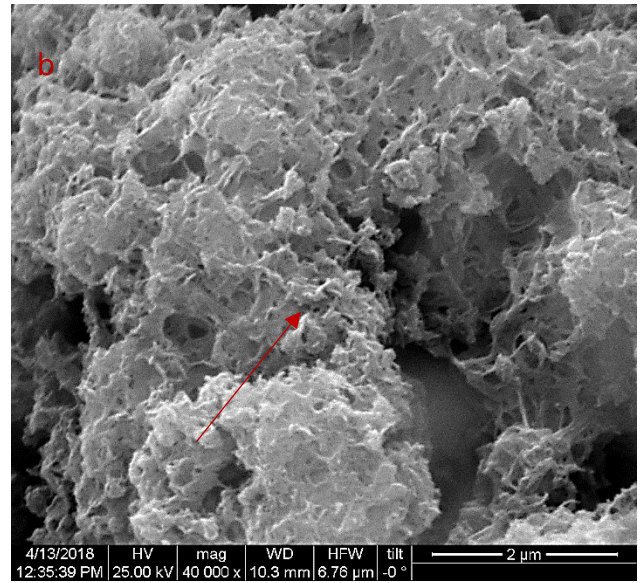
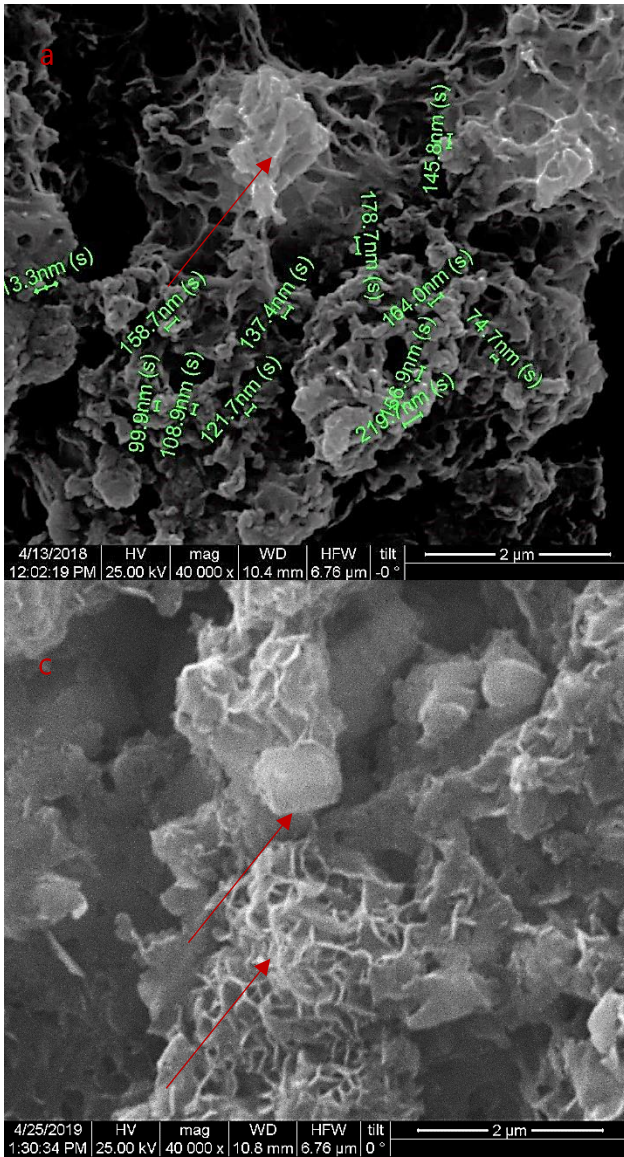


Fig. 5.31 Clusters of: (a) Flower-like morphology (C-S02NaS-C stage a) (scale bar at 2 μ m); (b) Flower-like morphology (C-S02NaS-C stage d) (scale bar at 2 μ m); and (c) Presence of flower-like morphology was reduced and the presence of conglomerates(C-S02NaS-C stage d 1y)(scale bar at 2 μ m)

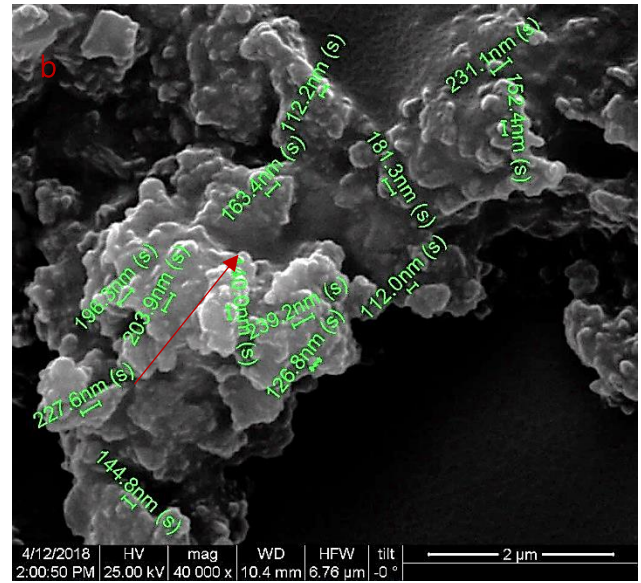
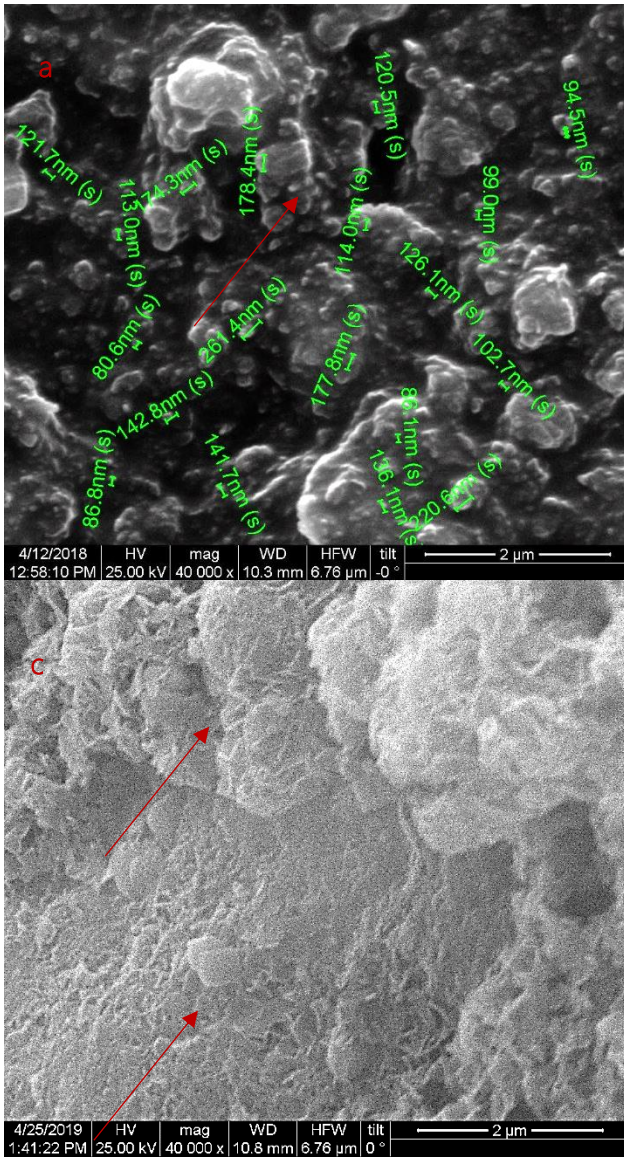


Fig. 5.32 Clusters of: (a) Large conglomerates consisted of $\text{Ca}(\text{OH})_2$ nanoparticles of dimension between 120 nm and 250 nm (C-S02Cel-C stage a) (scale bar at $2\mu\text{m}$); (b) Conglomerates consisted of $\text{Ca}(\text{OH})_2$ nanoparticles (C-S02Cel-C stage d) (scale bar at $2\mu\text{m}$); and (c) Compact material consisted of flake-like formations and $\text{Ca}(\text{OH})_2$ nanoparticles (C-S02Cel-C stage d 1y)(scale bar at $2\mu\text{m}$)

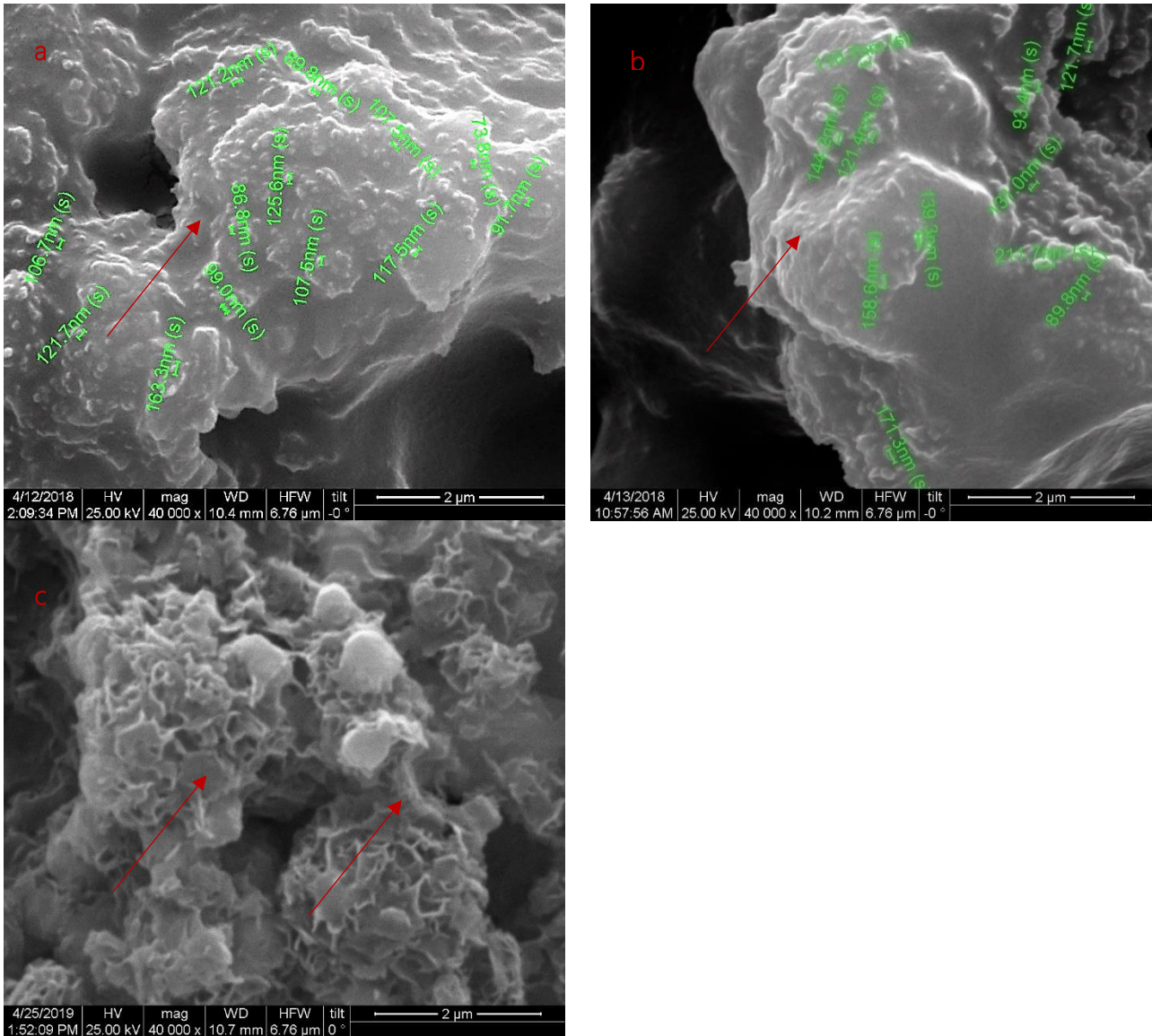


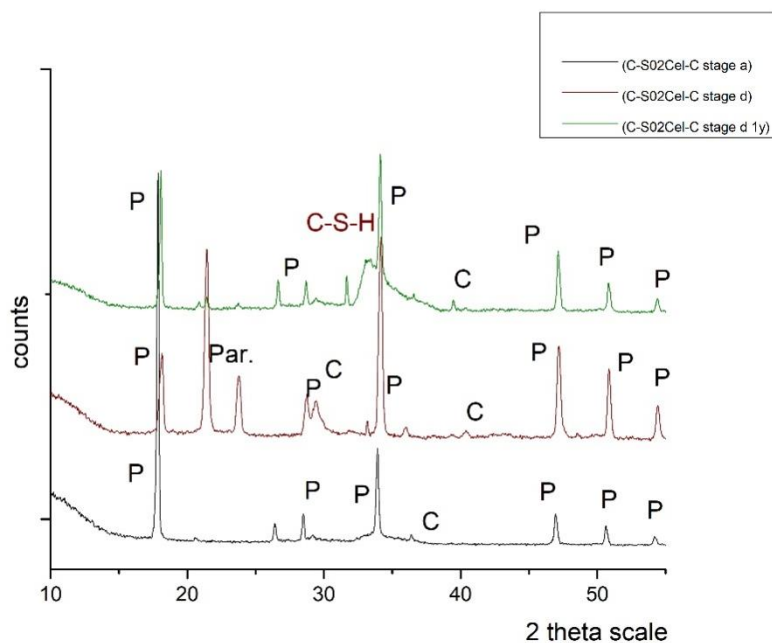
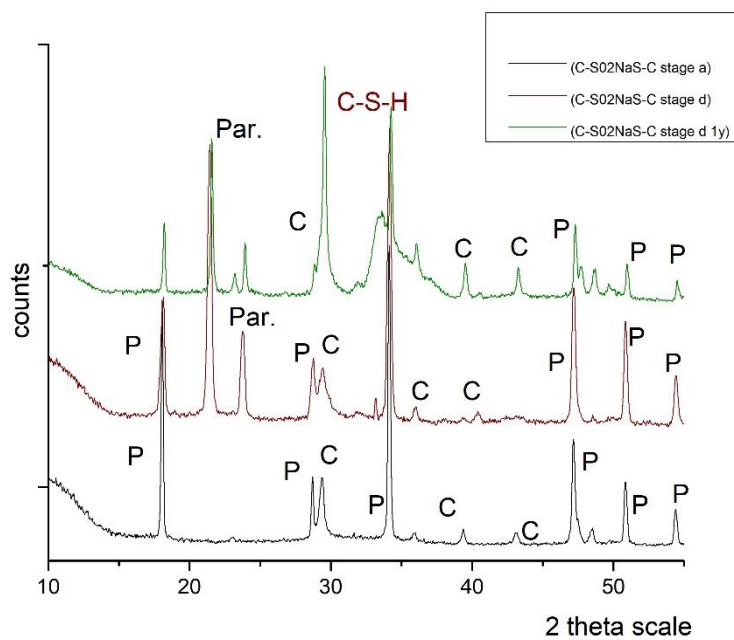
Fig. 5.33 Clusters of: (a) Large conglomerates consisted of Ca(OH)₂ nanoparticles of dimension between 88 nm and 180 nm (C-S02TEOS-C stage a) (scale bar at 2μm); (b) Large conglomerates consisted of Ca(OH)₂ nanoparticles (C-S02TEOS-C stage d) (scale bar at 2μm); and (c) Presence of flower-like morphology was reduced and the presence of conglomerates (C-S02TEOS-C stage d 1y) (scale bar at 2μm)

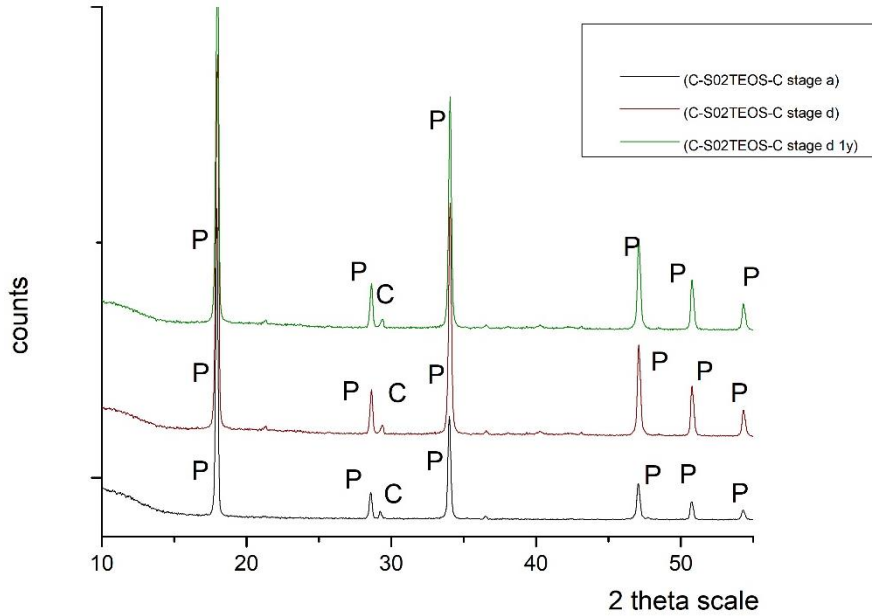
Mineralogical characterization - XRD results

The results of the mineralogical characterization of the all four synthetic procedures were characterized by the dominant presence of portlandite Ca(OH)₂, as indicated in the XRD diffractogram (Graph 5.23 a, b and c). Specifically, the presence of the major peaks 18,1°, 28,5°, 34,1°, 46,7° and 50,7° of portlandite of typical hexagonal crystals. corresponding to the XRD pattern of 44-1481. Other minor phase identified was that of calcite (CaCO₃) of rhombohedral crystals corresponding to the XRD pattern of 5-586.

Regarding the detection of the fabrication of the Ca-Si nanocomposite, the X-ray diffraction analysis indicated (Graph 5.23a and b) the appearance of the minor peak at 33,1° corresponding to the appearance of the C-S-H phase at the final stage of the experimental

procedure of the first two alterations (C-S02NaS-C and C-S02Cel-C). After a time period of one year, the intensity of the corresponding peak was higher, confirming the presence of the C-S-H phase and thus the fabrication of the nanocomposite in the first two alterations. Contrary to this, in the third application (C-S02Cel-C) the C-S-H phase was not detected. This was attribute to the completion of the polymerization of TEOS without any interaction with the $\text{Ca}(\text{OH})_2$ nanoparticles (Graph 5.23c).





Graph 5.23 (a). Representative X-ray Diffraction pattern of the stages of C-S02NaS-C (b). Representative X-ray Diffraction pattern of the stages of C-S02Cel-C and (c). Representative X-ray Diffraction pattern of the stages of C-S02TEOS-C

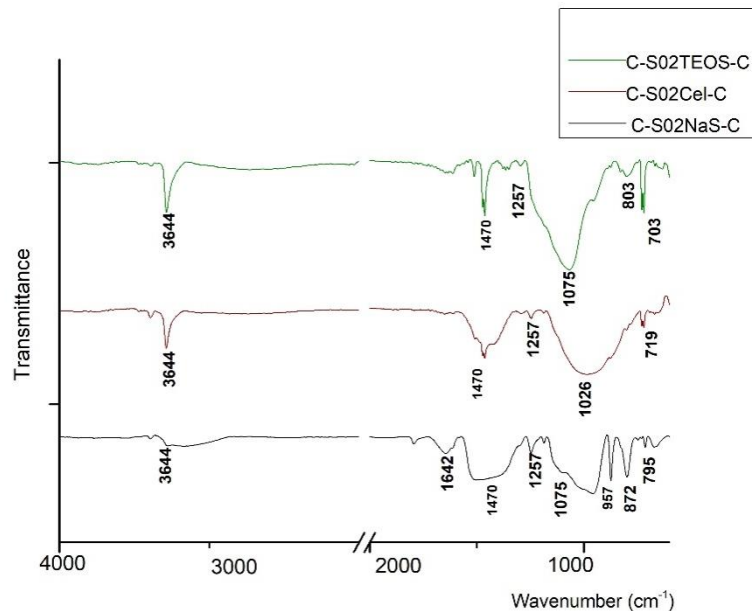
Chemical characterization - FTIR results

The FTIR spectrum of produced nanocomposites after one year (Graph 5.24) for all three alterations (C-S02NaS-C, C-S02Cel-C and C-S02TEOS-C) verified the presence of portlandite and calcite already identified in mineralogical analysis. In particular, the FTIR spectrum of the first alteration (C-S02NaS-C) presented a strong and sharp band at 3644 cm^{-1} corresponding to the OH^- stretching modes of portlandite. The presence of calcite was verified by the broad band centered at 1479 cm^{-1} corresponding to the ν_2 symmetric deformation of the carbonates $-\text{CO}_3^{2-}$ and the 872 cm^{-1} corresponding to the ν_3 asymmetric stretching of the carbonates $-\text{CO}_3^{2-}$. The bands at 1642 and 1440 cm^{-1} were attributed to isopropanol. The band of 967 cm^{-1} corresponded to the silanol group. The presence of the C-S-H was also verified by the widening of the Si-O asymmetric stretching vibrations in the C-S-H gel at 1075 cm^{-1}

The FTIR spectrum of the second alteration (C-S02Cel-C) presented a strong and sharp band at 3644 cm^{-1} corresponding to the OH^- stretching modes of portlandite. The presence of calcite was verified by the broad band centered at 1470 cm^{-1} corresponding to the ν_2 symmetric deformation of the carbonates $-\text{CO}_3^{2-}$ and the 719 cm^{-1} (corresponding to the ν_3 asymmetric stretching of the carbonates $-\text{CO}_3^{2-}$). The presence of the C-S-H was verified by the widening of the Si-O asymmetric stretching vibrations in the C-S-H gel at 1075 cm^{-1} and the absence of the 964 cm^{-1} band of the silanol group indicated the formation of the C-S-H gel.

Finally, the FTIR spectrum of the third alteration (C-S02TEOS-C) presented a strong and sharp band at 3644 cm^{-1} corresponding to the OH^- stretching modes of portlandite. The

presence of calcite was verified by the broad band centered at 1479 cm^{-1} corresponding to the ν_2 symmetric deformation of the carbonates $-\text{CO}_3^{2-}$ and 803 cm^{-1} corresponding to the ν_3 asymmetric stretching of the carbonates $-\text{CO}_3^{2-}$. The bands at 1076 cm^{-1} corresponding to the stretching of the Si-O-Si bond along with the bands 940 cm^{-1} and 703 cm^{-1} corresponding to the stretching of the Si-O bond were attributed to the presence of TEOS [196].



Graph 5.24 Comparative analysis of the FTIR spectra of the final stage of the three modifications after a time period of one year

5.7.3 Development of Si-Ca(OH)₂ nanocomposites through the Stöber reaction

The third experimental procedure involved the synthesis of Ca-Si nanocomposites through the implementation of the Stöber reaction with the addition of dispersion of Ca(OH)₂ nanoparticles.

Morphological characterization - SEM results

The completion of the original Stöber reaction (C-S_03st) resulted in the formation of spherical nanoparticles of SiO₂ of homogenous shape and size. The dimensions of spherical nanoparticles of SiO₂ varied between 143 nm to 152 nm (Fig. 5.31 a).

The implementation of the Stöber reaction with the addition of dispersion of Ca(OH)₂ nanoparticles synthesized via the bottom-up synthetic route (C-S_03stb) resulted in the synthesis of spherical nanoparticles of SiO₂ of dimensions between 140 nm to 150 nm. The presence of Ca(OH)₂ nanoparticles was also identified (Fig. 5.34b).

Finally, the implementation of the Stöber reaction with the addition of dispersion of Ca(OH)₂ nanoparticles synthesized via the top-up synthetic route (C-S_03stt) resulted in the synthesis

of spherical nanoparticles of SiO_2 of dimensions between 140 nm to 15 nm. The presence of $\text{Ca}(\text{OH})_2$ nanoparticles was also identified (Fig. 5.31 c). The unsuccessful incorporation of $\text{Ca}(\text{OH})_2$ nanoparticles inside the SiO_2 nanospheres was attributed to the difference in the size between the nanoparticles and the nanospheres.

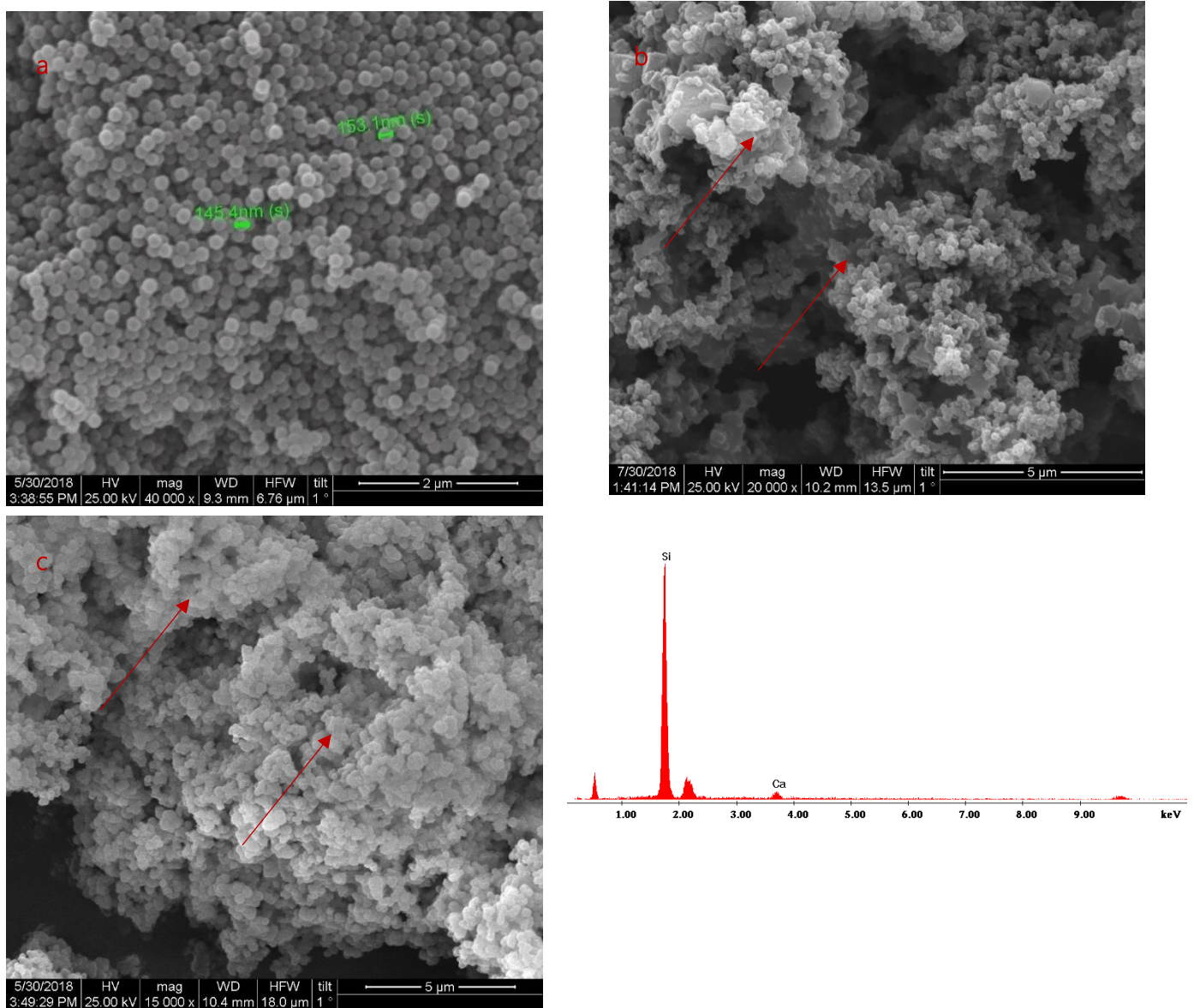


Figure 5.34 Clusters of: (a) Spherical nanoparticles of SiO_2 (C-S_03st)(scale bar at 2μm); (b) Spherical nanoparticles of SiO_2 and $\text{Ca}(\text{OH})_2$ nanoparticles (C-S_03stb)(scale bar at 5μm); (c) Spherical nanoparticles of SiO_2 and $\text{Ca}(\text{OH})_2$ nanoparticles (C-S_03st) (scale bar at 5μm); and (d) EDAX analysis of C-S_03st.

Overall, the successful synthesis of the Ca-Si nanocomposites was implemented via two methodologies:

- One pot synthesis via sol-gel methodology with Ca(OH)_2 and TEOS as initial reagents
- Development of janus nanoparticles with Ca(OH)_2 and waterglass or celitement as initial reagents

The synthesis of the Ca-Si nanocomposites was verified through the detection of the C-S-H bond after a time period of at least one year.

Chapter 6- Optimized dispersions of Ca(OH)₂ nanoparticles

6.1 Introduction

The interpretation of the results presented in Chapters 6 revealed the effect of different parameters on the morphological characteristics of the newly synthesized Ca(OH)₂ nanoparticles and the colloidal stability of their dispersions.

The comparative evaluation of the results underlined the beneficial effect of the reduction of surface tension between the Ca(OH)₂ nanoparticles and the dispersion medium on the morphological characteristics of the Ca(OH)₂ nanoparticles through:

- a) The functionalization of the surface of the Ca(OH)₂ nanoparticles with the addition of Triton X-100*
- b) The use of O₂ nanobubbles (nbs) enriched aqueous solution as dispersion medium*
- c) The use of a mixed polar dispersion medium, consisted of water and 2-propanol mixed solution*

Furthermore, the addition of 2-propanol increased the rheological stability of the dispersions. On this basis, the six Ca(OH)₂ dispersions presented in this chapter were synthesized (Table 6.1), taking into account the optimum conditions of all past experiments.

The dispersions were synthesized via the bottom-up synthetic route, in inert He-conditions, using probe sonication for the de-agglomeration of the Ca(OH)₂ nanoparticles.

The characterization of Ca(OH)₂ nanoparticles was implemented by the use of SEM, TEM, DLS and SSA evaluation (BET method). Moreover, the newly synthesized nanoparticles were characterized mineralogically through XRD. The colloidal stability of the dispersions was implemented by the use of UV-VIS spectroscopy.

Moreover, this chapter contains the results concerning the carbonation process of the newly formed Ca(OH)₂ nanoparticles. The study of the carbonation process was focused on the effect of the RH% conditions on the end-up product of the carbonation reaction. The implementation of this task was based on the chemical (FTIR) and mineralogical (XRD) characterization of the final product.

Table 6.1 Description of the six optimum dispersions of Ca(OH)₂ nanoparticles

<i>Sample I.D.</i>	<i>Description</i>				
	<i>Method</i>	<i>Water</i> (% v/v)	<i>O₂nbs</i> <i>water</i> (% v/v)	<i>2-propanol</i> (% v/v)	<i>Triton X-100</i>
B06_100nbs	Bottom-up	0	100	0	-
B06_100nbstx100	Bottom-up	0	100	0	✓
B06_50w50isptx100	Bottom-up	50	0	50	✓
B06_20nbs80isptx100	Bottom-up	0	20	80	✓
B06_20w80isptx100	Bottom-up	20	0	80	✓
T05_20w80isptx100	Top-down	20	0	80	✓

6.2 Characterization of Ca(OH)₂ nanoparticles

6.2.1 Morphological characterization of Ca(OH)₂ nanoparticles

Morphological characterization -SEM results

In the case of the **bottom-up synthetic route (B06_100nbs)**, the use of O₂ nanobubbles (nbs) enriched water resulted in the production of hexagonal and angular Ca(OH)₂ nanoparticles clusters, of dimensions in between 200 nm and 350 nm (Fig. 6.1 a), presenting random orientation.

The addition of the non-ionic surfactant Triton X-100 (B06_100nbsTx100), resulted in the production of hexagonal and undetermined shape Ca(OH)₂ nanoparticles clusters, of dimensions in between 150 nm and 300 nm (Fig. 6.1 b). Contrary to the first synthesis, the Ca(OH)₂ nanoparticles presented a preferential orientation and were characterized by uniform size and shape.

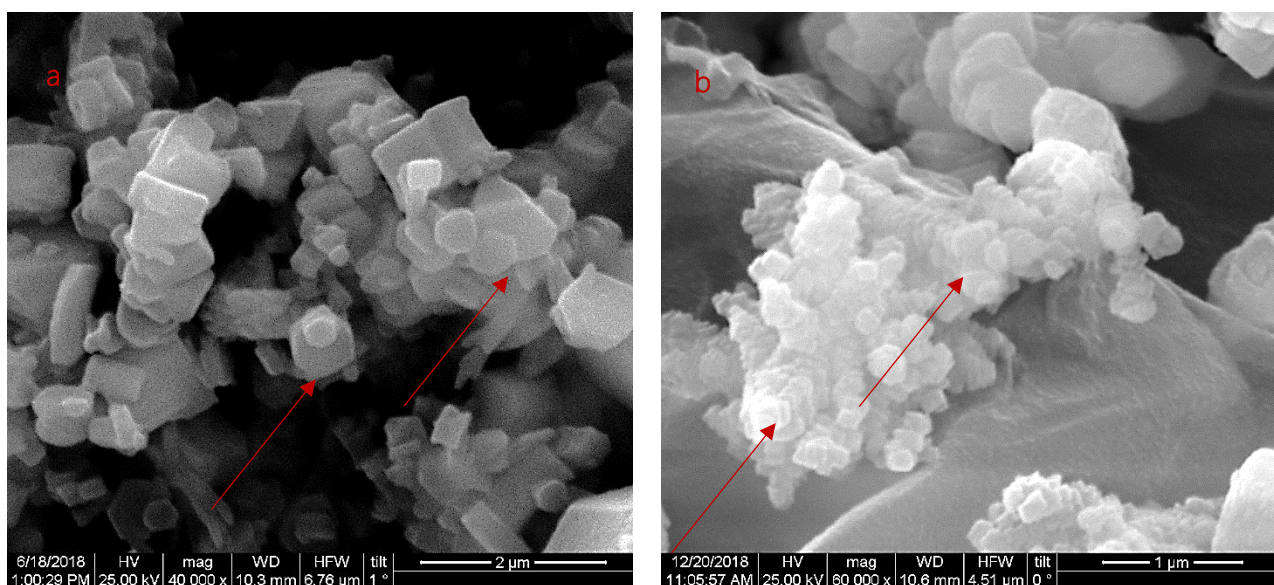


Figure 6.1 Clusters of: (a) Hexagonal and angular Ca(OH)₂ nanoparticles, of dimensions in between 200 nm and 350 nm (B06_100nbs)(scale bar at 2μm); (b) Hexagonal and undetermined shape Ca(OH)₂ nanoparticles, of dimensions in between 150 nm and 300 nm (B06_100nbsTx100)(scale bar at 1μm).

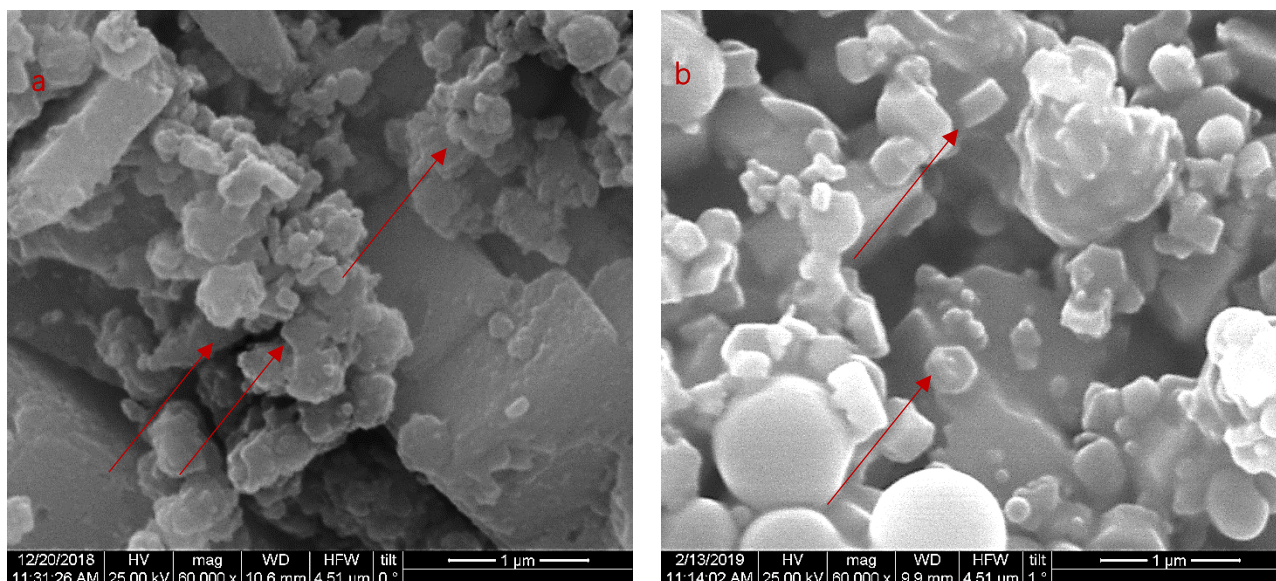


Figure 6.2 Clusters of:(a) Hexagonal, spherical and undetermined shape Ca(OH)_2 nanoparticles, of dimensions in between 250 nm and 350 nm (B06_50w50isptx100) (scale bar at 1 μm); (b) exagonal and undetermined shape Ca(OH)_2 nanoparticles, of dimensions in between 150 nm and 350 nm (B06_20nbs80isptx100) (scale bar at 1 μm).

The implementation of the bottom-up synthetic route with a 1:1 ratio of distilled water and 2-propanol mixed polar dispersion medium (B06_50w50isptx100) resulted in the production of hexagonal, spherical and of undetermined shape Ca(OH)_2 nanoparticles, of dimensions in between 250 nm and 350 nm (Fig. 6.2 a).

The use of a mixed polar dispersion medium consisted of 20% O_2 nanobubbles (nbs) enriched water and 80% 2-propanol (B06_20nbs80isptx100) resulted in the production of hexagonal and of undetermined shape Ca(OH)_2 nanoparticles, of dimensions in between 150 nm and 350 nm (Fig. 6.2 b).The newly formed Ca(OH)_2 nanoparticles presented also a relatively high width.

The use of a mixed polar dispersion medium consisted of 20% distilled water and 80% 2-propanol (B06_20w80isptx100) resulted in the production of hexagonal, rounded and of undetermined shape Ca(OH)_2 nanoparticles, of dimensions in between 200 nm and 370 nm (Fig. 6.3a).

The implementation of top-down route with the same mixed polar dispersion medium (T05_20w80isptx100) resulted in the production of hexagonal, rounded and of undetermined shape Ca(OH)_2 nanoparticles, of dimensions in between 210 nm and 380 nm (Fig. 6.3 b). Finally, the presence of larger agglomerated was a common characteristic of the results obtained by the two-last synthesis (B06_20w80isptx100 and B06_20w80isptx100).

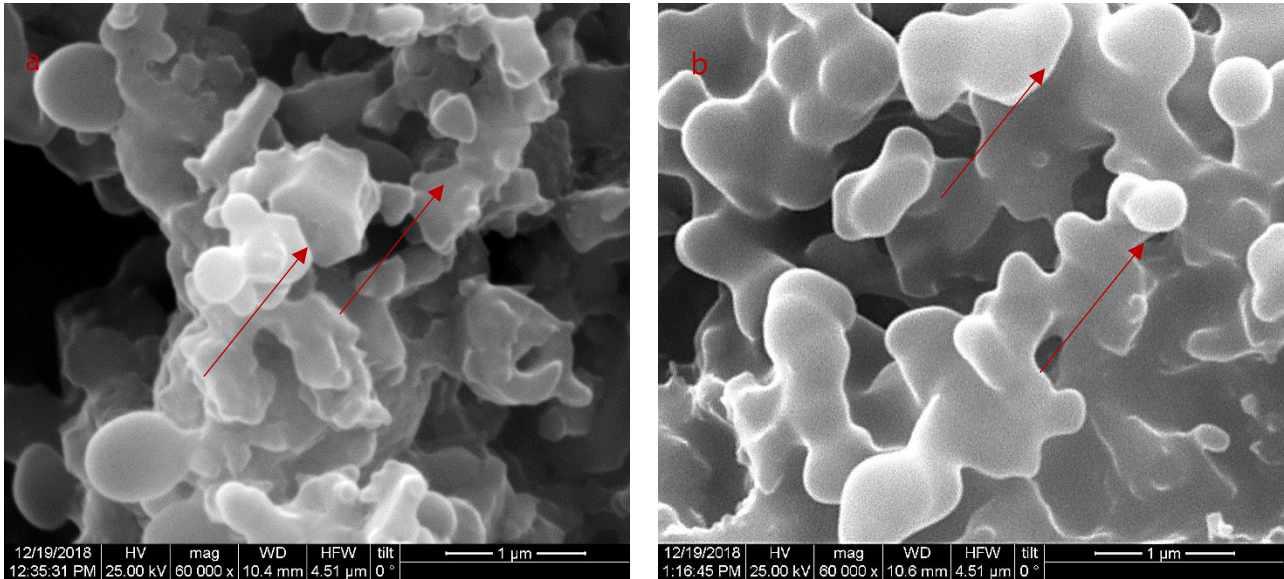


Figure 6.3 Clusters of: (a) Hexagonal, rounded and of undetermined shape $\text{Ca}(\text{OH})_2$ nanoparticles, of dimensions in between 200 nm and 370 nm (B06_20w80isptx100)(scale bar at 1 μm); (b) Hexagonal, rounded and of undetermined shape $\text{Ca}(\text{OH})_2$ nanoparticles, of dimensions in between 210 nm and 380 nm (B06_20w80isptx100) (scale bar at 1 μm).

Morphological characterization - TEM results

The TEM analysis revealed more information about the morphological characteristics of the newly formed $\text{Ca}(\text{OH})_2$ nanoparticles. In all six synthesis, the TEM analysis revealed the presence of $\text{Ca}(\text{OH})_2$ nanoparticles of dimensions between 50 nm to 100 nm.

In the case of the bottom-up synthetic route (B06_100nbs), the use of O_2 nanobubbles (nbs) enriched water resulted in production of hexagonal and plate-like 2-D $\text{Ca}(\text{OH})_2$ nanoparticles that seemed to be composed by a single nanoparticle. (Fig. 6.4 a).

The addition of the non-ionic surfactant Triton X-100 (B06_100nbsx100), resulted in production of plate-like $\text{Ca}(\text{OH})_2$ nanoparticles that seemed to be composed by smaller ones (Fig. 6.4 b). The SAED analysis confirmed that the smaller the $\text{Ca}(\text{OH})_2$ nanoparticle were monocrystalline (Fig. 6.4c). SAED analysis (Selected Area Electron Diffraction) is a crystallographic experimental technique performed inside the TEM. A parallel beam interacts with the sample and an area from which the diffraction pattern is recorded, is defined with the use of an aperture. It can be used for the determination of the crystallinity of the material. The spot patterns correspond to a single-crystal diffraction and the ring patterns to a powder diffraction from multiple crystals with variable orientations. In specific, the representation of diffuse rings is an indication of an amorphous material, the representation of bright spots is an indication of crystalline material and the representation of small spots creating a ring is an indication of a poly-crystalline material.

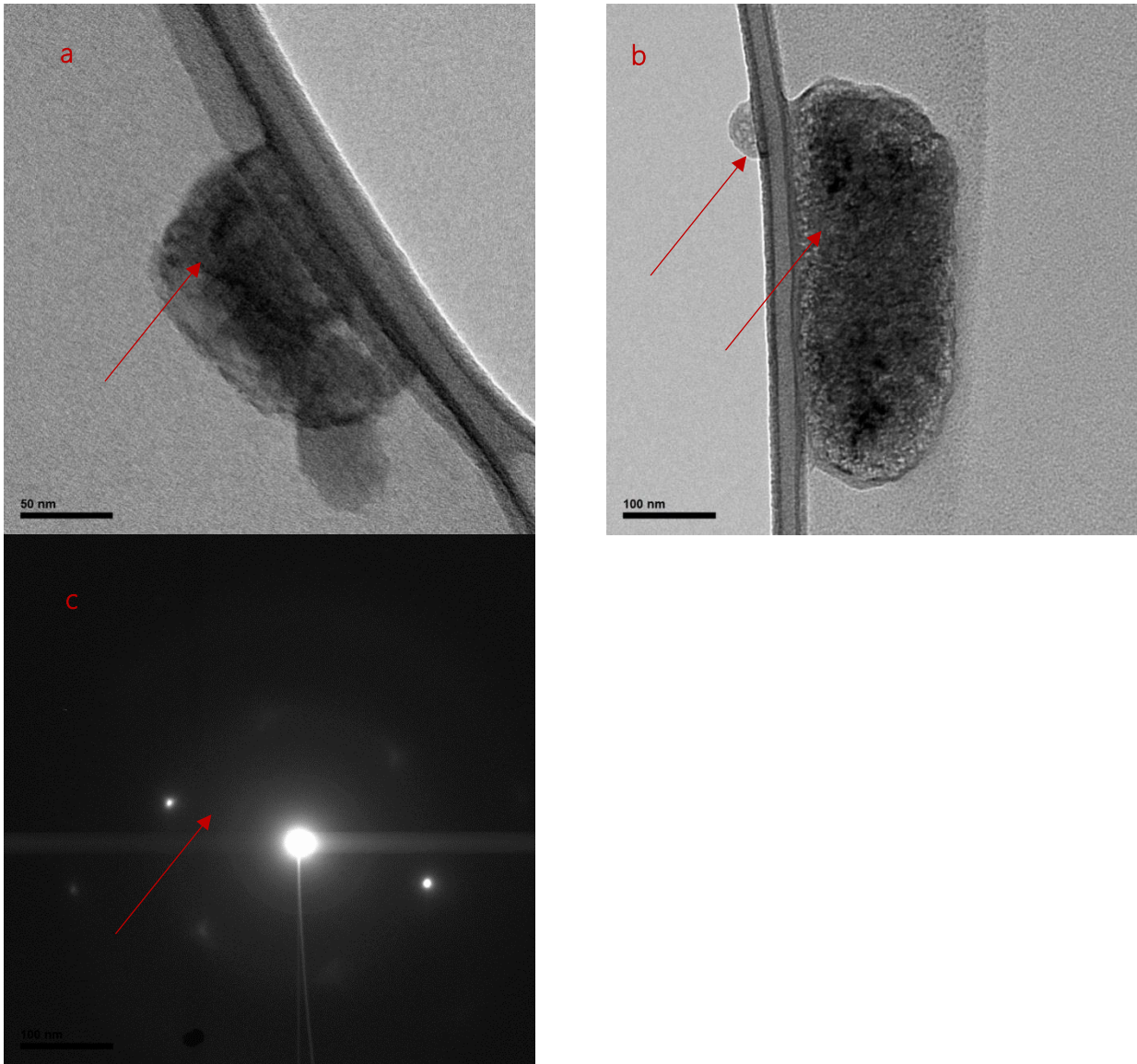


Figure 6.4 (a) Hexagonal $\text{Ca}(\text{OH})_2$ and plate-like nanoparticles (B06_100nbs) (scale bar at 50 nm); (b) Plate -like $\text{Ca}(\text{OH})_2$ nanoparticle composed by smaller ones (B06_100nbsx100)(scale bar at 100nm) and c) SAED analysis of B06_100nbsx100

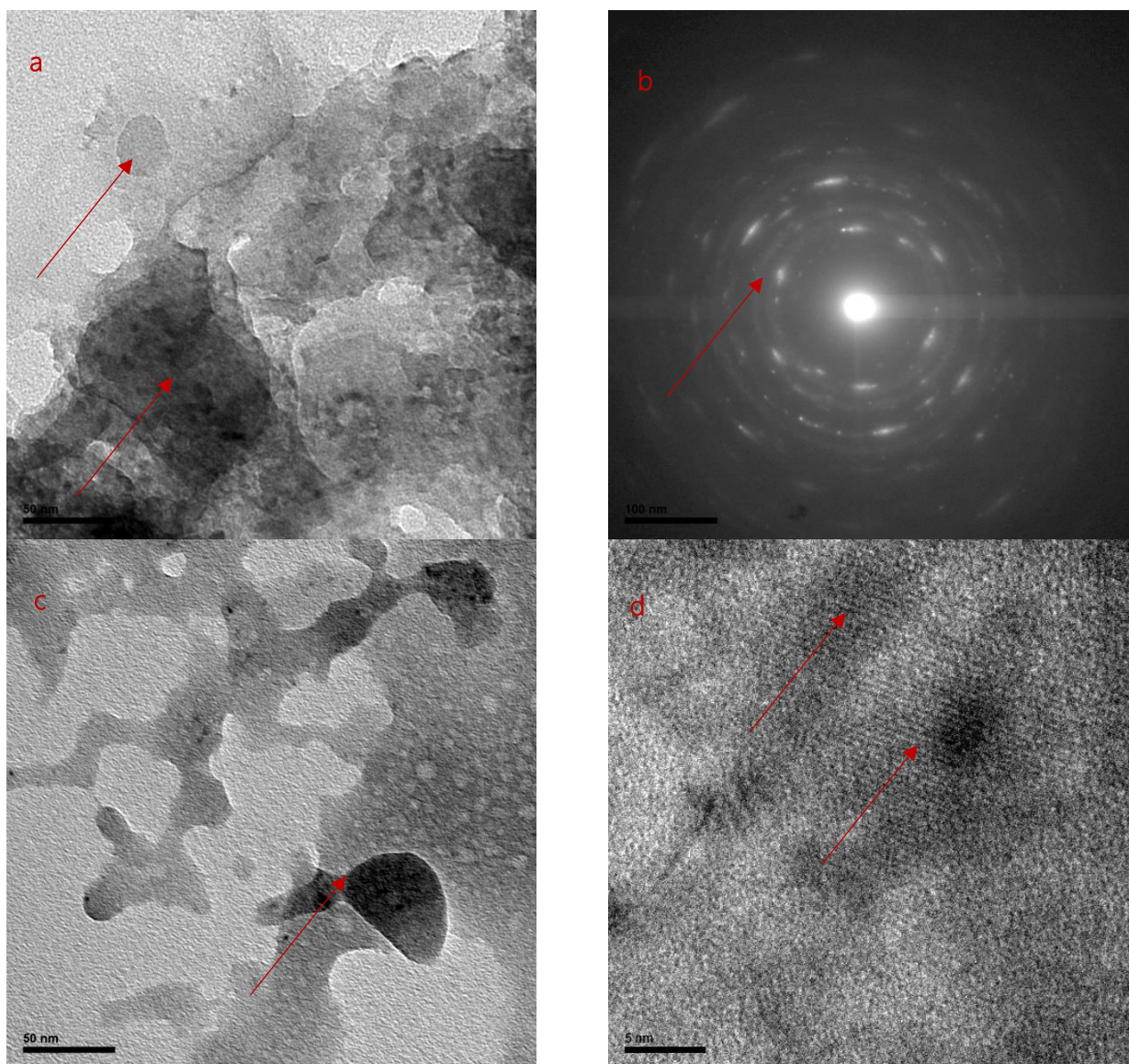


Figure 6.5 (a) Hexagonal and rounded Ca(OH)_2 nanoparticles (B06_50w50isptx100) (scale bar at 50 nm); (b) SAED analysis of B06_50w50isptx100; c) Plate-like Ca(OH)_2 nanoparticle (B06_20nbs80isptx100) (scale bar at 50 nm) and (d) oriented Moiré fringes in overlapping areas (B06_20nbs80isptx100) (scale bar at 5 nm)

The implementation of the bottom-up synthetic route with a 1:1 ratio of distilled water and 2-propanol mixed polar dispersion medium (B06_50w50isptx100) resulted in the production 2-D hexagonal and 0-D rounded Ca(OH)_2 nanoparticles (Fig. 6.5a). The rings observed through the SAED analysis of B06_50w50isptx100 were attributed to the diffraction of the polycrystalline newly formed Ca(OH)_2 nanoparticles (Fig. 6.5b), contrary to the previous synthesis (Fig. 6.4c).

The use of a mixed polar dispersion medium consisted of 20% O_2 nanobubbles (nbs) enriched aqueous solution and 80% 2-propanol (B06_20nbs80isptx100) resulted in the production plate-like Ca(OH)_2 nanoparticles (Fig. 6.5c). The presence of the Moiré fringes in overlapping areas between two nanoparticles revealed the crystallinity of the primary nanoparticles. The Moiré fringes were oriented (Fig. 6.5d). Moiré fringes are characterized

as pseudo-lattice fringes produced through the superposition of two lattices of equal or very small d spacings with a mutual orientation.

The use of a mixed polar dispersion medium consisted of 20% distilled water and 80% 2-propanol (B06_20w80isptx100) resulted in the production of 2-D hexagonal and 0-D rounded $\text{Ca}(\text{OH})_2$ nanoparticles (Fig. 6.6a). The presence of the Moiré fringes in overlapping areas between two nanoparticles revealed the crystallinity of the primary nanoparticles. The Moiré fringes were not oriented (Fig. 6.6b).

The implementation of top-down route with the same mixed polar dispersion medium (T05_20w80isptx100) resulted in the production of flake-like $\text{Ca}(\text{OH})_2$ nanoparticles (Fig. 6.6c). The different shape of the $\text{Ca}(\text{OH})_2$ nanoparticles was attributed to the aging procedure of the lime putty. Finally, the rings observed through the SAED analysis of T05_20w80isptx100 were attributed to the diffraction of the polycrystalline newly formed $\text{Ca}(\text{OH})_2$ nanoparticles (Fig. 6.6d).

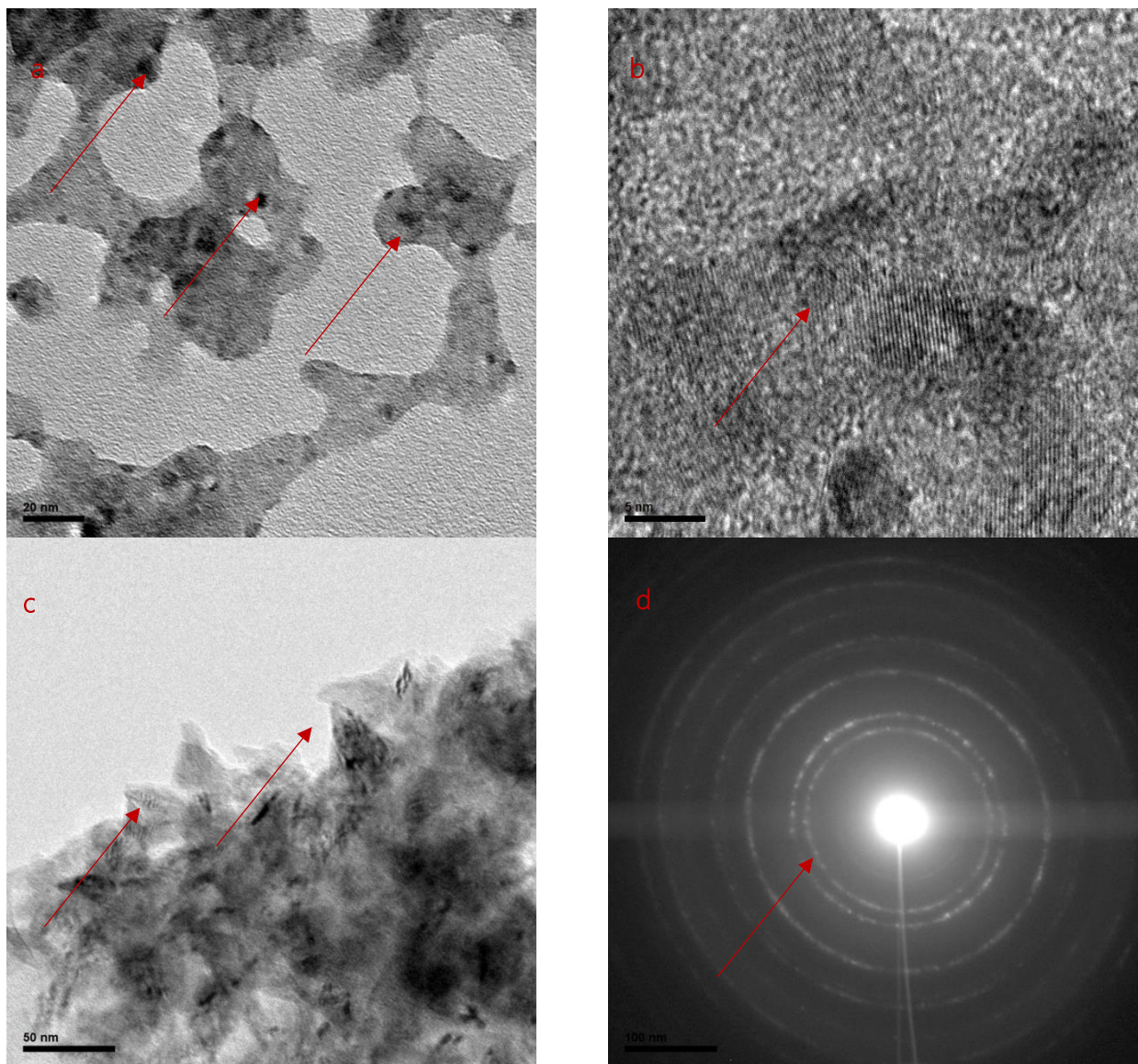


Figure 6.6 (a) Hexagonal and rounded $\text{Ca}(\text{OH})_2$ nanoparticles (B06_20w80isptx100) (scale bar at 20 nm); (b) Moire fringes in overlapping B06_20w80isptx100; c) Flake-like $\text{Ca}(\text{OH})_2$ nanoparticle (T05_20w80isptx100) (scale bar at 50 nm) and (d) SAED analysis of T05_20w80isptx100

Morphological characterization - DLS analysis

The size of $\text{Ca}(\text{OH})_2$ nanoparticles was additionally studied by DLS, calculating the average size and particle size distribution. It must be mentioned that the DLS analysis determined the hydrodynamic diameter of the particles. Also, the specific surface area of the newly formed $\text{Ca}(\text{OH})_2$ nanoparticles was determined as an indication of their reactivity.

The use of O_2 nanobubbles enriched water (B06_100nbs) resulted in the formation of $\text{Ca}(\text{OH})_2$ nanoparticles of 310 nm average size .

The addition of the non-ionic surfactant of Triton X-100 (B06_100nbstx100) resulted in the formation of $\text{Ca}(\text{OH})_2$ nanoparticles of average size of 278 nm. Both corresponding particle size distribution curves (Graph 6.1) presented a wider shape, indicating polydispersity of the shape of the produced $\text{Ca}(\text{OH})_2$ nanoparticles.

The implementation of the bottom-up synthetic route with a 1:1 ratio of distilled water and 2-propanol mixed polar dispersion medium (B06_50w50isptx100) solution resulted in the production of $\text{Ca}(\text{OH})_2$ nanoparticles of average size of 334 nm.

The use of a mixed polar dispersion medium consisted of 20% O_2 nanobubbles (nbs) enriched aqueous solution and 80% 2-propanol (B06_20nbs80isptx100) resulted in the formation of $\text{Ca}(\text{OH})_2$ nanoparticles of average size of 267 nm.

The use of a mixed polar dispersion medium consisted of 20% distilled water and 80% 2-propanol (B06_20w80isptx100) resulted in the production of $\text{Ca}(\text{OH})_2$ nanoparticles of average size of 360 nm.

The implementation of top-down route with the same mixed polar dispersion medium (T05_20w80isptx100) resulted in the formation of $\text{Ca}(\text{OH})_2$ nanoparticles of average size of 220 nm. The corresponding particle size distribution curves of the four-last synthesis (Graph 6.1) presented a narrower shape, indicating the homogeneity of the shape of the produced $\text{Ca}(\text{OH})_2$ nanoparticles.

The addition of 2-propanol in the cases of B06_50w50isptx100, B06_20nbs80isptx100 and B06_20w80isptx100 resulted in the increase of value of the specific surface area of the newly formed $\text{Ca}(\text{OH})_2$ nanoparticles in relation to the aqueous dispersions of B06_100nbs and B06_100nbstx100 (Table 6.2). Therefore, the addition of 2-propanol can be related to the increase of the reactivity of the $\text{Ca}(\text{OH})_2$ nanoparticles. The determination of the value of the value the specific surface area of the $\text{Ca}(\text{OH})_2$ nanoparticles obtained via the top-down

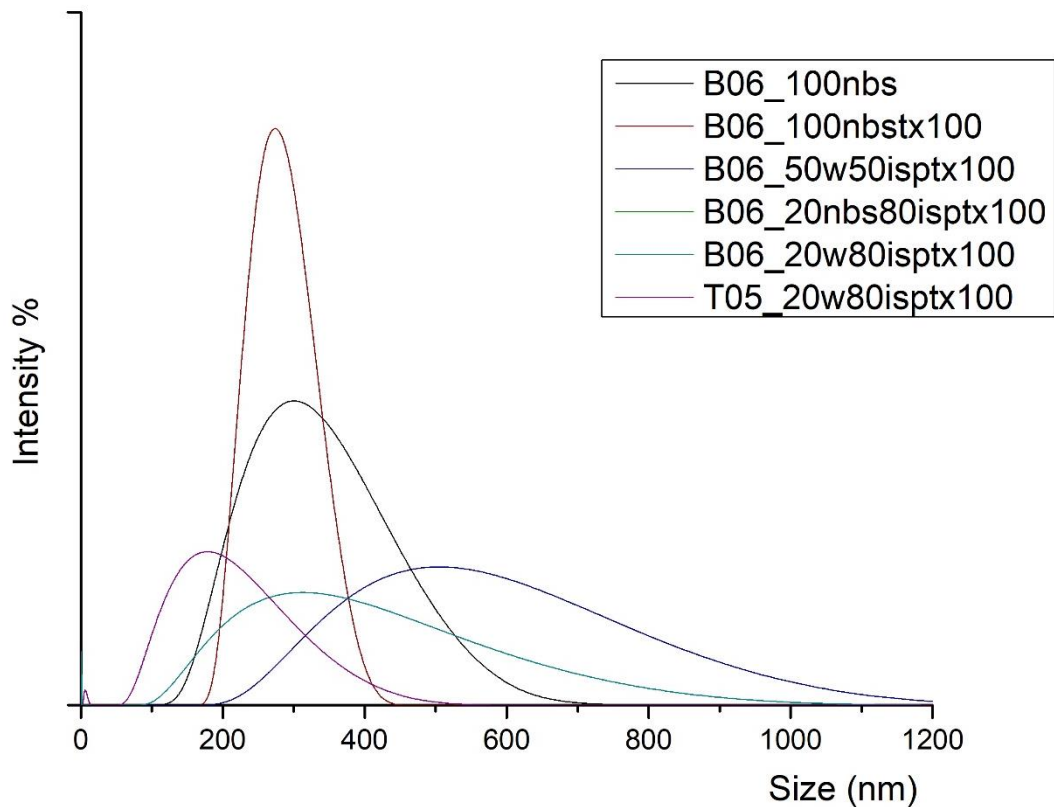
route (T05_20w80isptx100) was not realized. This was attributed to the retention of water among the $\text{Ca}(\text{OH})_2$ nanoparticles. As it can be observed from the results in Table 6.2 the addition of 2-propanol was connected with both increase of the size of the nanoparticles and with the increase of the specific area.

Table 6.2 Physical characteristics of portlandite particles determined by different techniques

<i>Alteration</i>	Cluster Nanoparticles' size (nm)	Mean values of the nanoparticle's size (nm)	SSA (m^2/g)
	<i>SEM</i>	<i>DLS</i>	<i>BET method</i>
B06_100nbs	200-350	310	4.25
B06_100nbstx100	150 – 300	278	4.49
B06_50w50isptx100	250 – 350	334	6.81
B06_20nbs80isptx100	150 – 350	267	6.79
B06_20w80isptx100	200-370	360	6.89
T05_20w80isptx100	210-380	220	-

Overall, the addition and increase of the amount of 2-propanol resulted in the development of spherical $\text{Ca}(\text{OH})_2$ nanoparticles (Fig. 6.2 and 6.3). Although there was no clear evidence on the exact mechanism that takes place, these clusters could be attributed to the adsorption (physiosorption) of the molecules of 2-propanol on the surface of the $\text{Ca}(\text{OH})_2$ particles [39] [154], during sonication, after the synthesis of the primary $\text{Ca}(\text{OH})_2$ nanoparticles and after the aging procedure of lime-putty in the case of the top-down synthetic route. The adsorption of 2-propanol molecules on the surface of the $\text{Ca}(\text{OH})_2$ may consequently have led to the development of Ca-alkoxide pseudomorphs seen in the top-down FTIR results (Section 6.4.2). The above mechanism could explain the make up of amorphous Ca-alkoxide phases [188], [230] that contribute to the development of the spherical $\text{Ca}(\text{OH})_2$ clusters [146].

The above assumption was supported by the absence of any spherical clusters in the porous substrates after 28 days of curing and carbonation time, indicating the metastable nature of these pseudomorphs (Chapter 7).

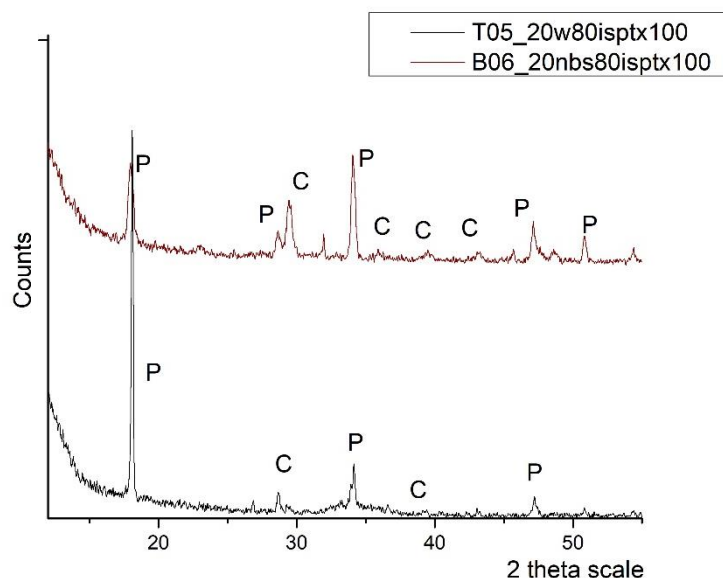


Graph 6.1 Particle size distribution by DLS of the six synthesis

[6.2.2 Mineralogical and chemical characterization of Ca\(OH\)₂ nanoparticles](#)

XRD results

The results of the mineralogical characterization of the all six synthetic procedures were characterized by the dominant presence of portlandite Ca(OH)₂, as indicated in the XRD diffractogram (Graph 6.2). Specifically, the presence of the major peaks 17,9°, 28,4°, 34,1°, 46,8° and 50,6° of portlandite of hexagonal crystals corresponding to the XRD pattern of 44-1481. Other minor phase identified was the one of calcite (CaCO₃) of trigonal crystals.



Graph 6.2 X-ray Diffraction pattern of the produced nanoparticles T05_20w80isptx100 and B06_20nbs80isptx100

The average crystallite size for six synthesis was determined with the Scherer equation, according to the methodology described in the previous chapter. The results are summarized in **Table 6.2**.

The use of O₂ nanobubbles enriched aqueous solution (B06_100nbs) resulted in the formation of Ca(OH)₂ nanoparticles of average crystallite size of 36 nm.

The addition of the non-ionic surfactant of Triton X-100 (B06_100nbstx100) resulted in the formation of Ca(OH)₂ nanoparticles of average crystallite size of 32 nm. T

he implementation of the bottom-up synthetic route with a 1:1 ratio of distilled water and 2-propanol mixed polar dispersion medium (B06_50w50isptx100) resulted in the formation of Ca(OH)₂ nanoparticles of average crystallite size of 32 nm.

The use of a mixed polar dispersion medium consisted of 20%O₂ nanobubbles (nbs) enriched aqueous solution and 80% 2-propanol (B06_20nbs80isptx100) resulted in the formation of Ca(OH)₂ nanoparticles of average crystallite size of 33 nm.

The use of a mixed polar dispersion medium consisted of 20%distilled water and 80% 2-propanol (B06_20w80isptx100) resulted in the formation of Ca(OH)₂ nanoparticles of average crystallite size of 41nm.

The implementation of top-down route with the same mixed polar dispersion medium(T05_20w80isptx100) resulted in the formation of Ca(OH)₂ nanoparticles of average crystallite size of 37 nm.

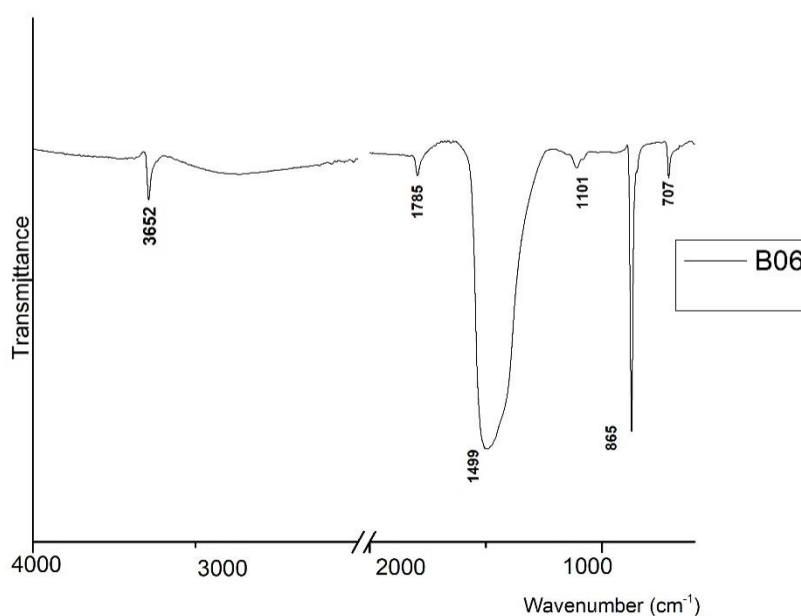
Only the use of a polar dispersion medium consisted of 20% distilled water and 80% 2-propanol in the bottom-up synthetic route proved to have a direct effect on a small increase of the average crystallite size of the $\text{Ca}(\text{OH})_2$ nanoparticles.

Chemical characterization -

FTIR results

The FTIR spectrum of nanoparticles produced through the bottom-up methodology (Fig. 6.3) verified the presence of portlandite and calcite already identified in mineralogical analysis. In particular, FTIR spectrum (Graph 6.3) presented a strong and sharp band at 3652 cm^{-1} corresponding to the OH^- stretching modes. The band were characteristics of portlandite.

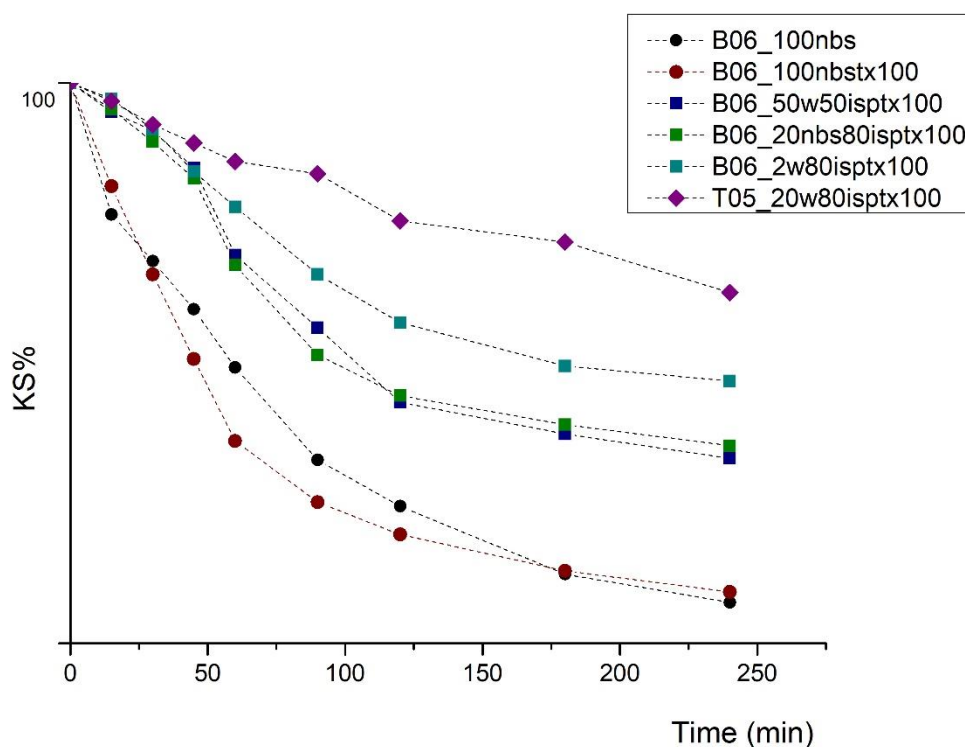
The presence of calcite was verified by the small and sharp band at 1785 cm^{-1} corresponding to the $\text{C}=\text{O}$ bonds of the carbonates $-\text{CO}_3^{2-}$, the broad band centered at 1469 cm^{-1} corresponding to the ν_2 symmetric deformation of the carbonates $-\text{CO}_3^{2-}$ and, finally, the 865 cm^{-1} corresponding to the ν_3 asymmetric stretching of the carbonates $-\text{CO}_3^{2-}$. The interpretation of the results from the mineralogical and chemical analysis showed no significance differences on the effect of the alterations of the dispersion mediums.



Graph 6.3 X-ray Representative FTIR spectrum the produced nanoparticles

6.3 Colloidal stability of Ca(OH)₂ nanodispersions

The kinetic stability of the six dispersions of Ca(OH)₂ nanoparticles was determined through the use of UV-VIS spectroscopy. As exhibited in Graph 6.4, there were notably differences in the colloidal stability between the six dispersions of Ca(OH)₂. The use of O₂ nanobubbles (nbs) enriched aqueous solution as dispersion medium in the bottom-up synthetic route (B06_100nbs) and the addition of the non-ionic surfactant of Triton X-100 (B06_100nbstx100) resulted to a reduced kinetic stability in relation to the other four synthesis with the mixed polar dispersion medium. The addition of 2-propanol (B06_50w50isptx100) and the increase of the percentage (B06_20nbs80isptx100, B06_20w80isptx100 and T05_20W80isptx100) proved to have a direct effect on the enhancement of the kinetic stability of the dispersions of Ca(OH)₂ nanoparticles. This was attributed to the steric stabilization of the dispersion medium and the inhibition of agglomeration phenomena. Finally, the implementation of the top-down route proved to have a direct effect on the increase of the colloidal stability of the dispersions. This could be attributed on the polydispersity of the size of Ca(OH)₂ nanoparticles leading to different sedimentation rates.



Graph 6.4 KS% of the six dispersions of Ca(OH)₂ nanoparticles

Overall, the use of O₂ nanobubbles (nbs) enriched water as dispersion medium at the bottom-up synthetic route led to a decrease of the size of the newly formed Ca(OH)₂ nanoparticles. Also, it led to the formation of monocrystalline hexagonal and plate-like crystals of Ca(OH)₂ and to the absence of aggregation phenomena. The modifications of the morphological characteristics of the newly formed nanoparticles were attributed to the nucleation of the nanobubbles on the surface of the nanoparticles.

The addition of the 2-propanol led to a decrease of the size of the Ca(OH)_2 nanoparticles and to an increase of their reactivity (though the increase of the value of the specific surface area).

Moreover, it led to the formation of polycrystalline hexagonal and plate-like crystals of Ca(OH)_2 and to the absence of agglomeration phenomena. The consequent reduction of the surface tension between the Ca(OH)_2 nanoparticles and the dispersion medium led to the modifications of their morphological characteristics and an increase of the colloidal stability of the newly formed dispersions.

6.4 Carbonation

6.4.1 The effect of Relative Humidity on the carbonation process

According to the relevant literature [160], [219], one of the major parameters affecting the kinetics of the carbonation reaction is the relative humidity (RH%). Relative humidity content can control the carbonation reaction rate and thus, the formation of the end-up product [93]. [166], [167]

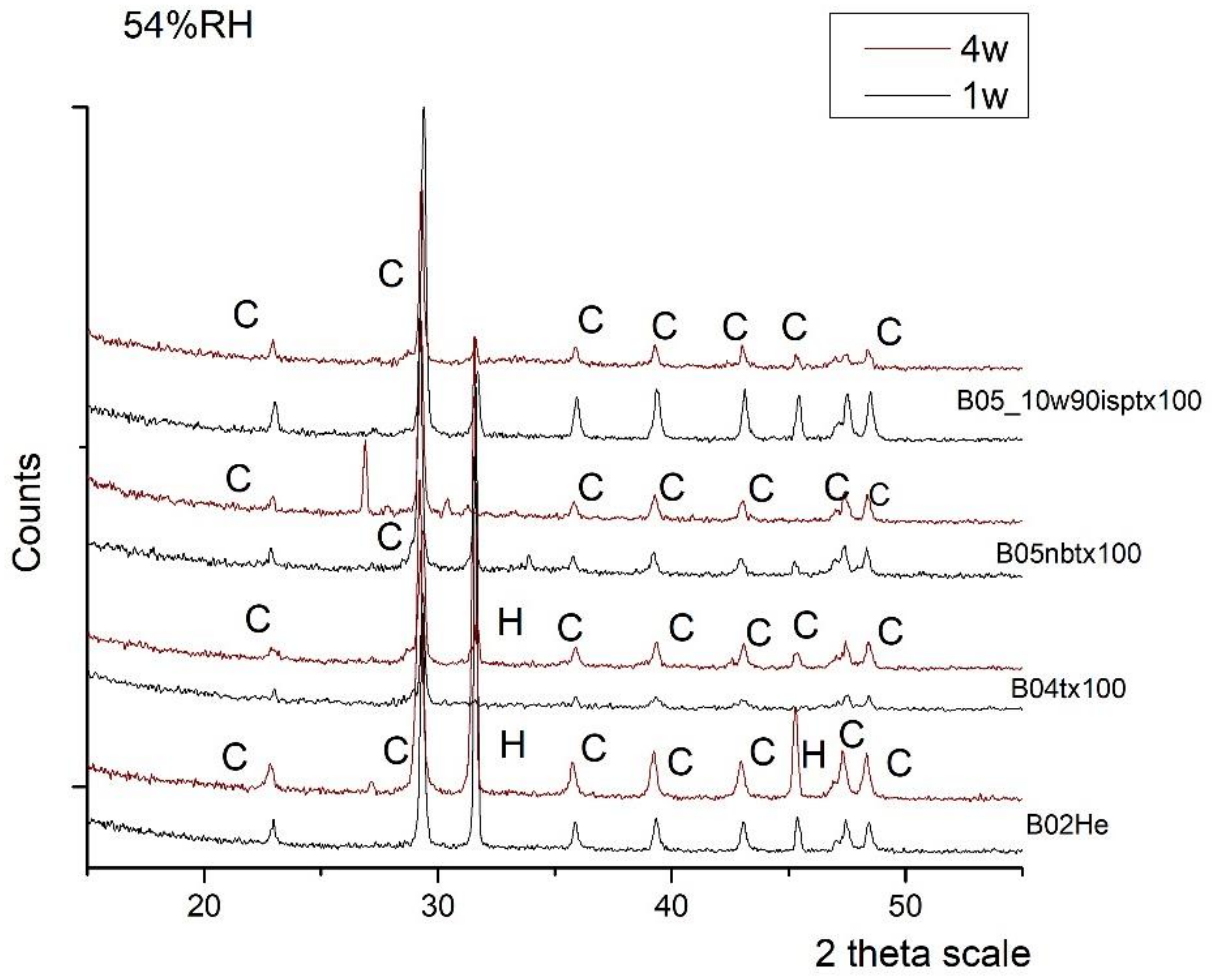
According to the results obtained in Chapter five, four (4) dispersions of Ca(OH)_2 that have been synthesized via the bottom-up route were selected for monitoring the carbonation process under two different Relative Humidity conditions : a) $\text{RH}\%=55\pm 2$ and b) $\text{RH}\%=95\pm 2$.

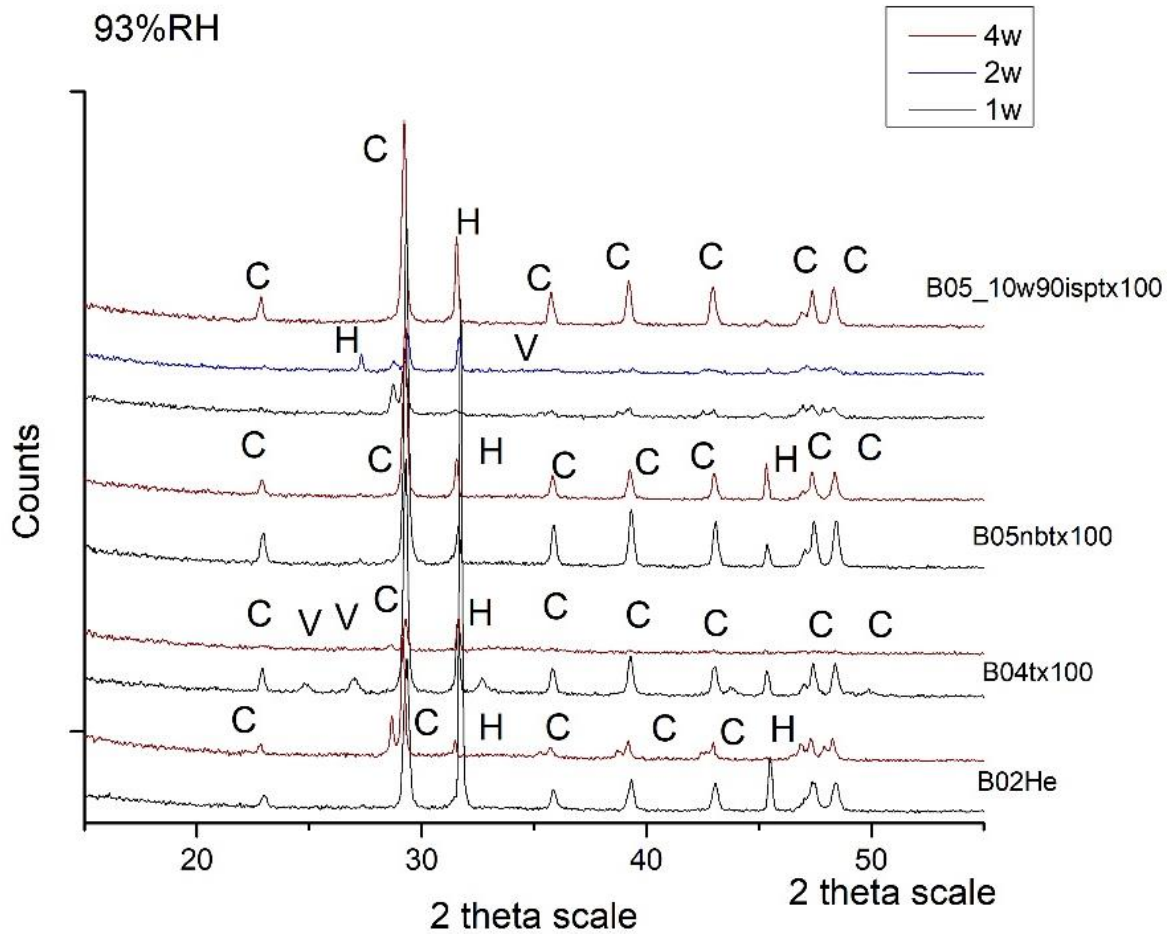
Table 6.3 Description of the four dispersion of Ca(OH)₂ nanoparticles

Sample I.D.	Description				
	Method	Water (%v/v)	O ₂ nbs (%v/v)	2-propanol (%v/v)	Triton X-100 (%v/v)
B02He	Bottom-up	100	0	0	-
B04tx100	Bottom-up	100	0	0	✓
B05nbt100	Bottom-up	0	100	0	✓
B05_10w90ispt100	Bottom-up	10	0	90	✓

Mineralogical characterization - XRD results

The mineralogical composition of the end-up products at the end of one, two and four weeks for all four nano-dispersions were characterized by the dominant presence calcite (CaCO₃), as indicated in the XRD diffractogram (Graph 6.5 a,b). Specifically, the presence of the major peaks 23,1°, 29,5°, 36,1°39,4° and 43,4° of calcite of in trigonal crystals corresponding to the XRD pattern of 5-586. This was in accordance with the relevant literature (references), where at RH% > 75 the realization of the carbonation process was accelerated due to the hydrophilic character of portlandite and the multilayer adsorption of water molecules onto the surface of the Ca(OH)₂ nanoparticle [160], [166]. According to this model, the carbonation of portlandite is characterized as a dissolution-precipitation process [186] where portlandite is dissolved into the water molecules to Ca²⁺ and reacts with the CO₃²⁻ derived from the dissolution of CO₂. This leads to the precipitation of CaCO₃ onto the surface of the nanoparticles within the aqueous film [166]. According to Daniele et al. 2010 [219], the carbonation procedure efficiency (yield) was estimated by the comparative evaluation of the ratio between the ratio between the CaCO₃ peaks area and the spectrum total area in respect with the time period of four weeks reaching an average value of 0.8.





Graph 6.5 (a) X-ray Diffraction pattern of the carbonation process of the $\text{Ca}(\text{OH})_2$ nanoparticles under 54% RH and (b)(a) X-ray Diffraction pattern of the carbonation process of the $\text{Ca}(\text{OH})_2$ nanoparticles under 93% RH

Minor content of the by-product halite (NaCl) in cubic crystals was also detected, though the detection of the major peaks $31,8^\circ$ and $45,5^\circ$. The comparative evaluation of the results of the mineralogical analysis on the basis of the two values of %RH revealed that in the case of the 93%RH, minor content of vaterite was detected. Specifically, in the mineralogical analysis of the carbonation product of B05nbtx100 in the first week and of B05_10w90isptx100 in the second week the major peaks of $3,57 \text{ \AA}$, $24,9^\circ$ and $27,2^\circ$ respectively, of vaterite of in hexagonal crystal structure.

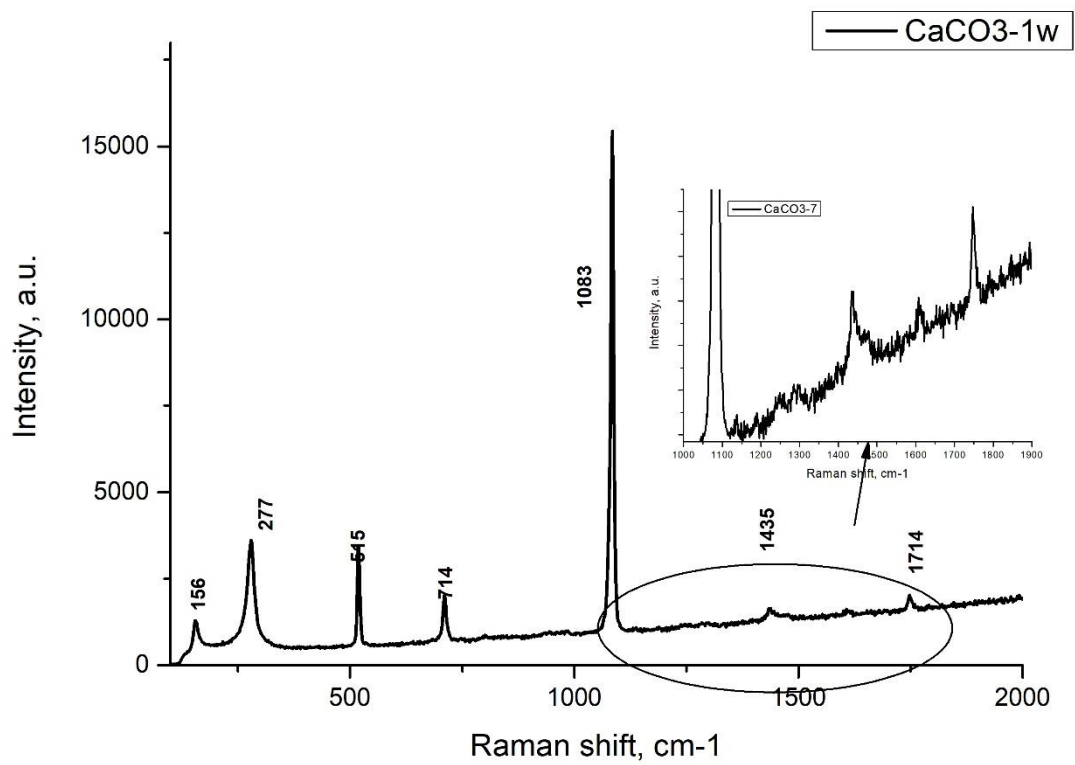
Chemical Characterization - Raman results

The interpretation of the results through the analytical techniques of Raman and FTIR analysis verified the presence of calcite observed in the XRD diffraction patterns (Graph 6.6). Specifically, after the time period of one week, the presence of the peaks 156, 277, 714, 1436 and 1714 cm^{-1} verified the presence of calcite (CaCO_3) [231]. The strong and sharp peak 1086 cm^{-1} verified the presence of portlandite, indicating that the carbonation reaction was not complete.

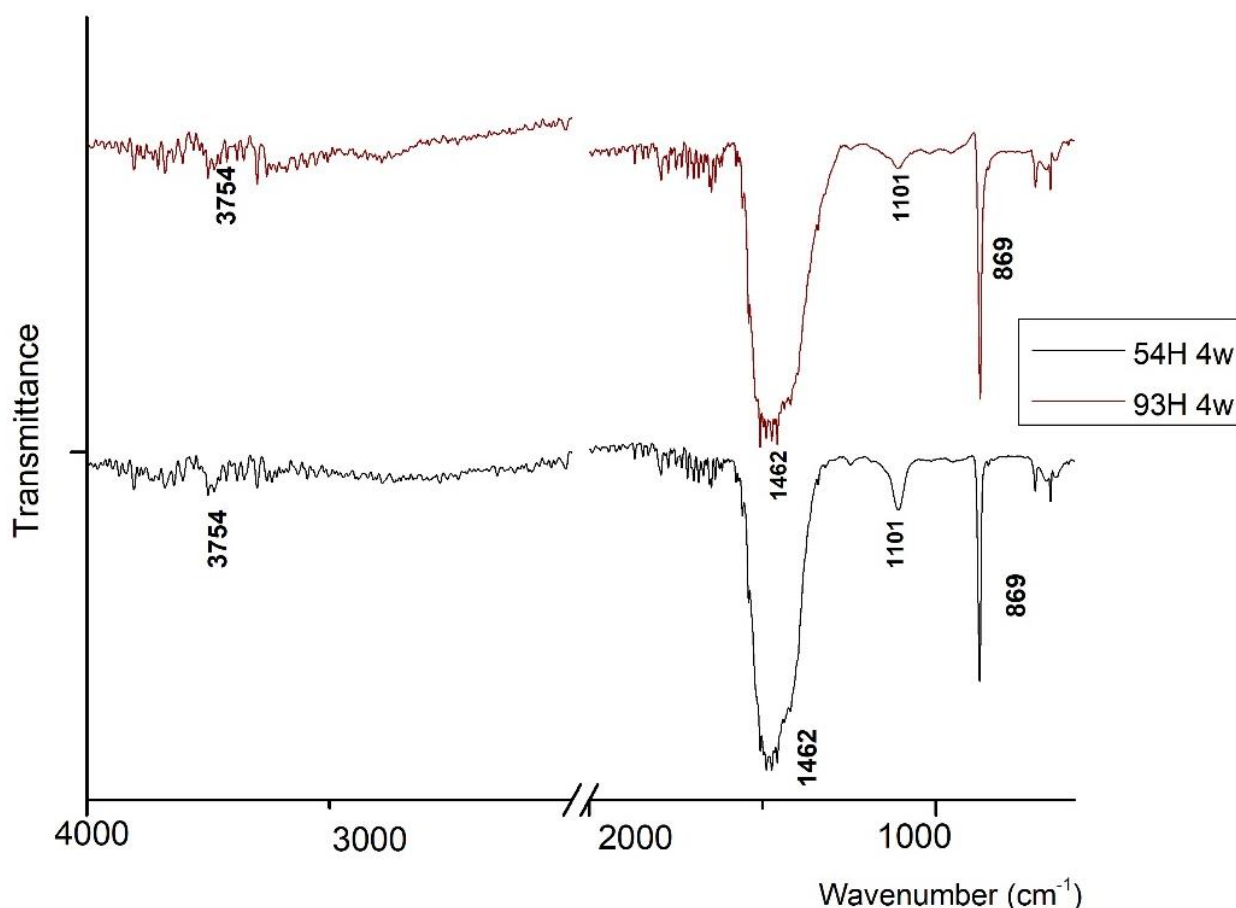
FTIR results

The results obtained through the use of Raman spectroscopy were verified through the use of FTIR. As it can be observed in Graph 6.7, verified the presence of portlandite and calcite already identified in Raman spectrum. In particular, FTIR spectrum (Graph 6.7) presented a strong and sharp band at 3752 cm^{-1} corresponding to the OH^- stretching modes. The band was characteristic of portlandite.

The presence of calcite was verified by, the broad band centered at 1462 cm^{-1} (corresponding to the ν_2 symmetric deformation of the carbonates $-\text{CO}_3^{2-}$ and the 869 cm^{-1} (corresponding to the ν_3 asymmetric stretching of the carbonates $-\text{CO}_3^{2-}$). The interpretation of the results from the mineralogical and chemical analysis showed no significant differences on the effect of the relative humidity values on the end-up product of the carbonation procedure after a time period of four weeks.



Graph 6.6 Representative Raman spectrum of the end-up product of the carbonation procedure under 54%RH after a time period of one week



Graph 6.7 Representative FTIR spectrum of the end-up product of the carbonation procedure under 54% RH and 93% RH after a time period of 4w

Overall, the comparative evaluation on the effect of the two different values of relative humidity revealed the dominant presence of calcite in both cases. This was connected with the high percentage of relative humidity that enabled the realization of the carbonation reaction, through the dissolution of portlandite in the water film adsorbed on its surface and the consequent realization of the carbonation reaction and precipitation of CaCO₃ [25], [186]. The identification of the metastable phase of vaterite in the case of %RH=93 was an indication of the realization of a non-classical nanoparticle-mediated process that led to the growth of amorphous calcium carbonate. And the consequent formation of primary vaterite nanoparticles through the heterogenous nucleation onto the ACC. The primary vaterite crystals aggregated then by mesoscale assembly into a nearly iso-oriented structure [25], [160]. Then, the metastable phase of vaterite was transformed into calcite. The presence of metastable phases was not identified in the case of %RH=54.

In addition to this, the presence of portlandite identified through the use of Raman and FTIR spectroscopy on the first and fourth week respectively, indicated that the carbonation reaction was not complete even after a time period of four weeks. This could be attributed to the inhibit of the completion of the carbonation reaction due to the thickness of the hexagonal plate-like crystals with thickness along the basal face [001] larger than 30 nm [25].

6.4.2 Carbonation of the six optimum dispersions of Ca(OH)₂ nanoparticles

The interpretation of the results concerning the monitoring of carbonation process (Table 6.4) nanoparticles was implemented. The six specimens were placed onto Si-wafers and left to dry for 24 hours at a constant temperature of 40°C. Then they were left under 75%RH at room temperature. The monitoring of the carbonation process was implemented through the XRD and FTIR analysis at a constant time period of 7 days (1 week).

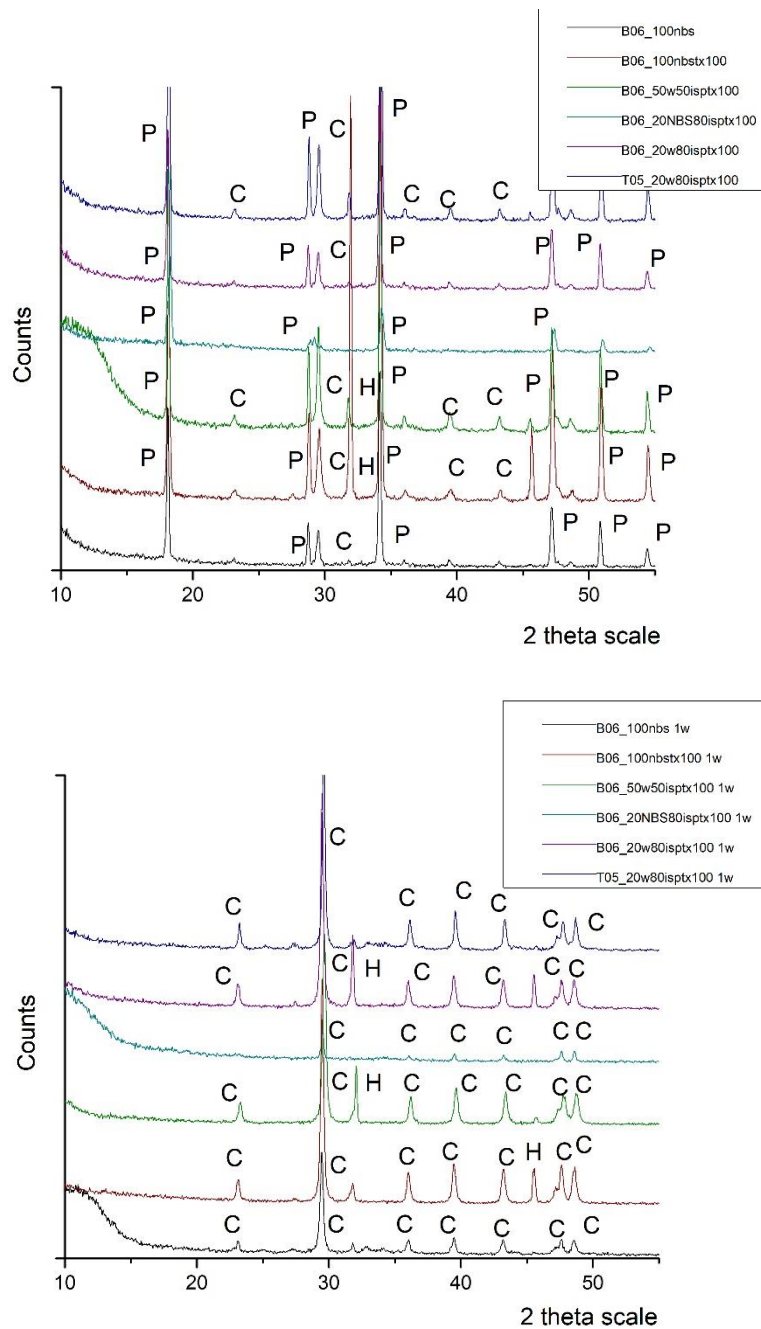
Mineralogical characterization - XRD results

The results of the mineralogical characterization of the all six synthetic procedures at the beginning of the carbonation process were characterized by the dominant presence of portlandite Ca(OH)₂, as indicated in the XRD diffractogram (Graph 6.8a). Specifically, the presence of the major peaks 17,9°, 28,4°, 34,1°, 46,8° and 50,6° of portlandite of hexagonal crystals corresponding to the XRD pattern of 44-1481. Other minor phase identified from the peaks 23,1°, 29,5°, 36,1°, 39,4° and 43,4° of calcite of in trigonal crystals corresponding to the XRD pattern of 5-586. The presence of the calcite phases could be attributed to the partial carbonation of the samples during drying, due to the CO₂ dissolved in water.

Table 6.4 Description of the six optimum dispersions of Ca(OH)₂ nanoparticles

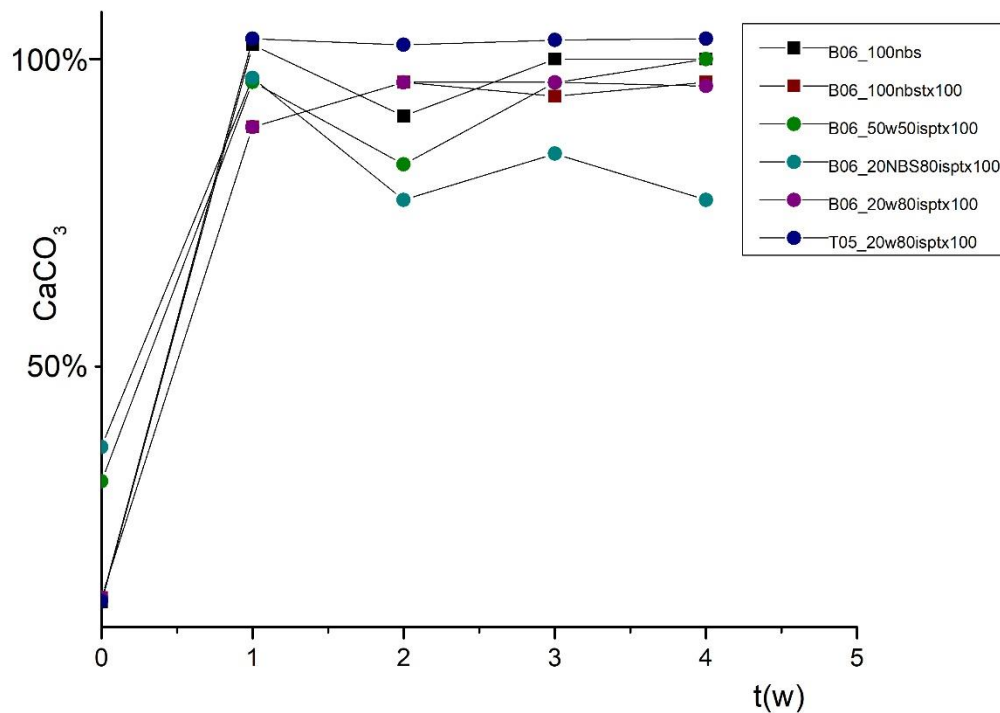
<i>Sample I.D.</i>	<i>Description</i>				
	<i>Method</i>	<i>Water</i>	<i>O₂nbs</i>	<i>2-propanol</i>	<i>Triton X-100</i>
B06_100nbs	Bottom-up	0	100%	0	-
B06_100nbstx100	Bottom-up	0	100%	0	✓
B06_50w50isptx100	Bottom-up	50%	0	50%	✓
B06_20nbs80isptx100	Bottom-up	0	20%	80%	✓
B06_20w80isptx100	Bottom-up	20%	0	80%	✓
T05_20w80isptx100	Top-down	20%	0	80%	✓

After a time period of one week the XRD diffractograms were characterized by the dominant presence of calcite CaCO₃ (Graph 6.8b). Specifically, the peaks 23,1°, 29,5°, 36,1°39,4° and 43,4° of calcite of in trigonal crystals corresponding to the XRD pattern of 5-586. The dominant presence of calcite along with the absence of portlandite was attributed to the realization of the carbonation process under a high percentage of relative humidity (RH=75%) that enabled the realization of the carbonation reaction, through the dissolution of portlandite in the water film adsorbed on its surface and the consequent realization of the carbonation reaction and precipitation of CaCO₃ [25], [196].



Graph 6.8 (a)X-ray Diffraction pattern of the initiation of the carbonation process of the Ca(OH)₂ nanoparticles under 75% RH and(b)(a)X-ray Diffraction pattern of the of the carbonation process of the Ca(OH)₂ nanoparticles under 75% RH after 1week

According to Daniele et al. 2010 [219], the carbonation procedure efficiency (yield) was estimated by the comparative evaluation of the ratio between the ratio between the CaCO₃ peaks area and the spectrum total area in respect with the time period of four weeks (Graph 6.9).



Graph 6.9 Carbonation procedure efficiency (yield) of the six optimum dispersions of $\text{Ca}(\text{OH})_2$ nanoparticles

The comparative evaluation between the carbonation procedure efficiency (yield) of the six optimum dispersions of $\text{Ca}(\text{OH})_2$ nanoparticles (Graph 6.9) verified the carbonation of portlandite to calcite from the first week, as it has been previously observed in paragraph 6.4.1. The higher carbonation yield was achieved in the case of the top down synthetic route (T05_20w80isptx100) in respect with the other five dispersions synthesized via the bottom-up synthetic route. This could be attributed to the reduced size of the $\text{Ca}(\text{OH})_2$ nanoparticles (220 nm, Table 6.1) which led to the increase of the surface to volume ratio of the nanoparticles, and thus, their reactivity. The comparative evaluation between the carbonation yield of the five dispersions of $\text{Ca}(\text{OH})_2$ nanoparticles synthesized via the bottom-up synthetic route revealed that the use of aqueous dispersion medium (in the case of B06_100nbs and B06_100nbstx100) led to a slight increase of the value of the carbonation yield in respect with the three dispersions of a mixed polar dispersion medium (B06_50w50isptx100, B06_520nbs80isptx100 and B06_20w80isptx100). This was in accordance with the relevant literature [219] and underlined the importance of the aqueous dispersion medium on the realization of the carbonation process and the increase of the carbonation efficiency (yield). Specifically, the presence of water in the form of adsorbed film on the surface of the $\text{Ca}(\text{OH})_2$ nanoparticles was essential for the dissolution of portlandite $\text{Ca}(\text{OH})_2$ and CO_2 and the formation and precipitation of calcite CaCO_3 .

Chemical characterization - FTIR results

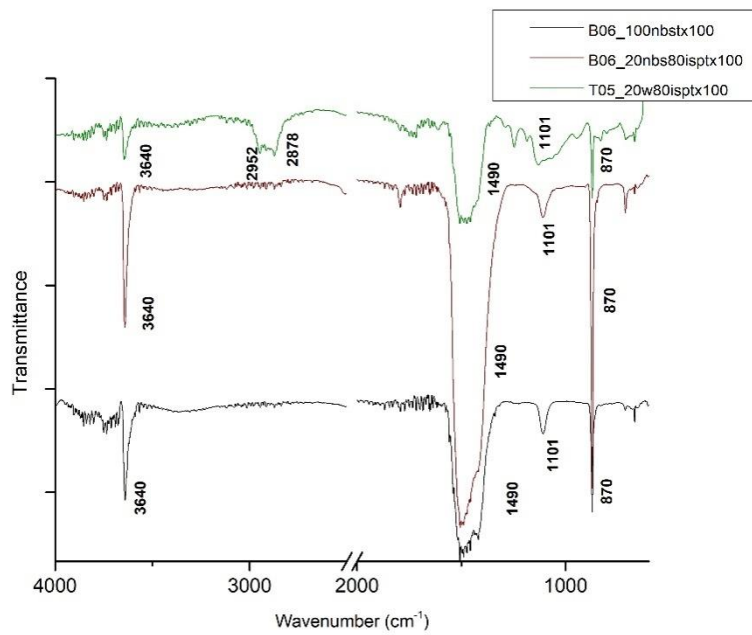
In order to investigate the early stages of the carbonation process, the six dispersions of $\text{Ca}(\text{OH})_2$ nanoparticles were placed on Si wafer and let under 60°C for 72 hours. In this way, the total evaporation of the dispersion medium was achieved. The FTIR spectrum of nanoparticles (Graph 6.10) verified the presence of portlandite and calcite already identified in mineralogical analysis. In particular, FTIR spectrum (Graph 6.10) presented a strong and sharp band at 3640 cm^{-1} corresponding to the OH^- stretching mode. The band was characteristic of portlandite.

The presence of calcite was verified by the broad band centered at 1490 cm^{-1} corresponding to the ν_2 symmetric deformation of the carbonates $-\text{CO}_3^{2-}$ and, finally, the 870 cm^{-1} corresponding to the ν_3 asymmetric stretching of the carbonates $-\text{CO}_3^{2-}$. The interpretation of the results from the mineralogical and chemical analysis showed no significance differences on the effect of the alterations of the dispersion mediums.

Only in the case of the dispersion of $\text{Ca}(\text{OH})_2$ synthesized via the top-down route with the of a mixed polar dispersion medium (T05_20w80isptx100), the well-defined peaks at 2952 and 2852 cm^{-1} were identified, corresponding to the C-H stretching modes of CH_3 and CH_2 . Those bands were attributed to the presence of newly formed alkoxides, since the 2-propanol was evaporated.

According to the relevant literature [25], [39], [160] [166] this was attributed to the realization of the reaction between the $\text{Ca}(\text{OH})_2$ nanoparticles and the 2-propanol of the mixed dispersion medium, resulting in the formation of a surface layer of Ca alkoxides. During the water adsorption onto the surface of $\text{Ca}(\text{OH})_2$ nanoparticles, the surface layer of Ca alkoxides could be partially hydrolyzed during the realization of the carbonation reaction, thus adding a hydro-alcoholic part at the aqueous film. The addition of the hydro-alcoholic part could be leading to the presence of the metastable phase of calcite (vaterite and aragonite).

According to the relevant literature, the detection of Ca-alkoxide was related with the preferential replacement of the center of the basal face [0001] of the $\text{Ca}(\text{OH})_2$ crystals by the Ca-alkoxides via an interface-coupled dissolution-precipitation mechanism. This was attributed to the presence of a high dislocation density in the center of the $\text{Ca}(\text{OH})_2$ crystals. During the top-down route, the core of the $\text{Ca}(\text{OH})_2$ nanoparticles was formed during the early stages of the slaking of lime [184] at a high supersaturation state, which favored the formation of defects [160] Dislocations can favor the dissolution of minerals and can act as preferred sites for the nucleation of new phases [160]. On the other hand, the observed absence of the Ca-alkoxides in the case of the $\text{Ca}(\text{OH})_2$ nanoparticles synthesized via the bottom-up synthetic route could be attributed to the absence of dislocations.



Graph 6.10 Representative FTIR spectrum of B06_100nbstx100, B06_20nbs80ispstx100 and T05_20w80ispstx100

Chapter 7- Trial application of nanolime dispersions on porous substrates

7.1 Application methodology

Aiming to evaluate the rheological properties of the most promising $\text{Ca}(\text{OH})_2$ nanodispersions, trial application of six nano-dispersions was carried out in six different porous substrates: a) three types of sintered glass filters, b) two types of natural stones and c) one type of historic lime mortar.

The building materials selected are considered representative of the materials used in the architectural heritage of the Mediterranean basin, while the glass filters offer the ability of penetration experiments in a specific pore-range. Moreover, the deposited $\text{Ca}(\text{OH})_2$ particles can be easily distinguished on the silicon background.

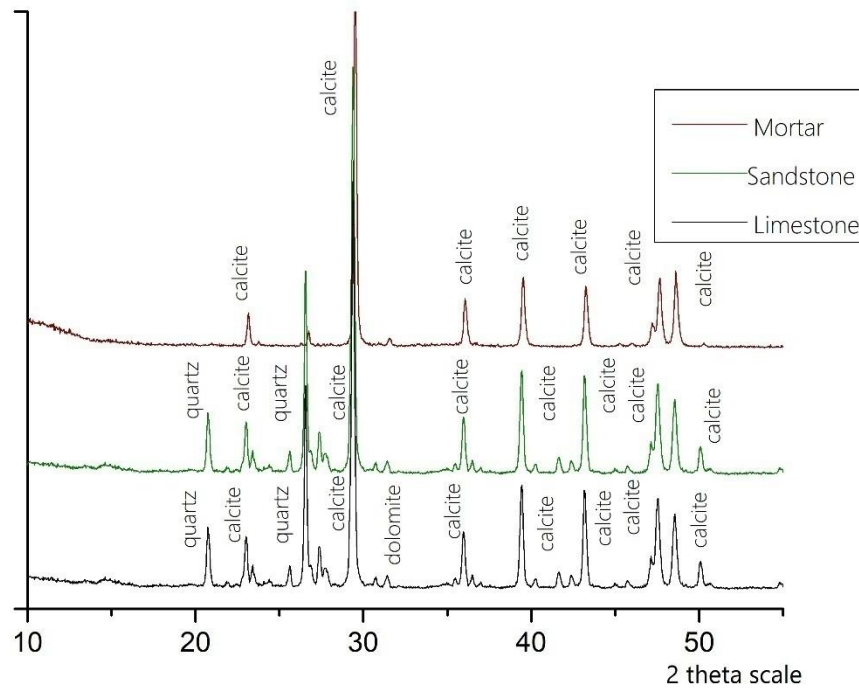
After the application of the six selected dispersions (B06_100nbs, B06_100nbstx100, B06_50w50isptx100, B06_20nbs80isptx100, B06_20w80isptx100 and T05_20w80isptx100), their penetration and diffusion ability inside the porous network of the substrates was studied, along with the consequent deposition and morphology of the $\text{Ca}(\text{OH})_2$ nanoparticles deposited on the pore network.

Table 7.1 Microstructural characteristics of the three sintered glass filters and inorganic substrates

Sintered glass filters	Specimens		Iso 4793 Identification mark	Normal max. pore size (μm)
	<i>P0</i>		250P	160 - 250
	<i>P4</i>		16P	10 - 16
	<i>P5</i>		1.6P	10 - 1.6

Inorganic porous substrates	Specimens		Open Porosity	Coefficient of water absorption by capillarity
			%	C (g/m ² *s ^{0.5})
	<i>Limestone</i>		26	233
	<i>Sandstone</i>		32	40
<i>Mortar</i>		34	143	

The mineralogical composition of the three porous building materials was analyzed by XRD (Graph 7.1). The results indicate the dominant presence of calcite in all samples. Quartz is present also in all samples as a minor phase.



Graph 7.1 X-ray Diffraction patterns of the three porous inorganic substrates

The microstructural characterization of the porous substrates was realized by examination in the stereomicroscope (Fig. 7.1). Their total porosity values were calculated by determining their apparent and real densities, using the so-called “fluid displacement method”. Additionally, the coefficient of water absorption by capillarity was also determined according to BS EN 1925:1999 (Table 7.2). Finally, their pore-size distribution was determined by Mercury Intrusion Porosity (Graph 7.2).

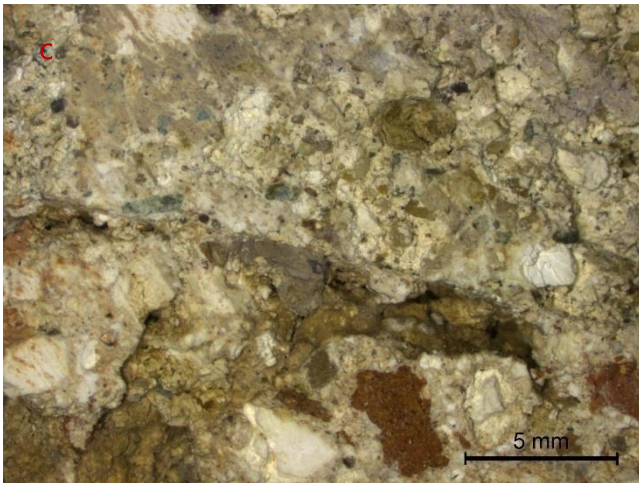
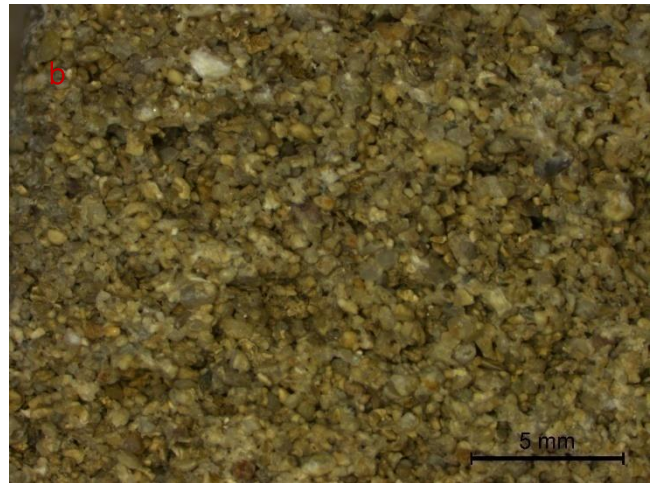
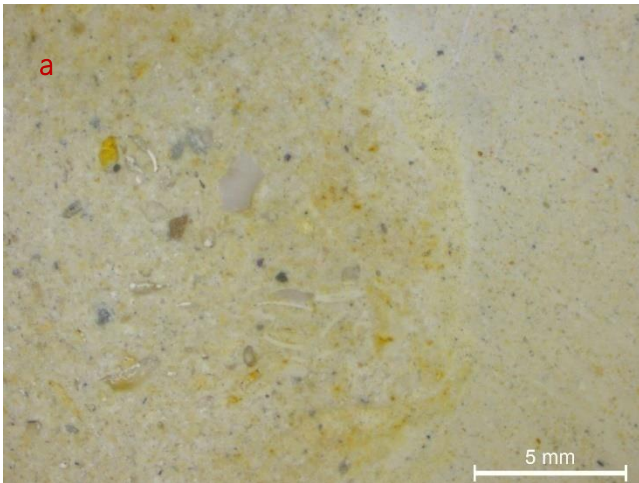
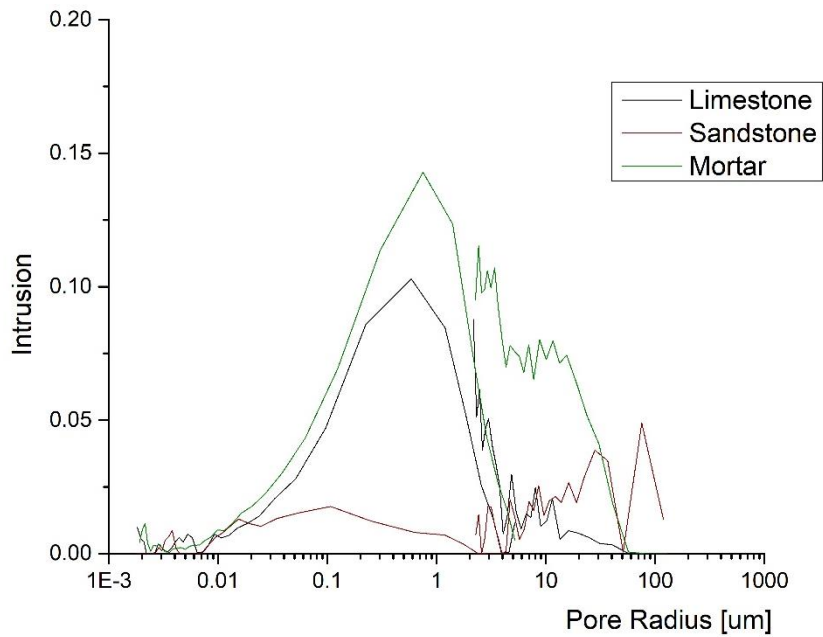


Fig.7.1 Cross section examination of the untreated substrates with the use of the stereomicroscope (a) Limestone untreated substrate (scale bar at 5mm); (b) Sandstone untreated substrate (scale bar at 5 mm) and (c) Mortar untreated substrate (scale bar at 5mm).



Graph 7.2 Pore size distribution curves of the untreated substrates of limestone, sandstone and mortar

The untreated limestone specimen was characterized by uniformity, both in terms of grains and pore structure (Graph 7.2). The reference sandstone was characterized by diversity both in terms of grains size and pore structure, where the presence of micritic calcite (micritic) was dominant (Graph 7.2). Finally, lime mortar was characterized by inhomogeneity both in terms of grains size and pore structure, exhibiting an extensive network of micro-cracks (Fig. 7.1c). In terms of the microstructural characteristics, limestone was characterized by lower open porosity values and enhanced water absorption by capillarity values, compared to the sandstone and the lime-mortar (Table 7.1).

Finally, the determination of the pore-size distribution curves of the three untreated substrates was characterized by a narrow peak around 0,001 to 1 microns and a sharp peak around 10 to 100 microns. In the cases of the limestone and calcareous mortar, an increased population of the capillary pores (mesopores) was observed (Graph 7.2). The sandstone exhibited a more uniform pore-network in respect to the other two building materials.

Application procedure

Cubic specimens ($3 \times 3 \times 3 \text{ cm}^3$) were cut off from larger blocks of the three porous building materials and dried at $60 \pm 5 \text{ }^\circ\text{C}$ to constant mass. Glass filters were used without any modification. All specimens were treated with the same drop-to-drop method in order to enable the comparison of the results between different substrates.

Recently formed nanolime dispersions were applied on the top surface of all specimens, by the use of a pipette and a brushstroke, allowing the nanolime dispersions to be fully absorbed between two consecutive applications (Fig.7.2).

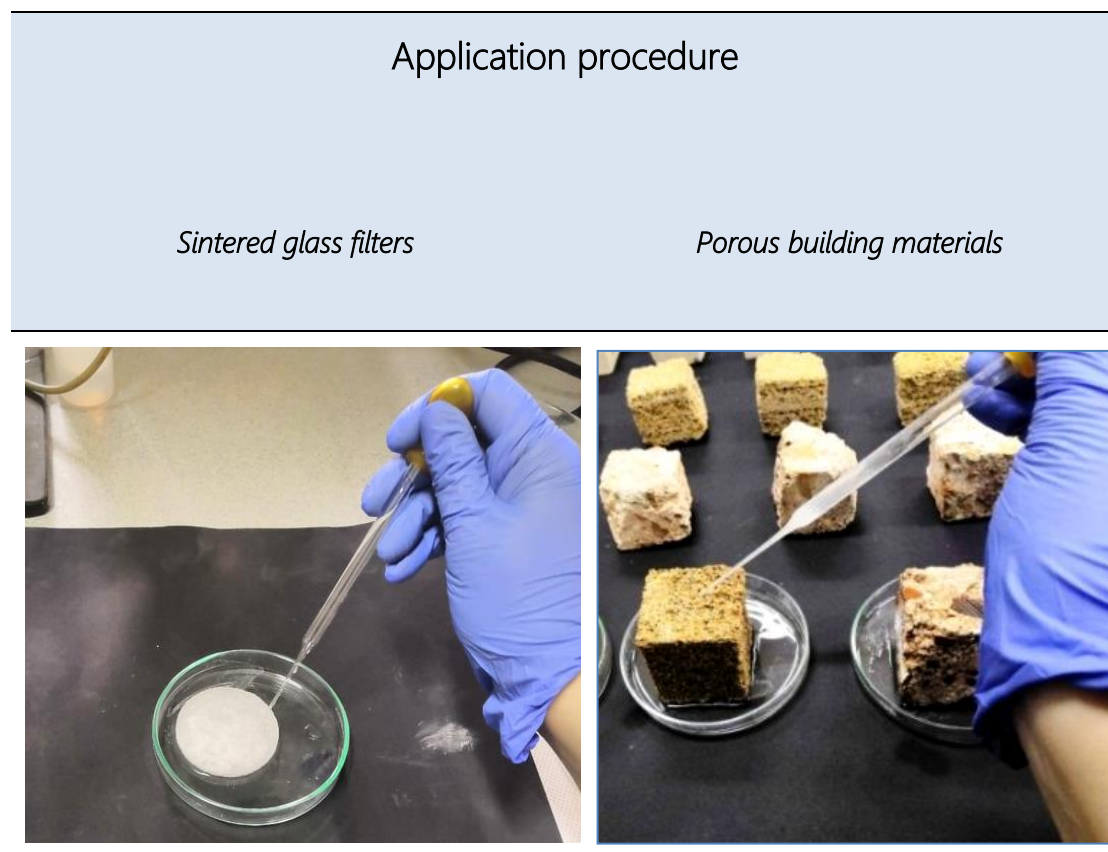


Fig.7.2 Application procedure of the newly synthesized dispersions of $\text{Ca}(\text{OH})_2$ via pipette

The nanolime dispersions were being placed under ultrasonic agitation throughout the application procedure. The application of the nanolime dispersion was completed after 10 consecutive applications. Upon application completion, the samples were stored in a sheltered box for 28 days, under laboratory atmospheric conditions ($T=20^\circ\text{C}$, $\text{RH}=60\text{-}80\%$). The curation time was 28 days, according to the common laboratory practice.

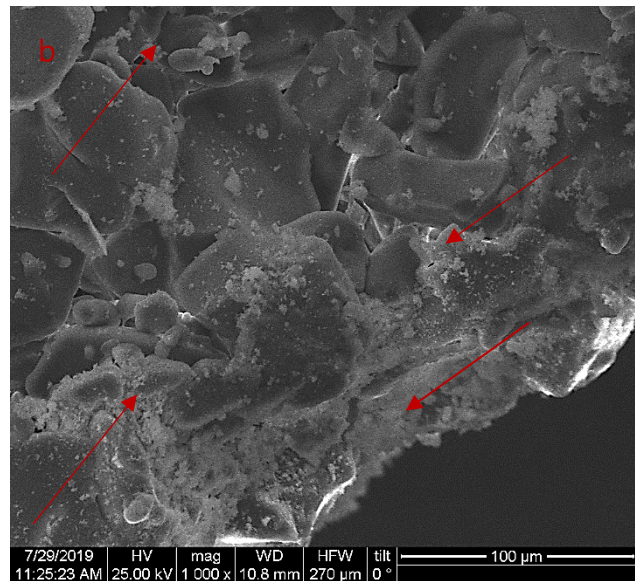
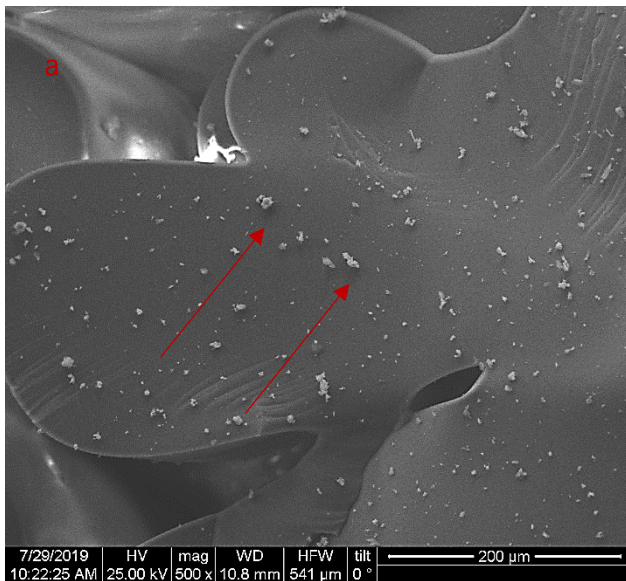
7.2 Application results

7.2.1 Application results on glass filter discs of various porosity

In all three filter disc specimens, the six dispersions of $\text{Ca}(\text{OH})_2$ nanoparticles penetrated throughout the full width of the specimens of 5mm without separation of the nano-particles. The deposition of $\text{Ca}(\text{OH})_2$ nanoparticles within the filter pore network is presented in Fig. 7.3, in fractured sections. The different dispersion mediums did not affect the penetration of the dispersions and the deposition of the $\text{Ca}(\text{OH})_2$ nanoparticles.

In all types of glass filters (P0, P4, P5), the nanoparticles were deposited on the grains and inside the pores, as illustrated in Figures 7.3 to 7.5. The deposition of nanoparticles is characterized as random or non-oriented. Compared to the P0 filter disc (160-250 μm), the deposition of the nanoparticles in the cases of P4 and P5 was denser, due to the smaller pore-size of these two specimens. In addition to this, all dispersions penetrated through the discs without the separation of the liquid and solid phase.

In all cases calcite crystals of rhombohedral structure and uniform size were observed after carbonation.



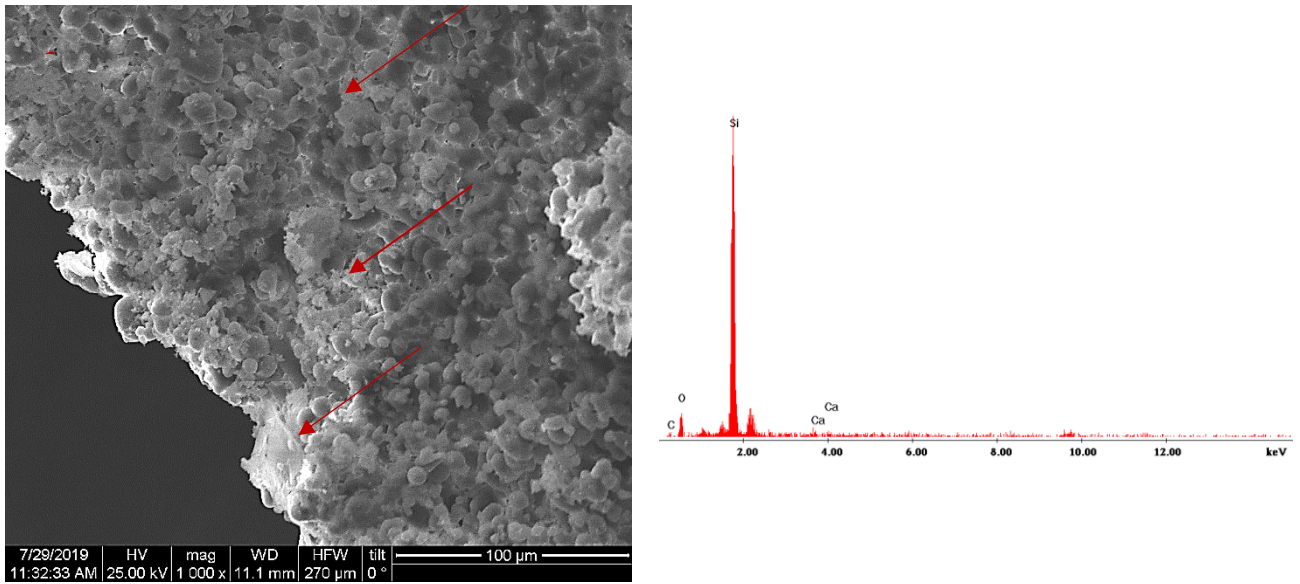


Fig.7.3 Representative images of the application of the dispersions and deposition of the $\text{Ca}(\text{OH})_2$ nanoparticles on the grains and inside the pores of (a) P0 filter disc ; (b) P4 filter disc ; (c) P5 filter disc and (d) EDAX of the filter disc substrate

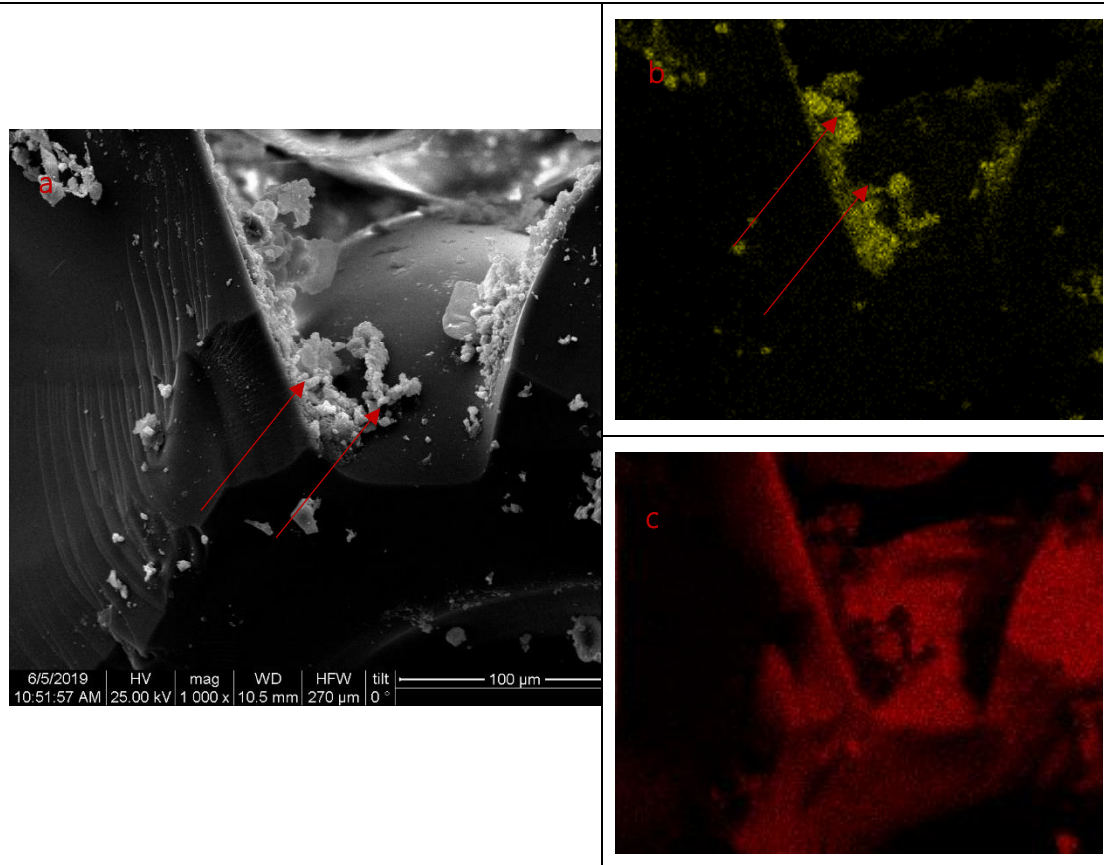


Fig.7.4 (a) $\text{Ca}(\text{CO})_3$ nanoparticle clusters deposited inside the pores of P0 filter disc (B06_20nbs80isptx100 scale bar at 100 μm); EDAX mapping analysis (b) of Ca and (c) of Si

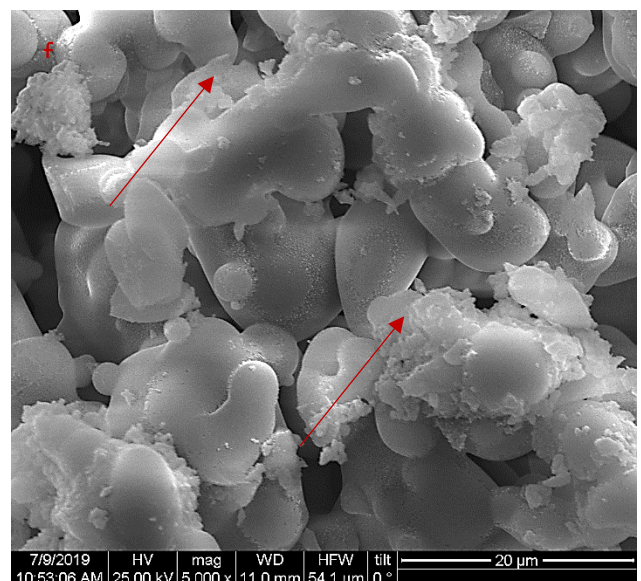
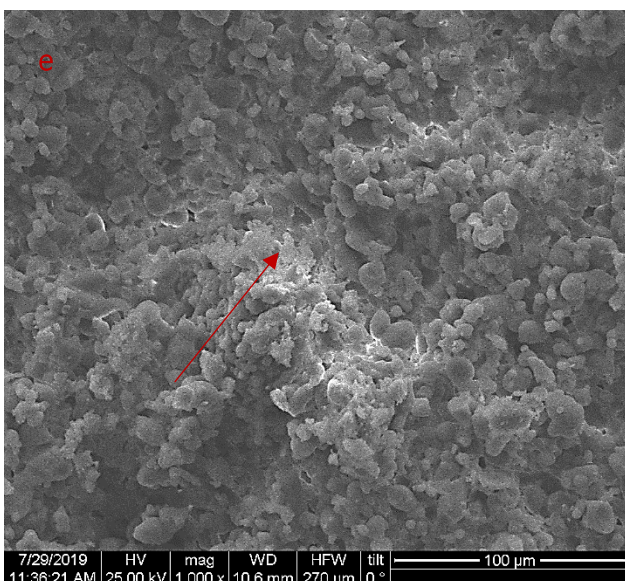
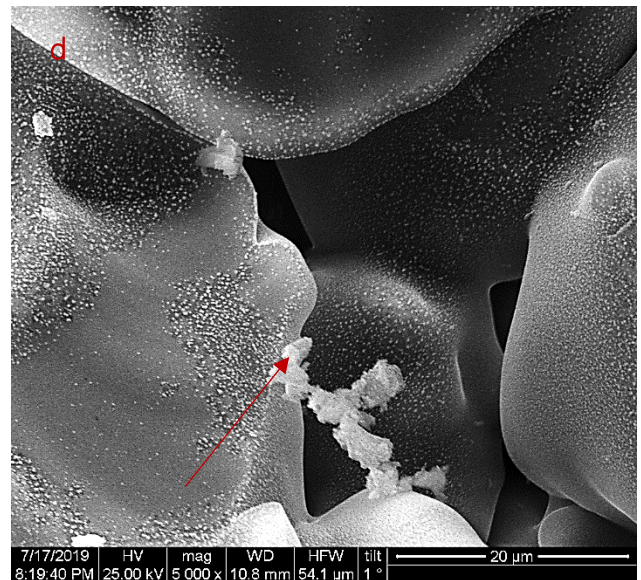
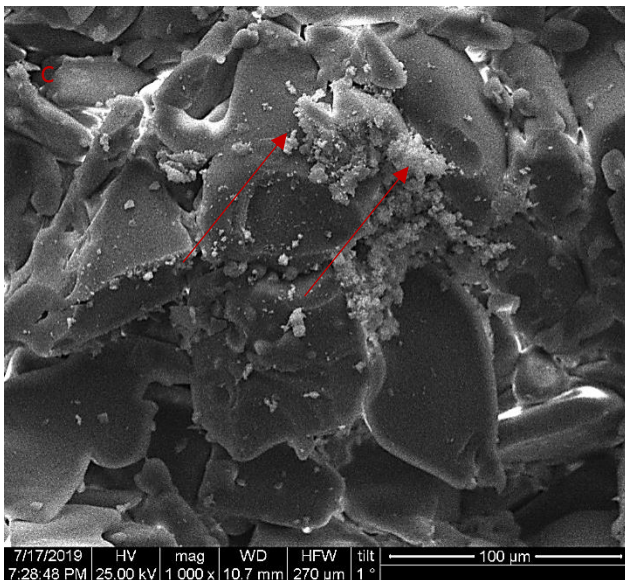
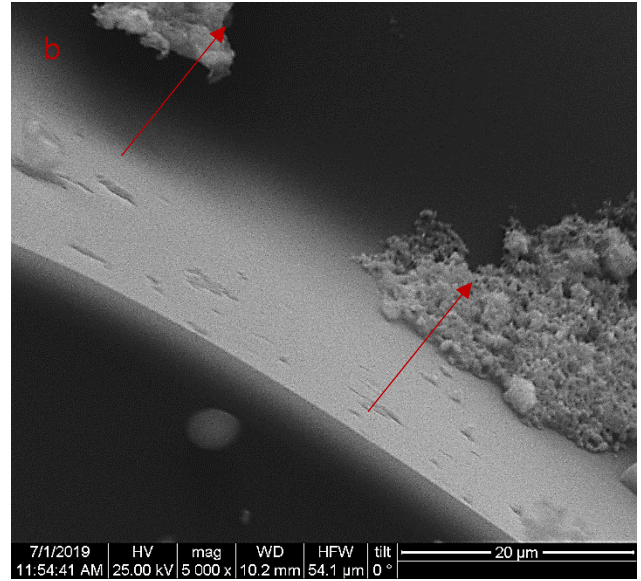
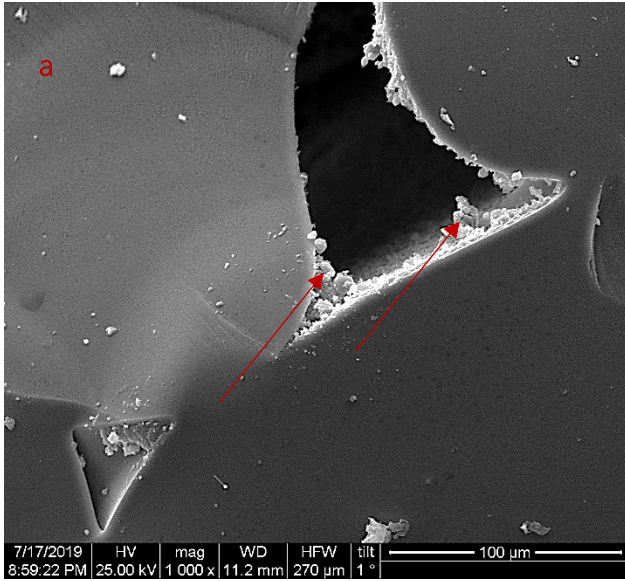


Fig.7.5 Representative images of SEM of the treated filtered discs of P0 (a) (scale bar art 100 μ m) and (b)(scale bar art 20 μ m); P4 (c) (scale bar art 100 μ m) and (d)(scale bar art 20 μ m); and P5 (e) (scale bar art 100 μ m) and (f) (scale bar art 20 μ m);

7.2.2 Application results on porous building materials

The evaluation of the penetration ability of the six Ca(OH)₂ dispersions indicated the easy penetration of the dispersions inside sandstone specimens, contrary to the poor and superficial penetration ability of the dispersions in the limestone and lime mortar (Fig. 7.6, 7.8 and 7.10 respectively).

In the case of the *limestone specimens*, the nanolime dispersions (B06_100nbs, B06_50w50isptx100 and B06_20w80isptx100) presented an increased penetration ability inside the limestone reaching the 2,2 mm (Fig. 7.6a, c and e), whereas B06_100nbs, B06_50w50isptx100and T05_20w80isptx100 nano-dispersions reached between 0,7 to 1,5 mm depth below surface (Fig. 7.6 b, d and f).

In the case of the *sandstone specimens*, B06_100nbs,B06_20nbs80isptx100, B06_20w80isptx100 and T05_20w80isptx100 nanodispersions reached an enhanced penetration ability inside the limestone reaching the 15 to 30 mm below surface (Fig. 7.8 a, d, e and f), whereas B06_100nbs100 and B06_50w50isptx100reached 8,4 to 11 mm (Fig. 7.8 b and c).

In the case of *lime mortars* , B06_100nbs, and B06_20nba80isptx100 nanodispersions exhibited limited penetration ability inside the mortars -about 1,1 mm (Fig. 7.10a and d), whereas B06_100nbs100 B06_50w50isptx100, B06_20w80isptx100, and T05_20w80isptx100 reached 0,7 mm (Fig. 7.10 b, c, e and f).

It must be mentioned that in the cases of B06_100nbs, B06_100nbs100 and B06_20nba80isptx100, the Ca(OH)₂ nano-dispersions were characterized by low colloidal stability (Graph 6.4) and enhanced penetration ability into the porous substrate. This underlined the fact that in the case of water enriched with O₂ NBs, there is no relation between stability and penetration ability.

Overall, the examination of the treated samples after 28 days in SEM/EDX (Fig. 7.7, 7.9 and 7.11) underlined the enhanced penetration inside sandstone specimens (Fig. 7.9), contrary to the poor penetration close to the surface, observed in the cases of the limestone (Fig. 7.7) and mortar specimens (Fig. 7.11).

Carbonation inside pores

The examination of the treated specimens in SEM after 28 days indicated the formation of calcite crystals of uniform size and the absence of portlandite crystals. The SEM examination revealed the following results:

- In the case of the *limestone* specimens the formation of scalenohedral calcite crystals were identified (Fig. 7.6 b and c). The size of the calcite crystals was categorized into two groups: a) larger calcite crystals of dimensions between 190 nm and 240 nm (Fig. 7.6b) and b) smaller calcite crystals of dimensions between 60 nm and 130 nm (Fig. 7.6c). The presence of the latter category could be attributed to the pore-network of the limestone specimens.
- In the case of the *sandstone* specimens the formation of tabular and scalenohedral calcite crystals were identified (Fig. 7.8 b and c). The presence of tabular calcite crystals in the cases of B06_100nbstx100 and B06_50w50isptx100 (Fig. 7.8 b) could be attributed to the aqueous part of the dispersion medium. Finally,
- in the case of the lime *mortar* specimens, the formation of scalenohedral calcite crystals of dimensions between 190 nm to 270 nm were identified (Fig. 7.10b and c). The analytical presentation of all results of the deposition of the six optimum dispersions are presented in Appendix E.

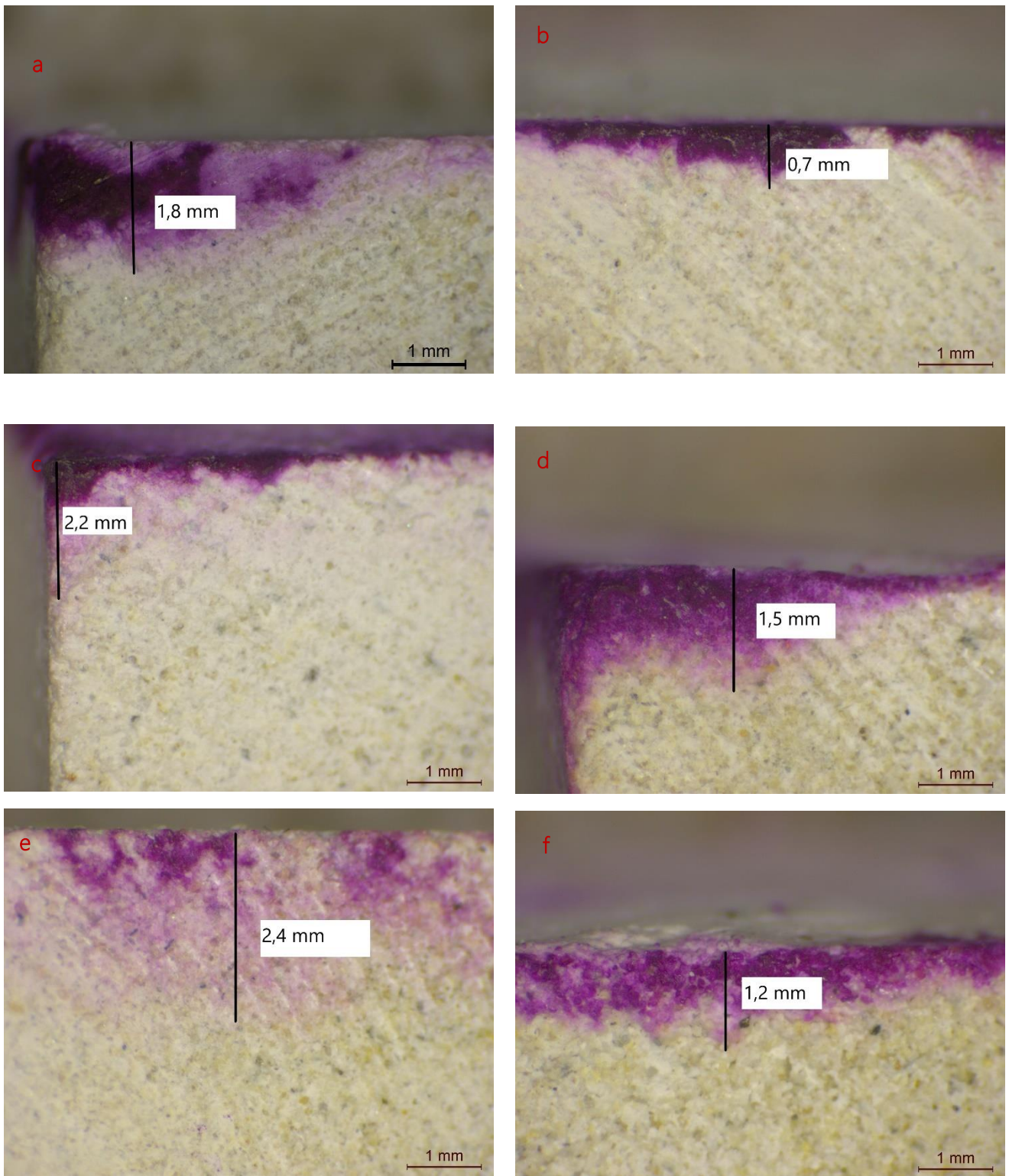


Fig.7.6 Observations of the penetration ability of the dispersions through the phenolphthalein test on the top of the limestone specimens (a) B06_100nbs ; (b) B06_100nbstx100; (c) B06_50w50isptx100; (d) B06_20nbs80isptx100; (e) B06_20w80isptx100; and (f) T05_20w80isptx100 (scale bar at 1 mm)

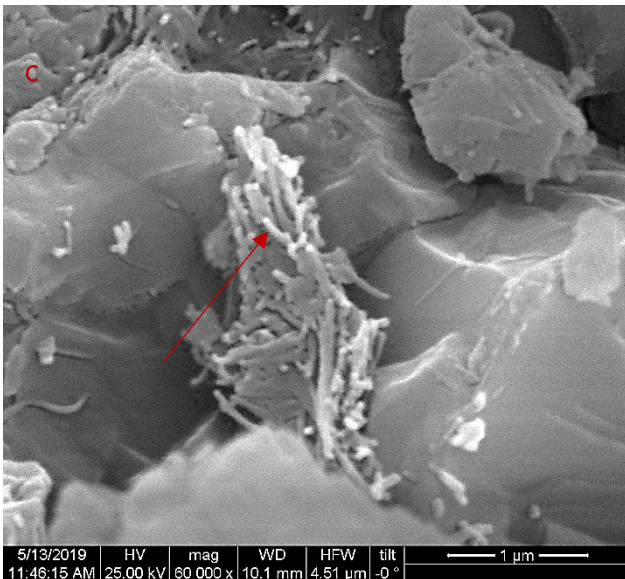
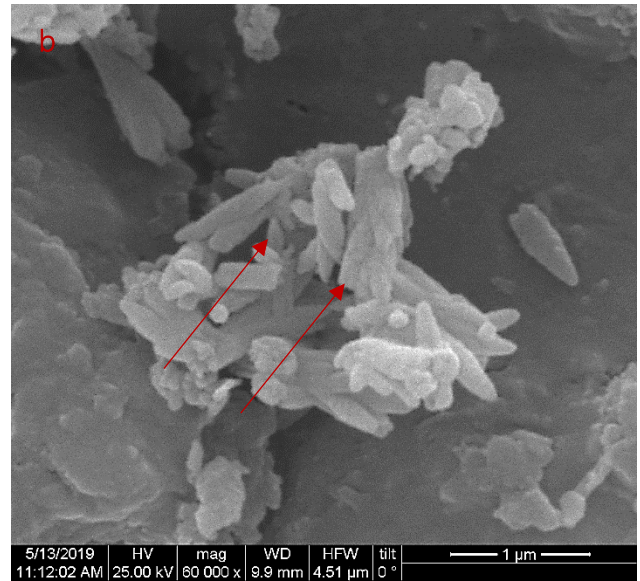
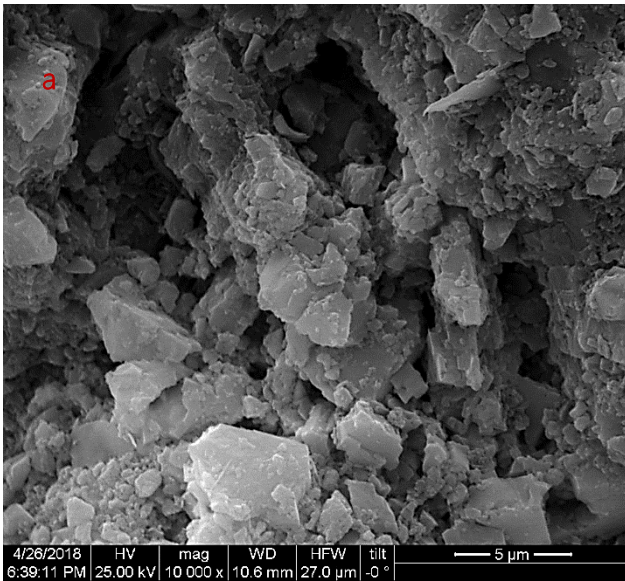


Fig.7.7 Representative SEM observations of the limestone samples (a) untreated (scale bar at 1 μm) and treated (b) and (c) (scale bar at 1 μm)

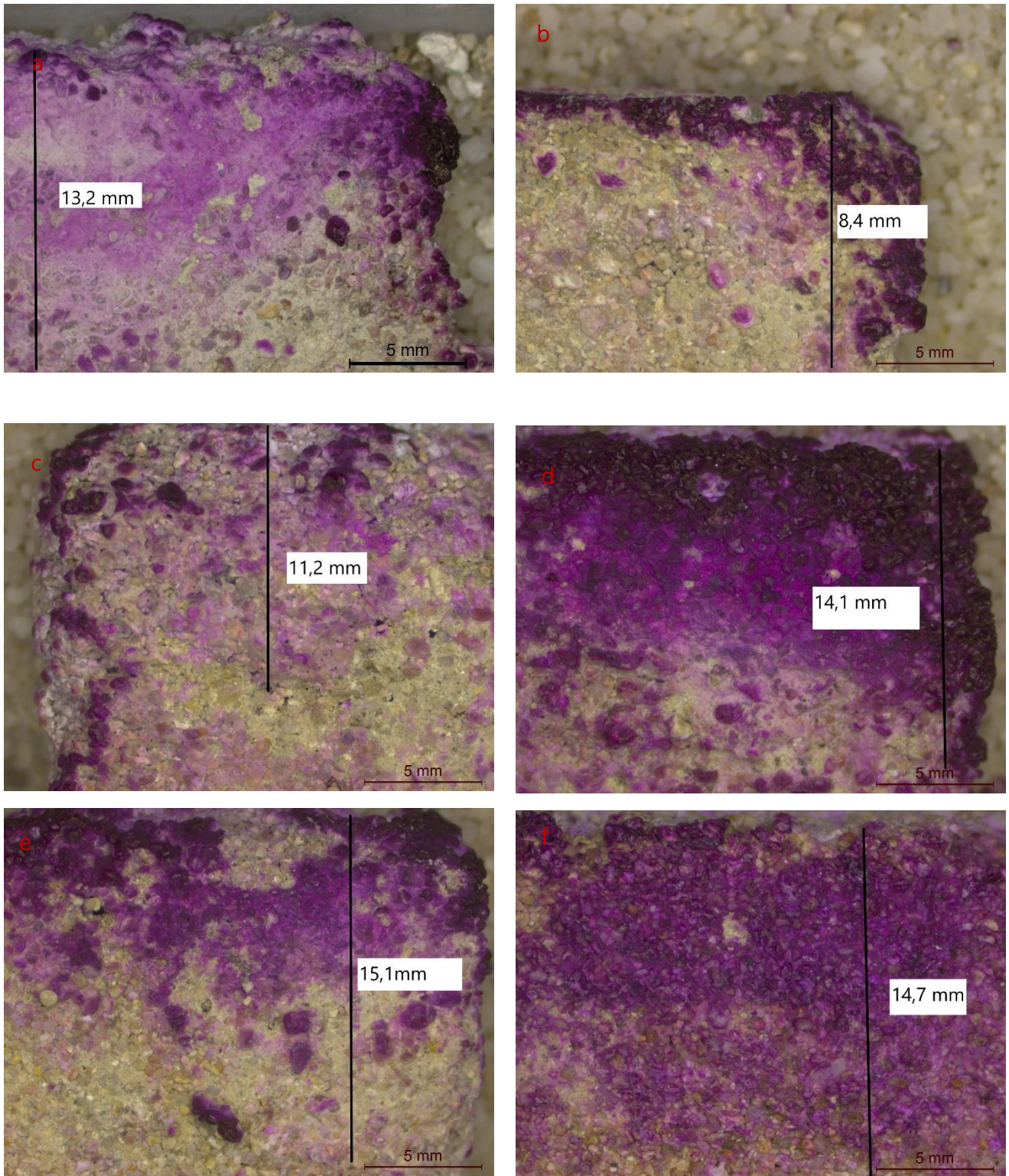


Fig. 7.8 Observations of the penetration ability of the dispersions through the phenolphthalein test on the top of the sandstone specimens (a) B06_100nbs ; (b) B06_100nbstx100; (c) B06_50w50isptx100; (d) B06_20nbs80isptx100; (e) B06_20w80isptx100; and (f) T05_20w80isptx100 (scale bar at 5 mm)

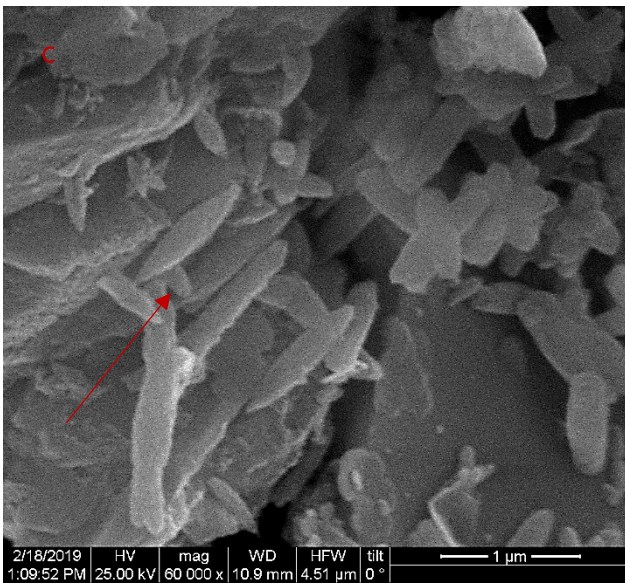
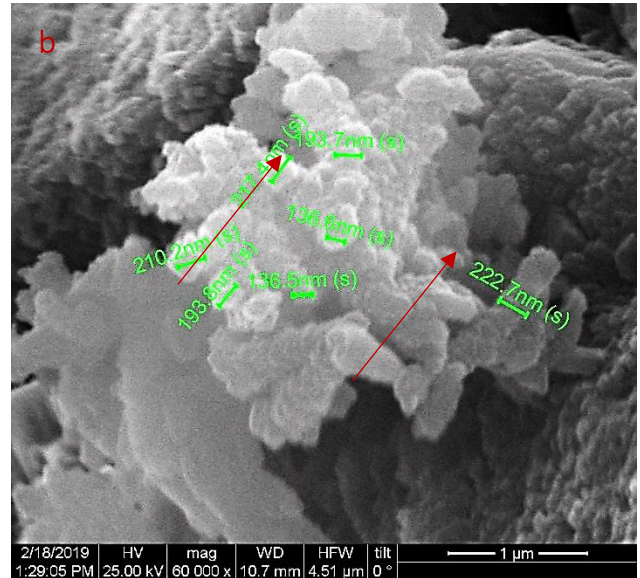
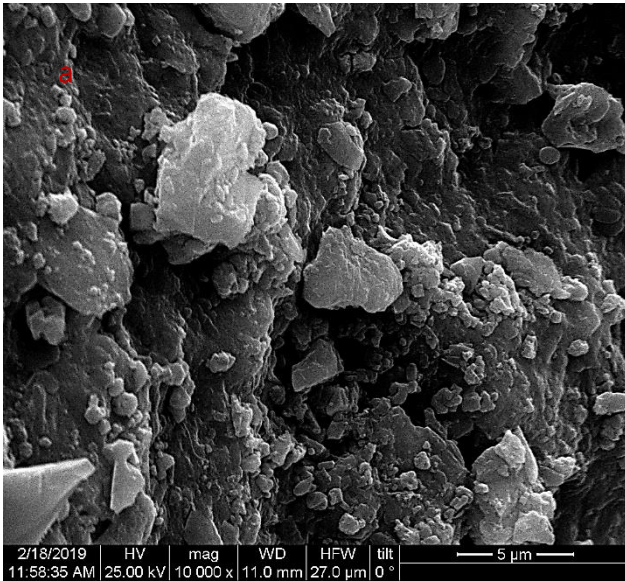


Fig.7.9 Representative SEM observations of the sandstone samples (a) untreated (scale bar at 1 μm) and treated (b) with B06_100nbstx100 and B06_50w50isptx100 and (c) (scale bar at 1 μm)

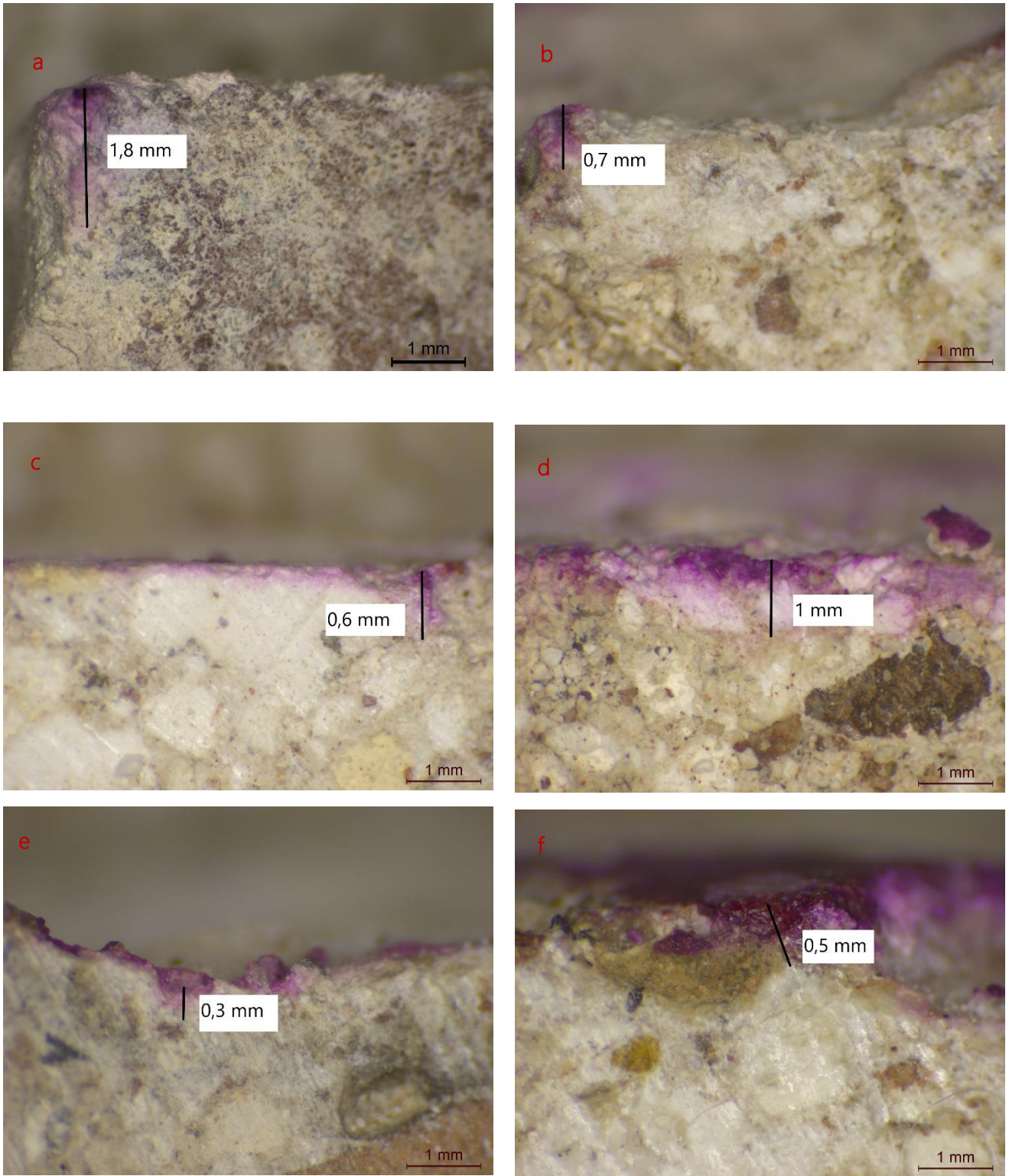


Fig. 7.10 Observations of the penetration ability of the dispersions through the phenolphthalein test on the top of the mortar specimens (a) B06_100nbs ; (b) B06_100nbstx100; (c) B06_50w50isptx100; (d) B06_20nbs80isptx100; (e) B06_20w80isptx100; and (f) T05_20w80isptx100 (scale bar at 1 mm)

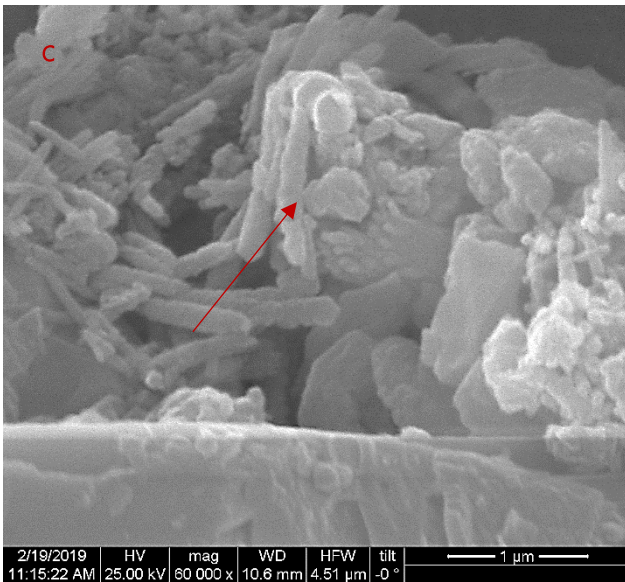
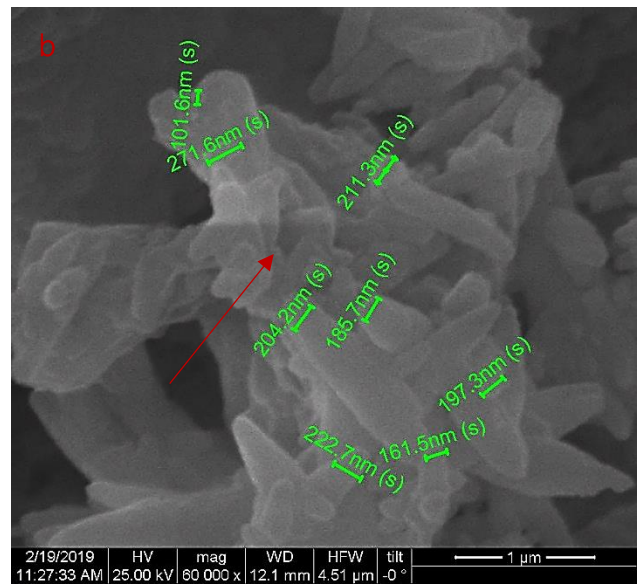
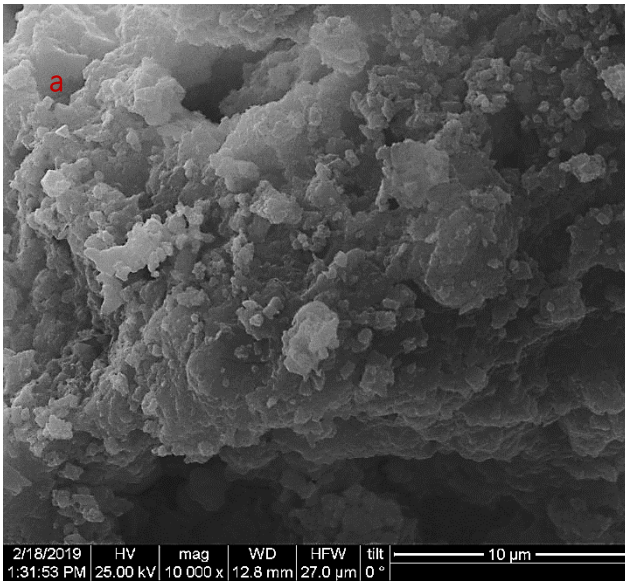


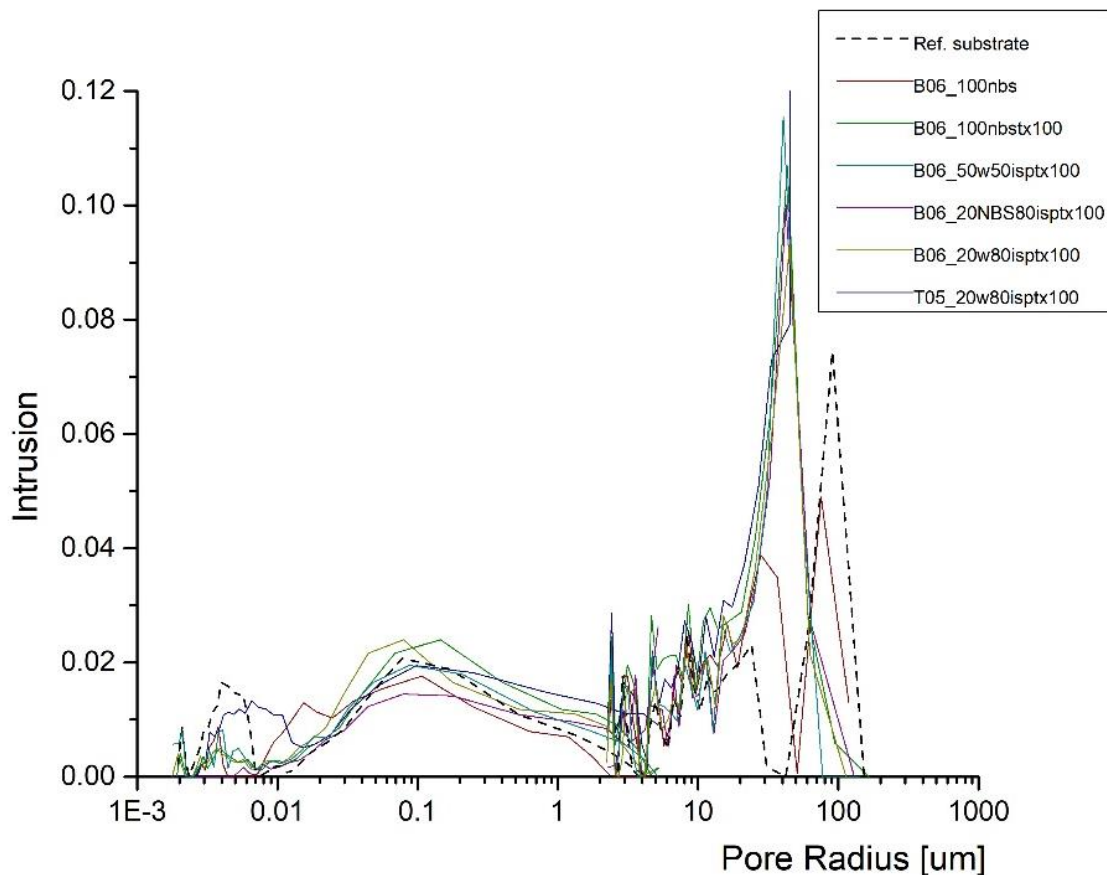
Fig.7.11 Representative SEM observations of the limestone samples (a) untreated (scale bar at 1 μm) and treated (b) and (c) (scale bar at 1 μm)

Porosity effects

Based on the enhanced penetration ability of the optimized nanolime in the sandstone specimens, the pore size distribution curve of the treated sandstone samples was determined by MIP.

As observed in Graph 7.3, the application of the six dispersions the application of the six nanolime dispersions led to the intense reduction of the pore volume at the pores of 100 μm and to a slight reduction of pore volume at the pores range of 1 to 10 nm. The curve was shifted downwards at the range of the larger pores (1 to 10 μm) and presented a slight increase at the range of the capillary pores (1 to 1000 nm). The discontinuity presented on the curve was due to the interval between the measurement under low pressure (for the coarser pores) and the high pressure (finer pores).

The reduced size of $\text{Ca}(\text{OH})_2$ nanoparticles (150 to 350 nm, Table 6.2) facilitated their access to the finer pores, sifting the main curve downwards at the range of the larger pores (10 to 100 microns). This can be attributed to the way of the deposition of the nanoparticles forming populations of rhombohedral calcite crystals with scalenohedral terminations inside the pores of the substrate of the treated sandstones.



Graph 7.3 Pore size distribution curves of the untreated and treated sandstone specimens

Chapter 8 – Conclusions

8.1 Conclusions

Within the context of this research thesis, the synthesis of aqueous dispersions of $\text{Ca}(\text{OH})_2$ nanoparticles was studied. This was realized through the study of the parameters affecting the morphological characteristics (size and shape) of the $\text{Ca}(\text{OH})_2$ nanoparticles and the rheological characteristics of their consequent dispersions (colloidal stability and penetration ability) was carried out. The effect of the modification parameters was examined on both top-down and bottom-up synthetic routes, while the interpretation of the results was implemented on the basis of their effect on:

- a) morphological characteristics of the $\text{Ca}(\text{OH})_2$ nanoparticles (*Module 1*),
- b) colloidal stability of the dispersions developed (*Module 2*)
- c) penetration and deposition of $\text{Ca}(\text{OH})_2$ nanoparticles in porous substrates (*Module 3*)

The interpretation of the research results derived from this research project are presented below:

8.1.1 Morphological characteristics of the $\text{Ca}(\text{OH})_2$ nanoparticles

A. The top-down method

The examination of the 8-years matured lime putty in the SEM and XRD revealed the beneficial effect of time in the drastic reduction of $\text{Ca}(\text{OH})_2$ particles size. However, the presence of several agglomerates of $\text{Ca}(\text{OH})_2$ nanoparticles underlined the need of high-energy ultrasonic agitation, in order to produce effective nanolime dispersions through the top-down route .

The experimental results indicated that the shape and the size of $\text{Ca}(\text{OH})_2$ nanoparticles produced through the top-down route depend on:

a) the sonication energy

The continuous application of 500W for a time period of 30 minutes resulted in the de-agglomeration of the $\text{Ca}(\text{OH})_2$ nanoparticles and the formation of rounded, needle like and of undetermined shape $\text{Ca}(\text{OH})_2$ nanoparticles of dimensions between 160 nm to 800 nm.

b) the type of dispersion medium during sonication

- i) The innovative use of O_2 nanobubbles (nbs) enriched water resulted in the production of rounded and undetermined shape $\text{Ca}(\text{OH})_2$ nanoparticles, of dimensions in between 200 nm and 500 nm. However, some agglomerates of $\text{Ca}(\text{OH})_2$ nanoparticles were also present.
- ii) The use of a mixed polar dispersion medium with the addition of 2-propanol resulted in the formation of rounded $\text{Ca}(\text{OH})_2$ nanoparticles of dimensions around 200 nm. Further

interpretation of the results of the top-down route revealed the presence of flake-like $\text{Ca}(\text{OH})_2$ nanoparticles, being characterized by a polycrystalline structure.

The flake-like shape of the $\text{Ca}(\text{OH})_2$ nanoparticles was attributed to the aging procedure of the lime putty.

The rounded shape of the nanoparticles was attributed to the adsorption of the molecules of 2-propanol on the surface of the $\text{Ca}(\text{OH})_2$ nanoparticles.

c) the use and the type of surfactants

The addition of Triton X-100 led to the reduction of the size of nanoparticles and the absence of agglomerates, due to the adsorption of the polar head of the Triton X-100 onto the surface of the $\text{Ca}(\text{OH})_2$ nanoparticles.

The addition of n-octylamine led to a small reduction of size of the nanoparticles and to the presence of agglomerates.

B. The bottom-up method

The implementation of the bottom-down synthetic route led to the formation of hexagonal $\text{Ca}(\text{OH})_2$ particles in the macro-scale and $\text{Ca}(\text{OH})_2$ nanoparticles of undetermined shape. The large size of the hexagonal particles underlined the need of modification of the parameters of the experimental procedure.

The experimental results indicated that the shape and the size of $\text{Ca}(\text{OH})_2$ nanoparticles produced through the bottom-up method depend on:

a) the sonication energy

The continuous application of 500W for a time period of 30 minutes resulted to the de-agglomeration of the $\text{Ca}(\text{OH})_2$ nanoparticles and to the formation plate-like regular $\text{Ca}(\text{OH})_2$ nanoparticles of dimensions between 80 nm to 400 nm. The plate-like shape of the nanoparticles is connected with the increase of the specific surface area and so to the increase of their reactivity. Also, it presented an homogeneity in terms of the size of the nanoparticles.

The reduction of time subjected to sonication did not had any effect on the size of the nanoparticles and the increase of the time period from 30 min to 60 min had negative effect on their shape. So, the selected time period, the intensity of the energy that was transferred to the $\text{Ca}(\text{OH})_2$ nanoparticles had a direct effect on the morphological characteristics of the nanoparticles.

b) the dispersion medium

i) The innovative use of O_2 nanobubbles (nbs) enriched water as dispersion medium at the bottom-up synthetic route led to a slight decrease of the particles size

Also, supported the formation of hexagonal and plate-like crystals of $\text{Ca}(\text{OH})_2$ absence of agglomeration and aggregation phenomena. The newly formed $\text{Ca}(\text{OH})_2$ nanoparticles were characterized as monocrystalline structures.

The modifications of the morphological characteristics of the newly formed nanoparticles were attributed to the nucleation of the nanobubbles on the surface of the nanoparticles, forming a new homogenous population of nanoparticles of a diameter in between the diameter of the original nanoparticles and the O_2 -nanobubbles. In this way, the phenomenon of steric stabilization was implemented.

ii) The use of a mixed polar dispersion medium with the addition of 2-propanol led to the formation of rounded nanoparticles of reduced dimensions and increased specific surface area values. This alteration of the shape of the $\text{Ca}(\text{OH})_2$ was attributed to the adsorption of the molecules of 2-propanol on the surface of the $\text{Ca}(\text{OH})_2$ nanoparticles.

c) the use and the type of surfactants

i) The addition of non-ionic surfactant Triton X-100 led to a significant decrease of the nanoparticles. Moreover, it led to the absence of agglomeration and aggregation phenomena reflecting the steric stabilization. Also, it led to the production of nanoparticles of homogeneity in terms of size.

The reduced size of the nanoparticles can be attributed to the reported interaction between Ca^{2+} and the functional polyoxyethylene group of Triton X-100, that has proven to inhibit the further nucleation of the primary particles and the presence of aggregation phenomena. This was reflected to the reduction of both the size of the nanoparticles and the average crystallite size of the results of the bottom-up synthetic route.

ii) the addition of n-octylamine led to the formation of hexagonal and plate-like $\text{Ca}(\text{OH})_2$ nanoparticles, but the results were characterized by a large variety of different dimensions of $\text{Ca}(\text{OH})_2$ nanoparticles. It also resulted in the reduction of the size of the nanoparticles due to the adsorption of the polar head of the n-octylamine onto the surface of the $\text{Ca}(\text{OH})_2$ nanoparticles through the formation of H-bonds.

iii) The addition of the cationic surfactant amylamine led to a decrease of the size of the newly formed $\text{Ca}(\text{OH})_2$ nanoparticles when compared to the results of the original bottom-up synthetic route. But the results characterized by a large variety of different dimensions of $\text{Ca}(\text{OH})_2$ nanoparticles. The reported modifications were attributed to the adsorption of amylamine on the surface of the $\text{Ca}(\text{OH})_2$ nanoparticles.

d) the dispersion medium and the use of surfactant during sonication

The combined modification of the polar dispersion medium along with the addition of Triton X-100 proved to have a direct effect on the morphological characteristics of the $\text{Ca}(\text{OH})_2$ nanoparticles. The combined use of Triton X-100 with the O_2 nanobubbles (nbs) enriched

aqueous solution led to the synthesis of hexagonal and plate-like Ca(OH)_2 nanoparticles and nanoparticle clusters of reduced size and to the absence of aggregates. Also, the nanoparticles were characterized as crystalline. The addition of 2-propanol proved to act as a steric barrier inhibiting the formation of agglomerates.

e) the environment of the synthesis (open air vs inert conditions)

The inert He-conditions resulted in the reduction of the size of the nanoparticles and to the synthesis of plate-like Ca(OH)_2 nanoparticles of homogeneity in terms of size and shape. The modification of the experimental equipment led to the development of a system similar to a batch reactor. In this way, the implementation of the bottom-up synthetic route was realized under conditions of constant temperature of 90°C favoring the realization of the reaction.

f) the mixing processes

The modification of the drop to drop mixing of the aqueous solutions of $\text{CaCl}_2/\text{Triton X-100}$ and NaOH instead of the immediate mixing proposed by the literature review led to the production of hexagonal and plate-like nanoparticles of reduced size. The Ca(OH)_2 nanoparticles were characterized by homogeneity in terms of size and shape.

8.1.2 Development of Si- Ca(OH)_2 nanocomposites:

The synthesis of Si- Ca(OH)_2 nanocomposites was accomplished through the implementation of two different synthetic routes: a) one pot synthesis via the sol-gel method and b) fabrication of janus nanoparticles.

The experimental results indicated that the morphological characteristics of the Si- Ca(OH)_2 nanocomposites were modified due to the formation of the C-S-H phase after a time period of at least 1 year.

a) one pot synthesis via the sol-gel method

The presence of calcite at the end of fourth day (final stage) of the reaction (underlined the realization of the carbonation reaction). In fact, the realization of the carbonation reaction proved to be favored, instead of the potential formation of calcium-silicate-hydrate (C-S-H) phases. However, after two years, the calcium-silicate-hydrate (C-S-H) phase was detected indicating a post-reaction with Ca ions.

b) fabrication of janus nanoparticles.

The monitoring of the first modification revealed the domination of the flower-like morphology attributed to the use of the waterglass. Inside this formation Ca(OH)_2 nanoparticles were observed. The monitoring of the modification revealed the presence of large conglomerates consisted of Ca(OH)_2 nanoparticles. The presence of film that

covered the conglomerates of the Ca(OH)_2 was attributed to the hydration procedure of celitement. After one year the presence of compact material consisted of flake-like formations and Ca(OH)_2 nanoparticles was evident. After one year the calcium-silicate-hydrate (C-S-H) phase was detected.

[8.1.3 Colloidal stability of the dispersions \$\text{Ca\(OH\)}_2\$ nanoparticles \(Module 2\)](#)

The comparative evaluation between the two synthetic routes underlined the increase colloidal stability in the case of the top-down route, underlined enhanced colloidal stability of the dispersion produced via the top-down route. Overall, the increase of the colloidal stability of the dispersions was attributed to the decrease of the surface tension between the Ca(OH)_2 nanoparticles and the dispersion medium. Specifically:

The addition of the non-ionic surfactant Triton X-100 resulted to the increase of the colloidal stability due to the formation of a steric barrier leading to the inhibit of the agglomeration between the Ca(OH)_2 nanoparticles.

The use of the O_2 nanobubbles (nbs) enriched water as dispersion medium at the bottom-up synthetic route resulted to a slight increase of the colloidal stability of the newly formed dispersions due to the steric stabilization though the use of adsorption of nanobubbles on the surface of the nanoparticles.

The colloidal stability of the newly formed Ca(OH)_2 nanodispersions was enhanced by increasing the amount of 2-propanol in the dispersion medium. The enhanced colloidal stability was attributed to the adsorption of the 2-propanol molecules on the surface of Ca(OH)_2 nanoparticles, leading to the steric stabilization of the dispersion and inhibiting the agglomeration phenomena.

[8.1.4 Carbonation monitoring](#)

The systematic monitoring of carbonation at two different relative humidity conditions (55% and 95%) revealed the immediate formation of calcite from the first hour. The comparative evaluation on the effect of the two different values of relative humidity revealed the dominant presence of calcite in both cases. This related to the high percentage of relative humidity that enabled the realization of the carbonation reaction, through the dissolution of portlandite in the water film adsorbed on its surface and the consequent realization of the carbonation reaction and precipitation of CaCO_3 . The use of 2-propanol proved to have a slight decrease of the carbonation efficiency (yield) of the final product.

The formation of Ca-alkoxides in the case of the top-down route was documented, in the presence of 2-propanol. This was attributed to the reaction between the Ca(OH)_2 nanoparticles and the 2-propanol.

Penetration and deposition of the dispersions in porous substrates

i) Penetration ability: The evaluation of the penetration ability in different porous substrates underlined the key role of the microstructural characteristics of the substrates on the final result, since all tested nanodispersions exhibited very similar penetration ability in the same type of substrates.

Thus, the better performance was resulted for all nanodispersions in the sandstone substrates, that are characterized by an open and large pores network.

ii) In the case of the O₂ nanobubbles (nbs) enriched water as dispersion medium the Ca(OH)₂ nano-dispersion proved to be characterized by low kinetic stability and enhanced penetration ability into the porous substrate. This underlined the fact that in this case, the relation between kinetic stability and the penetration ability of the nano-dispersions are not follow the same trend. The study and application of this dispersion medium was characterized as promising since it improves the morphological characteristics of the nanoparticles and is characterized by the absence of aggregation phenomena between the nanoparticles and seems to increase the penetration ability of the nanoparticles

iii) Deposition of the Ca(OH)₂ nanoparticles and completion of the carbonation process: The evaluation of the penetration ability of the dispersions of Ca(OH)₂ nanoparticles underlined the penetration of the dispersions inside the porous substrates of the sandstone specimens, contrary to the poor penetration at the layers close to the surface, observed in the cases of the limestone and calcareous mortar specimens. The Ca(OH)₂ nanoparticles were precipitated and deposited on the grains and the binding medium of the substrates and inside the pores. Upon completion of the carbonation process, in all cases t scalenohedral calcite crystals of uniform size and of morphological characteristics similar to micritic calcite were observed. In the case of the limestone, smaller scalenohedral calcite crystals were detected. Also, in the case of the sandstones, the application of dispersions of high percentage of the aqueous part non-oriented calcite crystals were detected. These underlined the effect of the pore-network of the substrate and the dispersion medium on the precipitation of the nanoparticles

8.2 Future Research

This present research focused on the effect of different parameters on the synthesis of aqueous dispersions of Ca(OH)_2 nanoparticles of improved morphological and rheological characteristics. According to the experimental and theoretical issues raised during the implementation of this research, further topics that could be studied in the future are suggested:

- a) The results obtained through the use of O_2 nanobubbles, indicated a promising dispersion medium for the dispersions of Ca(OH)_2 nanoparticles. The use of different gases such as nitrogen (N_2), argon (Ar) or ambient air can be further studied. In this directions, other parameters that could be modified include the size and the concentration of nanobubbles, focusing on the steric stabilization of the Ca(OH)_2 nanodispersion.
- b) The development of Si- Ca(OH)_2 nanocomposites with controlled surface properties (hydrophobic or hydrophilic), based on the nanostructured texture of their surface
- c) To increase of the colloidal stability of the aqueous dispersions of Ca(OH)_2 nanoparticles though the reduction of the surface tension without the increase of the percentage of 2-propanol.
- d) The detailed monitoring and understanding of the implementation and completion of the carbonation process. This would lead to the control of the calcite phases and of the kinetics of the reaction through the modification of the parameters concerning the dispersions of Ca(OH)_2 nanoparticles leading to the increase of the efficacy of the consolidation action.

Appendix

A Presentation of all dispersions of Ca(OH)₂ nanoparticles

Sample I.D.	Description					
	Method	Water	O ₂ nbs	Organic solvent	Surfactant	Ultras.
T01	Top-down	100%	-	-	-	bath
B01	Bottom-up	100%	-	-	-	bath
B_03OHresin	Bottom-up (Dowex resin)	100%	-	-	-	bath
T02ultr	Top-down	100%	-	-	-	probe
B02ultr	Bottom-up	100%	-	-	-	probe
B02He	Bottom-up (Inert conditions)	100%	-	-	-	probe
T03tx100	Top-down	100%	-	-	TX100	bath
B04tx100a	Bottom-up	100%	-	-	TX100 (immediate mix.)	bath
B04TX100b	Bottom-up (Inert conditions)	100%	-	-	TX100 (immediate mix.)	probe
B04tx100c	Bottom-up (Inert conditions)	100%	-	-	TX100	probe
T03oc	Top-down	100%	-	-	n- Octylamine	probe
B04oc	Bottom-up (Inert conditions)	100%	-	-	n- Octylamine	probe

					(immediate mix.)	
B04oca	Bottom-up (Inert conditions)	100%	-	-	n- Octylamine	probe
B04am	Bottom-up (Inert conditions)	100%	-	-	Amylamine	probe
T04nb	Top-down	-	100%	-	-	bath
B05nbtX100a	Bottom-up	-	100%	-	TX100 (immediate mix.)	bath
B05nboca	Bottom-up	-	100%	-	n- Octylamine (immediate mix.)	bath
B05nb	Bottom-up (Inert conditions)	-	100%	-	-	probe
B05nbtX100	Bottom-up (Inert conditions)	-	100%	-	TX100	probe
T04_100w	Top-down	100%	-	-	TX100	probe
T04_80w20isp	Top-down	80%	-	20%isp	TX100	probe
T04_50w50isp	Top-down	50%	-	50%isp	TX100	probe
T04_20w40isp40ac	Top-down	20%	-	40%isp- 40%ac	TX100	probe
T04_20w80eth	Top-down	20%	-	80%eth	TX100	probe
T04_20w80isp	Top-down	20%	-	80%isp	TX100	probe

T04_10w90isp	Top-down	10%	-	90%isp	TX100	probe
B05_10w90isp	Bottom-up (Inert conditions)	10%	-	90%isp	TX100	probe
B06_100nbs	Bottom-up (Inert conditions)	0	100%	0	-	probe
B06_100nbstx100	Bottom-up (Inert conditions)	0	100%	0	TX100	probe
B06_50w50isptx100	Bottom-up (Inert conditions)	50%	0	50%isp	TX100	probe
B06_20nbs80isptx100	Bottom-up (Inert conditions)	0	20%	80%isp	TX100	probe
B06_20w80isptx100	Bottom-up (Inert conditions)	20%	0	80%isp	TX100	probe
T05_20w80isptx100	Top-down	20%	0	80%isp	TX100	probe

B Summary of the modified parameters of the synthetic procedures and their effect on the morphological characteristics of the Ca(OH)₂ nanoparticles

Presentation of the parameters and their effect on the morphological characteristics of the Ca(OH) ₂ nanoparticles		
Parameter	Top-down	Bottom-up
Sonication Energy	Dissolution of agglomerates Rounded, needle-like and of undetermined shape nps	Reduction of size Plate-like nps Homogeneity of size
Inert conditions	-	Hexagonal, plate-like and needle-like nps
Triton X-100 (non-ionic surfactant)	Reduction of size	Reduction of size Plate-like nps of hexagonal habit Homogeneity of size and shape
n-octylamine (non-ionic surfactant)	Presence of agglomerates	Reduction of size Plate-like nps of hexagonal habit
Amlylamine (cationic surfactant)	-	Increase of size Hexagonal, needle-like and rounded nps Polydispersity in terms of size and shape
O ₂ nbs enriched water	-	Reduction of size Plate-like nps of hexagonal habit Homogeneity of size and shape Absence of agglomerates and aggregates

		Monocrytalline structures
Mixed polar dispersion medium (2-propanol)	Reduction of size Rounded nps Presence of agglomerates Polycrystalline structures	Reduction of size Rounded and hexagonal nps Polycrystalline structures Increase of the specific surface area of the nps

C. Time period for subsection on ultrasound probe

The T4_100w was subjected to sonication with the use of an ultrasound probe for different time intervals in order to determine the optimum one for the experimental procedures. As it can be observed with the absence of the sonication procedure leads to the presence of large agglomerates and aggregates composed of the $\text{Ca}(\text{OH})_2$ nanoparticle clusters (Fig. Ap. Ca). After being subjected to sonication for a time period of 5 minutes, the T4_100w morphological characterization was characterized by the presence of $\text{Ca}(\text{OH})_2$ nanoparticle clusters and reduced presence of agglomerates (Fig. Ap. Cb). The subsection to sonication for a time period of 30 min resulted in presence of spherical and hexagonal $\text{Ca}(\text{OH})_2$ nanoparticles, of dimensions in between 100 nm and 350 nm and to the further reduction of the presence of agglomerates (Fig. Ap. Cc). Finally, the subsection to sonication for a time period of 60 min resulted in the further agglomeration of the nanoparticle clusters (Fig. Ap. Cd).

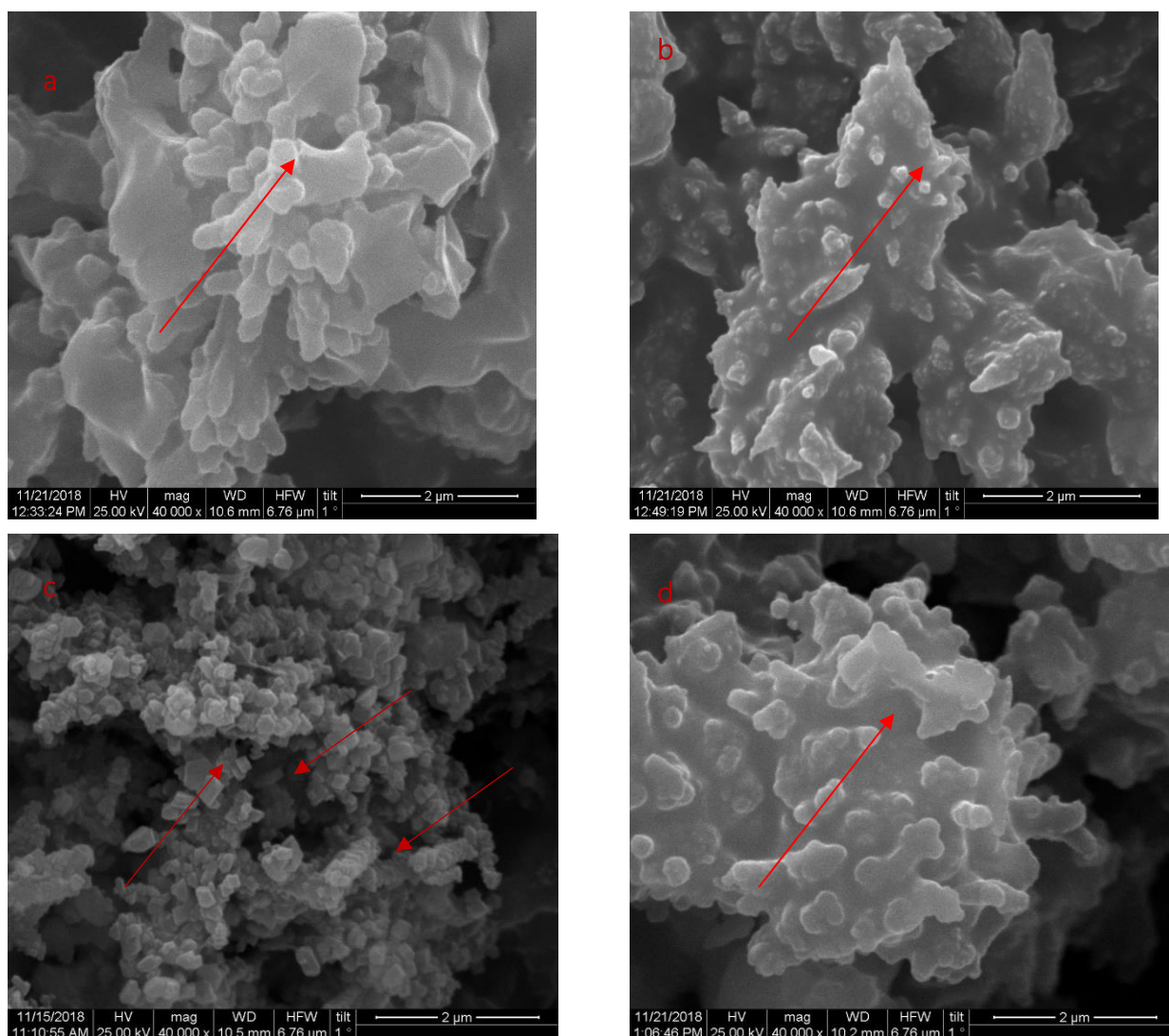


Fig. Ap. C SEM observations of T04w subjected to sonication for (a) 0 min. ; (b) 5 min. ; (c) 30 min. to ultrasound probe) and (d) 60 min. to ultrasound probe (scale bar at 2μm)

D. Addition of Triton X-100

The appropriate time period for the addition of non-ionic surfactant Triton X-100 to the bottom-up synthetic route (B01) was investigated by the use of SEM. The addition of the Triton X-100 in the aqueous solutions of CaCl_2 prior to the realization of the bottom-up synthetic route resulted in the synthesis of $\text{Ca}(\text{OH})_2$ nanoparticle clusters of regular and angular shape (Fig. Ap. Da). The nanoparticle clusters were characterized by a uniform shape and their dimensions vary between 200 nm to 270 nm. (Fig. Ap. Da). The addition of the Triton X-1001 after the completion of the synthetic procedure resulted to the synthesis of larger $\text{Ca}(\text{OH})_2$ particle clusters with flower-like formations. The non-ionic surfactant did not present to have any effect on the nucleation of the $\text{Ca}(\text{OH})_2$ particles (Fig. Ap. Db).

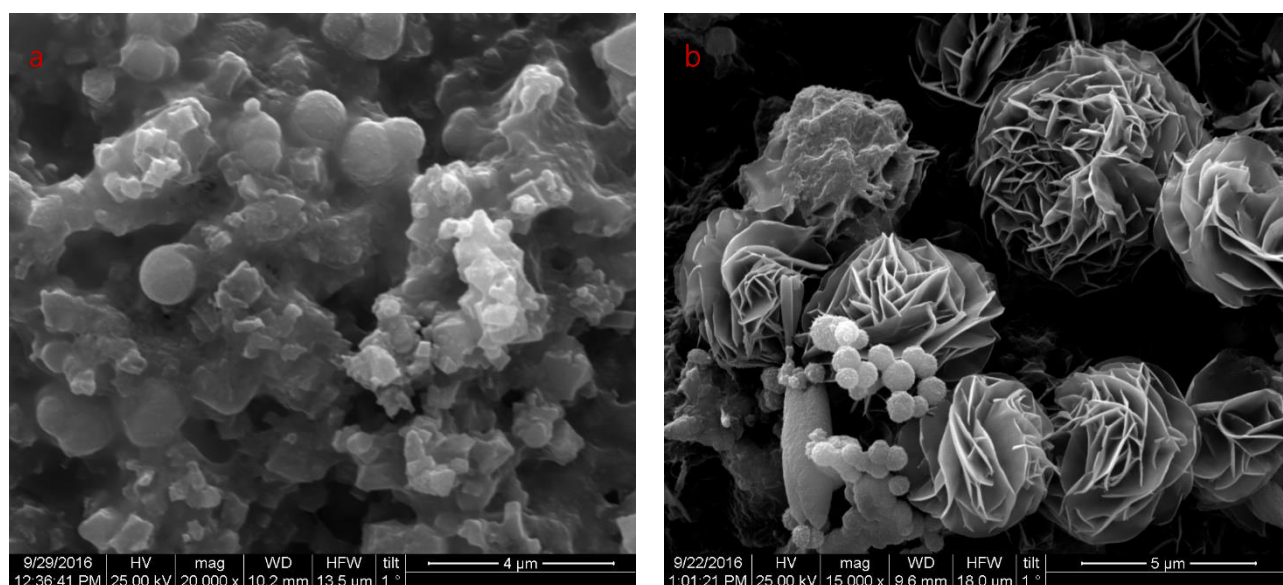


Fig. Ap. D SEM observations of the modification of the bottom-up synthetic route by the addition of the non-ionic surfactant (a) before the experimental procedure (scale bar at 4 μm) and (b) after the completion of the experimental procedure (scale bar at 5 μm)

E. Dowex resin-testing

The sufficient time period for the magnetic stirring of the B03OHresin was investigated by the use of SEM. The direct mixing of the aqueous solution of CaCl_2 and the anionic resin resulted in the formation of large aggregates (Fig. Ap. Ea). The subjection to magnetic stirring for a time period of 60 minutes resulted in the production of particle clusters of broad range of morphological characteristics (specifically: hexagonal, prismatic, fiber-like and of undetermined shape) with dimensions in the range of micro-scale. The particle clusters produced present a high tendency to form conglomerates (Fig. Ap. Eb). The increase of the time period of the experimental procedure (90min under magnetic stirring) did not present any improvements of the morphological characteristics in terms of the reduction of the size of the particles or the absence of agglomerates (Fig. Ap. Ec). Finally, the addition of the non-ionic surfactant Triton X-100, resulted production of hexagonal $\text{Ca}(\text{OH})_2$ particle clusters of dimensions belonging to the micro-scale (Fig. Ap. Ed).

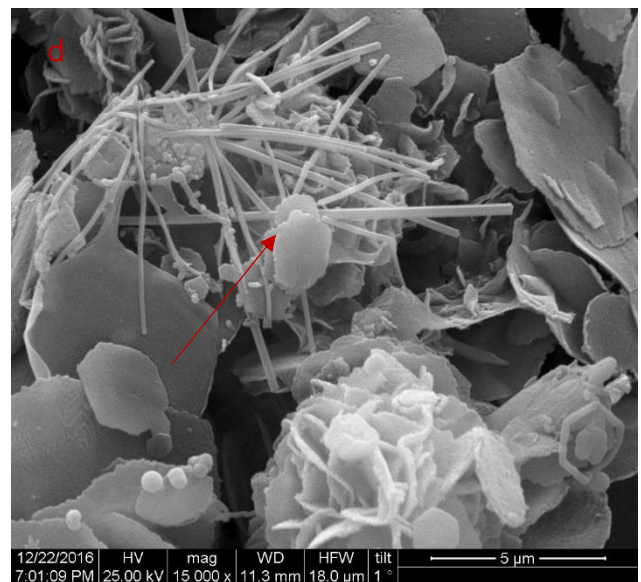
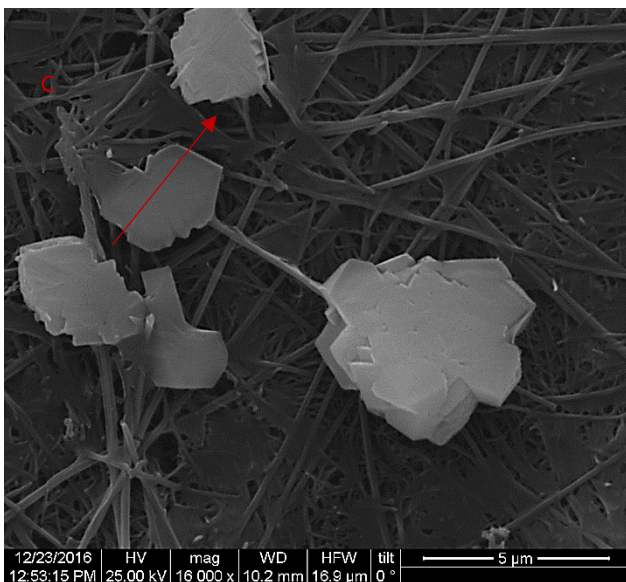
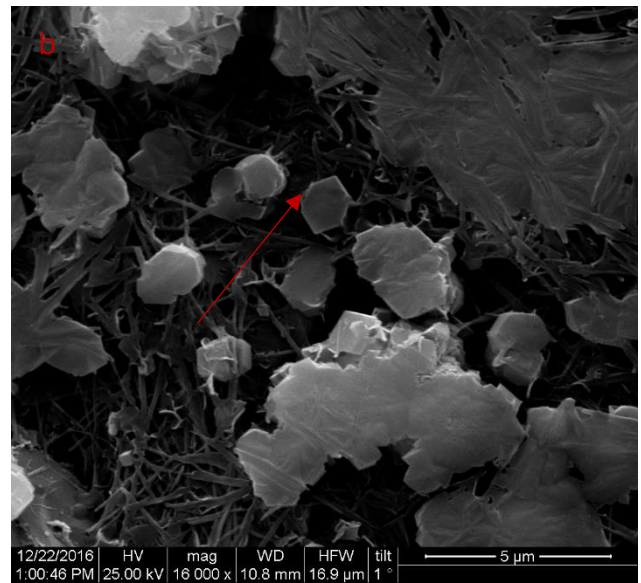
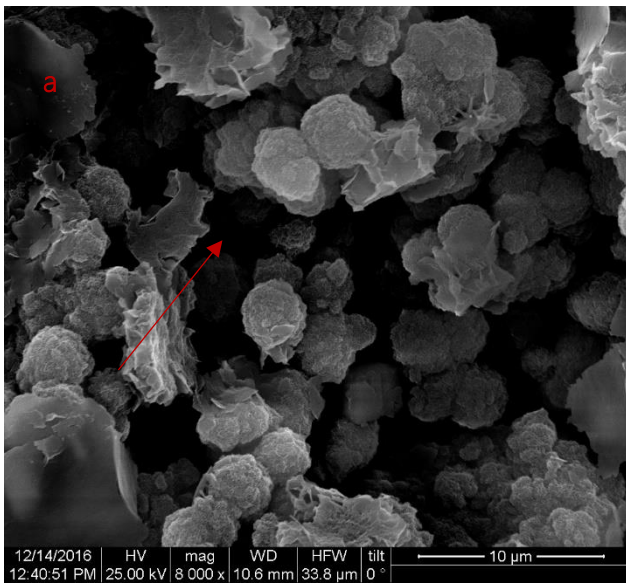


Fig. Ap. E SEM observations of B_03OHresin results after magnetic stirring for (a) 0 min. (scale bar at 10 μm); (b) 60 min.(scale bar at 5 μm); (c) 90 min. (scale bar at 5 μm) and (d) 60 min. with the addition of the non-ionic surfactant Triton X-100 (scale bar at 5 μm)

F. Deposition and carbonation of the $\text{Ca}(\text{OH})_2$ nanoparticles on the three porous building materials (limestone, sandstone and mortar)

The examination of the treated samples after 28 days was implemented by the use of SEM/EDX (Fig. Fig. Ap. F1, 2 and 3). Overall, the evaluation of the penetration ability of the six dispersions of $\text{Ca}(\text{OH})_2$ nanoparticles underlined the penetration of the dispersions inside the porous substrates of the sandstone specimens (Fig. Ap. F2), contrary to the poor penetration at the layers close to the surface, observed in the cases of the limestone (Fig. Ap. F1) and calcareous mortar specimens (Fig. Ap. F3).

Upon completion of the carbonation process, in all cases the calcite crystals that were observed could be characterized by uniformity in size. In the case of the *limestone* treated specimens scalenohedral calcite crystals were identified (Fig. Ap. E1). The size of the calcite crystals was categorized into two groups: a) larger calcite crystals of dimensions between 190 nm and 240 nm and b) smaller calcite crystals of dimensions between 60 nm and 130 nm (Fig. Ap. F1). The presence of the latter category could be attributed to the pore-network of the limestone specimens.

In the case of the *sandstone* treated specimens of tabular and scalenohedral calcite crystals were identified (Fig. Ap. F2). The presence of tabular calcite crystals in the cases of B06_100nbstx100 and B06_50w50isptx100 (Fig. Ap. F2c) could be attributed to the aqueous part of the dispersion medium. Finally, in the case of the *calcareous mortar* treated specimens scalenohedral calcite crystals were identified (Fig. Ap. F3). The $\text{Ca}(\text{OH})_2$ nanoparticles were and deposited inside the pores of the surface layers.

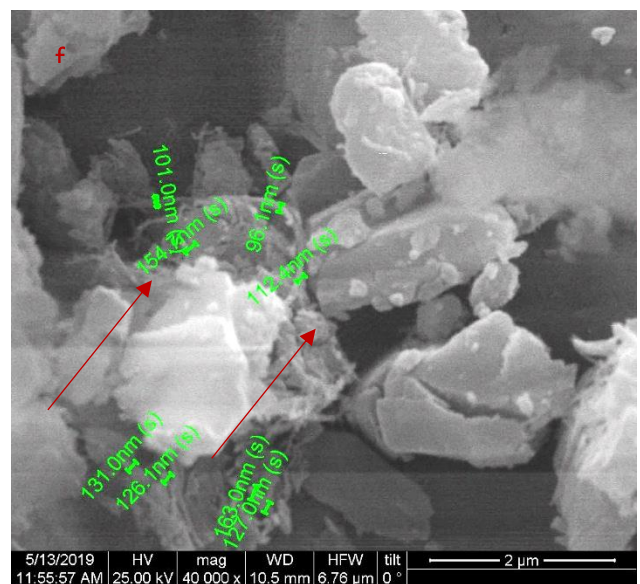
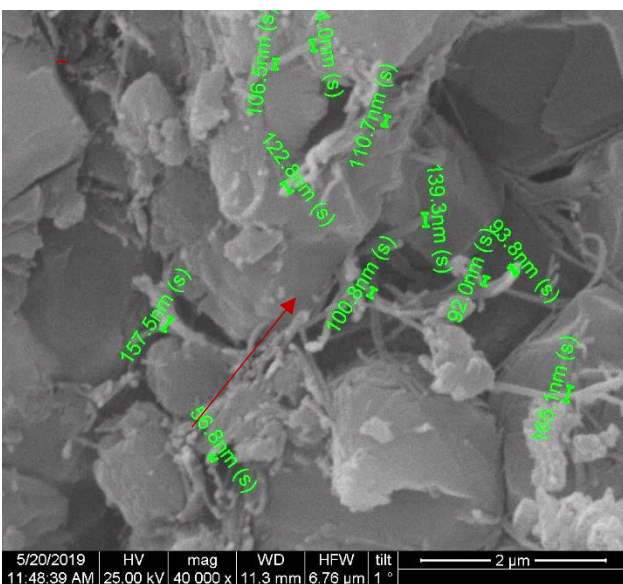
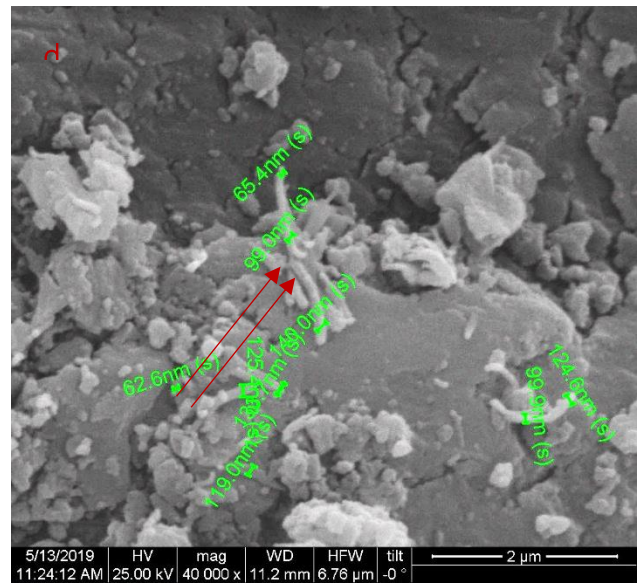
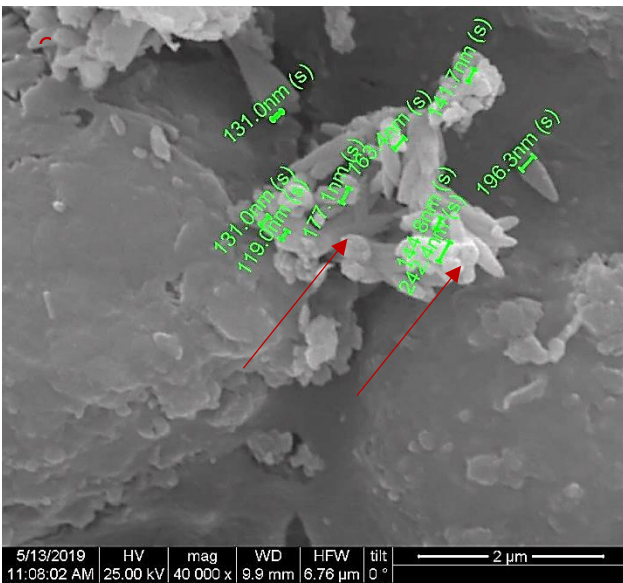
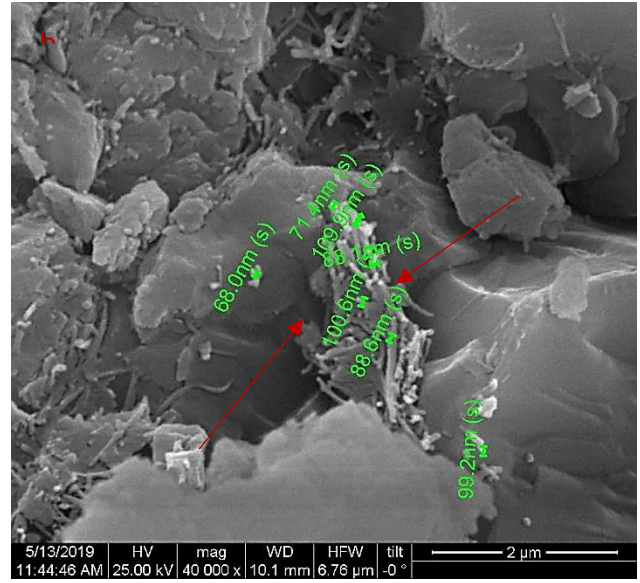
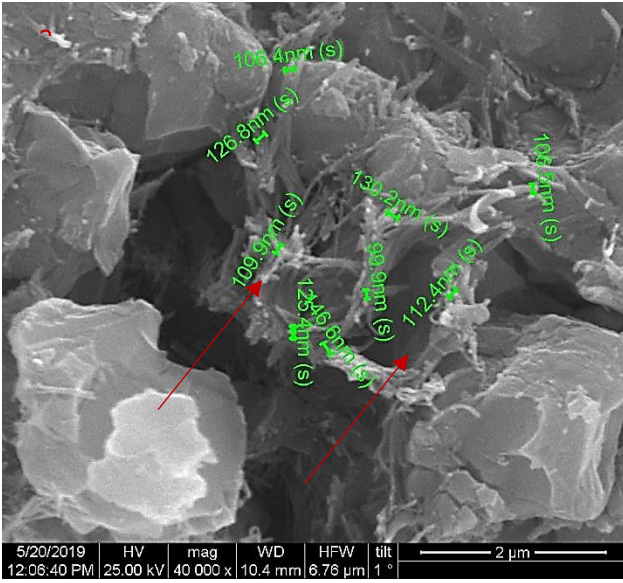
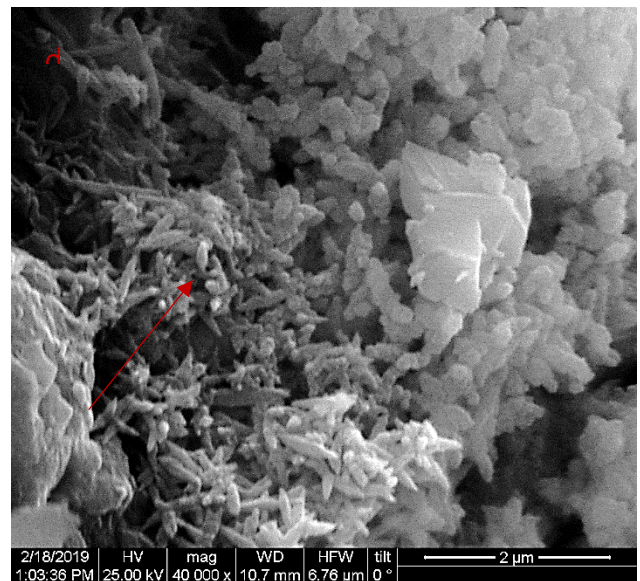
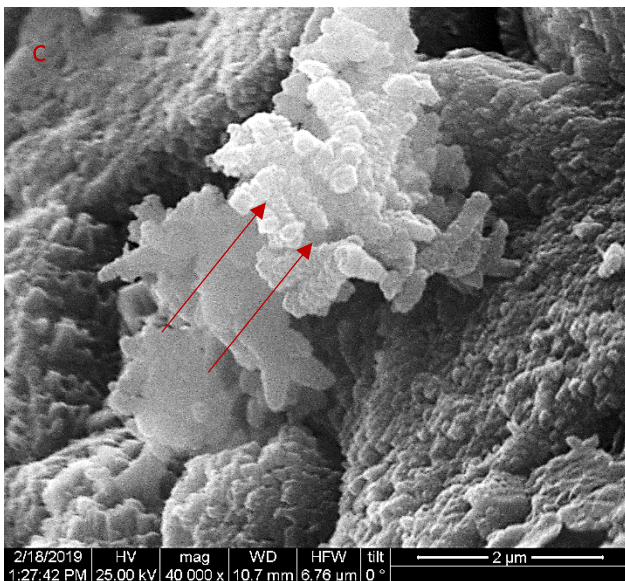
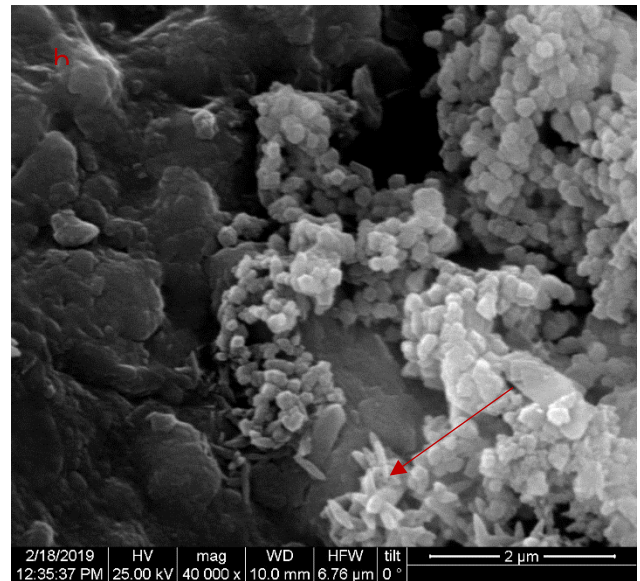
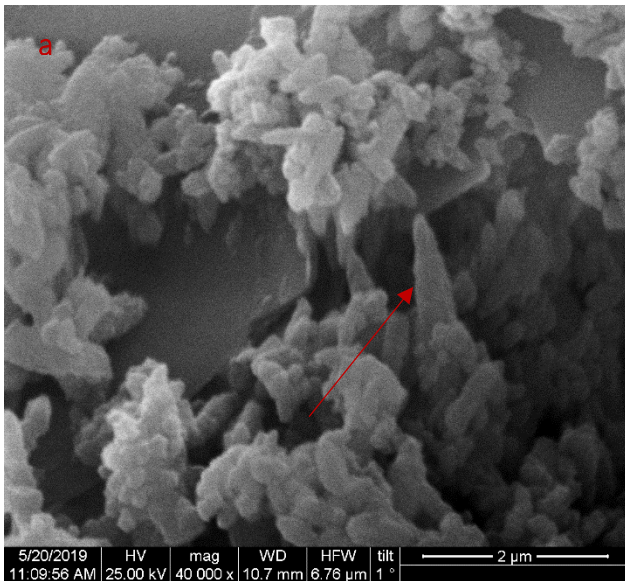


Figure Ap.F.1 SEM observations of the treated limestone specimens (a) B06_100nbs ; (b) B06_100nbstx100; (c) B06_50w50isptx100; (d) B06_20nbs80isptx100; (e) B06_20w80isptx100; and (f) T05_20w80isptx100 (scale bar at 2µm)



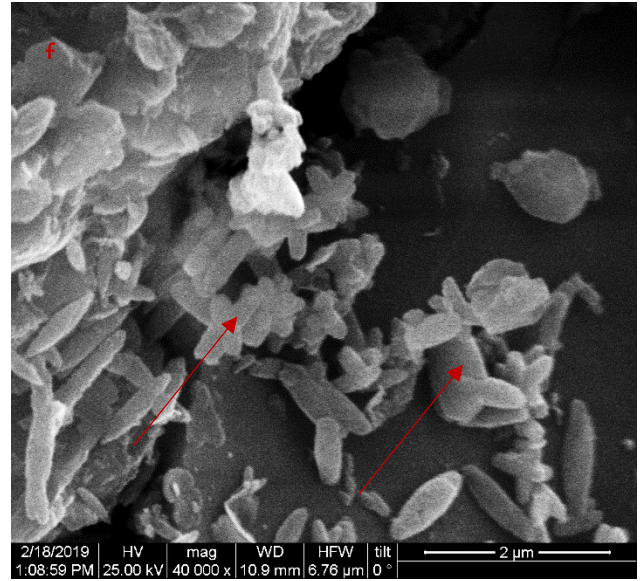
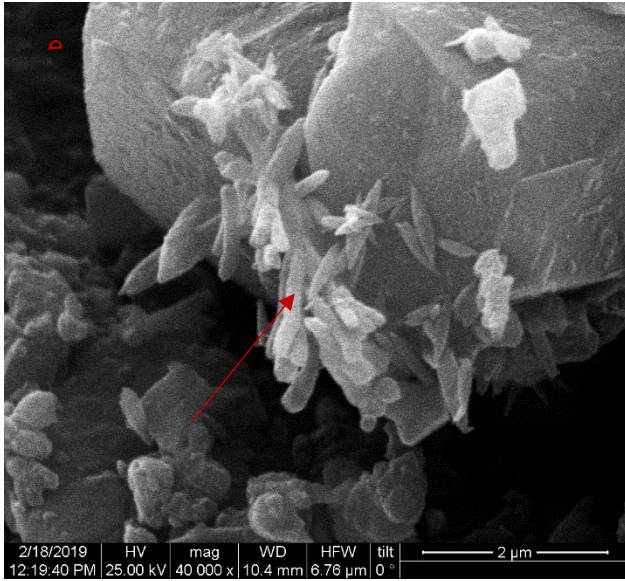


Figure Ap.F.2 SEM observations of the treated sandstone specimens (a) B06_100nbs ; (b) B06_100nbs100; (c) B06_50w50isptx100; (d) B06_20nbs80isptx100; (e) B06_20w80isptx100; and (f) T05_20w80isptx100 (scale bar at 2μm)

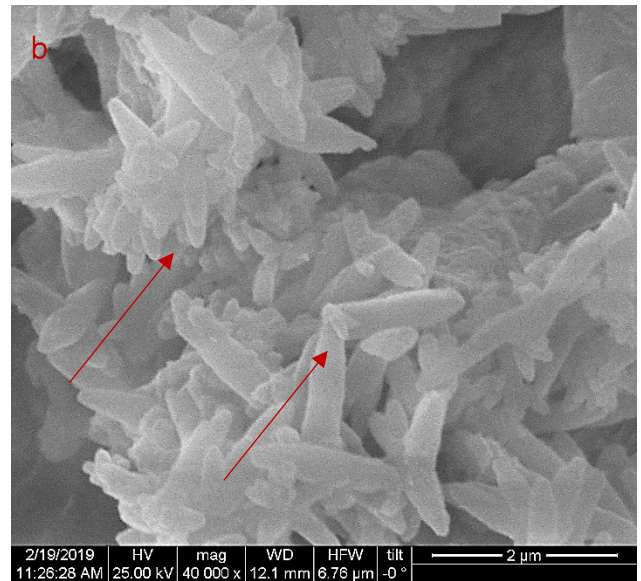
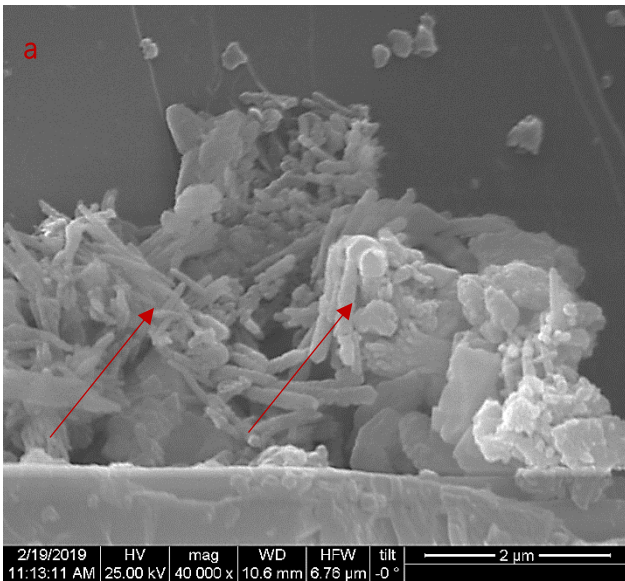


Figure Ap.F.3 SEM observations of the treated mortar specimens (a) B06_20nbs80isptx100 and (b) B06_20w80isptx100(scale bar at 2μm)

References

1. Schramm L.L (2014), *Emulsions, Foams, Suspensions, and Aerosols: Microscience and Applications*, 2ND edition, Wiley publications
2. Baglioni P., Giorgi R., (2006) "Soft and hard nanomaterials for restoration and conservation of cultural heritage", *Soft Matter*, 2, p.293–303
3. Blee A., Matison J.G., "Nanoparticles and the conservation of cultural heritage", Cairney J.M., Ringer S.P, Wuhrer R., *Materials Forum*, 32, p. 121-128
4. Baglioni P., Chelazzi D., O'Brien P., (eds.), (2013), *Nanoscience for the Conservation of Works of Art*, RCR Nanotechnology and Nanoscience N. 28, Royal society of Chemistry, Cambridge
5. Sanchez F., Sobolev K., (2010), *Nanotechnology in concrete – A review*, *Construction and Building Materials* 24, p.2060–2071
6. Borm P., Robbins D., Haubold S., Kuhlbusch T., Fissan H., Donaldson K., Schins R., Stone V., Kreyling W., Lademann J., Krutmann J., Warheit D., Oberdorster E. (2006), *The potential risks of nanomaterials: a review carried out for ECETOC*, *Particle and Fibre Toxicology*, p. 3-11
7. Chelazzi D., Giorgi R, Baglioni P. (2018), *Microemulsions, Micelles, and Functional Gels: How Colloids and Soft Matter Preserve Works of Art*, *Angewandte Chemie International Edition*, 57:25 p. 7296-7303
8. Ambrosi, M., Dei L., Giorgi R., Neto C., Baglioni P. (2001) *Colloidal Particles of Ca(OH)₂: Properties and Applications to Frescoes Restoration*, *Langmuir*, 17, p.42-51
9. Salvadori B., Luigi Dei L. (2001), *Synthesis of Ca(OH)₂ Nanoparticles from Diols*, *Langmuir*, 17:8, pp 2371–2374
10. Andrievski R., Glezer A. (2001), *Size effects in properties of nanomaterials*, *Scripta mater.* 44, p.1621–1624
11. Solans C., Izquierdo P., Nolla J., Azemar N., Garcia-Celma M, (2001), *Nano-emulsions*, *Current Opinion in Colloid & Interface Science*, 10, p.102 – 110
12. Albanese A., Tang P., Chan W. (2012), *The Effect of Nanoparticle Size, Shape, and Surface Chemistry on Biological Systems*, *Annual review of biomedical engineering*, 14:1, p.1-16

13. Yu X., Zhancorresponding Z. (2014) The effects of the size of nanocrystalline materials on their thermodynamic and mechanical properties, *Nanoscale Research Letters.*, 9:1, p.51-6
14. Chelazzi D., Poggi G., Jaidar Y., Toccafondi N., Giorgi R., Baglioni P. (2013), Hydroxide nanoparticles for cultural heritage: Consolidation and protection of wall paintings and carbonate materials, *Journal of Colloid and Interface Science*, 392, p. 42–49
15. Daehne A., Herm C., (2013), hydroxide nanosols for the consolidation of porous building materials - results from EU-STONECORE, *Heritage Science*, p.1-11
16. Arai Y. *The Preparation of Powder* (1996) Scarlett, B., Ed.; Chapman & Hall: London
17. Baglioni P., Chelazzi D., Giorgi R., Poggi G. (2013) Colloid and Materials Science for the Conservation of Cultural Heritage: Cleaning, Consolidation, and Deacidification, *Langmuir*, 29, p.5110-5122
18. Baglioni P., Chelazzi D. (2014), Commercial Ca(OH)₂ nanoparticles for the consolidation of immovable works of art, *Applied Physics A*, 114 p.723-732
19. Baglioni P., Berti D., Bonini M., Carretti E., Dei. L., Fratini E., Giorgi R. (2014), Micelle, microemulsions, and gels for the conservation of cultural heritage, *Advances in Colloid and Interface Science*, 205, p. 361–371
20. Lee S.W., Grhee J., (2018), Size Effects in Nanomaterials and Their Use in Creating Architected Structural Metamaterials, (eds) Van de Voorde M., Werner M., Fecht H.J., Wiley Online Library
21. Toy R., Hayden E., Shoup C., Baskaran H., Karathanasis E. (2011), The effects of particle size, density and shape on margination of nanoparticles in microcirculation, *Nanotechnology*, 22:11, p.101-115
22. Ashraf M., Peng W., Rhee Y., (2018) Effects of Size and Aggregation/Agglomeration of Nanoparticles on the Interfacial/Interphase Properties and Tensile Strength of Polymer Nanocomposites, *Nanoscale Research Letter*, 90:3, p. 2-14
23. Costa D., Delgado Rodrigues J. (2012), Consolidation of a porous limestone with nanolime, paper presented in the 12th International Congress on the Deterioration and Conservation of Stone Columbia University (2012), New York

24. Dei L., Salvadori B. (2006), Nanotechnology in cultural heritage conservation: nanometric slaked lime saves architectonic and artistic surfaces from decay, *Journal of Cultural Heritage*, 7, p.110–115
25. Rodriguez-Navarro C., E. Ruiz-Agudo (2017), Nanolimes: From synthesis to application, *Pure and Applied Chemistry*, 90:3
26. Pozo-Antonio, Otero J., Alonso P., Mas X., Barbera I. (2019), Nanolime- and nanosilica-based consolidants applied on heated granite and limestone: Effectiveness and durability, *Construction and Building Materials*, 201, p. 852–870
27. Wheeler G.(2008), Alkoxysilanes and the consolidation of stone: where we are now, in: J. Delgado-Rodriguez, J.M. Mimoso (Eds.), *Stone Consolidation in Cultural Heritage: Research and Practice*, Proceedings of the International Symposium, LNEC (Laboratorio Nacional de Engenharia Civil), Lisbon, Portugal, pp. 41–52.
28. J. Otero, A.E. Charola, C.A. Grissom, V. Starinieri (2017), An overview of nanolime as a consolidation method for calcareous substrates, *Ge-conservación*, 11, p.71–78
29. Hansen E., Doehne E., Fidler J., Larson J., Martin B., Matteini M., Rodriguez-Navarro C., Pardo E.S., Price C., De Tagle A., Teutonico J.M., Weiss N., (2003), A review of selected inorganic consolidants and protective treatments for porous calcareous materials, *Reviews in Conservation*, 4, p. 13-25
30. Borsoi G, Tabares M., Veiga R., Santos-Silva A. (2012), Microstructural Characterization of Consolidant Products for Historical Renders: An Innovative Nanostructured Lime Dispersion and a More Traditional Ethyl Silicate Limewater Solution, *Microscopy and Microanalysis*, 18, p.1181–1189
31. Favaro M., Mendichi R., Ossola F., Russo S., Simon S., Tommasin P., Vigato P.A. (2006), Evaluation of polymers for conservation treatments of outdoor exposed stone monuments. Part I: photooxidative weathering, *Polymer Degradation and Stability*, 91, p. 3083-3096
32. Favaro M., Mendichi R., Ossola F., Simon S., Tommasin P., Vigato P.A. (2007), Evaluation of polymers for conservation treatments of outdoor exposed stone monuments. Part II: Photo-oxidative and salt-induced weathering of acrylic-silicone mixtures, *Polymer Degradation and Stability*, 92, p.335-351

33. Mosquera M.J., De los Santos D.M., Rivas T., Sammartin P., Silva B. (2009), New Nanomaterials for Protecting and Consolidating Stone, *Journal of Nano Research*, 8, pp. 1-12
34. Michalopoulou A., Favvas E.P., Mitropoulos A.C., Maravelaki P., Kilikoglou V., Karatasios I. (2018), A comparative evaluation of bottom-up and top-down methodologies for the synthesis of calcium hydroxide nanoparticles for the consolidation of architectural monuments, *Materials Today: Proceedings*, 5:14, p. 27425-27433
35. Ziegenbalg G, Brummer K, Pianski J. (2010), Nano-Lime –a new material for the consolidation and conservation of historic mortars. In: Válek J, Groot C, Hughes JJ, editors. Proceedings of the 2nd Historic Mortars Conference and RILEM TC 203-RHM Final Workshop – HMC10, Prague, September 11–14, RILEM Publications, pp. 1301–1309
36. Borsoi G., Lubelli B., Van Hees R., Veiga R., Santos-Silva A. (2017), Application Protocol for the Consolidation of Calcareous Substrates by the Use of Nanolimes: From Laboratory Research to Practice in *Restoration of Buildings and Monuments Materials science*, 22:4-6
37. Borsoi G., Lubelli B., VanHees R., Veiga R., Santos Silva A., Colla L., Fedele L., Tomasin A. (2016), Effect of solvent on nanolime transport within limestone: How to improve in-depth deposition, *Colloids and Surface A: Physicochemistry and Engineering Aspects*, 497, p. 171-181
38. Lanzon M, Madrid J.A., Martínez-Arredondo A., Monaco S. (2016), Use of diluted $\text{Ca}(\text{OH})_2$ suspensions and their transformation into nanostructured CaCO_3 coatings: A case study in strengthening heritage materials (stucco, adobe and stone), *Applied Surface Science*, 424:1, p. 20-28
39. Rodríguez-Navarro C., Suzuki A., Ruiz-Agudo E. (2013), Alcohol Dispersions of Calcium Hydroxide Nanoparticles for Stone Conservation, *Langmuir*, 29, p. 11457–11470
40. Sierra-Fernandez A., Gomez-Villalba L.S., Rabanal M.E., Fort R. (2017) New nanomaterials for applications in conservation and restoration of stony materials: A review, *Materiales de Construcción*, 67:325
41. S. Boggs S. Jr., Principles of sedimentology and stratigraphy (2006) 4nd ed., Pearson Prentic Hall, New Jersey

42. Borsoi G, Lubellia B., VamHees R., Veiga R., Santos Silva A. (2016), Understanding the transport of nanolimeconsolidants within Maastricht limestone, *Journal of Cultural Heritage*, 18, p. 242-249
43. Verganelaki A., Kapridaki C., Maravelaki-Kalaitzaki P. (2015), Modified Tetraethoxysilane with Nanocalcium Oxalate in One-Pot Synthesis for Protection of Building Materials, *Industrial and Engineering Chemistry Research*, 54, p. 7195–7206
44. Daniele D., Taglieri G., Quaresima R. (2008) The nanolimes in Cultural Heritage conservation: Characterization and analysis of the carbonatation process, *Journal of Cultural Heritage*, 9, p. 294-301
45. Zornoza-Indart A., Lopez Arce P. (2016), Silica nanoparticles (SiO₂): Influence of relative humidity in stone consolidation, *Journal of Cultural Heritage*, 18, p. 258–270
46. Zornoza-Indart A., Lopez Arce P., Leal N., Simao J., Zoghlami K. (2016), Consolidation of a Tunisian bioclastic calcarenite: From conventional ethyl silicate products to nanostructured and nanoparticle based consolidants, *Journal of Cultural Heritage*, 116, p. 188–202
47. Pinho L., Elhaddad F., Facio D.S., Mosquera M.S. (2013), A novel TiO₂-SiO₂ nanocomposite converts a very friable stone into a self-cleaning building material, *Applied Surface Science*, 275, p. 389– 396
48. Calia A., Masieri M., Baldi G., Mazzotta C. (2012), The evaluation of the nanosilica performance for consolidation treatment of an highly porous calcarenite, paper presented in the 12th International Congress on the Deterioration and Conservation of Stone Columbia University (2012), New York
49. Falchi L., Balliana E., Izzo F.C., Agostinetto, Zendri E. (2013), Distribution of nanosilica dispersions in Lecce stone, *Scienze da Foscari*, p. 40-46
50. Vasaneli E., Calia A., Masieri M., Baldi G. (2019), Stone consolidation with SiO₂ nanoparticles: Effects on a high porosity limestone, *Construction and Building Materials*, 219, p. 154–163
51. Lichelli M., Malagodi M., Wethimuni M., Zanchi C. (2013), Nanoparticles for conservation of bio-calcarenite stone, *Applied Physics A*, 114:3, p. 562-571
52. Barbenera-Fernandez A.M., Blanco Varela M.T., Carmona-Quiroga P.M. (2019), Use of nanosilica- or nanolime-added TEOS to consolidate cementitious materials in

- heritage structures: Physical and mechanical properties of mortars, *Cement and Concrete Composites*, 95, p. 271-276
53. Iucolano F., Colella A., Liguori B., Calcaterra D. (2019), Suitability of silica nanoparticles for tuff consolidation, *Construction and Building Materials*, 202, p. 73–81
54. Natali I., Saladino A.M., Andriuloa F., Martino D.C., Caponetti E., Emiliano Carrettia E., Deia L. (2014), Consolidation and protection by nanolime: Recent advances for the conservation of the graffiti, Carceri dello Steri Palermo and of the 18th century lunettes, SS. Giuda e Simone Cloister, Corniola (Empoli), *Journal of Cultural Heritage*, 15, p. 151–158
55. Bourguignon E., Tomasin P., Detalle V., Vallet J.M., Laboure M., Oltenu I., Favaro M., Chiurato M.A., Bernardi A., Becherini F. (2018), Calcium alkoxides as alternative consolidants for wall paintings: Evaluation of their performance in laboratory and on site, on model and original samples, in comparison to conventional products, *Journal of Cultural Heritage*, 29, p. 54–66
56. Tomasin P., Mondin G., Zuena M., El Habra N., Nodari L., Moretto L.M. (2019), Calcium alkoxides for stone consolidation: Investigating the carbonation process, *Powder Technology*, 344, p. 260–269
57. Favaro M., Tomasin P., Ossola F., Vigato A.P. (2008), A novel approach to consolidation of historical limestone: the calcium alkoxides, *Applied Organometallic Chemistry*, 22, p. 698–704
58. Favaro M, Chiurato M, Tomasin P, Ossola F, El Habra N, Brianese N, Svensson I, Beckers E, Forrat Pérez V, Romero Sánchez M, Oriol G, Bourguignon E, Bernardi A. (2013) Alkaline earth alkoxides for conservation treatment of stone and wood in built heritage. *Built Heritage Monitoring Conservation Management*, p. 1296 -1303
59. Ossola F., Tomasin P., De Zorzi C., El Habra N., Chiurato M., Favaro M. (2012), New calcium alkoxides for consolidation of carbonate rocks. Influence of precursors' characteristics on morphology, crystalline phase and consolidation effects, *New Journal of Chemistry*, 36, p. 2618–2624
60. Sassoni E., Franzonia E., Pigino B., Scherer G.W., Naiduc S. (2013), Consolidation of calcareous and siliceous sandstones by hydroxyapatite: Comparison with a TEOS-based consolidant, *Journal of Cultural Heritage*, 14, p. 103–108

61. Sassoni E., Naidu S., Scherer G.W. (2011), The use of hydroxyapatite as a new inorganic consolidant for damaged carbonate stones, *Journal of Cultural Heritage*, 12, p. 346–355
62. Sassoni E., Graziani G., Franzoni E. (2017), An innovative phosphate-based consolidant for limestone. Part 1: Effectiveness and compatibility in comparison with ethyl silicate, *Construction and Building Materials*, 102:1, p. 918-930
63. De Ferri L., Lottici P.P, Lorenzi A., Montenero A., Salvioli-Mariani E. (2011), Study of silica nanoparticles – polysiloxane hydrophobic treatments for stone-based monument protection, *Journal of Cultural Heritage*, 12, p. 356–363
64. Pinho L., Mosquera M.J. (2011), Titania-Silica Nanocomposite Photocatalysts with Application in Stone Self-Cleaning, *Journal of Physical Chemistry C*, 115, p. 22851–22862
65. Verganelaki A., Kilikoglou V., Karatasios I., Maravelaki-Kalaitzaki P. (2014), A biomimetic approach to strengthen and protect construction materials with a novel calcium-oxalate–silica nanocomposite *Construction and Building Materials*, 62, p.8–17
66. Mariani, A., Capelletti P., Brunetti A (2008), Frontal polymerization: A new approach to the consolidation of stone., paper presented in Stone Consolidation in Cultural Heritage: Research and Practice; Proceedings of the 8th International Symposium, Lisbon, 6–7 May 2008, ed. J. Delgado Rodrigues and J. M. Mimoso, p.91–100. Lisbon: LNEC (Laboratorio Nacional de Engenharia Civil).
67. Burgos-Cara A., Rodriguez-Navarro C., Ortega Huertas M., Ruiz-Agudo E. (2019), Bioinspired alkoxy silane conservation treatments for building materials based on amorphous calcium carbonate and oxalate nanoparticles, *ACS Applied Nano Materials*, *in press*
68. Kapridaki C., Maravelaki-Kalaitzaki P. (2013), TiO₂–SiO₂–PDMS nano-composite hydrophobic coating with self-cleaning properties for marble protection, *Progress in Organic Coatings*, 76, p. 400– 410
69. Kapridaki C., Pinho L., Mosquera M.J., Maravelaki-Kalaitzaki P. (2014), Producing photoactive, transparent and hydrophobic SiO₂-crystalline TiO₂nanocomposites at ambient conditions with application as self-cleaning coatings, *Applied Catalysis B: Environmental*, 156–157, p. 416–427

70. Coltelli M.B., Paolucci D., Castelvetro V., Bianchi S., Mascha E, Panariello L., Pesce C. Weber J., Lazzeri A. (2018), Preparation of Water Suspensions of Nanocalcite for Cultural Heritage Applications, *Nanomaterials*, 8, 254, 1-20
71. Bergamonti L., Bondiolia F., Alfieri I. Alinovi S., Lorenzi A., Predieric G., Lottici P.P. (2018), Weathering resistance of PMMA/SiO₂/ZrO₂ hybrid coatings for sandstone conservation, *Polymer Degradation and Stability*, 147, p. 274–283
72. Becerra J., Zaderenko A.P., Gómez-Morón A.M., Ortiz P. (2019), Nanoparticles Applied to Stone Buildings, *International Journal of Architectural Heritage*, in press
73. Taglieri G., Daniele V., Del Re G., Volpe R. (2015), A New and Original Method to Produce Ca(OH)₂ Nanoparticles by Using an Anion Exchange Resin, *Advances in Nanoparticles*, 4, p. 17-24
74. <http://iscs.icomos.org/glossary.html>
75. Torraca G. (2009), Lectures on materials science for architectural conservators, J. Paul Getty Trust, The Getty Conservation Institute, Los Angeles, California
76. Σκουλικίδης Θ.Ν. (2000), Διάβρωση και συντήρηση των δομικών υλικών των μνημείων, Πανεπιστημιακές Εκδόσεις Κρήτης, Ηράκλειο
77. Tosun I. (2013), Chapter 1 - Review of the First and Second Laws of Thermodynamics, Elsevier
78. Amiri M., López Droguett E., Mehdi N., Iyer S. (2015), The second law of thermodynamics and degradation of materials paper presented at: Conference: ESREL 2015: the 25th ESRA Conference At: ETH, the Swiss Federal Institute of Technology, in Zürich
79. Doehne E., Price C.A (2010), Stone conservation: An overview of current research, 2nd ed., J. Paul Getty Trust, The Getty Conservation Institute, Los Angeles, California
80. Brimblecombe, P., Grossi C.M. (2007), Damage to buildings from future climate and pollution. *APT Bulletin*, 38:2–3, p. 13–18.
81. Bonazza A., Vidorni G., Natali I., Cianetli C., Giosu C., Tittarelli F. (2017), Durability assessment to environmental impact of nano-structured consolidants on Carrara marble by field exposure tests, *Science of The Total Environment*, 575, p. 23-32

82. Ogburn D., Sillar B., Serrar J.C. (2013), Evaluating effects of chemical weathering and surface contamination on the insitu provenance analysis of building stones in the Cuzco region of Peru with portable XRF, *Journal of Archaeological Science*, 40:4, p. 1823-1837
83. Rabat M., Tomas C.R. (2020), Effect of water saturation on strength and deformability of building calcarenite stones: Correlations with their physical properties, *Construction and Building Materials*, 232,117259
84. Heidari M., Torabi-Kaveha M., Chastre V. Ludovico-Marques M., Mohseni H., Akefi H. (2015), Determination of weathering degree of the Persepolis stone under laboratory and natural conditions using fuzzy inference system, *Construction and Building Materials*, 145, p.28-41
85. Striani R., Esposito Corcione C., Dell Anna M., Frionione M. (2017), Durability of a sunlight-curable organic–inorganic hybrid protective coating for porous stones in natural and artificial weathering conditions, *Progress in Organic Coatings*, 101, p. 1-14
86. El-Gohary M.A. (2017), Environmental impacts: Weathering factors, mechanism and forms affected the stone decaying in Petra, *Journal of African Earth Sciences*, 135, p. 204-212
87. Maravelaki-Kalaitzaki P., Kallithrakas-Kontos N., Agioutantis Z., Maurigiannakis, S, Korakaki D. (2008), A comparative study of porous limestones treated with silicon-based strengthening agents, *Progress in Organic Coatings*, 62, p. 49–60
88. Karatasios I., Theoulakis P., Kalagri A., Sapalidis A., Kilikoglou V. (2009), Evaluation of consolidation treatments of marly limestones used in archaeological monuments, *Construction and Building Materials*, 23, p. 2803–2812
89. Young M., Cordiner P., Murray M., (2003), Research Report: Chemical consolidants and water repellents for sandstones in Scotland, Historic Scotland, Edinburgh
90. Nardini I., Zendri E., Biscotin G., Selva D., Sgobbi, D. Influence of the application method on the distribution of consolidation products within a porous material, in DelgadoRodrigues J, Mimoso JM, (eds), (2008) Proceedings of the International Symposium Stone consolidation in cultural heritage. Lisbon: Laboratorio Nacional de engenharia civil, p. 151-158
91. Ferreira Pinto A.P., Delgado Rodrigues J. (2008), Stone consolidation: The role of treatment procedures, *Journal of Cultural Heritage*, 9, p. 38-53

92. Adolfs N. C., (2007) Die Anwendung von Calciumhydroxid-Sol als Festigungsmittelfür historische Putze – erste Versuche und deren Überprüfung, Diplomarbeit anhang, Institut für Restaurierungs und Konservierungswissenschaft, Fakultät Kulturwissenschaften der Fachhochschule, Köln
93. D'Armada P., Hirs, E. (2012), Nano-Lime for Consolidation of Plaster and Stone, *Journal of architectural conservation*, 94, 18:1, p. 63-80
94. Snethlage R., Sterflinger K., (2011), Stone Conservation in S. Siegesmund, R. Snethlage, (eds), *Stone in Architecture: Properties, Durability*, 4th edn, Springer, Berlin
95. Theoulakis P., Karatasios I., Stefanis N.A., Performance criteria and evaluation parameters for the consolidation of stones, paper presented in Delgado Rodrigues J. and J. M. Mimoso J.M., (eds), (2008), *Stone Consolidation in Cultural Heritage: Research and Practice; Proceedings of the International Symposium, Lisbon, 6–7 May*, , p.279-288. Lisbon: LNEC (Laboratorio Nacional de Engenharia Civil).
96. Matteini, M., & Moles, A., *La Chimica nel Restauro – I Materiali dell'Arte Pittorica*, Nardini Editore, Firenze 2003.
97. Matteini, M. (2008). Inorganic Treatments for the Consolidation and Protection of Stone Artefacts, *Conservation Science in Cultural Heritage*, 8, p. 13-27.
98. Van Hees, R.P.J., Veiga, R., and Slizkova, Z. (2017), Consolidation of Renders and Plasters, *Materials and Structures*, p. 50-65
99. Toniolo L., Paradisi A., Goidanich S., Pennati G. (2010), Mechanical Behaviour of Lime Based Mortars After Surface Consolidation, *Construction and Building Materials*, 25, p.1553–1559
100. Hall C., Hoff W.D. (2009), *Water Transport in Brick, Stone and Concrete*, 2nd edition, CRC Press, U.S.A
101. Delgado Rodrigues J. (2001), Consolidation of decayed stones: A delicate problem with few practical solutions, in Lourenço P.B., Roca P. (Eds.), *Historic Constructions*, Guimarães, p. 3-14
102. Siegesmund S., Snethlage R., (eds), (2011) *Stone in Architecture: Properties, Durability*, 4th edn, Springer, Berlin

103. Moropoulou A., Kouloumbi N., Haralampopoulos G., Konstanti A., Michailidis P. (2003), Criteria and methodology for the evaluation of conservation interventions on treated porous stone susceptible to salt decay, *Progress in Organic Coatings*, 48, p.259–270
104. Clifton R.J., Frohnsdoff G.J.C. (1982), Stone consolidation materials: a status report. Conservation of Historic Stone Building and Monuments, National Academic Press, Washington, p. 287-311
105. Price, C., Ross K., White (G) (1988), A further appraisal of the “lime technique” for limestone consolidation, using a radioactive tracer, *Studies in Conservation* 33 (4): 178–86
106. Λαμπρόπουλος Β.Ν, Διάβρωση και συντήρηση της πέτρας, Εκδόσεις Παπασωτηρίου, σελ. 74-90
107. Teutonico J.M., (1998), A laboratory manual for architectural conservators, ICCROM, Rome
108. López-Arce P., Gómez-Villalba L.S, Martínez-Ramírez S., Álvarez de Buergo M. , R. Fort R. (2011) Influence of relative humidity on the carbonation of calcium hydroxide nanoparticles and the formation of calcium carbonate polymorphs, *Powder Technology*, 205 p. 263–269
109. Possenti E., Colombo C., Conti C., Marinoni N., Merlini M., Negrotti R., Realini M., Gatta G.D. (2019), Consolidation of building materials with a phosphate-based treatment: Effects on the microstructure and on the 3D pore network, *Materials Characterization*, 154, p.315-324
110. Feng B., Yong, A.K., An H. (2007), Effect of various factors on the particle size of calcium carbonate formed in a precipitation process, *Materials Science and Engineering A*, 445–446, p. 170–179
111. Mwaiuwinga S., Ayano T., Sakata K. (1997), Influence of urea in concrete, *Cement and Concrete Research*, Vol. 27, No. 5, p. 733-745
112. Drdácký M, Slížková Z., Calcium hydroxide based consolidation of lime mortars and stone, in: DelgadoRodrigues J, Mimoso JM, (eds) (2008) Proceedings of the International Symposium Stone consolidation in cultural heritage. Lisbon: Laboratorio Nacional de engenharia civil, p. 299–308

113. Wheeler.G., Goins E.S. (2005), Alkoxysilanes and the Consolidation of Stone. Research in Conservation, Getty Conservation Institute, Los Angeles
114. Ksinopoulou, Bakolas A., Moropoulou A. (2016), Modifying Si-based consolidants through the addition of colloidal nanoparticles, *Applied Physics A*, 122, p.267-277
115. Cai Y., Hou P., Duan C., Zhang R., Zhou Z., Cheng Z., Shah S. (2016), The use of tetraethyl orthosilicate silane (TEOS)for surface-treatment of hardened cement-based materials:A comparison study with normal treatment agents, *Construction and Building Materials*, 117, p. 144–151
116. Franzoni E., Graziani G., Sassoni E. (2015), TEOS-based treatments for stone consolidation: acceleration of hydrolysis–condensation reactions by poulticing, *Journal of sol-gel science technology*, 74, p.398–405
117. Gheno G., Badetti E., Brunelli A., Gnzerla R., Marcomini A., (2018) Consolidation of Vicenza, Arenaria and Istria stones: A comparison between nano-based products and acrylate derivatives, *Journal of Cultural Heritage*, 32, p. 44-52
118. Haake S., Simon S., Favaro M. (2004), The Bologna Cocktail - Evaluation of Consolidation Treatments on Monuments in France and Italy after 20 years of natural aging in Proceedings of the 10th International Congress on Deterioration and Conservation of Stone, Stockholm, June 27th -July 2nd p.423-430
119. Favaro M., Mendichi R., Ossola F., Simon S., Tomasin P., Vigato P.A, (2007), Evaluation of polymers for conservation treatments of outdoor exposed stone monuments. Part II: Photo-oxidative and salt-induced weathering of acrylic-silicone mixtures, *Polymer Degradation and Stability*, 92 p.335-351
120. Selwitz C.M. (2011), The Use of Epoxy Resins for Stone Consolidation, MRS Online Proceeding Library Archive 185
121. Ferreira Pinto A.P., Delgado Rodrigues J. (2012), Consolidation of carbonate stones: Influence of treatment procedures on the strengthening action of consolidants, *Journal of Cultural Heritage* 13, p. 154-166
122. Goueygou M., Lafhaj Z., Kaczmarek M. (2003), Relationship between porosity, permeability and ultrasonic parameters in sound and damaged mortar, International Symposium (NDT-CE 2003) -Non-Destructive Testing in Civil Engineering

123. Ozcelik Y., Ozguven A. (2014), Water absorption and drying features of different natural building stones, *Construction and Building Materials*, 63, p. 257–270
124. Benavente D., F. Martinez-Verdu F., Bernabeu A., Viqueira V., Fort R., Garcia del Cura M.A., Illueca A., Ordonez S. (2003), Influence of surface roughness on color changes in building stones, *Color research and application*, Volume 28, Number 5, p. 343-352
125. Fink J. (2015), Chapter 21 - Dispersions, emulsions, and foams in *Petroleum Engineer's Guide to Oil Field Chemicals and Fluids (Second Edition)*, p. 741-774
126. Jiang J., Oberdorster G., Biswas P. (2009), Characterization of size, surface charge, and agglomeration state of nanoparticle dispersions for toxicological studies, *Journal of Nanoparticle Research*, 11:1 p. 77-89
127. Texter J. (2004), Nanoparticle dispersion- Challenges and solutions, conference paper
128. Arshady R. (1992), Suspension, emulsion, and dispersion polymerization: A methodological survey, *Colloid and Polymer Science*, 270:8, p. 717-732
129. Thanh N.T.K., Mackean N., Mahiddine S. (2014), Mechanisms of Nucleation and Growth of Nanoparticles in Solution, *Chemistry Review*, 114:15, p. 7610-7630
130. Cushing B.L, Kolesnichenko V.L., O' Connor C. (2004), Recent Advances in the Liquid-Phase Syntheses of Inorganic Nanoparticles, *Chemistry review*, 104, p. 3893-3946
131. Wu Z., Yang S., Wu W. (2016), Shape control of inorganic nanoparticles from solution, *Nanoscale*, 8, p. 1237–1259
132. Karthika T., Radhakrishnan K., Kalaichelvi P. (2016), A Review of Classical and Nonclassical Nucleation Theories, *Crystal Growth*, 16:11, p. 6663-6681
133. Polte J. (2015), Fundamental growth principles of colloidal metal nanoparticles – a new perspective, *CrystEngComm*, 17, p. 6809-6830
134. Lifshitzl. V, Slyozov V. (1961), The kinetics of precipitation from supersaturated solid solutions, *Journal of physics and chemistry of solids*, p.19-35
135. Watzky M. A., Finke R. G. (1997), Nanocluster Size-Control and “Magic Number” Investigations. Experimental Tests of the “Living-Metal Polymer” Concept and of Mechanism-Based Size-Control Predictions Leading to the Syntheses of Iridium (0) Nanoclusters Centering about Four Sequential Magic Numbers, *Chemistry of materials*, 9, p. 30-83

136. Zheng H., Smith R.K., Jun Y.-W Kisielowski C., Dahmen U., Alivisatos, A. P. (2009), Observation of Single Colloidal Platinum Nanocrystal Growth Trajectories, *Science*, 324:5932, pp. 1309-1312
137. Peng X., Manna L., Yang W., Wickham J., Scher E., Kadavanich A., Alivisatos A. P. (Nature), Shape control of CdSe nanocrystals, *Nature*, 40:4, p. 59-61
138. Michalopoulou A., Maravelaki P., Kilikoglou V., Karatasios I., Morphological characteristics of water-based nanolime dispersions for the conservation of built heritage, *Journal of Cultural Heritage*, under review
139. Han S.J., Yoo, M.Y., Kim D.W., Wee J.H., (2011) Carbon Dioxide Capture Using Calcium Hydroxide Aqueous Solution as the Absorbent, *Energy fuels*, 25:8, p. 3825-3834
140. Giorgi R., Dei L., Baglioni P. (2000), A new method for consolidating wall paintings based on dispersions of lime in alcohol, *Studies in Conservation*, 45, p. 154–161
141. Saoud K.M., Ibala I., El Ladki D.E., Ezzeldeen O., Saeed, S. (2014), Microwave Assisted Preparation of Calcium Hydroxide and Barium Hydroxide Nanoparticles and Their Application for Conservation of Cultural Heritage in Euro-Mediterranean Conference EuroMed 2014: Digital Heritage. Progress in Cultural Heritage: Documentation, Preservation, and Protection, pp 342-352
142. Ozcelik B, Tasman F., Ogan C. (2000), A Comparison of the Surface Tension of Calcium Hydroxide Mixed with Different Vehicles, *Journal of Endodontics*, 26-9
143. Otero J., Starinieri, V., Charola A.E. (2018), Nanolime for the consolidation of lime mortars: A comparison of three available products, *Construction and Building Materials*, 181, p. 394-407
144. Henry A. (eds.), (2006), *Stone Conservation: Principles and Practice*, Routledge
145. Otero J., Starinieri V., Charola A.E. (2019) Influence of substrate pore structure and nanolime particle size on the effectiveness of nanolime treatments, *Construction and Building Materials*, 181, p. 394-407
146. Michalopoulou A., Michailidi E., Favvas E., Maravelaki P., Kilikoglou V., Karatasios I. (2020) Comparative evaluation of the morphological characteristics of nanolime dispersions for the consolidation of architectural monuments, *International Journal of Architectural Heritage*, doi: 10.1080/15583058.2020.1745323

147. Franzoni E., Sassoni E., Graziani G., (2015), Brushing, poultice or immersion? The role of the application technique on the performance of a novel hydroxyapatite-based consolidating treatment for limestone, *Journal of Cultural Heritage*, 16, p. 173–184
148. Giorgi R., Baglioni M., Berti D., Baglioni P. (2010), New Methodologies for the Conservation of Cultural Heritage: Micellar Solutions, Microemulsions, and Hydroxide Nanoparticles, *Accounts of chemical research*, 43:6, p. 695-704
149. Rodriguez-Navarro C., Ruiz-Agudo E., Ortega-Huertas M., Hansen E., (2005), Nanostructure and Irreversible Colloidal Behavior of $\text{Ca}(\text{OH})_2$: Implications in Cultural Heritage Conservation, *Langmuir*, 21, p. 10948-10957
150. Lyklema J. (1995), Electric Double Layers, *Fundamentals of Interface and Colloid Science*, 2, p. 313-232
151. Park S.J., Seo M.K. (2011), Intermolecular Force in Interface Science and Technology, 18, p. 1-57
152. Adair J.H., Suvac E., Sindel, J. (2001), Surface and Colloid Chemistry in *Encyclopedia of Materials: Science and Technology* (Second Edition), p. 1-10
153. Ohshima H. (2014), Interaction of colloidal particles in *Colloid and Interface Science in Pharmaceutical Research and Development*, p. 1-28
154. Frattini E., Page M.G., Giorgi R., Colfen H., Baglioni P., Deme B., Zemb T. (2007), Competitive Surface Adsorption of Solvent Molecules and Compactness of Agglomeration in Calcium Hydroxide Nanoparticles, *Langmuir*, 23, p. 2330-2338
155. Hetschler T. (2005), *Ultrasonic production of nano-size dispersions and emulsions*, ENS, Paris
156. Boufi S., Bel Haaj S., Magnin A., Pignon F., Imperor-Clec M., Mortha G. (2018), Ultrasonic assisted production of starch nanoparticles: Structural characterization and mechanism of disintegration, *Ultrasonics Sonochemistry*, 41, p. 327-336
157. Kaur I., Ellis L.J., Romer I., Tantra R., Variere M., Allard S., Mayne-L'Hermite M., Minelli C., Unger W., Potthoff A., Rades S., Valsami-Jones E. (2017), Dispersion of Nanomaterials in Aqueous Media: Towards Protocol Optimization, *Journal of Visualized Experiments*, 130, p. 56-74

158. Taurozzi J.S., Hackley V.A., Wiesner M.R. (2011), Ultrasonic dispersion of nanoparticles for environmental, health and safety assessment--issues and recommendations, *Nanotoxicology*, 5:4, p.711-129
159. Gelen B., Jordens J.M., Thomassen L., Braeken L., Van Gerven T. (2017), Agglomeration Control during Ultrasonic Crystallization of an Active Pharmaceutical Ingredient, *Crystals*, 7:2
160. Rodriguez-Navarro C., Elert K., Sevcik R. (2016), Amorphous and crystalline calcium carbonate phases during carbonation of nanolimes: implications in heritage conservation, *CrystEngComm*
161. Montes-Hernandez G., Pommerol A., Renard F., Beck P., Quirico E., Brissaud O. (2010), In situ kinetic measurements of gas–solid carbonation of $\text{Ca}(\text{OH})_2$ by using an infrared microscope coupled to a reaction cell, *Journal of Chemical Engineering*, 161(1-2), p. 250-256
162. Bond G.M., Stringer J., Brandvold D.K., Simsek F.A., Medina M.G., Egeland G. (2001), Development of integrated system for biomimetic CO_2 sequestration using the enzyme carbonic anhydrase, *Energy and Fuels*, 15:2, pp. 309–316
163. Cizer O., Balen K., Elsen J., Van Gemert D. (2012), Real-time investigation of reaction rate and mineral phase modification of lime carbonation, *Construction and Building Materials*, 35, p. 741–751
164. Ambrosi M., Fratini E., Canton P., Dankesreiter S., Baglioni P. (2012) Bottom-up/top-down synthesis of stable zirconium hydroxide nanophases, *Journal of Materials Chemistry*, 22, p. 23497–23505
165. Ruiz-Agudo E., Kudłacz K., Putnis C.V., Putnis A., Carlos Rodriguez-Navarro C. (2013), Dissolution and Carbonation of Portlandite [$\text{Ca}(\text{OH})_2$] Single Crystals, *Environmental Science and Technology*, 47, p. 11342–11349
166. Beruto D., Botter R. (2000), Liquid-like H_2O Adsorption Layers to Catalyze the $\text{Ca}(\text{OH})_2$ - CO_2 Solid-gas Reaction, *Journal of European ceramic society*, 20, p.497-503
167. López-Arce P., Gómez-Villalba L.S., Pinho L., Fernández-Valle M.E., Alvarez de Buergo M., Fort. R. (2010), Influence of porosity and relative humidity on consolidation of dolostone with calcium hydroxide nanoparticles: Effectiveness assessment with non-destructive technique, *Materials Characterization*, 61:2

168. Gomez-Villalba L.S., López-Arce P., Alvarez de Buergo M. (2012) Nucleation of CaCO₃ polymorphs from a colloidal alcoholic solution of Ca(OH)₂nanocrystals exposed to low humidity conditions, *Applied physics A*, 106, p. 213–217
169. Gomez-Villalba L.S., López-Arce P., Alvarez de Buergo M. (2011) Structural stability of a colloidal solution of Ca(OH)₂ nanocrystals exposed to high relative humidity conditions, *Applied physics A*, 104, p.124- 1259
170. Sand K.K., Rodriguez-Blanco J., Makovicky E., Benning L.G., Stipp L.S. (2012), Crystallization of CaCO₃ in Water–Alcohol Mixtures: Spherulitic Growth, Polymorph Stabilization, and Morphology Change, *Crystal growth and design.*, 12:2, p. 842-853
171. Nakama Y. (2017), *Surfactants in Cosmetic Science and Technology, Theoretical Principles and Applications*, p. 231-244
172. Rosen M.J., Kunjappu J.T. (2012), *Surfactants and Interfacial Phenomena*. (Eds.) John Wiley & Sons, Inc.
173. Daniele V., Taglieri G. (2012), Synthesis of Ca(OH)₂ Nanoparticles with the Addition of Triton X-100. Protective Treatments on Natural Stones: Preliminary Results, *Journal of Cultural Heritage*, 3, p. 40-46
174. Iyyappan, Wilson P., Sheela K., Ramya R. (2016) Role of Triton X-100 and hydrothermal treatment on the morphological features of nanoporous hydroxyapatite nanorods, *Materials science and engineering C*, 63, p.554–562
175. Yang Y.J, Corti D.S., Franses E.I. (2017), Effect of Triton X-100 on the stability of titania nanoparticles against agglomeration and sedimentation: A masked depletion interaction, *Colloids and Surfaces A: Physicochemical and Engineering Aspects*, 516, p.296–304
176. Gao Q., Chen W., Chen Y, Werner D., Cornelissen G., Xing B., Tao S., Wang X. (2016), Surfactant removal with multiwalled carbon nanotubes, *Water research*, 1:106, p. 531-538
177. Wang G.Y., Wang Y.Y., Wang X.H. (2017), Aggregation behaviors of mixed systems for imidazole based ionic liquid and Triton X-100, *Journal of Molecular Liquids*, 232, p. 55–61

178. Zdziennicka A. (2009), The adsorption properties of short chain alcohols and Triton X-100 mixtures at the water–air interface, *Journal of Colloid and Interface Science*, 335, p.175–182
179. Fainerman V.B., Aksenenko E.B., Mucic N., Javadid A., Miller R. (2014), Thermodynamics of adsorption of ionic surfactants at water/alkane interfaces, *Soft Matter*, 36
180. Iyyappan E, Wilson P. (2013), Synthesis of nanoscale hydroxyapatite particles using Triton X-100 as an organic modifier, *Ceramic International*, 39:1, p. 771–777
181. Prado A., Airoidi C (2002), Different neutral surfactant template extraction routes for synthetic hexagonal mesoporous silicas, *Journal of materials chemistry*, 12, p. 3823–3826
182. Mosquera M.J., De los Santos D., Rivas T. (2010), Surfactant-Synthesized Ormosils with Application to Stone Restoration, *Langmuir*, 26:9, p. 6737–6745
183. Arriaga L.R., Drenckhan W., Salonen A., Rodrigues J.A., Iniguez-Palomares R., Langevin L. (2012), On the Long-Term Stability of Foams Stabilised by Mixtures of Nanoparticles and Oppositely Charged Short Chain Surfactants, *Soft matter*, 8:43, p.11085-11097
184. Venkatathri N. (2012), Hollow Nano Silica: Synthesis, Characterization and Applications in Smart Nanoparticle Technology Chapter: Hollow Nano Silica Synthesis, characterization and Applications
185. Yener D., Sindel J., Randal V., Adair J. (2002), Synthesis of Nanosized Silver Platelets in Octylamine-Water Bilayer Systems, *Langmuir*, 18, p. 8692-8699
186. Ruiz-Agüido E., Rodríguez-Navarro C. (2010), Microstructure and Rheology of Lime Putty, *Langmuir*, 26:6, p.3868–3877
187. Cazalla O, Rodríguez-Navarro C., Sebastian R., Cultrone G. (2000), Aging of Lime Putty: Effects on Traditional Lime Mortar Carbonation, *Journal of American Society.*, 83-5, p. 1070–76
188. Bastone S., Chillura Martino D.F., Renda V., Saladino M.L., Poggi G., Caponetti E., (2017), Alcoholic nanolime dispersion obtained by the insolubilisation-precipitation method and its application for the deacidification of ancient paper, *Colloids and Surfaces A: Physicochemical and Engineering Aspects*, 513, p. 241–249
189. Darčanova O., Beganskienė, A., Kareiva A. (2015), Sol–gel synthesis of calcium nanomaterial for paper conservation, *chemija*, 26:1, p. 25–31

190. Roy A., Bhattacharya J. (2010) Synthesis of Ca(OH)₂ Nanoparticles by Wet Chemical Method. *Micro & Nano Letters*, 5, p. 131-134
191. Nanni A, Dei L. (2003), Ca(OH)₂ Nanoparticles from W/O Microemulsions, *Langmuir*, 19-3, p. 933–938
192. Liu T., Zhua Y., Zhang X., Zhanga T., Zhanga T. , Xingguo L, (2010), Synthesis and characterization of calcium hydroxide nanoparticles by hydrogen plasma-metal reaction method, *Materials Letters*, 64, Issue 23-15, p. 2575–2577
193. Taglieri G., Mondelli C., Daniele V., Pusceddu E., Trapanti A. (2103), Synthesis and X-Ray Diffraction Analyses of Calcium Hydroxide Nanoparticles in Aqueous Suspension, *Advances in Materials Physics and Chemistry*, 3, p. 108-112
194. Otero J., Charola A.E., Starinieri V. (2019), Sticky rice–nanolime as a consolidation treatment for lime mortars, *Journal of Materials Science*.
195. Martinez- Ramirez S., Higuera L., Cascales I., Martin Garrido M., Blanco Varela M, (2019), New approach to nanolime synthesis at ambient temperature, *Applied Sciences*
196. Barberena-Fernández A.M., Carmona-Quiroga P.M., Blanco-Varela M.T. (2015), Interaction of TEOS with cementitious materials: Chemical and physical effects, *Cement & Concrete Composites*, 55, p.145–152
197. Sandrolini F., Franzoni E., Pigino B. (2012), Ethyl Silicate for surface treatment of concrete-Part I: Pozzolanic effect of ethyl silicate, *Cement & Concrete Composites*, 34:3, p. 306-312
198. Lin Q., Xu Z., Lan X., Lu C (2011), The reactivity of nano silica with calcium hydroxide, *Society for biominerals*, 99B:2, p. 239-246
199. Perro A., Meunier F., Schmitt V., Ravaine S. (2016), Production of large quantities of “Janus” nanoparticles using wax-in-water emulsions, *Colloids and Surfaces A: Physicochemical Engineering Aspects* 332, p. 57–62
200. Zhou W., Zhong X. (2007) (eds.) Scanning Microscopy for Nanotechnology Techniques and Applications
201. <https://www.gla.ac.uk/schools/ges/researchandimpact/researchfacilities/isaac/services/scanningelectronmicroscopy>
202. Tang C.V., Yang Z., (2017) Transmission Electron Microscopy in Membrane Characterization

203. Lusvarghi S., Ghirlando R., Davison J., Bewley C. (2018) Chemical and Biophysical Approaches for Complete Characterization of Lectin–Carbohydrate Interactions, *Methods Enzymol.*, 598, p. 3–35
204. <https://www.slideshare.net/HORIBA/characterizing-nanoparticles-used-in-bio-applications>)
205. Kruk B., Chmura J, Krzeminski K., Ziemia A.W., Nazar K., Pekkarinen H., Kaciuba-Uscilko (2000), Influence of caffeine, cold and exercise on multiple choice reaction time, *Psychopharmacology*, 157:2, p. 197-201
206. Groen J.C., Pefer L.A.A., Perez-Ramirez J. (2003) Pore size determination in modified micro- and mesoporous materials. Pitfalls and limitations in gas adsorption data analysis, *Microporous and Mesoporous Materials*, 60, p. 1–17
207. Sing K.S.W , D. H. Everett, R. A. W. Haul, L. Moscou, R. A. Pierotti, J. Rouquérol, T. Siemieniewska, (1985), Reporting Physisorption Data for Gas/Solid Systems With Special Reference to the Determination of Surface Area and Porosity, *Pure and Applied Chemistry*, 57, 603
208. McQuarrie Donald A. (1997) Physical Chemistry: A molecular Approach. Sausalito: University Science Books
209. Smith C. (1996), Fundamentals of Fourier Transform Infrared Spectroscopy, CRC press
210. Ma K., Van de Voort V.F., Sedman A., Ismail A. (1997) Stoichiometric determination of hydroperoxides in fats and oils by fourier transform infrared spectroscopy, *Journal of the American Oil Chemists Society*, 74: 8, p. 897–906
211. Bumbrah G.S, Sharma R.M. (2016), Raman spectroscopy – Basic principle, instrumentation and selected applications for the characterization of drugs of abuse, *Egyptian Journal of Forensic Sciences*, 6, p.209-215
212. Warren Ball (2006), Field Guide to Spectroscopy
213. [https://www.researchgate.net/publication/277907574 Real-time microscopic phase-shifting profilometry/figures?lo=1](https://www.researchgate.net/publication/277907574_Real-time_microscopic_phase-shifting_profilometry/figures?lo=1)
214. Nagai T., Ito T., Hattori T., Yamanaka T. (2000), Compression mechanism and amorphization of portlandite, *Physics and chemistry of minerals* p. 462-466
215. Antao S.M., Hassan I. (2010) Temperature dependence of the structural parameters in the transformation of aragonite, *The Canadian Mineralogist*, 48-5, p. 1225-1236.

216. Habte N., Shiferaw D. Mulatu T., Thenepalli R., Chilakala J.W. Ahn (2019), Synthesis of nano-calcium oxide from waste eggshell by sol-gel method, *Sustainability*, 11, p. 31-96
217. Tang H., Yu J., Zhao X. (2009), Controlled synthesis of crystalline calcium carbonate aggregates with unusual morphologies involving the phase transformation from amorphous calcium carbonate, *Materials Research Bulletin*, p. 44,831–835
218. Margalha M.G., Santos Silva A. Veiga M.R. De Brito J., Ball R.J., Allen G.C. (2012) Microstructural changes of lime putty during ageing, *Journal of Materials in Civil Engineering*, 25, p. 1524-1532
219. Daniele V., Taglieri G (2010), Nanolime suspensions applied on natural lithotypes: The influence of concentration and residual water content on carbonatation process and on treatment effectiveness, *Journal of Cultural Heritage*, 11, p.102–106
220. Cho S.-H., Kim J.-Y., Chun J.-H., Ki, J.-D. (2005), Ultrasonic formation of nanobubbles and their zeta-potentials in aqueous electrolyte and surfactant solutions *Colloids and Surfaces A: Physicochemical and Engineering Aspects*, 269, p. 28-34
221. Oh S.H., Kim J.-M. (2017), Generation and stability of bulk nanobubbles *Langmuir* 33, p. 3818- 3828
222. Ohgaki K., Khanh N.Q., Joden Y., Tsuji A., Nakagawa T. (2010), Physicochemical approach to nanobubble solutions *Chemical Engineering Science* 65-3, p. 1296-1300
223. Azevedo A., Etchepare R., Calgaroto S., Rubio J. (2016), Aqueous dispersions of nanobubbles: Generation, properties and features. *Minerals Engineering*, 94, p. 29-37
224. Kyzas Z., Bomis G., Kosheleva R.I., Efthimiadou E.K., Favvas E.P., Kostoglou M., Mitropoulos, A.C. (2018). Nanobubbles effect on heavy metal ions adsorption by activated carbon, *Chemical Engineering Journal* 356, p.91-97
225. Mitropoulos, A.C., and Bomis, G. 2016. European Patent 2995369A1
226. Mitropoulos, A.C., Stefanopoulos, KL., Favvas, E.P., Vansant, E.F. Hankins, N. (2015), On the Formation of Nanobubbles in Vycor Porous Glass During Desorption of Halogenated Hydrocarbons, *Scientific Reports* 5:1, p.9-14
227. Favvas E., Mitropoulos A., Bomis G., Varoutoglou A., Kosheleva R., Michailidi E. and Efthimiadou E. (2017), Hellenic Industrial Property Organisation Application for Patent (Submitted)

228. Michailidi E.D, A., Bomis G., Varoutoglou A., Efthimiadou E.K., Mitropoulos A.C. and Fawvas, E.P., (2019), Fundamentals and applications of nanobubbles in Kyzas, G. Z. and Mitropoulos, A.C. Advanced Low-Cost Separation Techniques in Interface Science, Volume 30 Academic Press
229. Egerton R. (2007), Physical Principles of Electron Microscopy: An Introduction to TEM, SEM, and AEM, Springer
230. Rodriguez-Navarro C., Vettori I., and Ruiz-Agudo E. (2016), Kinetics and mechanism of calcium hydroxide conversion into calcium alkoxides: implications in heritage conservation using nanolimes. *Langmuir* 32, p. 5183-5194
231. Schimid T., Dariz P (2015), Shedding light onto the spectra of lime: Raman and luminescence bands of CaO, Ca(OH)₂ and CaCO₃, *Journal of Raman Spectroscopy*, 46:1, p. 141-146